An advanced instrument for Time- and Angle-resolved photoemission spectroscopy

A Dissertation presented

by

Peng Zhao

to

The Graduate School

in Partial Fulfillment of the

Requirements

for the Degree of

Doctor of Philosophy

in

Chemistry

(Physical Chemistry)

Stony Brook University

August 2019

Stony Brook University

The Graduate School

Peng Zhao

We, the dissertation committee for the above candidate for the

Doctor of Philosophy degree, hereby recommend

acceptance of this dissertation

Thomas K. Allison - Dissertation Advisor
Assistant Professor, Departments of Physics and Chemistry

Michael G. White - Chairperson of Defense
Professor, Department of Chemistry

Christopher J. Johnson - Third Internal Member
Assistant Professor, Department of Chemistry

Jerzy T. Sadowski - External Outside Member
Staff Scientist, Brookhaven National Laboratory

This dissertation is accepted by the Graduate School

Eric Wertheimer
Dean of the Graduate School

Abstract of the Dissertation

An advanced instrument for Time- and Angle-resolved photoemission spectroscopy

by

Peng Zhao

Doctor of Philosophy

in

Chemistry

(Physical Chemistry)

Stony Brook University

2019

Time- and Angle-resolved photoemission spectroscopy (tr-ARPES) from surfaces can be used to record the dynamics of electrons and holes in condensed matter and chemical reactions on ultrafast time scales. Applying extreme ultraviolet (XUV) light to tr-ARPES can greatly increase the energy and momentum range probed in these experiments. However, tr-ARPES experiments with XUV are technically challenging for various reasons such as the availability ultrafast XUV sources, space charge effects, the difficulty of constructing XUV beamlines and electron collection and detection efficiency. The data rate in tr-ARPES presents a major challenge, and thus has mostly restricted tr-ARPES experiments to strongly excited samples. However, many areas of interesting physics can only accessed by pertubatively excited tr-ARPES, such as observing various quasiparticle dynamics in solids.

I have designed and developed an advanced XUV tr-ARPES instrument with significantly improved performance. This instrument consists of a novel light source, an XUV beamline and an advanced photoelectron detector. Space charge effects, which have severely limited previous efforts, are elimi-

nated by employing an ∼80 MHz XUV light source based on cavity-enhanced high harmonic generation (CE-HHG). The light source and beamline deliver tunable XUV light pulses (8 eV to 40 eV, <100fs) with flux up to 3 $\times 10^{11}$ photons/second to the sample. This enables ultrafast time-resolved ARPES experiments with nano-Ampere sample photocurrents comparable to those employed in synchrotron experiments. This is an increase of approximately two orders of magnitude compared with conventional HHG sources at comparable energy resolution and spot size.

The electron detector is critical for the tr-ARPES instrument. I have implemented a time of flight electron momentum microscope (TOF k-mic). This detector features highly parallel electron detection in energy and momentum space, full solid angle collection, and μm spatial resolution. We have been improving its performance such as electron filtering so it adapts to the 80 MHz tr-ARPES experiments. This detector improves the data rate by approximately another two orders of magnitude.

I benchmark the performance of the instrument by static photoemission and laser assisted photoelectric effects (LAPE) on Au(111). The time resolution of the instrument is 180 fs which is measured by the cross correlation of the LAPE signal. I demonstrate perturbatively excited time resolved photoemission by studying the ultrafast electron dynamics of a thin C60 film. Spatial-, time- and angle- resolved photoemission spectrocopy on a highly oriented pyrolytic graphite sample is also discussed.

In all, we believe this instrument improves the data-rate for ultrafast time-resolved ARPES measurements by approximately 4 orders of magnitude, enabling experiments in a qualitatively new regime.

Dedication Page

To my mother Qimei Liang and my wife Yue Shi

Contents

List of Figures

Acknowledgements

I would like to thank my adviser Prof. Thomas Allison. Tom has been always inspiring not only as an enthusiastic and responsible scientist but also as a dedicated advisor who values my education. I would like to thank Prof. Michael G White, who has helped me over my PhD like an co-adviser. I would like to thank Dr. Christopher Corder who worked with me for most years of my Ph.D. Chris trained me how to work and think as an experimentalist. We had great time working together to build this wonderful tr-ARPES machine. I would like to thank Jin, who is going to take over this project and move it forward. I also thank other excellent coworkers in Allison lab, including Yuning, Xinlong, Prof. Melanie Reber,Myles Silfies, Anthony Catanese, Jose Bautista, Jay Rutledge for helping me out in the lab. There are definitely more people supposed to be included in the list and excuse me for not listing all names here. I would like to thank my other thesis committee members Prof. Christopher Johnson and Jerzy (Jurek) Sadowski. I would like to thank Dr. Matthew Kershis and Dr. Amanda Muruca for helping me in BNL. I also would like to thank Prof. Phillips Johnson, Prof. Trevor Sears, Prof. Michael White for generous equipment donations. I'd like to thank the awesome staff members in the physical machine shop and chemistry electronic shop.

I would like to thank my wife Yue Shi who has been so dedicated and supportive. No man succeeds without a good woman behind him. Thank you for the delicious meals every day and selfless support. I would like to thank my little angel Sophia Zhao who filled the my life with love and happiness. I would like to thank my mother-in-law Chunxiang Yue and father-in-law Jun Shi who is so kind and supportive. I would like to thank my sister Yuhui Zhao who is so sweet and help me so much when I had a baby. Last, I would like to thank my parents Qimei Liang and Lirong Zhao. My father taught me keep fighting and never give up while my mother gives me all her love, care and trust. Their wisdom benefits me throughout my life.

Chapter 1

Introduction

1.1 Angle resolved photoemission spectroscopy

In 1887, Hertz discovered that the solid surface can emit electrons under the radiation of UV light which is known as photoelectric effect [17]. In 1905, Albert Einstein explained this phenomenon by the hypothesis that the light waves consist of tiny bundles or packets of energy known as photons [17]. When the photons impinge on the solid surface, the energy of the photons $h\nu$ is absorbed by the electrons. If the energy of the photon is higher than an energy barrier known as work function ϕ, the electrons then can escape the surface and become free electrons with kinetic energy K. These emitted photoelectrons are characteristic of their original electronic states, and the information of energy level structure in its matrix material can be probed by the kinetic energy of the photoelectrons K. The binding energy U of the electrons is given by

$$U = h\nu - K - \phi \tag{1.1}$$

Equ. (1.1) is simply the results of energy conservation. This technique is known as photoemission spectroscopy. It has been widely used to measure the the energy levels of atomic and molecular orbitals [18, 19]. Photoemission spectroscopy is one of the important techniques for measuring the energy level structures because of the following reasons:

- As shown in Equ. (1.1), the definition of binding is very simple and clear. The measurement results of photoemission spectroscopy are very intuitive and straightforward to interpret.

- Photoemission spectroscopy can be applied to a wide range of materials. Compared to absorption spectroscopy, in order to study certain transitions, specific wavelengths are required, photoemission is mostly an allowed process and no dark state exists.

- Photoemission spectroscopy is very sensitive. The electron detection is very sensitive and single electrons can be detected. The measurement results can have orders of magnitude dynamic range. Energy levels with small density of states can be detected.

- Photoemission spectroscopy can be done with high resolution. The modern electron energy analyzer can have an energy resolution on the order of meV, when used with narrow linewidth light sources, the binding energy of electrons can be determined with meV resolution.

Moreover, in the case of crystal surface, Angle resolved photoemission spectroscopy (ARPES) can directly measure the energy dispersion relation or band structure. The momentum of the photoelectrons in free electron state is given by

$$\hbar k = \sqrt{2mK} \tag{1.2}$$

where m is the electron mass. Because translational symmetry requires that the component of electron momentum on the surface be conserved, the momentum of electron parallel to the surface $k_{\parallel}$ can be measured by the angle of the electron emitted on the surface θ as shown in Fig. 1.1.

$$\hbar k_{\parallel} = \sqrt{2mK}\sin\theta \tag{1.3}$$

The perpendicular component of momentum $k_{\perp}$ cannot be determined directly since the momentum normal to the surface is not conserved. In order to determine the value of $k_{\perp}$, several approaches have been proposed [17]. One typical way is based on the assumption of a free electron final state in the crystal. In this case, the value of $k_{\perp}$, can be determined as:

$$\hbar k_{\perp} = \sqrt{2m(h\nu + V_0)} \tag{1.4}$$

where V_0, the so-called "inner potential", is the band depth from the vacuum level. It can be determined by examining only the electrons emitted perpendicular to the surface [20].

For condensed matter research [21, 22, 23], ARPES can probe the momentum dependent electronic structure of solids providing detailed information on band dispersion and Fermi surface as well as on the strength and nature of many-body correlations, which may profoundly affect the macroscopic physical properties. It is of vital importance in elucidating the connection between electronic, magnetic, and chemical structure of solids, in particular for those complex systems which cannot be appropriately described within the independent-particle picture. Besides its application in condensed matter research, ARPES is also applied in physical chemistry. For example, in the heterogeneous catalysis reactions, chemical reaction happens at the interface of the solid catalyst and the adsorbate. The band structure of the catalyst plays an important role in the chemical reaction [24, 25]. On the other hand, it has been demonstrated that ARPES can also be used to directly image the molecular orbitals of the adsorbate molecules in the momentum space [26]. This enables direct observation of the evolution of molecular orbitals in the chemical reactions.

1.2 Time resolved angle resolved photoemission spectroscopy

Although the APRES has been widely applied for scientific research, only occuped electronic state can be probed by APRES, this limits the application of ARPES to the electronic states below the Fermi level. A full understanding of the material properties requires studying the unoccuped or excited states and associated dynamics processes involved with over a wide range of time scales. For example, one important part of condensed matter physics study is various dynamics of quasiparticles such as electron - electron scattering, electron - phonon coupling, and phonon - phonon coupling. The time scale of these interactions spans over several orders of magnituide from less than a femtosecond to microsecond or longer. These interactions affect the electronic and thermal properties of the materials in a fundamental way. Similarly, chemical dynamics also consists of various dynamics such as bond-breaking and bond-making, surface diffusion, adsorption and desorption, intermediate states formation and dissociation. These processes also span several orders of magnitude time scales. Moreover, many elemen-

tal processes in chemical reations are kinetic processes with barriers. The time scale of these processes can vary orders of magnitude depending on the activation energy and the temperature. For example, photo-induced chemistry reaction on the semiconductor surface is a very complicated dynamic process [27, 28, 29, 30, 31, 32]. Photo absorption can happen in less than 1 fs. The photo-excited carriers, generated in the bulk, move to the surface/interface and induce the photovoltage effect in the time-scale from 10 fs to 10 ps. The carriers recombine through radiative or non radiative pathways in the fs scale to ns scale. The subsequent charge transfer and separation processes, which consist of various elementary processes, proceed in a wide time scales from 10 fs to 10 ps. Both the excited states of adsorbate molecules and substrate material play an important role in this process.

Hence a detailed understanding of physcial and chemical properties requires a time resolved spectroscopy method with femtosecond time resolution and nanosecond or longer time span. Therefore, there exists a strong and growing need for time- and angle- resolved photoemission spectroscopy (tr-ARPES) with sub-pico second time resolution.

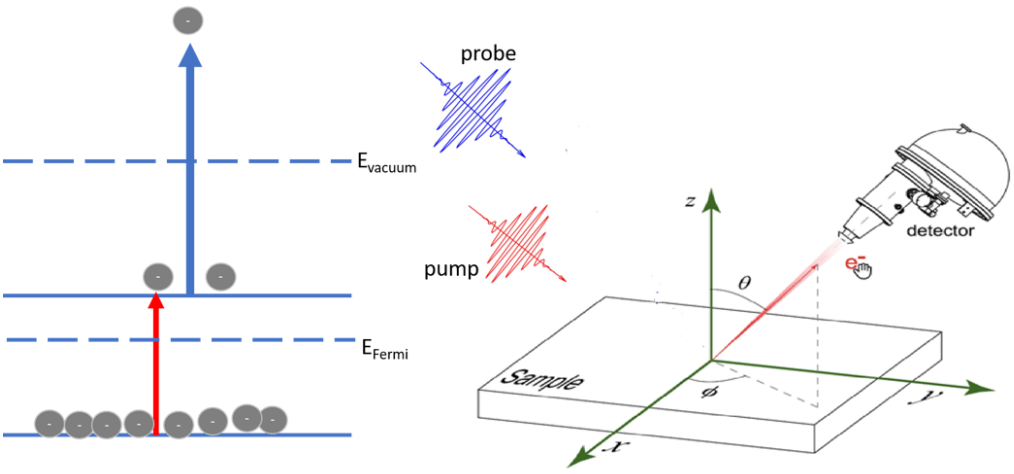

Figure 1.1: Schematic representation of time resolved angle resolved photoemission spectroscopy Instrument.

The typical tr-ARPES experiment set up is shown in Fig. 1.1. It adopts a pump probe configuration. A pump pulse is used to excite a small fraction of the electrons in the material to the excited states above the Fermi level. After a time delay, the probe pulse comes and ejects electrons from the

material. The kinetic energy and the emission angle of the ejected electrons are measured by an electron detector. A hemispherical energy analyzer or a time of flight detector is typically used in ARPES experiments. By scanning the time delay, the dynamics of the transiently populated excited states can be recorded.

Time- resolved ARPES has emerged as a leading experimental technique to investigate the electron dynamics. However, most of the tr-ARPES experiments reported in the literature are two photon photoemission (2PPE) experiments based on UV/VIS sources so far [33]. The reason is the limited availability of high photon energy sources. Compared to the 2PPE experiments, XUV wavelength with photon energy 10-100 eV is highly desirable for the following reasons:

- Good surface sensitivity. According to the universal curve [34], the inelastic mean free path of electrons in the solid has a minimum at 10 − 100 eV, and is typically less than 1 nm , so XUV light is essentially probing the surface electronic structure.

- Deep energy range. As shown in Equ. (1.1), the energy range can be probed is not bigger than the photon energy. Compared to the 2PPE experiments using visible/UV sources, the XUV photon energy usually is enough to cover most molecular orbitals and the valence bands of solids.

- Broad momentum range. As shown in Equ. (1.3) and Equ. (1.4), the momentum range that can be probed in photoemission experiments is also related to the photon energy. XUV light is usually needed in order to probe the full Brillouin zone of the solid and molecules.

- Less background. The majority of electrons produced in photoemission experiments are the secondary electrons. The large background made of secondary electrons can add noise to the signal. With the high photon energy of XUV, the signal is lifted to the high kinetic energy part of the spectrum, leaving the secondary tail in the low energy part. Thus, the measurements can have higher signal to noise ratio.

1.2.1 Data rate in tr-APRES experiments

The data rate of tr-ARPES experiments with XUV light source is demanding for several reasons.

- Multidimensional data binning. In ARPES experiments, data is already dispersed in energy and momentum space. In tr-ARPES, the pump excitation adds additional dimensions to the data set. At a minimum, data should be recorded at several pump-probe delays and pump fluences, and there are also the parameters of pump wavelength and polarization.

- Inherently small signal. In tr-ARPES experiments, the signal of interest is inherently small, since only a small fraction of the samples electrons are excited by the pump. The excitation fraction is usually limited by sample damaging, space charge effects or the physics of interest. The time resolved signal is thus orders of magnitude smaller than the signal from occupied states.

- Space charge effects. As will be discussed in section. 1.3, space charge effects limits the number of electrons per pulse produced by the probe pulse. For the XUV experiment, this is particularly a problem because the most electrons are secondary electrons that don't contribute to the signal but contribute to the space charge effects.

Pertubatively excited tr-ARPES

Due to the demanding data rate in tr-ARPES, experiments have then been almost exclusively restricted to strongly excited samples using absorbed fluences on the order of 1 mJ/cm^2 such that laser excitation produces changes to the EDC visible on a linear scale. [35, 32] For high fluence nonperturbative experiments, the physics under study is usually photoinduced phase transitions or nonthermally accessible metastable states having a well-defined order parameter. There are a lot of interesting physics that can only be accessed in the low-fluence regime (< 100 μJ/cm^2) [36, 37]. Some examples and their lifetime are shown in Fig. 1.2. In condensed matter physics, tr-ARPES is widely used to study various elementary process in the material such as charge carrier dynamics and electron phonon coupling. The density of the excited electron strongly influence the dynamic process. For example, in Ref. [38], tr-ARPES is used to measure the photoinduced vaporization of a charge ordered state in the potential excitonic insulator 1T-$TiSe_2$. As the pump fluence increases from 200 μJ/cm^2, to 5 mJ/cm^2, the lifetime of the long range ordered excited state becomes exceptionally short, and strongly depends the pump fluence. The reason is that transiently generated high

density free carrier dominates the electron dynamics instead of the oscilation of the charge density wave. As another example, in Ref. [39], tr-ARPES is used to study the electron thermalization and electron-phonon coupling in photoexcited bismuth. The electron life time strongly depends on the pump fluence. As the pump fluence increases from 120 μJ/cm^2 to 840 μJ/cm^2, the lifetime of excited states goes from a few hundred fs to less than their time resolution (50 fs). The lifetime is dominated by the electron-phonon coupling in low fluence regime while in high fluence regime, the lifetime is dominated by electron-electron interaction. In the chemical reaction studies, there exist similar excited molecular annihilation processes. For example, Ref. [40] reports the excitation fluence dependence of the singlet fission in a crystalline rubrene, as the fluence change from 100 μJ/cm^2, to 20 mJ/cm^2, the singlet exciton lifetime is significantly shorten due to the singlet-singlet annihilation. Besides the high density excition, the sample damaging effect and sample heating effects in high rep rate experiments can also restrict the pump fluence.

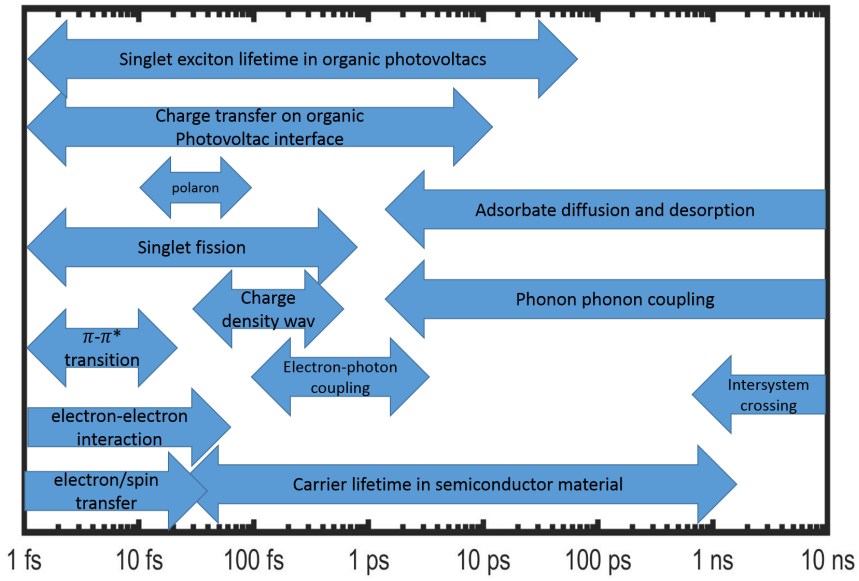

Figure 1.2: The physics only accessible in pertubatively excited tr-ARPES and their timescales.

The excitation fraction in perturbatively excited tr-ARPES experiments

should be on the order of 10^{-3} or less. Compared to the static ARPES experiments, the signal is then orders of magnitude smaller. Usually, experiments need be repeated at several different pump fluence to check the results. The data rate and signal to noise of tr-APRES experiments is challenging.

Spatial resolved tr-ARPES

In ARPES experiments, a typical beam spot size in the synchrotron light source is about a few hundred micrometers. In the lab environment, discharge lamps are widely used. The spot size of the lamps can be much bigger. The measurement result is an average of the material over the beam spot. The typical sample used for ARPES is a single crystal. However, for many interesting materials, growth of a few hundred micrometer single crystal is hard. For example, the typical single crystal domain size of transition metal dichalcogenides is a few μm [41]. The measurements averaging over large area of the inhomogeneous sample can blur and even completely miss the desired feature. In such cases, the capability of spatially resolving the sample is required in the ARPES experiment on the inhomogeneous sample.

Performing ARPES and tr-ARPES experiment on μm sized sample spot pose significant challenges [42]. There are typically two ways to do this. First, if the light source can provide a extremely small beam spot, less than a single domain size, then APRES experiment is naturally spatial resolved. The spatial resolution is roughly the beam spot size. However, to achieve such a small beam spot, dedicated focusing optics are required [43]. Only a few synchrotrons like Advanced Light Source (ALS) have such setups. The availablity is the problem. Besides that, the synchrotron light has long pulse duration. tr-ARPES with femtosecond resolution can't be performed. It also requires a high precise sample positioning, especially when the sample has to be rotated to scan the momentum space. The other way is to use a photoemission electron microscope (PEEM) machine with a small field aperture as discussed in chapter 8. The spatial resolution comes from the field aperture cropping the region of interest on the sample. The spatial resolution can be less than a micrometer. The beam spot size can be much bigger than the domain size of the crystal assuming sufficient photon flux. It also relieves the requirement of the sample position accuracy. As long as the sample is position well enough so the PEEM can work properly, the sample positioning is fine. Compared to the hemisphere energy analyzer which has a typically collection angle less than 30 degrees, it has full solid

angle collection, no sample rotation is needed for the experiments. However, the spatial resolution comes at the cost of significant loss of the data rate. The data rate loss is due to the beam spot may be much bigger than the region of interest. All the electrons coming out is region of interest is blocked by the field aperture. The signal loss is proportional to the ratio of beam area to the region of interest. In the case of 100 μm spot size and 1 μm spatial resolution, the loss is 4 orders of magnitude. The data rate in the tr-ARPES experiments is already challenging, with spatial resolution, the data rate is even more challenging.

Space charge effects also play an interesting role here. Since the space charge effects blur not only the energy resolution but also the spatial and angle resolution. In the space charge limited system, making the beam size smaller doesn't necessarily increase the data rate. Space charge effects ultimately limits the photon flux and data rate as the beam spot size shrinks.

1.3 Space Charge Effect

Time resolved ARPES experiments on the solid surface is technically challenging, particularly restrictive in its data rate and data quality. One of the major limitations is the well known space charge effects. Because tr-ARPES experiment typically requires small spot size, low rep rate sources can generate high density electrons on the surface, The Coulomb repulsion within a short electron cloud can distort the energy distribution of the electrons and result in a considerable loss in data fidelity and restricts the data rate of the experiments. In XUV experiments, most electrons are the secondary electron with low kinetic energy, those secondary electrons usually don't have information of binding energy but still contributes to the space charge effects which cause distortion to the primary electrons. Moreover, in tr-ARPES, a pump beam is used to excite the sample. An intense pump pulse can also generate electrons through multi-photon ionization, and the electrons generated by the pump beam all contribute to the space charge effects. The indication of the space charge effects are, for example, the broadening and shifting of electron energy distribution, high energy electron tail and the appearance of the ghosting peaks.

As discussed in Ref. [44, 45], the spacial distribution of the electron cloud can strongly influence the space charge effects. As shown in Fig. 1.3, the electrons starts with velocity v, the average distance between cloud electrons

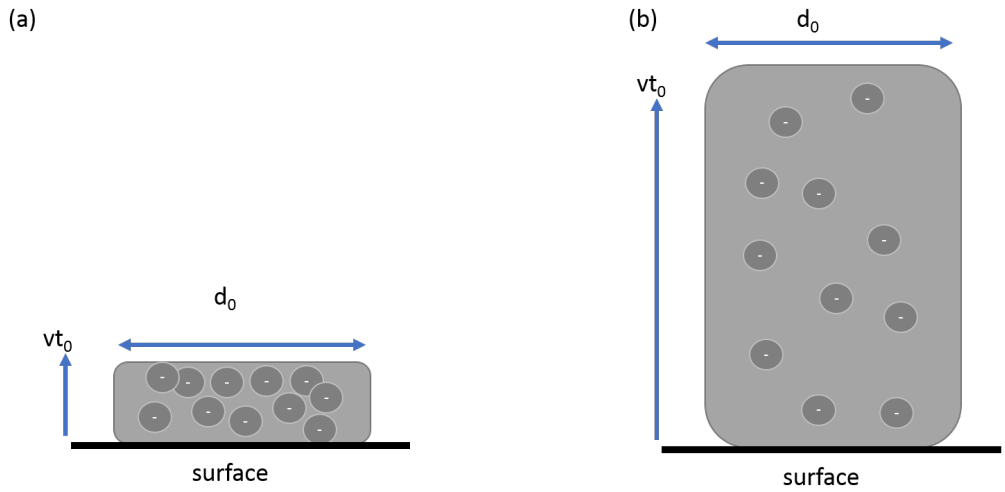

Figure 1.3: Comparison of space charge effects in short pulse regime (a) and long pulse regime (b).

perpendicular to the surface is determined by vt_0 where t_0 is the pulse duration and characteristic length parallel to the surface is the source size d_0. In the short pulse regime in which $vt_0 \ll d_0$, all the electrons reside in a quasi 2D slab on the surface as shown in Fig. 1.3 a) while in long pulse limit where $vt_0 \gg d_0$, the electrons forms a column shape shown in Fig. 1.3 b). The femtosecond pulses generate slab shaped electron cloud which has greater electron density while the electron cloud generated by synchrotron pulse with $\sim$ 100 ps pulse duration is between the slab shape and the column shape, depending on the spot size. For the beam spot size on the order of 100 μm, the electron cloud is still close to the slab shape, while for the tens of nm spot size used in nano-Arpes, the electron cloud is column shaped, the electron density is strongly diluted due to the temporal spread [44, 45]. Because of that, The femtosecond pulse which generates a thin slab shaped electron cloud cause more severe space charge effects [46].

Since electrons are born on the surface with a high potential energy, as the electron cloud leaves the surface and propagates, its potential energy is released into kinetic energy, and cause a change in observed kinetic energy and redistribution of energy between electrons. Some electrons speed up, others slow down. The energy broadening ΔE_b and shifting ΔE_s have been extensively studied by experiments and simulations [47, 48, 49, 50, 51, 52, 53].

In the short pulse limit, The scaling of ΔE_b and ΔE_s is proportional to the linear electron density shown in Equ. (1.5), N is the total number of electrons, D is the diameter of the electron spot, and $m_{b(s)}$ is the scaling constant. The electron density can be written with sample current I_{sample} and the rep rate f_{rep}

$$\Delta E_{b(s)} = m_{b(s)} \frac{N}{D} = m_{b(s)} \frac{I_{\text{sample}}}{e f_{\text{rep}} D} \tag{1.5}$$

This linear scaling makes bigger spot size less effective in order to reduce the space charge effects. Plus tr-ARPES experiments usually can't use a spot size much bigger than a milimeter due to the momentum resolution and the required pump power. In ref. [53], classical simulation method is used to model electron cloud propagation in free space, their simulation confirms the linear scaling relation. The scaling factor has been experimentally measured by several groups. These measurements generally agree with each other within a factor of two. for exmaple, in ref. [50] by Plötzing et. al, the 3d peak of Cu(001) surface is used to monitor the space charge effect of a HHG based source, the scaling constant m_b is measured to be 2.1 meVμm , and m_s is measured to be 3.15 meV$\cdot\mu$m. Using a synchrotron, in ref. [49] by Zhou et. al, the fermi edge of a gold polycrystaline is used to study the space charge, m_b is measured to be 2.9 meV$\cdot\mu$m , and m_s is measured to be 2.2 meVμm.

Due to space charge effect, for the low rep rate HHG based light source, even achieving moderate energy resolution is challenging. For example, to achieve 50 meV energy resolution with a 100 μm spot size, the electrons need be less than 2500 e/pulse, assuming 1 kHz rep rate source, the attainable sample current is less than 1 pA. Compared to the nanoamps sample current typically achieved at the synchrotron light source, the data rate is orders of magtitude lower. In term of usable photon flux, assuming 10% quantum efficiency and 20 eV photon energy, the usable power is less than 100 pW, but such an HHG source typically can generate XUV light on μW power level. Only tiny amount of the light can be used in the experiments.

In photoemission electron microscope (PEEM) experiments, space charge effects are even a bigger problem. In a conventional electron detector, the energy distortion happens during a short propagation distance after the electrons leave the surface. In PEEM, all the electrons are accelerated and sucked by its objective lens and travel through the electron optics. The space charge occurs, to a large extent, due to the propagation inside the PEEM [54, 55].

The space charge effects not only affect the energy distribution, but also the imaging resolution. Ref. [55] shows the ultimate spatial resolution of the PEEM is limited by the space charge effect. With a beam spot size of $\sim$10 μm, 600 electron/pulse gives a resolution of 18 nm which is much bigger than the theoretical resolution 2 nm. A detailed discussion about space charge effects in PEEM is in section. 8.5.

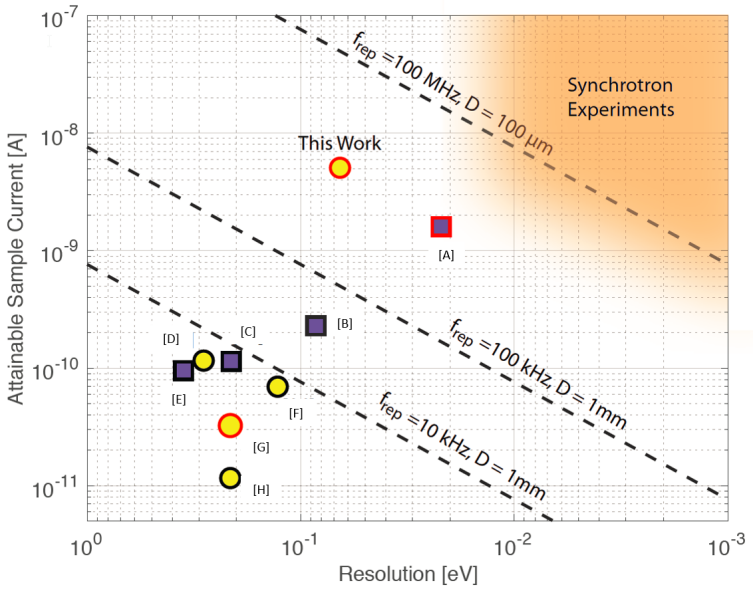

Figure 1.4: Constraints on sample current and energy resolution due to space charge effects. Dashed lines are created by evaluating Equ. (1.5) for different repetition rates assuming 1 mm spot size and symbols represent published results applying HHG to surface photoemission. A in Ref. [1],B in Ref. [2],C in Ref. [3], D in Ref. [4], E in Ref. [5], F in Ref. [6], G in Ref. [7],H in Ref. [8]. This figure is adapted from Ref. [9].

Equ. (1.5) indicates the space charge effect is inversely dependent on the rep rate of the source. This can be understood by the number of electron per pulse decreases as the rep rate increases if the sample current is kept as a constant. Increasing the rep rate is an effective way of mitigating the space charge effects. Figure 1.4 illustrates the constraints on attainable sample current for a given resolution according to Equ. (1.5). The dashed lines indicate the space charge limits for sub-ps laser-based systems of different

repetition rates assuming a 1 mm spot size - large by ARPES standards. Yellow circles represent results from tunable HHG systems and purple squares represent setups where the photon energy is not tunable in-situ. Symbols with black edges represent space-charge limited spectrometers, and symbols with red edges represent systems that are not yet space-charge limited. For space-charge-limited systems, the (x, y) positions represent the case where space charge broadening and the photon bandwidth add equally in quadrature. Even at the high repetition rate of 100 kHz and the coarse resolution of 100 meV, space charge constraints still limit the sample current to 760 pA. These low data rates then often restrict experiments to strongly excited samples using absorbed fluences on the order ~ 1 mJ/cm^2 [35, 32, 56]. At these fluences ultrashort pump pulses also produce many electrons through multiphoton processes which add to the space-charge problem [57, 58, 59].

The inverse dependence of Equ. (1.5) on f_{rep} has motivated a great deal of work on high-power lasers and HHG source development. Although the highest HHG repetition rates have been reported using high-power frequency combs resonantly enhanced in optical cavities [60, 61], their reliability and suitability for time-resolved photoemission has faced skepticism from several authors [62, 63, 64]. Instead, there has been great investment in other approaches including HHG from high-power Ti:Sapphire and parametric amplifiers [63, 65], HHG from high power fiber lasers [66], HHG generated within [67] and at the output [68] of thin-disk lasers, HHG from solids [69, 70], and HHG in the near-fields of nanostructures [71]. Despite these intense efforts, HHG-based photoemission comparable to that done with tunable synchrotron radiation has not been realized using any platform. Some of the material in this section is reproduced from Ref. [9].

1.4 Considerations for tr-ARPES instrument

An ARPES instrument typically consists of three major sections: the light source, the beam line and the experiment end station. The development of the tr-ARPES instruments has been driven by the advance of the light source. The application of new light sources offers intriguing prospects for the investigation of ultrafast dynamics in complex electron systems. The considerations about the light source of tr-ARPES instrument includes:

- Photon energy. The photon energy determines the energy and momentum range of the experiment can probe. XUV (10-100 eV) is highly

desirable. Moreover, it is critical that photon energy can be tuned in the XUV range in order to study the dispersion relation perpendicular to the surface. Besides that, the selection rule and detailed spectrum shape is dictated by the dipole matrix element, which critically depends the final state of the electron [72]. The dipole matrix element therefore depends the photon energy which changes the final state. So tunable photon energy is useful to study the final state effects [73].

- Rep rate. To mitigate the space charge effects, high rep rate on the order of tens of Megahertz is required.
- Photon linewidth. The photon linewdith sets the fundamental limit of the energy resolution in the tr-ARPES experiments. Typically, < 100 meV photon linewidth is required. For some high resolution experiment, <10 meV is ideal.
- Photon flux. For fast data rate, the photon flux comparable to the synchrotron radiation which is higher than 10^{11} γ/s is required. Notice that in the low rep rate system, the usable photon flux can be severely limited by the space charge effects.
- Pulse duration. The pulse duration sets the time resolution in the tr-ARPES experiments. To study the electron related dynamic process, time resolution less than or on the order of 100 fs is typically required. Notice that the pulse duration sets the lower limit of the photon linewidth. In the tr-ARPES experiment, there is a trade-off between the time resolution and the energy resolution.
- Noise and long term stability. The noise performance of the light source sets an upper limit of the S/N of the instrument. The signals in the tr-ARPES experiments are usually small. To identify the small signal, a low noise and stable light source is critical.
- Cost. The cost of building the XUV facilities such as synchrotron and free electron laser can be enormous. It's important to control the cost for the lab environment.

The XUV beamline filters and delivers the photons to the experiments. The performance of the beamline is important for the overall instrument, particularly in the XUV wavelength. The considerations for the beamline includes:

- Broad tuning range. As the tunable photon energy is required in the experiments, the beamline is required to deliver the photons with tens of eV bandwidth.

- Wavelength selection. For a broad band source, the wavelength selection is necessary. The resolution of the wavelength selection may contributes to the final energy resolution of the instrument. Besides that, due to the high dynamic range of the electron detection, a "pure" single wavelength with high contrast is required. The contamination wavelength could cause potential confusions of the spectrum feature.

- Photon transmission. The majority of photons generated by the source could be lost in the beamline due to the difficulty of the XUV optics.

- Beam spot size. Beam spot affects the pump power required for certain fluence. It is also critical for the momentum resolution of the electron detector. For the conventional electron energy analyzer, a beam spot size < 100 μm is ideally used in the tr-ARPES experiments.

- Simple construction. Due to the high vacuum and sophisticated optics required by the XUV, The construction and alignment of the XUV beamline can be quite complicated.

The electron detector is critical for the tr-ARPES instrument. The hemisphere energy analyzer and the time of flight energy analyzer are the two common types used in the ARPES experiment. The consideration of the electron detector include:

- Electron detection efficiency. The electron detection efficiency is critical for the data rate.

- Electron energy resolution. Ideally, the energy resolution of the detector is smaller than the photon linewidth, so it doesn't affect the overall energy resolution. The state of art hemisphere energy analyzers have energy resolution of 1 meV while the time of flight detectors have demonstrated resolution on the order of 10 meV [16].

- Electron momentum range. The momentum range of ~ 2 $\mathring{A}^{-1}$ is typically needed for tr-ARPES. The momentum range of the detector is

related to the collection angle of the electron detector. Ideally, the detector can collect 2π solid angle which is the half side of the sphere. In that case, the momentum range is only limited by the photon energy.

- Electron momentum resolution. A typically tr-ARPES experiment requires the momentum resolution on the order of 0.1 $\mathring{A}^{-1}$.

- Maximum count rate. The maximum count rate of the detector sets an upper limit of the data rate. For the commonly used micro-channel plate (MCP) based detector, the maximum count rate is on the order of million counts per second(Mcps).

- Electron filters. The electron filters used to select the electrons in energy, momentum and real space are important for some tr-ARPES experiments. Besides that, electron filters are also critical when the data rate of the experiments is limited by the maximum count rate of the detector.

- Spatial resolution. For some samples such as 2D materials, the single crystal domain size is typically on the order of micrometer. The capability of spatially resolving the sample can greatly relieve the the requirement on the beam spot size.

1.5 High harmonic generation

There is a lack of suitable XUV sources for tr-ARPES experiments with femtosecond pulse duration. Synchrotron radiation provides high rep rate and high average flux XUV photons, but its pulse duration is inherently long [74]. The free electron laser (FEL) which is also an accelerator based facility can provide femtosecond XUV pulses with high flux, However, due to its low rep rate, the space charge effects severely limits the data rate of the tr-ARPES experiments. Besides the space charge effects, the fluctuation from pulse to pulse in FEL can be a concern.

The laser based light sources with extraordinary coherence and short pulse duration are ideal. However, there are few lasers working at XUV wavelength [75, 76]. This can be understood through a common scaling argument [77]. To obtain population inversion in the XUV wavelength, the excitation rate in the gain medium must be bigger than the spontaneous

emission rate which scales with third power of the optical frequency. Plus the photon energy of the pump also scales linearly with the optical frequency. The pump power needed to make a XUV laser is at least to the 4th power of the optical frequency. The amount of pump power required therefore is enormous.

Fortunately, the development of the ultrafast laser techology provides new ways of frequency upconversion such as high harmonic generation (HHG). The high harmonic generation was first observed first by McPherson and colleagues in 1987 [78] and and later by Ferray et al. in 1988 with better understanding [79]. With intense femtosecond laser pulse focused into a gas medium, high order harmonic can be generated. The high harmonics were found to decrease in intensity as the order goes up for the low orders, but then form a plateau, with the intensity of the harmonics remaining approximately constant extending into the XUV regime. Shortly after its discovery, HHG based XUV source was used for the ARPES experiments. [80, 81, 82].

In HHG, an atom is ionized by the field of the intense pulse. The ionization mechanisms can be classified into two main categories: the multiphoton ionization and the strong field ionizaiton. Multiphoton ionization occurs in the perturbative regime. The field required is much lower than the atomic field strength which is on the order of ~ 50 V/$\mathring{A}$. The atom is ionized due to the absorption of several photons simultaneously. The ionization rate strongly depends the number of photons required.

As the field strength approaches to the atomic field, the potential barrier of the atom is lowered and made short, leading to quantum mechanical tunneling of the electron wave function to the continuum. This is called strong field regime. The Keldysh parameter shown in Equ. (1.6) is typically used to estimated the field strength.

$$\gamma = \sqrt{\frac{I_p}{2U_p}} \tag{1.6}$$

where I_p is the ionization potential and U_p is the ponderomotive energy. The ponderomotive energy is defined as the average kinetic energy of a free electron in the oscillating light field. It can be calculated by Equ. (1.7)

$$U_p = \frac{e^2E^2}{4m\omega_0^2} \tag{1.7}$$

where E is the electric field amplitude, m is the electron mass and ω_0 is the

optical frequency. For a pulse with $\gamma \gg 1$, the multiphoton ionization is dominant. Usually HHG is conducted in a regime where $\gamma \sim 1$.

1.5.1 Three step model

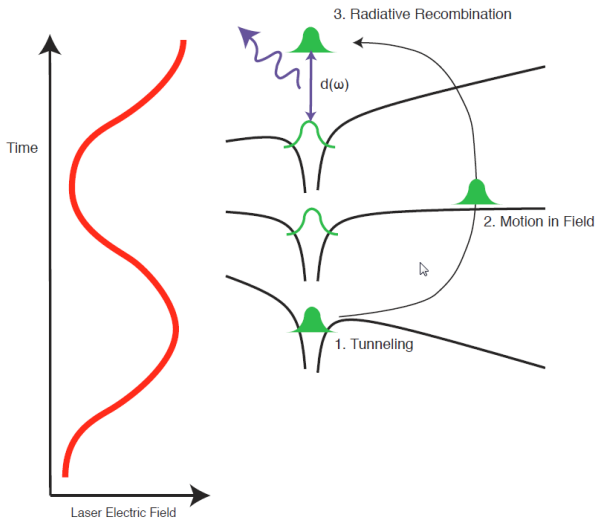

Figure 1.5: Schematic illustration of the three step model. Atoms are tunnel-ionized near a peak in the electric field. The electron can then gain kinetic energy from motion in the field and recombine, emitting a high energy photon. This image is taken from Ref. [10]

To fully explain the HHG process requires quantum mechanical treatment of the electron wavefunction under strong field [83, 84]. However, it is interesting that the many important features of HHG are well described by the semi-classical three-step model pioneered by Corkum [85] and Lewenstein [86], and illustrated in Fig. 1.5. In this simple model, the ionization mechanism of the electron from the parent ion is tunneling but the interaction of the free electron in the incident electric field is treated classically. In the first step, the electron tunnels out from the parent ion and get into free electron states with zero kinetic energy. In the second step, the free electron is accelerated by the the field like a classical particle, completely free from any influence of the ion. As the oscillating field reverses direction,

the electron will accelerate back towards the parent ion. In the third step, There is a chance that the free electron returns to the position of the parent ion, radiatively recombines and emits a photon. This photon will possess all the kinetic energy gained in the interaction with the driving field plus the ionization energy of the atom. The maximum of the photon energy which is the cut-off of the HHG spectrum can be calculated from consideration of the classical trajectories and is given by

$$\hbar\omega_c = I_p + 3.17U_p \tag{1.8}$$

Notice that U_p scales inversely with the square of the driving frequency because electron spends longer time in the field and gains more energy. It has been demonstrated that the harmonics generated by high power mid IR laser can extend all the way into hard X ray regime exceeding 1 keV photon energy. [87].

With multi-cycle drive laser pulses, the HHG happens every half cycle of the drive laser field. In the time domain, the harmonics are generated twice as the optical frequency of the drive field. As a result, in the frequency domain, the harmonics spectrum is characterized by discrete peaks separated by twice the photon energy of the drive laser.

1.5.2 Phase matching

The growth of harmonics power as it propagate through the target gas depends on the phase matching. The intensity of harmonic q generated over a medium with density ρ and length L can be described as Equ. (1.9) [88, 10, 89]

$$I_q(t) = \frac{|d_q(t)|^2}{\lambda_q^2} \frac{(\rho L)^2}{(\Delta k(t)L)^2 + (\alpha_q L)^2} \left(1 + e^{-2\alpha_q L} - 2e^{-\alpha_q L}\cos\left(\Delta k(t)L\right)\right) \tag{1.9}$$

where α_q is the absorption coefficient of the gas for harmonic q, λ_q is the harmonic wavelength, L is the medium length, ρ is the atom density, $\Delta k(t) \equiv qk_0 - k_q$ is the time-dependent wave-vector mismatch between the fundamental and the q-th harmonic, and $d_q(t)$ is the single atom HHG dipole at harmonic order q.

It is imperative that harmonics generated at the front of the gas target be in phase with harmonics generated at the back of the target. Otherwise destructive interference can occur and harmonic power will be affected. We

can define the time dependent phase matching factor $F_q(t)$ as the ratio of $I_q(t)$ to its value at $\Delta k = 0$ as shown in Equ. (1.10)

$$F_q(t) = \left| \frac{\alpha_q L e^{\alpha_q L}}{(i\Delta k(t) + \alpha_q) L} \left(e^{i\Delta k(t) L - e^{-\alpha_q L}} \right) \right|^2 \tag{1.10}$$

In the single pass HHG, F_q could exhibit a transient peak at a degree of ionization where dispersion due to the neutral gas atoms and the plasma electrons balance. Only harmonics generated during this time window satisfy the phase condition. This creates a so-called ionization gate on the harmonic emission. The transform limited harmonic line width in principle depends on the emission window of the harmonics an therefore can be broadened by the ionization gate.

Δk in the equation consists of four terms [10]:

$$\Delta k = q k_0 - k_q = \Delta k_{atomic} + \Delta k_{plasma} + \Delta k_{Gouy} + \Delta k_{dipole} \tag{1.11}$$

Δk_{atomic} is the phase mismatch caused by the neutral atoms. All the equation in the section will be in CGS unit. The index of refraction for a gas can be expressed in terms of the atomic scattering factors f_1^0 and f_2^0.[90]

$$n(\omega) - 1 = -\rho \frac{r_0 \lambda^2}{2\pi} \left(f_1^0(\omega) - i f_2^0(\omega) \right) \tag{1.12}$$

where r_0 is the classical radius of the electron. The numerial values of atomic scattering factors can be found in Ref.[10]. The index of the gas obviously depends on the density ρ or gas pressure. Then Δk_{atomic} also depends on the gas density

$$\Delta k_{atomic} = q \frac{\omega_0}{c} \left[n(\omega_0) - n(\omega_q) \right] = -q \rho r_0 \lambda_0 \left(f_1^0(\omega_0) - \frac{1}{q^2} f_1^0(\omega_q) \right) \tag{1.13}$$

The gas medium is rapidly ionized by the drive laser pulse in the HHG process. This forms a free electron plasma with time dependent plasma frequency

$$\omega_p(t) = \sqrt{\eta(t) \frac{4\pi \rho e^2}{m}} \tag{1.14}$$

where $\eta(t)$ is the time dependent ionization fraction. The index of refraction of plasma can be expressed as

$$n(\omega) = \sqrt{1 - \frac{\omega_p^2}{\omega^2}} \tag{1.15}$$

For the optical and XUV frequencies of the drive laser and the harmonics and gas densities used for HHG, $\omega_p \ll \omega$, and

$$n(\omega) - 1 \approx -\frac{1}{2}\frac{4\pi\rho e^2}{m\omega^2} \tag{1.16}$$

The time dependent phase mismatch caused by the plasma $\Delta k_{plasma}(t)$ can be expressed as

$$\begin{aligned}\Delta k_{plasma}(t) =& q\frac{\omega_0}{c}\left[n(\omega_0) - n(\omega_q)\right] \\ &\approx q\frac{\omega_0}{c}\left(-\eta(t)\frac{2\pi\rho e^2}{m\omega_0^2}\right) \\ &= -q\eta(t)\rho r_0\lambda_0\left(1 - \frac{1}{q^2}\right)\end{aligned} \tag{1.17}$$

The Gouy phase term Δk_{Gouy} comes from the fact that the fundamental and the harmonic experience different Gouy phase when they go through the focus. It depends on the HHG gas nozzle position z_c from the focus

$$\Delta k_{Gouy} = -\frac{q}{z_R}\frac{1}{1 + \frac{z_c^2}{z_R^2}} \tag{1.18}$$

where $z_R = \pi w^2/\lambda$ is the Rayleygh range of the gaussian beam. Notice that the Gouy phase term is purely geometrical and therefore scaled with z_R and it doesn't depend on the time or intensity at all. However,the phase mismatch caused by the Gouy phase Δk_{Gouy} is not a constant, it varies on the distance along the laser beam z. For the HHG with tight focus which means short z_R, the Gouy phase term could be the dominant phase error. Since the Gouy phase term Δk_{Gouy} rapidly changes with the distance, It makes sense to make the gas nozzle opening shorter than the Raighley range z_R in HHG. The Gouy phase also explains why the conversion efficiency of HHG with very tight focus is low, although high intensity on the order of 1×10^{14} W/cm^2 can be achieved with moderate pulse energy $\sim \mu$J and very tight focus on the order of μm.

The dipole phase term Δk_{dipole} depends the gas nozzle position z_c and the peak intensity

$$\Delta k_{dipole} = \frac{2|\alpha_q^j|I_{peak}}{z_R}\frac{\frac{z_c}{z_R}}{\left(1 + \left(\frac{z_c}{z_R}\right)^2\right)^2} \tag{1.19}$$

where α_q^j is the intensity dependent phase coefficient which depends on whether the harmonic is in the plateau or cutoff region of the spectrum and the quantum path dominating the single atom dipole. For harmonics in the plateau, $|\alpha_q^j|$ is 1×10^{-14} cm^2/W for the short quantum path and 25×10^{-14} cm^2/W for the long quantum path [91, 92].

The plasma and neutral gas dispersion have opposite signs and for long trajectories it's in principle possible to make them cancel each other at a certain plasma density (~ 10 % ionization [88]). The sign of the dipole term depends on the position of the gas nozzle with respect to the laser focus. It's possible to make the dipole term cancel the Gouy phase term in a short length window by positioning the gas nozzle before the focus.

1.6 Frequency Comb and enhancement cavity

High-power ultrafast lasers are usually required to drive high harmonic generation, providing XUV ultrashort pulses with a table-top setup. Due to the high pulse energy required by HHG, The repetition rate is then limited by the average laser power available, usually to less than 100 kHz. However, to mitigate the space charge effects in tr-ARPES experiments, higher repetition rate HHG source is ideal. An elegant way to achieve this is via resonant enhancement of the fundamental pulse train in a femtosecond enhancement cavity[93, 94] The technique is called cavity enhanced high harmonic generation (CE-HHG).

1.6.1 Energy relations in optical cavities

Here we briefly introduce the fields and intensities calculation in ring cavity [95]. Consider the 6 mirror bowtie cavity shown in Fig. 1.6, with a input coupler mirror and 5 high reflector mirrors with the same reflectivity R. The incident light field is E_0, the circulating field is E_c and the total reflected field is E_r. The field transmission and reflection coefficients of the input coupler are t_1 and r_1. Using the convention in [96], r_m given by r^5 where $r = \sqrt{R}$ is field reflection coefficient of the other mirrors. r_m represents the total reflection of the other 5 mirrors.

The total phase shift of one round trip is ψ. The total reflected field E_r is a sum of the reflected field and the transmitted field through the input

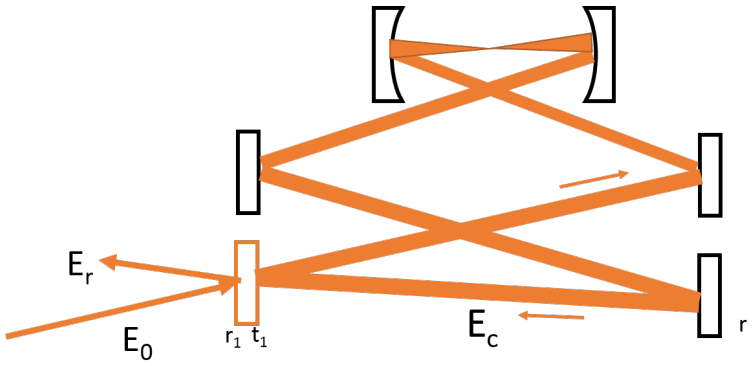

Figure 1.6: A schematic of ring-cavity to show the fields and intensities.

coupler from different round-trips.

$$\begin{aligned} E_r &= -E_0 r_1 + E_0 r_m t_1^2 e^{-i\psi} + E_0 r_1 r_m^2 t_1^2 e^{-2i\psi} + \dots \\ &= E_0 \frac{r_m e^{-i\psi} - r_1}{1 - r_1 r_m e^{-i\psi}} \end{aligned} \tag{1.20}$$

The field circulating the cavity is

$$\begin{aligned} E_c &= E_0 t_1 + E_0 r_1 r_m t_1 e^{-i\psi} + E_0 r_1^2 r_m^2 t_1 e^{-2i\psi} + \dots \\ &= E_0 \frac{t_1}{1 - r_1 r_m e^{-i\psi}} \end{aligned} \tag{1.21}$$

Using $cos\psi = 1 - 2\sin^2\frac{\psi}{2}$, we get the intensities of the reflected and circulating light.

$$\begin{aligned} I_r &= I_0 \frac{(r_1 - r_m)^2 + 4 r_1 r_m \sin^2 \psi/2}{(1 - r_1 r_m)^2 + 4 r_1 r_m \sin^2 \psi/2} \\ I_c &= I_0 \frac{t_1^2}{(1 - r_1 r_m)^2 + 4 r_1 r_m \sin^2 \psi/2} \end{aligned} \tag{1.22}$$

The circulating intensity is maximum when the round-trip phase shift ψ is an integer multiple of π. The cavity finesse is defined as the ratio of free spectral range and cavity linewidth $\Delta\nu_{1/2}$.

$$\mathcal{F} \equiv \frac{\text{free spectral range}}{\Delta\nu_{1/2}} = \frac{\pi\sqrt{r_1 r_m}}{1 - r_1 r_m} \tag{1.23}$$

Using equation 1.22, the highest achievable power buildup B is when the round-trip phase shift ψ is an integer multiple of π.

$$B = \frac{I_c}{I_0} = \frac{t_1^2}{(1 - r_1 r_m)^2} = \frac{1 - r_1^2}{(1 - r_1 r_m)^2} \tag{1.24}$$

When $r_1 = r_m$, the cavity is impedance matched. For a ring cavity operating at impedance matched condition, and also with $r_1^2 + t_1^2 = 1$, the power enhancement factor B is

$$B = \frac{I_c}{I_0} = \frac{t_1^2}{(1 - r_1 r_m)^2} = \frac{1}{t_1^2} = \frac{\mathcal{F}}{\pi} \tag{1.25}$$

For the over-coupled cavity which means $r_1 < r_m$, the round-trip loss is dominated by the input coupler mirror, Then the power buildup factor is $\frac{2\mathcal{F}}{\pi}$ instead of $\mathcal{F}/\pi$.

$$B = \frac{I_c}{I_0} \approx \frac{(1 - r_1)^2}{(1 - r_1)^2} \approx \frac{2}{1 - r_1} \approx \frac{2\mathcal{F}}{\pi} \tag{1.26}$$

Notice that for the same cavity finesse, nearly twice higher power buildup factor can be obtained by using the over-coupled cavity. So we adopt the over-coupled cavity for our CE-HHG source.

1.6.2 Frequency comb

An optical frequency comb is a laser source with a spectrum consisting of many precisely equally spaced, narrow linewidth lines as shown in Equ. (1.27).

$$\nu_n = f_0 + n f_{rep} \tag{1.27}$$

The frequency comb can be understood in frequency domain and time domain as shown in Fig. 1.7. In frequency domain, The frequency comb laser can be viewed as a great many CW lasers simultaneously emitting at frequency spacing f_{rep} and offset f_0. In time domain, frequency comb is a repetitive pulse train. The pulse train has a precise repetition rate f_{rep}. For each pulse, the carrier-envelope offset phase of the pulse advances by $\Delta\phi_{CE}$ related to f_0 by Equ. (1.28).

$$f_0 = \frac{\Delta\phi_{CE}}{2\pi} f_{rep} \tag{1.28}$$

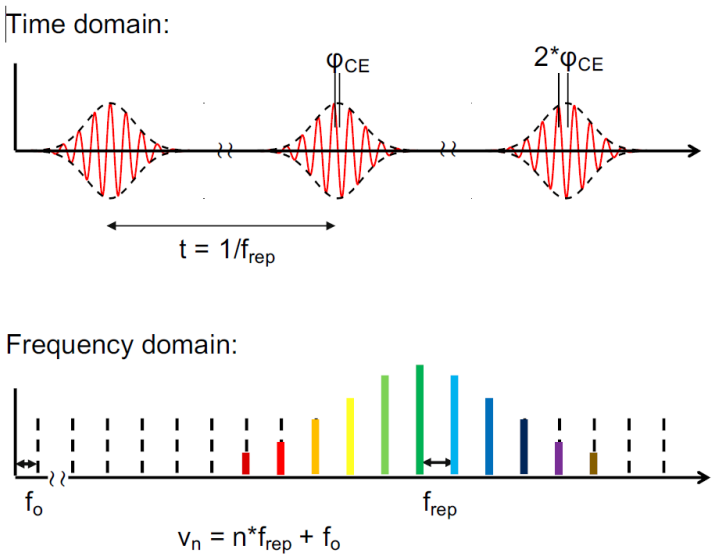

Figure 1.7: Schematic illustration of frequency comb in time domain and frequency domain.

As a Nobel prize winning technology, the frequency comb has had an impact on many aspects of science and technology. Frequency comb has been used as an frequency ruler which provides a direct link from radio frequencies to optical frequencies. The optical frequency can be measured with great accuracy, related applications include high-precision spectroscopy, optical communications, optical atomic clock and so on. On the other hand, broadband frequency comb can be femtosecond pulse train. After the passive amplification in the enhancement cavity, we use the frequency comb for nonlinear frequency up conversion in high harmonic generation.

1.6.3 frequency comb optical cavity coupling

Assuming the cavity is in the vacuum, the cavity resonance frequencies are solutions to Equ. (1.29)

$$\frac{\omega_m}{c}L + \phi_{mirror}(\omega_m) + \phi_{Gouy} = 2\pi m \tag{1.29}$$

where m is an integer, c is the speed of light, L is the vacuum path length, and ϕ_{Gouy} is the Gouy phase of the cavity. Interestingly, different from the single

pass case, the Gouy phase experienced by the intracavity light doesn't depend on the wavelength and it only depends on the geometry of the cavity [97, 98, 99]. $\phi_{mirror}(\omega_m)$ is the round-trip frequency-dependent phase shift imparted to the light by the mirrors. Expanding this ideal mirror spectral phase around a central frequency ω_c and truncate at the linear term

$$\phi_{mirror}(\omega_m) = \phi_0(\omega_c) + \phi_1(\omega_m - \omega_c) + \frac{1}{2}\phi_2(\omega_m - \omega_c)^2 \tag{1.30}$$

Ignore the second order term for now, then the cavity resonance frequencies can be written as

$$\frac{\omega_m}{c}L + \phi_{Gouy} + \phi_0 + \phi_1(\omega_m - \omega_c) = 2\pi m \tag{1.31}$$

After some transformation, the cavity resonant frequencies can be written in a similar way as the frequency comb

$$\begin{aligned} f = \frac{\omega_m}{2\pi} =& m\frac{1}{\frac{L}{c} + \phi_1} + \frac{1}{2\pi}\frac{\phi_{Gouy} + \phi_0 - \phi_1\omega_c}{\frac{L}{c} + \phi_1} \\ &= mf_{rep} + f_0 \end{aligned} \tag{1.32}$$

where f_{rep} and f_0 of the cavity mode can be written as

$$f_{rep} = \frac{1}{\frac{L}{c} + \phi_1} \tag{1.33}$$

$$f_0 = \frac{1}{2\pi}\frac{\phi_{Gouy} + \phi_0 - \phi_1\omega_c}{\frac{L}{c} + \phi_1} \tag{1.34}$$

The coupling between a frequency comb and a cavity could be understood in both frequency domain and time domain as shown in Fig. 1.8. In the frequency domain, the f_{rep} and f_0 of the frequency comb is matched to the f_{rep} and f_0 of the cavity. Since the frequency comb has only two degrees of freedom, matching f_{rep} and f_0 will automatically match every cavity mode to the frequency comb teeth. In the time domain, the femtosecond pulse circulating inside the cavity constructively interference with the incoming pulse at the input coupler mirror, with the right time and right phase. By doing this, the broad spectrum of the frequency comb can be coupled into the cavity and the power can build up as Equ. (1.24).

Notice that the comb teeth of the frequency comb are precisely equally spaced, While the cavity mode is only approximately equally space because

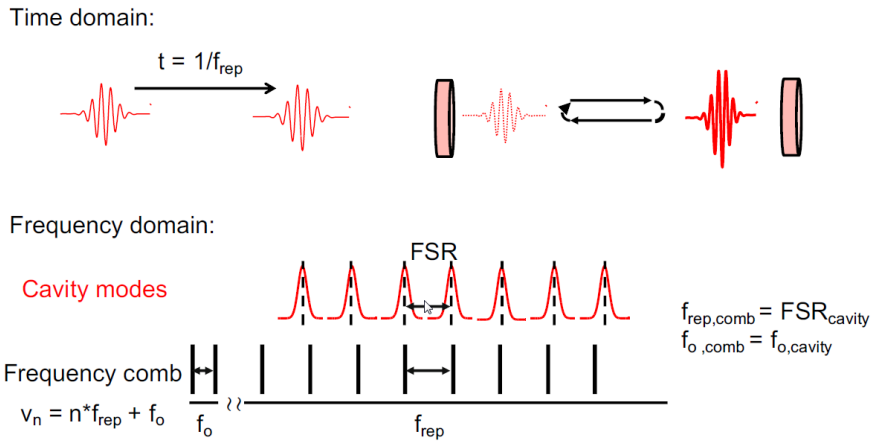

Figure 1.8: Schematic illustration of coupling a frequency comb into a cavity.

Equ. (1.30) truncated at the linear term. The second order term ϕ_2 which is the group delay dispersion (GDD) of the mirror coating can cause the cavity modes to no longer be evenly spaced. So in order to couple bandwidth $\Delta\omega$ into the cavity, the mirror coating should have a flat phase within $\pi/\mathcal{F}$ over the bandwidth. The tolerance of the second order phase ϕ_2 can be estimated by

$$\frac{1}{2}\phi_2\Delta\omega^2 < \frac{\pi}{\mathcal{F}} \tag{1.35}$$

1.6.4 Power scaling of the enhancement cavity

Ioachim Pupeza and coworkers from Max-Planck-Institute has systematically investigated the power scaling of the enhancement cavity [100, 101, 102, 103, 104, 105, 106]. The major limiting factors of the intracavity power are nonlinear effects and thermal effects. In Ref. [101], an intracavity average power of 18 kW was demonstrated for 200 fs pulse in an empty bowtie cavity. The power is limited by the nonlinear effects of the mirror coatings. By stretching the pulse to > 2 ps, the intracavity power can reach 72 kW limited by the thermal lensing effect of the mirrors. In Ref. [100], by using optimized mirror coating and low expansion mirror substrates, 400 kW average power with 250 fs pulse duration is demonstrated, the power limiting factor is the thermal lensing of the input coupler mirror. Then by using a sapphire sub-

strate input coupler mirror and stretching the pulse to 10 ps, 670 kW power was obtained. This sets the world record of the highest power in an empty cavity so far. This power level can't be reached with compressed pulses due to the optical damage of the input coupler mirror. The Laser Interferometer Gravitational-Wave Observatory (LIGO) also uses an enhancement cavity with a different geometry, It has an intracavity power of 20 kW with 10 W CW input light at 1064 nm [107].

For the cavity with a Brewster plate or HHG gas nozzle, the nonlinear effect put a severe limit on the power scaling. The constructively interference with the pulse is required every round trip, so the round trip phase error in the cavity should be less than $\pi/\mathcal{F}$ over the entire bandwidth, including any nonlinear phase shift. In Ref. [108, 106], an 5 kW intracavity power was obtained with a quartz plate inserted in the cavity and compressed pulse, the thermal and nonlinear effects in the Brewster plate led to a coupling among transverse cavity higher-order modes which limits the power scaling. In Ref. [109], 12 kW is reported with fused silica brewster plate, however, after a few minutes, the Brewster plate was damaged. We have demonstrated stable >12 kW intracavity power with 250 μm sapphire brewster plate [12]. The sapphire Brewster plate doesn't damage at this power level. However, the nonlinear effects prevents the cavity power from going up. Although the nonlinear effects limits the power scaling, the Brewster plate can be used to compensate the thermal lensing effect of the mirrors. In Ref. [102], 160 kW cavity power is reported with good beam spatial mode aided by thermal lensing cancellation. However, in this work, the pulse has to be stretched in order to avoid nonlinear effects. Although the nonlinear effects in the enhancement cavity is detrimental, when it is properly manged, it can support broad bandwidth soliton-like pulses in the cavity. Recently, self-compressed and self-stabilizing dissipative solitons in nonlinear optical resonators with a Brewster plate are demonstrated [110].

1.7 Time- and angle- resolved photoemission instrument layout

During my PhD, I have designed and built an advanced instrument for time- and angle- resolved photoemission spectroscopy. The instrument consists of 4 major part: the 80 W frequency comb laser discussed in chapter 2, the

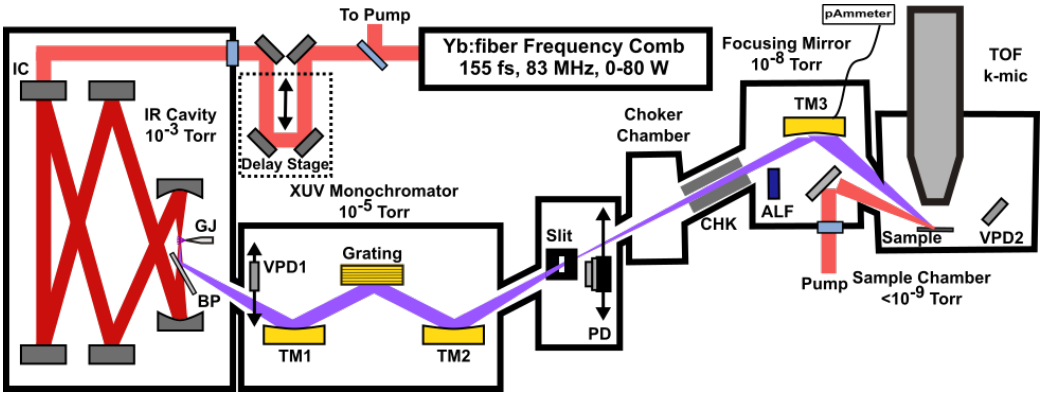

Figure 1.9: Time- and angle- resolved photoemission instrument layout. IC= input coupler, GJ= gas jet, BP= Brester plate, VPD=vacuum photodiode, TM= toroidal mirror, PD= photodiode, CHK=choker, ALF= aluminum filter.

XUV source based on CE-HHG in chapter 3, the XUV beamline discussed in chapter 4 and the surface science chamber discussed in chapter 5 with Time of flight electron momentum microscope detector (TOF k-mic) discussed in chapter 8. To demonstrate the the capability of this instrument, I applied the instrument to the study of laser assisted photoemission on Au(111) surface in chapter 6, the electron dynamics of a thin C60 film in chapter 7 and the occupied electron states of HOPG sample in chapter 9.

The layout of the instrument is shown in Fig. 1.9. A home-built 80 W, 155 fs frequency comb laser with a repetition rate about 80 MHz at 1.035 μm ($h\nu$ = 1.2 eV) is used to drive the enhancement cavity. The enhancement cavity is bow-tie cavity consisting of 6 mirrors. Typically 5-10 kW average power builds up in the cavity. Harmonics are generated by flowing noble gas to the cavity focus and then reflected into the beamline by a sapphire wafer placed at Brewster's angle. The beamline consists of a time preserving XUV monochromator, a choker chamber for differential pumping and a refocusing mirror. The monochromator consists of toroidal mirrors TM1, a grating, toroidal mirror TM2 and the slit. A single XUV wavelength is selected by the monochromator, and then focused to 100 μm spot on the sample housed in a surface science chamber. A choker (CHK) is inserted between the monochromator and the refocusing mirror for differential pumping. The light source and beamline deliver tunable XUV light pulses (8 eV to 40 eV,

$<$ 100fs) with flux up to 3×10^{11} photons/second to the sample. Thanks to the high rep rate, space charge effects which have severely limited previous tr-ARPES experiments are eliminated. This enables ultrafast time-resolved ARPES experiments with nano-Ampere sample photocurrents comparable to those employed in synchrotron experiments. This is an increase of approximately two orders of magnitude compared with conventional HHG sources at comparable energy resolution and spot size.

The surface science chamber serves as the experiment end station and it is integrated with a complete set of surface science instruments including X-ray gun, hemisphere energy analyzer, sputter gun, mass spectrometer, RGA, LEED. For the energy detector in the tr-ARPES experiments, a TOF k-mic is used, which features highly parallel electron detection in energy and momentum space, full solid angle collection, and μm spatial resolution. We have been improving its performance such as electron filtering so it adapts to the 80 MHz tr-ARPES experiments. This detector improves the data rate by approximately another two orders of magnitude. In all, this instrument improves the data-rate for ultrafast time-resolved ARPES measurements by approximately 4 orders of magnitude, enabling tr-ARPES experiments in the pertubatively excited regime.

Chapter 2

High-power low-noise Yb:fiber frequency comb laser

2.1 Introduction

Originally intended for the precise measurement of optical frequencies, femtosecond optical frequency combs have since found many other applications outside of their original purpose.[111, 112] They are now used for the calibration of astronomical spectrographs,[113] laser ranging,[114] high-order harmonic generation,[60] attosecond physics,[115, 116] and direct frequency comb spectroscopy,[117, 118] among other things. In our case, for example, we passively amplify the frequency comb laser to 100 μJ pulse energy by an enhancement cavity and use the high energy pulse to generate high order harmonics at full rep rate. Thus for a frequency comb with a full rep rate, low noise and high average power is needed.

Ytterbium-based systems then stand out as providing an excellent platform for average power scaling due to the very small quantum defect of Yb and the capability of high doping in both glasses and crystals. [119, 120, 121] Since the first Yb-based femtosecond lasers,[122, 123] progress in this field has moved at a rapid pace using fibers, thin disks, and slabs. Yb:fibers are particularly attractive for average power scaling, due to the large surface area to volume ratio of fibers, large gain bandwidth,[119] and the availability of double-clad fibers for use with low-brightness (and thus low-cost) pump diodes. Indeed, kW scale femtosecond lasers have been reported using high-power Yb:fiber amplifier systems,[124, 125] and amplified Yb-combs have

demonstrated high phase coherence.[126] Yb:fiber has sufficient gain bandwidth to support sub-200 fs pulses through linear chirped pulse amplification (CPA), in which the total nonlinear phase shift accumulated in the amplifier chain is kept less than 1 radian.[127] Recently, shorter pulses have been generated at high average power through nonlinear amplification,[128, 129] in which nonlinear propagation in the gain fibers is harnessed for generating additional spectral components. With narrow linewidth and controllable combs,[126, 130, 131, 132] the simultaneous combination of high peak and average power can be obtained through enhancement in passive optical cavities.[93, 94, 133, 130]

We present a detailed account of the design, construction, and operation of two high-power Yb:fiber laser frequency combs that we built in our laboratory. Much of the material in this chapter is reproduced from Li et al. [11]. A block-diagram outlining both lasers is shown in figure 2.1. The laser is made from all commercial components, most of which are stock items at major distributors, and can be assembled with only basic fiber tools. For example, a fiber splicer capable of splicing standard single-mode fibers is sufficient and you do not need more expensive models capable of handling polarization maintaining fibers or photonic crystal fibers (PCF), which cost many times more.

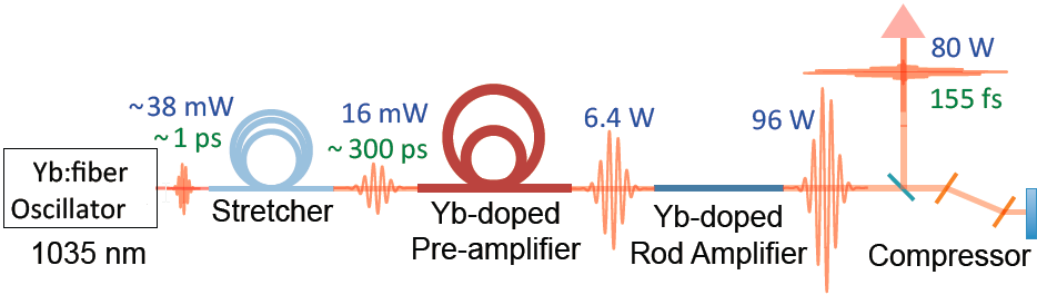

Figure 2.1: Overview of the laser systems. Chirped pulse amplification using a fiber-based stretcher and simple PCF amplifiers provides minimal complexity. More detailed schematics are shown in figures 2.2, and 2.7. This figure is reproduced from Ref. [11].

In section 2.2, we describe the construction of Yb:fiber oscillators passively mode locked using nonlinear polarization evolution (NPE) and run near zero net cavity group delay dispersion (GDD) for the lowest noise and narrowest comb-tooth linewidth.[132]. In section 2.3, we describe CPA to 80

W using a PCF rod amplifier. The amplifier uses fiber-based pulse stretching with anomalous third order dispersion fibers,[134, 131] which require careful initial design, but then dramatically simplify the mechanical design of the laser system.

2.2 Yb:fiber oscillators

The large nonlinear phase shifts accumulated when an ultrashort pulse propagates for a distance in the confined space of an optical fiber can give rise to many phenomena.[135, 136, 137, 138] Inside a laser cavity, this high nonlinearity can allow for mode-locked operation over a very wide range of parameters. Unlike Ti:sapphire oscillators, in which a few standard designs that emerged in the 1990's [139, 140] are found in most ultrafast laser labs, there are many fiber oscillator designs working at repetition rates from 100 kHZ [141] to 10 GHz,[142] and the literature presents a large and daunting landscape to navigate. We attempt a brief summary here with the goal of putting our lasers in context.

Mode-locked fiber lasers can be broadly classified by their net cavity GDD and the saturable loss mechanism by which they are mode locked.[120, 143] With large anomalous GDD, soliton-like pulse shaping produces nearly chirp-free pulses, but with limited power.[144, 120] Lasers working with large normal GDD, even with all normal dispersion elements,[143] can support wave-breaking free pulses of very large energy. For example, Baumgartl *et al.*[145] have even demonstrated 66 W of average power and μJ pulses directly from an oscillator without subsequent amplification. However, for the quietest operation, with both the lowest phase and amplitude noise most suitable for comb applications, it is desirable to operate the laser near net zero cavity GDD. [132, 146, 147, 148, 126] Unlike Er-doped fiber lasers operating at 1.5 μm, where it is easy to make fibers with normal or anomalous dispersion, silica fibers predominantly have normal dispersion in the 1.0-1.1 μm range amplified by Yb, so that dispersion compensation is usually done with a free-space dispersive delay line [132, 149, 150] or fiber Bragg gratings.[126, 148] Fiber Bragg gratings can allow for all-fiber designs, but require very careful design before assembly, as the dispersion is not adjustable. Oscillators with a free-space dispersive delay line allow tuning to find zero dispersion. As we show in section 2.2.3, with transmission gratings, fine-tuning of the grating separation in such a delay line using piezo-electric actuators can also be used

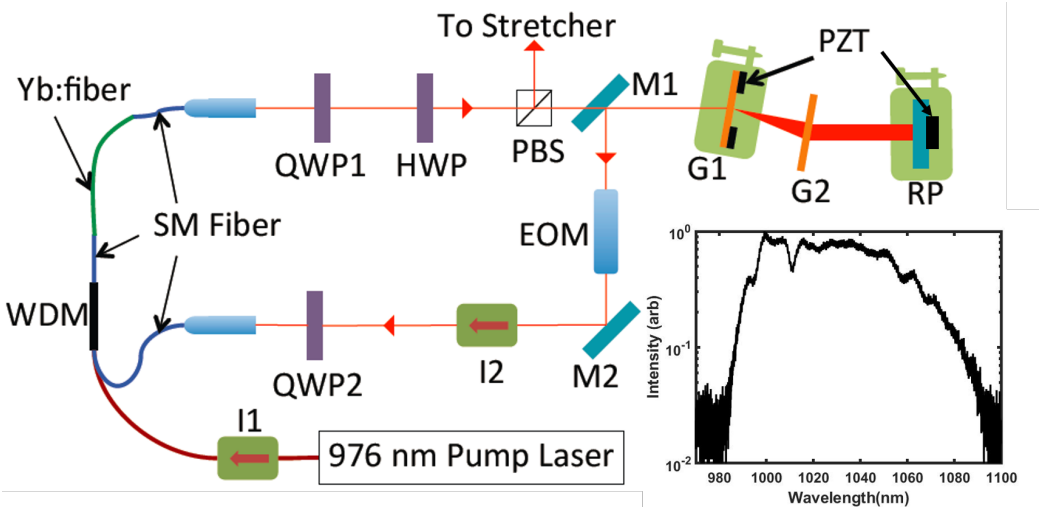

Figure 2.2: NPE ring oscillator design. I = Faraday isolator, WDM = wavelength division multiplexer, QWP = quarter-wave plate, HWP = half-wave plate, PBS = polarizing beam splitter, SM = single-mode, EOM = electro-optic modulator, G = grating, RP = roof reflecting prism (or retroreflector, used to change the beam hight by two reflections), M = mirror. Inset: Typical mode-locked spectra for oscillator operating near zero net GDD. This figure is reproduced from Ref. [11].

to control the comb's carrier-envelope offset frequency.

For mode locking, NPE in fiber[138, 137, 151] provides a fast artificial saturable absorber[152] that does not require any special components, but is sensitive to temperature or humidity changes. On the other hand, lasers based on real saturable absorbers, such as semiconductor saturable absorber mirrors (SESAM), can be made very environmentally stable, but typically have larger phase and amplitude noise.[153, 154][1] In our lasers, we use NPE mode locking, and have observed free-running comb-tooth linewidths less than 30 kHz and residual intensity noise less than -130 dBc/Hz for frequencies above 10 kHz (see figure 2.10). We have also observed reasonable long-term stability in a laboratory setting (more details below).

[1]The quiet Yb-oscillators described in references[126] and [131] actually use a combination of both NPE and the SESAM

2.2.1 Oscillator Construction

The basic layout for both Yb:fiber oscillators is shown in figure 2.2. The fiber section provides gain and nonlinearity while the components in the free space section compensate the dispersion of the fiber, manipulate the polarization, and actuate on the pulse's round-trip group delay and carrier-envelope offset phase.

The laser components of the oscilator including the mirror coating, isolator, WMD are designed to operate at 1035 nm. The pitch of the diffraction gratings is 600 groove/mm. The pump laser is a fiber Bragg grating stabilized diode laser operating at 976 nm (Oclaro LC96L76P-20R). Basic current and temperature controllers from Thorlabs (LDC210C and TED200C) are used to drive the pump laser. The noise specifications of this diode current controller are sufficient to obtain low-noise operation because the effect of high-frequency pump power fluctuations is suppressed by the low-frequency roll-off of the pump-modulation transfer function observed for these Yb:fiber oscillators, shown in figure 2.3a). Although the pump laser's fiber is polarization maintaining (PM), we simply splice this onto non-PM fiber for injection into the oscillator cavity with a fused wavelength division multiplexer (WDM). In addition to the WDM, a polarization insensitive isolator (I1) is used to isolate the pump laser from the oscillator light.

The fiber assembly is terminated on each end with anti-reflection (AR) coated angled FC/APC connectors which are then plugged into a fiber coupler lens assembly (Thorlabs PAF-X-5-C). These AR coated fiber tips are obtained simply by splicing the ends of AR coated patch cables (Thorlabs P4-980AR-2) to the ends of the gain fiber and WDM fiber pigtail. The use of connectorized fiber tips enables replacing the fiber assembly with minimal realignment and also allows for the rough alignment of the cavity using another fiber coupled laser, if desired. Single-mode Yb-doped gain fiber can be purchased from a variety of companies (Nufern, Thorlabs, Cor-active, ...) with a variety of Yb doping concentrations. We have used either YB1200-4/125 or YB1200-6/125DC from Thorlabs with similar results. The fiber assembly is spliced together with a basic optical fiber fusion splicer. In our lab, we use a refurbished Ericsson FSU 995FA.

The specifics of the fiber lengths are important for a few reasons. The first is that mode locking depends upon the amount of nonlinearity in the fiber[155] and the more fiber there is, particularly following the gain fiber, the easier it is to mode lock. Second, if the AR coated fiber tips become

damaged, this is usually due to the gain fiber being too long, and is not remedied simply by reducing the pump power. However, the overall length of the assembly and the relative lengths of the different sections does not have be controlled with high precision. By changing the fiber assembly, we have operated oscillators with repetition rates from 70 MHz to 97 MHz with the same free-space section and obtained similar performance.

In the free-space section, zeroth-order waveplates are used for polarization control and tuning of the laser, a Faraday isolator ensures uni-directional operation, an EOM enables phase modulation, and a pair of transmission gratings is used for dispersion compensation. A polarization beam splitter cube (PBS) is used as an output coupler, reflecting vertically polarized light out of the cavity. The first diffraction grating (G1) is mounted on a manual translation stage for finding zero dispersion, and a piezo-electric transducer (PZT) for fine-tuning the comb's carrier-envelope offset frequency. A high reflector mirror serves as the retroreflector in the dispersive delay line. This high reflector mirror is slightly tilted, changing the beam height by 5 mm and allowing the beam which initially crossed above to be reflected by D-shaped mirror (M1, which has a straight edge). The high reflector mirror is also mounted on a PZT actuator for fast laser cavity length actuation. In section 2.2.3, we describe the PZT and EOM actuators more carefully using fixed-point analysis.[153, 156]

For suppression of acoustic noise and mechanical vibration,the oscillator is enclosed in aluminum sheet metal boxes sided with "egg-crate" style sound damping foam and built on honeycomb optical breadboards that are supported on the optical table with a $5/8''$ thick piece of sorbothane rubber. Light is coupled from the oscillator to the amplifier chain via the single-mode fiber pigtail of the stretcher fiber module.

2.2.2 Alignment, mode locking, and long-term stability

Since the stress-induced birefringence of the coiled fiber assembly is unknown, finding the correct positions of the waveplates for NPE mode locking is a somewhat random process. If one simply randomly rotates the three waveplates, this amounts to searching a three-dimensional space. We have instead developed a reliable procedure for finding mode locking that simplifies the search considerably. First, the oscillator is aligned with the goal of min-

imizing the pump power necessary for lasing, minimizing the CW lasing threshold, which includes optimizing beam alignment and iterative rotation of polarizers. The pump power is then increased to around 200 mW, well above the minimum pump power that can maintain mode locking, which is about 100 mW. The quarter-wave plate just before the input fiber coupler (QWP2) is rapidly rotated a few degrees back and forth. If mode locking is not achieved, the half-wave plate (HWP) should be stepped a few degrees and then the QWP2 rotation repeated. This process should be repeated until mode locking is achieved, usually within a few iterations. Once the first quarter-wave plate (QWP1) is set for lowest CW lasing threshold, it is generally not necessary to rotate it to find mode locking.

A major problem with NPE Yb:fiber oscillators is that they are prone to multi-pulsing,[157] or the production of more than one pulse circulating in the cavity. The separation between pulses can occur on many different time scales, and thus one needs a range of instruments to detect it. Unlike a Ti:sapphire oscillator, we have frequently observed multi-pulsing to occur with the particularly troublesome separation of 1-500 ps: too short to measure with a typical oscilloscope, but too long to observe easily as interference fringes in the optical spectrum. To be able to detect multi-pulsing at all separations, we employ a combination of three instruments: (1) a low resolution USB optical spectrometer for small pulse separations <3 ps, (2) a simple scanning autocorrelator using a GaAsP two-photon photodiode [158] for the 1-50 ps range, and (3) a fast photodiode (Electro Optics Technology Inc. ET-3010) and sampling oscilloscope (Tektronix 11801C with an SD-26 sampling head, 20 GHz equivalent bandwidth) for longer timescales. A collinear, interferometric autocorrelator is preferred so that one can align it well enough to have confidence in the alignment for longer stage travels, and a two-photon photodiode simplifies the nonlinear signal detection. When multi-pulsing occurs, the first step is to make sure there is nothing terribly wrong with the oscillator. Specifically, check the CW lasing threshold and make sure it is low (typically less than 50 mW). Turn the waveplates, starting with either the HWP or QWP2, until it stops multi-pulsing.

Once stable mode locking is found, one can search for the lowest noise. The grating spacing for net zero GDD can in principle be calculated using the material parameters for the fibers and other optical elements in the cavity, and this is a good place to start, but it is generally necessary to fine tune this spacing once mode locked. The GDD can be measured using the technique of Knox,[159] changing the center wavelength either by inserting a knife edge

into the dispersed beam or rotating QWP2 slightly (or both). While tuning the grating separation, we monitor oscillator performance using two metrics that can be evaluated quickly: (1) The oscillator relative intensity noise (RIN), measured on a low noise, high bandwidth photodiode, and (2) the free-running heterodyne beat between the oscillator and a narrow linewidth (<1 kHz) CW Nd:YAG laser (Innolight Mephisto). Cingöz *et al.*[160] showed that the phase noise and the RIN are correlated, and as reported by Nugent-Glandorf *et al.*[132] the laser comb-tooth linewidth depends strongly on the net cavity GDD. Indeed, we have observed optical linewidths ranging between 2 MHz and less than 30 kHz this way, depending on the grating separation. Ref. [95] has detailed discussion.

An important question is: with what precision do I have to find zero GDD? Previously, some authors have emphasized the importance of being slightly normal.[126, 120] In our lab, we have observed very similar performance on either side of zero dispersion, within approximately ± 2000 fs^2, in agreement with references [132] and [161]. We have also found that being near zero dispersion is a necessary, but not sufficient, condition to obtaining low-noise performance, and the noise can also depend on the details of NPE and the waveplate angles.

Once satisfactory mode-locked performance is found, we leave the oscillator on indefinitely, and have enjoyed stable hands-free operation for many months at a time in a laboratory setting with reasonable temperature and humidity control (± 1 °C, 20-60% relative humidity). The parts of the laser that in principle have finite lifetimes, the pump diode and the gain fiber, are inexpensive. We have not observed significant degradation of the pump diode performance over three years of nearly continuous operation. However, we have observed that the gain fibers can fail after about one year of continuous operation. The main symptom of this is that the laser just won't mode lock. Lasing thresholds and output powers are similar, but stable mode-locked operation is not re-attained until the gain fiber is replaced, or a new fiber assembly with a fresh gain fiber is installed in the oscillator.

2.2.3 Comb Stabilization

The key element defining an optical frequency comb is that its comb teeth are evenly spaced to an extraordinary precision. [162, 163] This occurs naturally in mode-locked lasers and can also occur in other comb-generating systems such as microresonators [164] and broad-band electro-optically modulated

light fields.[165] Once even spacing is established, the comb has two degrees of freedom that determine the frequencies of the comb teeth. Usually this is expressed in terms of the electronically countable repetition rate f_{rep} and carrier-envelope offset frequency f_0 via the familiar comb formula

$$\nu_n = n f_{\mathrm{rep}} + f_0 \tag{2.1}$$

where n is an integer and the ν_n are the optical frequencies. Indeed, for self-referenced combs this may be the most sensible parameterization, as it is f_{rep} and f_0 that are actively controlled. However, for optically referenced combs, combs coupled to cavities, or when discussing the effects of actuators or noise sources, the discussion is often simplified by using a fixed point analysis,[166, 156, 153] writing the comb's optical frequencies as

$$\nu_n = (n - n^*) f_{\mathrm{rep}} + \nu_{n^*} \tag{2.2}$$

where n^* is an integer representing a fixed point of the frequency comb that does not change due to a particular perturbation such as noise or intentional actuation on the laser. In the fixed point picture, one considers the comb teeth simply expanding and contracting around the fixed point via changes in f_{rep}. The larger the frequency difference is between the fixed point and a particular comb tooth, the more the frequency of that comb tooth changes due to the perturbation.

Since the frequency comb has two degrees of freedom, one needs two feedback loops and two actuators to stabilize the comb. Ideally, these two feedback loops would have zero cross-talk. For example, if one directly stabilizes f_{rep} and f_0, ideally one actuator would actuate only on f_{rep} and the other only on f_0. In practice, this goal is almost never reached exactly, which is acceptable as long as one feedback loop can be significantly slower than the other, such that the faster loop can adiabatically track and correct for the cross-talk from the competing loop.

For coupling a frequency comb to an optical cavity, or locking the frequency comb to another optical reference, it is desirable to have one fast actuator with its fixed point far from the optical frequency and another actuator with fixed point near the optical frequency. This allows the fast actuator to have large travel at optical frequencies that are being stabilized, and the second actuator to simply cause the comb to breath around this locked point.

A commonly used combination of actuators to accomplish this is a fast intracavity EOM [167, 168, 169, 170, 171, 172, 173] for cavity length changes,

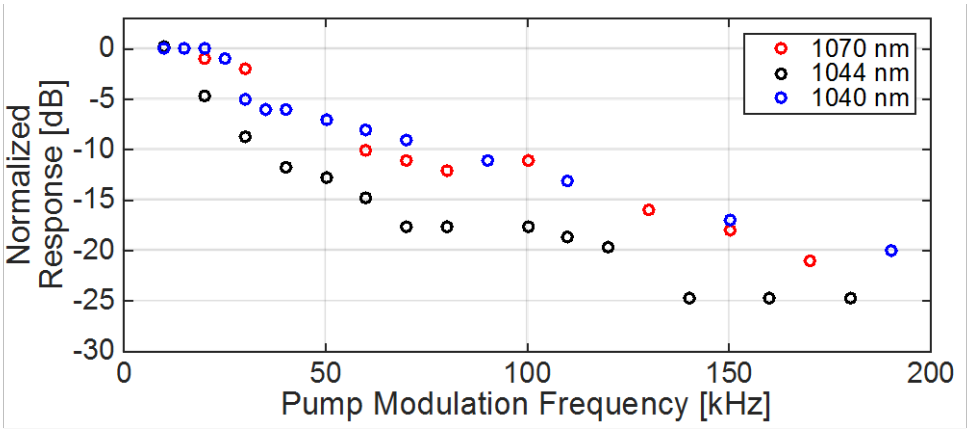

Figure 2.3: Pump amplitude to laser amplitude modulation transfer function. This figure is reproduced from Ref. [11].

with fixed point near DC ($n^* \sim 0$), and the pump laser power for changing the intracavity pulse's round trip phase shift, with fixed point near the optical carrier frequency.[153, 156, 174] While fast bandwidth can be obtained via actuating on the pump current in some laser designs,[160] the bandwidth attainable with this actuator depends on the details of the laser and population inversion dynamics.[175] In the current ring cavity design with lower loss and smaller gain than the laser in reference [160], and thus lower relaxation oscillation frequency, we have observed the bandwidth of pump power modulation to be quite limited, as shown in figure 2.3. To record this data, we modulate the pump diode current sinusoidally and record the amplitude modulation on the comb light with a photodiode and a spectrum analyzer. The pump current to pump power transfer function (not shown) was independently verified to be flat out past 1 MHz modulation frequencies with this setup, confirming that the roll-off is due to the transfer function of the Yb laser.

In our lasers instead of the pump power, we use a PZT mirror which serves as the retro-reflector of the grating compressor for actuation with a fixed point near DC, and we use a slower μm-scale piezo-electric adjustments of the grating spacing, which we show below has a fixed point near the optical frequency.

For the PZT mirror actuator, A bullet shaped holder [176] is used to provide support to the piezo, bullet shaped holder is made of copper shell

filled with lead core. A half inch mirror is glued to the 10 mm × 10 mm square piezo, and the piezo is glued to the magic bullet with the mirror by Loctite Hysol 1C-LV epoxy (also sold under the trade name Torr-seal). The substrate of the half inch mirror is cut to 0.1 inch to reduce the mass of the actuator. The transfer function of the PZT mirror actuator is measured by a Microson intefrometer. The result is shown in Fig. 2.4. The actuator has a broad band flat response. The 1st resonance ocurrs at 140 kHz and the 2nd resonance is at about 240 kHz.

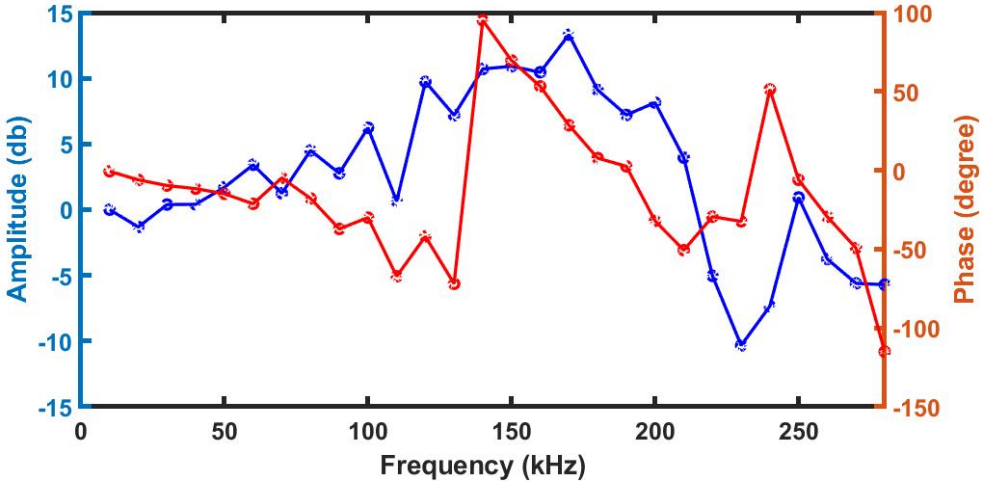

Figure 2.4: The amplitude and phase of the PZT mirror actuator transfer funciton. This figure is reproduced from Ref. [11].

We supply a 2 MHz sinusoidal voltage to the EOM to put frequency modulation (FM) sidebands on the comb that enable Pound-Drever-Hall (PDH) locking of the combs to passive optical cavities.[94, 177, 178] We measured the residual amplitude modulation (RAM) on the output light of the oscillator to be less than -90 dBc when driving the EOMs with a 20 V (peak to peak) sine wave (more than what is typically required for PDH locking). The EOM alignment can be fine-tuned *in situ* by minimizing this RAM.

For actuation on the grating spacing, the first grating is glued to a ring PZT (Noliac NAC2125) using Torr-seal, and this allows $>$ 10 kHz of bandwidth before encountering mechanical resonances. Shifting the carrier-envelope offset phase of a pulse by actuation on the grating separation of a pulse compressor has been employed for carrier-envelope offset phase stabi-

lization in amplified Ti:sapphire lasers (after the amplifier chain)[179] but to our knowledge this is first report of doing this inside a laser cavity. Here we derive the resulting frequency shifts for a transmission grating geometry and show that for transmission gratings operated in Littrow condition, the fixed point is at the optical carrier frequency ν_{optical}, such that the change in f_0 is approximately $\nu_{\text{optical}}/f_{\text{rep}}$ larger than the change in f_{rep}.

For the parallel grating pulse compressor illustrated in figure 2.5, the total phase shift for one pass through the grating pair is given by:[180]

$$\phi_g(\omega) = \frac{\omega}{c} p(\omega) - \frac{2\pi}{d} G \tan(\beta) \tag{2.3}$$

where $\omega = 2\pi\nu$ is the angular frequency, $\phi_g(\omega)$ is the spectral phase, $p(\omega)$ is the frequency dependent optical path length through the compressor, β is the angle of diffraction determined from the grating equation, $\sin(\alpha) + \sin(\beta) = \lambda/d$, with α the angle of incidence measured from normal, d is the grating pitch, λ is the wavelength, and G is the distance between the gratings measured perpendicular to the grating surfaces. The second term in equation (2.3) accounts for the 2π phase shift encountered by the light for each grating groove traversed and must be included to obtain correct results.[180] Careful inspection of the angle-dependent path length shows that

$$\frac{d\phi_g}{dG} = \frac{\omega}{c}\left(\frac{1}{\cos(\beta)} - \frac{\cos(\alpha+\beta)}{\cos(\beta)}\right) - \frac{2\pi}{d}\tan(\beta) \tag{2.4}$$

Now one is tempted to locate the fixed point, ω^*, by setting equation (2.4) equal to zero and solving for ω, but this is not generally correct because mode locking demands that the comb teeth remain evenly spaced, and thus the differential phase shift between comb tooth $n+1$ and n must be the same as the differential phase shift between comb tooth $n+2$ and comb tooth $n+1$. Enforcing this fact that the comb has only two degrees of freedom amounts to linearizing the spectral phase using the phase shifts obtained near the optical carrier frequency, viz.

$$\frac{d\phi_{\text{comb}}}{dG} = \left.\frac{d\phi_g}{dG}\right|_{\omega_0} + \left.\frac{d\tau}{dG}\right|_{\omega_0} (\omega - \omega_0) \tag{2.5}$$

where $\tau = d\phi_g/d\omega$ is the frequency dependent group delay, which is evaluated at the optical carrier frequency ω_0 in equation (2.5). The fixed point is then

given by

$$\omega^* = \omega_0 - \left(\left. \frac{d\phi_g}{dG} \right|_{\omega_0} \right) \left(\left. \frac{d\tau}{dG} \right|_{\omega_0} \right)^{-1} \tag{2.6}$$

At the Littrow condition, $\alpha = \beta(\omega_0) = \sin^{-1}(\pi c/\omega_0 d)$, one can show that the phase shift due to changing the grating separation, $d\phi_g/dG$, is identically zero and the fixed point is thus at the optical carrier frequency. For the more realistic scenario that the gratings end up slightly off-Littrow, one can use equations (2.2), (2.4), and (2.6) along with the relation $df_{\mathrm{rep}}/dG = -f_{\mathrm{rep}}^2 \, d\tau/dG|_{\omega_0}$ in order to determine the changes in comb tooth frequencies. One can also derive relations for the changes in f_{rep} and f_0. For two passes through the grating pair, under Littrow conditions, the result is:

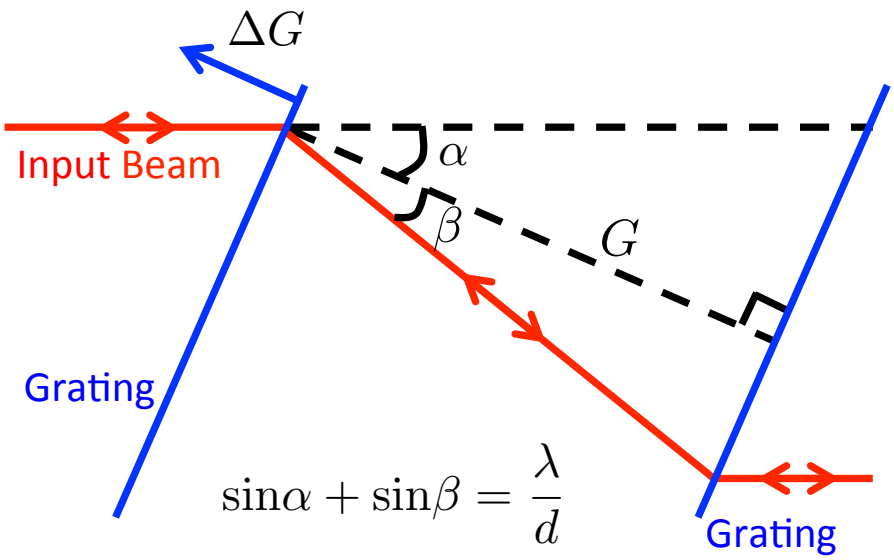

Figure 2.5: Transmission grating geometry. Illustration of the notation for the intracavity grating compressor. The grating spacing is adjusted slightly (ΔG) using a PZT to control the comb's carrier-envelope offset frequency. The arrow indicates the direction of positive ΔG. This figure is reproduced from Ref. [11].

$$\frac{df_{\mathrm{rep}}}{dG} = -\frac{4\pi f_{\mathrm{rep}}^2}{\omega_o d} \tan(\alpha). \tag{2.7}$$

$$\frac{df_0}{dG} = -n^* \frac{df_{\text{rep}}}{dG} = \frac{2f_{\text{rep}}}{d} \tan(\alpha). \tag{2.8}$$

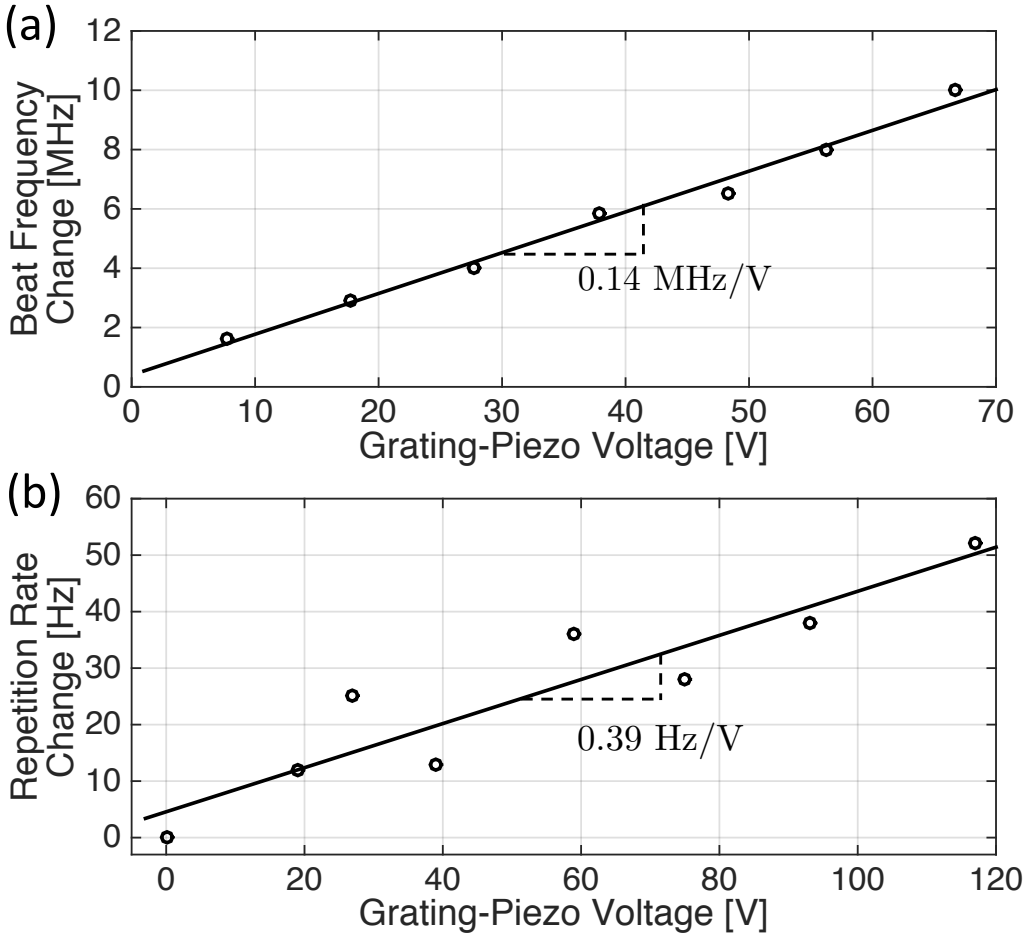

Figure 2.6: Grating actuation. a) 1064 nm beat frequency change with grating separation. b) Repetition rate change with grating separation. The data indicate that the fixed point is near the optical frequency. This figure is reproduced from Ref. [11].

We have experimentally verified this analysis by recording changes in the comb repetition frequency and an optical comb tooth near 1064 nm with oscillator A when voltage is applied to the grating PZT. The data are shown in figure 2.6. The repetition rate changes are measured using a

photodiode and a frequency counter. The changes in the optical frequency are measured by recording the beat frequency of an unstabilized heterodyne beat between the comb and the CW Nd:YAG laser. Linear fits to the data give slopes of $\frac{d\nu_{\text{beat}}}{dV} = 0.14$ MHz/V and $\frac{df_{\text{rep}}}{dV} = 0.39$ Hz/V. The number of comb teeth between 1064 nm and the fixed point can then be simply calculated from the ratio $\Delta\nu_{\text{beat}}/\Delta f_{\text{rep}} = 3.3 \times 10^5$. So the fixed point lies only approximately 30 THz away from the optical carrier frequency of 283 THz. This is consistent with the above equations and α deviating from the Littrow angle by approximately 4 degrees, which is realistic given our ability to initially set the grating angle in the laser and the α dependence of the grating's diffraction efficiency.

The grating can also be used to make a shift purely in f_0, if the grating is moved parallel to its surface, similar to the motion of a sound wave in an acousto-optic frequency shifter. Here the phase shift is simply 2π per grating pitch moved,[181] and the fixed point is at $\nu = \infty$. Using both parallel and perpendicular motions, in principle one could completely control the comb with only μm-scale motions of the grating alone, as the two motions have different fixed points.

2.3 Chirped-Pulse Amplification in Large Mode Area Photonic Crystal Fibers

Amplification of continuous wave lasers to high average power in Yb:fiber is straightforward, but amplification of femtosecond pulses presents additional complications. The long length of fiber presents a large amount of dispersion even for large mode area (LMA) fibers, and it is much more difficult to avoid accumulated nonlinear phase shifts than in bulk solid-state lasers. Designers of ultrafast fiber lasers usually take one of two approaches: embrace nonlinearity [136, 135, 128, 182, 129] or use stretchers and compressors with very large GDD to avoid it.[131, 183, 184, 124, 185] For comb applications, linear amplification, in which the B-integral, or accumulated nonlinear phase shift throughout the amplifier chain, is less than one, is generally preferred because then the amplified comb's coherence properties are determined mainly by the oscillator. In nonlinear amplification, amplitude noise from the high-power pump diodes in the amplifier chain could write phase noise on the amplified comb,[186, 120] although we are aware of some recent efforts using

high-power nonlinear fiber amplification for comb applications.[187, 188]

In our lasers, we have used linear CPA, but have strived to maintain modest stretcher/compressor dispersion by (1) seeding the amplifiers with very broad spectra and (2) maximizing the mode area of the seed light throughout the amplifier chain, even if this means seeding amplifiers below saturation. For simplicity and low-cost, we make use of fiber stretchers based on anomalous third-order dispersion depressed cladding fibers (OFS) and grating compressors based on inexpensive polymer transmission gratings (Wasatch Photonics).

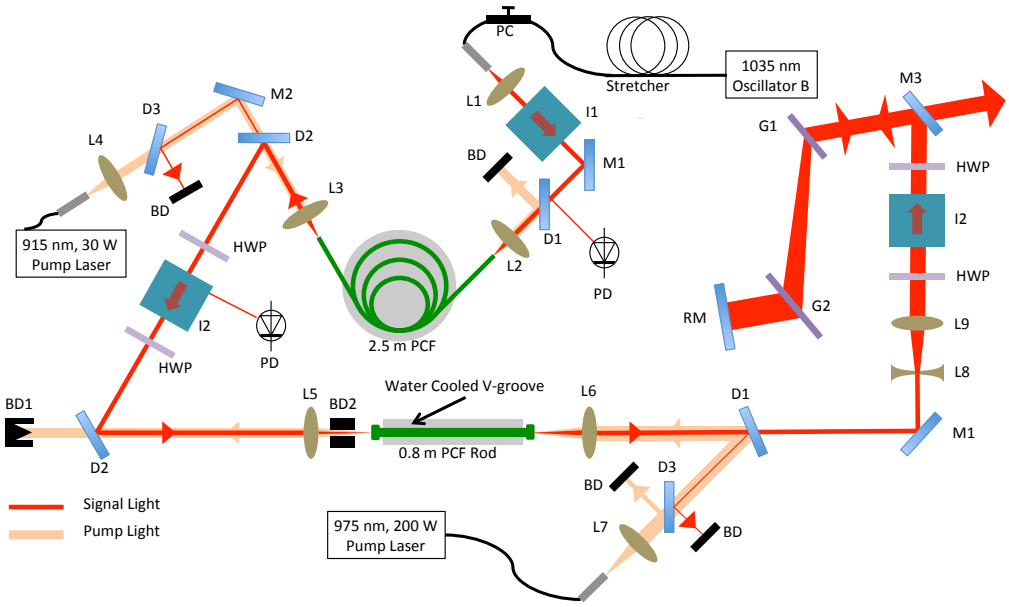

Figure 2.7: 80 W amplifier layout. Chirped pulses are amplified first in a 2.5 m flexible photonic crystal fiber and then in a 0.8 m rod fiber. L = lens, D = dichroic mirror, M = mirror, I = isolator, HWP = half wave plate, BD = beam dump, G = grating, RM = retroreflector mirror, PC= polarization controller, PD = photodiode. This figure is reproduced from Ref. [11].

A schematic of the 80 W CPA scheme is shown in figure2.7. It adopts a two stages amplications configuration.

For the first stage, The light from the oscillator is coupled into a stretcher fiber module custom made by OFS Specialty Photonics Division with FC/APC connectorized SMF-980 fiber pigtails. Between the stretcher and the following Faraday isolator (I1), about half the seed power is lost. After the dichroic

mirror (D1), which is used to isolate the pump light and seed (or signal) light, about 15 mW is launched into the 2.5 m amplifier fiber. The amplifier fiber is a doped, LMA (760 μm^2) PCF terminated with sealed ends and copper SMA 905 connectors, purchased from NKT Photonics. This fiber is end pumped with a 30 W, 915 nm pump diode (nLight Element). After the second dichroic mirror (D2), the beam is expanded to 4.2 mm ($1/e^2$ diameter), sent through another Faraday isolator.

The coiled amplifier fiber is supported on a circular aluminum plate. The pump end, where the optical power is the highest, is mounted in a water-cooled copper clamshell assembly. The seed end of the amplifier fiber is screwed into an SMA connector (Thorlabs HFB001) mounted on a flexure stage (Thorlabs MicroBlock MBT616D). The heavy copper mode-stripper assembly of the fiber is further supported by shims placed on the flexure stage. The output of the stretcher fiber and pump diode fiber are mounted on flexure stages in similar fashion. For delivering the pump light, the pump diode fiber pigtail is spliced onto the end of an AR coated multimode patch cable (Thorlabs M105L02S-B). The pump light is launched counter-propagating to the amplified seed light to reduce the accumulated nonlinear phase shift (B-integral) in the amplifier fiber. Despite not being "all-fiber", we have observed consistent performance from this mechanical setup without alignment for more than 5 years of operation.

The saturation power for the LMA PCF amplifier is more than 200 mW, and many previously reported amplifier systems using these PCF amplifiers have employed a fiber pre-amplifier with smaller mode area between the oscillator and the PCF amplifier [131, 185, 184, 187, 188] in order to seed the power amplifier at saturation. Since we are seeding the amplifier well below the saturation power, a threshold-like behavior is observed in the amplified power vs. pump power curves shown in figure 2.8(a), reducing the efficiency of the amplifier. While this one-stage amplification scheme is less efficient, it is much simpler because (1) there are no pre-amplifier components and (2) the pulses do not have to be stretched as much to avoid nonlinearity, since all the high power propagation is done in LMA fiber. A smaller stretching/compression ratio allows for looser tolerances on matching the higher-order dispersion of the stretcher and compressor. The a few Watts of pump power wasted before the amplifier reaches saturation are not really of consequence, due to the low cost of high-power pump diodes.

Two concerns with underseeding the amplifier are (1) noise due to amplified spontaneous emission (ASE),[138] and (2) catastrophic damage to the

amplifier fiber due to self-lasing and Q-switching. Regarding (1), despite the expectation of increased ASE, the measured RIN spectrum of the amplified light (see pre-amplifier curve in figure 2.10) indicates that the main source of noise on the amplified light is due to the pump diode RIN, not ASE. Regarding (2), while we do not know what the lowest necessary seed power is to avoid catastrophic damage, we can say that we have run these PCF amplifiers (both at 1035 nm and 1060 nm) for many hours with seed powers as low as 10 mW without observing damage. We continuously monitor the seed light with a fast (100 MHz bandwidth) photodiode (PD) and a simple interlock circuit, which immediately shuts off the pump diode in the event that the RF power from the photodiode drops below a set threshold, indicating reduced power or loss of mode locking. Pump diode drivers from VueMetrix Inc. shut off in less than 50 microseconds upon receiving an electronic signal, much shorter than the energy storage time in Yb of approximately 1 ms. [119].

For the second stage, a 0.8 m long Yb-doped PCF rod (NKT Photonics, aeroGAIN-ROD-PM85-POWER) with a 3,400 μm^2 mode field area, end pumped by a 200 W pump diode module (LIMO, LIMO200-F200-DL980-S1886) is used for the rod amplifier. When seeding the rod with 6.4 W, 96 W emerges with excellent beam quality when pumping the rod with 200 W of pump power. The large mode field diameter of the rod allows the laser to maintain linear amplification to μJ pulse energies using only a modest stretcher dispersion of 5.3 ps^2, or stretched pulse durations of only approximately 300 ps. Then the light is sent to a beam expander to expand the beam diameter ($1/e^2$) to 5.8 mm to avoid down stream optics damage. The the light issent through another Faraday isolator, and compressed using a pair of polymer transmission gratings (Wasatch Photonics) and a roof reflector (RM, or retroreflector, two mirrors with a 90 angle, to change the beam height by two reflections).

The available rod fibers are shorter than flexible PCF, necessitating pumping at 975 nm and amplification in the more conventional 1030-1040 nm region to achieve efficient gain. With the amplified center wavelength at 1035 nm, we observe significant gain narrowing[189, 77] in the amplifier chain, as shown in figure 2.8c). However, we are still able to compress the rod amplifier output to very clean 155 fs pulses, as shown in figure 2.8d). Pumping at 975 nm requires tighter control over the pump diode wavelength, increasing the cost of the pump diode. In our system we do not actively control the temperature, and this is the reason for the nonlinear amplified power vs. pump power curves of figure 2.8 - the pump laser wavelength is changing as

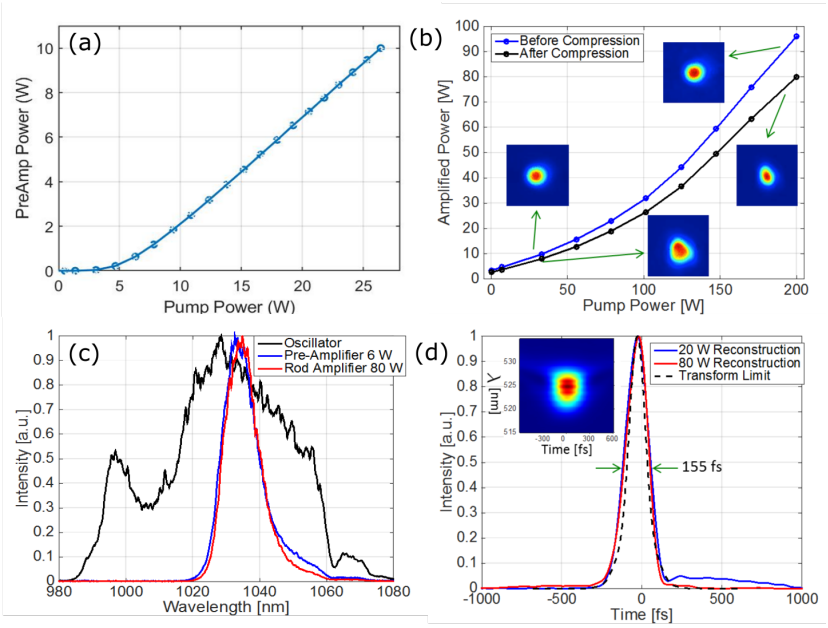

Figure 2.8: Rod amplifier performance. a) The output power of the PCF preAmp. b) Output power of the Yb:fiber rod amplifier, pumped by a counterpropagating 975 nm pump diode. The beam mode at lower power and full power is shown for both the output of the rod fiber and the compressor. c) Laser spectra measured from the oscillator and amplifier output. c) Raw FROG trace at 80 W (inset) and retrieved pulse shapes of the compressed pulses compared to the transform limit calculated from the spectrum in d) for both low and high power operation. This figure is reproduced from Ref. [11].

the power is increased.

The rod fiber is supported along its length by a water-cooled aluminum V-groove, held loosely by only two pieces of kapton tape. The end caps, the parts that are critical for alignment, are rigidly located in V-shaped jaws mounted on the optical table separate from the V-groove. The high pump power of the rod amplifier can bring complications. When pumped with 200 W, more than 40 W of pump light comes out from the seed end of the rod fiber with NA=0.5, which could heat the mount of the lens L5 or the mirror mount for D2, causing a dangerous drift in the seed light alignment. We dump the pump light safely using two water-cooled black-anodized aluminum beam dumps, the annular BD2 to protect the lens mount and BD1 to collect the

pump light transmitted through the dichroic mirror (D2).

The dispersion budget for the 80 W comb is shown in table 2.1 and figure 2.8d) shows a second harmonic generation (SHG) frequency resolved optical gating (FROG) trace taken with the laser at full power using a commercial FROG system (Mesa Photonics FROGscan Ultra).

The oscillator pulses are stretched to approximately 300 ps duration in the fiber stretcher module. While a free-space Offner-type stretcher[190, 191] would allow for more tunability than the fiber stretcher module, and perhaps better compensation of higher order dispersion,[192] it would also add substantial mechanical complexity and cost. The fiber stretcher module is alignment free, and we have observed nearly transform-limited performance using these for these stretcher modules.

Then the pules are compressed after amplification using a Treacy-style compressor with 1250 groove/mm transmission gratings (Wasatch Photonics). The compressor has an overall efficiency of 86%, corresponding to a grating diffraction efficiency of $(0.86)^{1/4} = 96\%$. Clean 155 fs pulses are observed at both high and low power. The absence of pulse distortion at high power indicates that linear amplification has been achieved.

Another problem with high average power is thermal lensing and distortions of the beam quality. As shown in figure 2.8, an excellent, nearly Gaussian, spatial profile is observed in the amplified light from the rod amplifier at both low and high power. However, even at low power, we observe distortions of the beam after four diffractions from the inexpensive polymer gratings. At higher power, despite the large expanded beam size of 5.8 mm $1/e^2$ diameter after the telescope (L8 and L9), thermal lensing is observed, and the output mode measured 1.8 m after the compressor is significantly smaller. Inspection of the beam at various points indicates that the thermal lensing occurs either in this telescope or the Terbium Gallium Garnet crys-

Component	GDD (ps^2)	TOD (fs^3)	notes
Stretcher	5.27	-2.16×10^7	
Amplifier	0.063	1.36×10^5	FS, L_{tot}=3.3 m
Isolators	0.017	9.9×10^3	TGG, L_{tot}=12 cm
Compressor	-5.32	2.15×10^7	

Table 2.1: Dispersion budget for the 1035 nm laser. FS stands for fused silica. TGG = Terbium Gallium Garnet.

tal of the optical isolator. However, despite the obvious thermal lensing, we can still obtain nearly constant coupling efficiency to the TEM_{00} mode of an external femtosecond enhancement cavity (fsEC) for the full power range of the laser by simply changing the lens spacing in a mode-matching telescope between the compressor and the fsEC. One of the authors (T. K. Allison) has observed similar behavior for the laser described in reference [131].

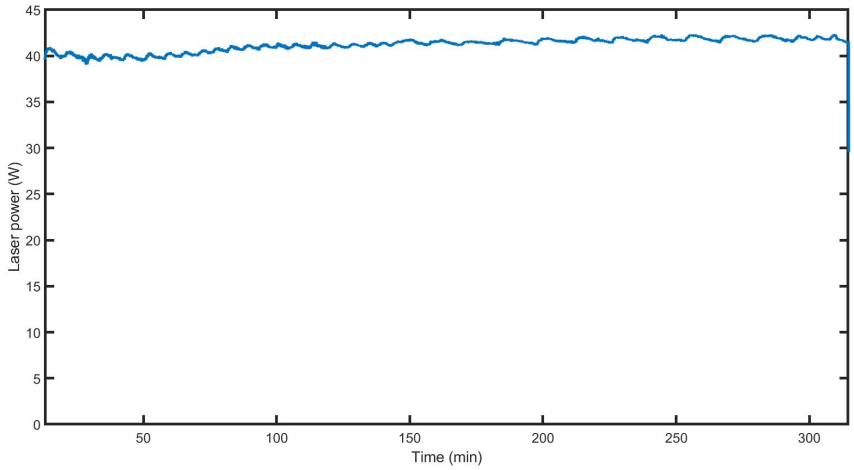

Figure 2.9: The laser power over 5 hours.

Fig. 2.9 shows the laser power over 5 hours continuous running. The laser power reaches the normal power level immediately after turned on and remains steady for 5 hours. We see some small periodic fluctuations with 15 min cycle. Because 15 min happens to be the working cycle of the AC in the lab, these fluctuations are possibly caused by small temperature change in the lab. There are also some small power drift in the first two hours after the laser turned on, However, that's completely gone after two hours of warming up.

Figure 2.10 shows the RIN measured in various parts of the laser system. The pump diode RIN spectra are nearly flat out to frequencies of 1 MHz at -100 dBc/Hz for the 30 W pump diode and -85 dBc/Hz for the 200 W pump diode. The 200 W pump diode is driven by a 1500 W power supply from TDK Lambda (GEN 20-76). For both the pre-amplifier and the rod amplifier, the storage time of the Yb:fiber gain medium provides a low-pass filter to the pump diode RIN. Figure 2.10 also shows the RIN spectrum for

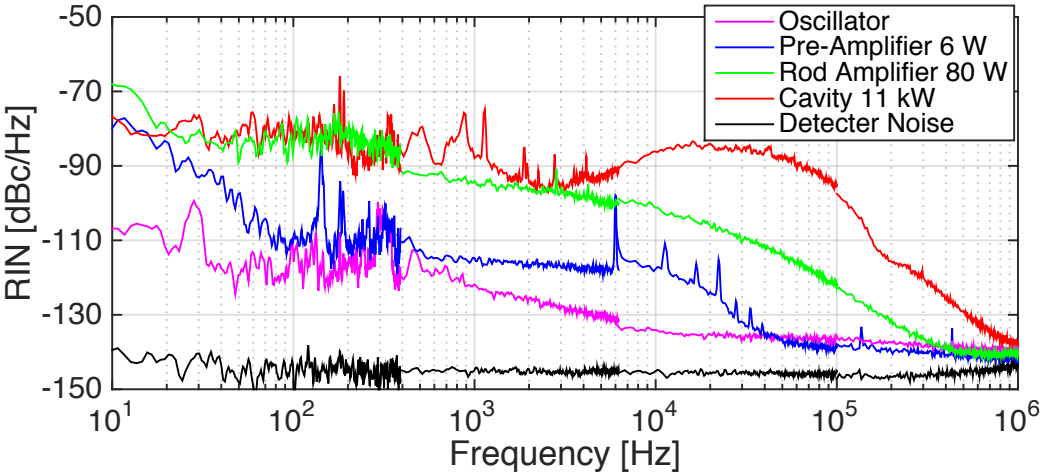

Figure 2.10: Intensity noise. RIN spectra at various places throughout the 80 W laser system. This figure is reproduced from Ref. [11].

the intracavity light of a fsEC operating with 11 kW of intracavity power. The cavity is locked to the comb using the PDH method[177, 178] and a PZT on one of the fsEC mirrors. A servo bump is observed at ∼30 kHz due to the finite bandwidth of the PZT lock, but for lower frequencies an intracavity RIN level is obtained nearly equal to the RIN of the comb.

2.4 Second and third harmonic generation

In tr-ARPES experiments, pump pulses are needed to generate the electron excitation. The photon energy of the pump pulse depends on the energy levels of the transition. In our case, we have been mainly doing research on metals, semiconductors and organic photovoltacs. Most transitions we are interested in requires the wavelength from NIR to UV. The second harmonic generation (SHG) and third harmonic generation (THG) of 1.03 μm provides us convenient femtosecond pulse synchronized with the XUV. Although the wavelength can't be tuned to target certain specific transitions, they usually can create some excitions for the preliminary experiments.

The SHG and THG setup is shown in Fig. 2.11. First we have a polarizer and $\lambda/2$ wave plate to control the input IR Power. Limited by the crystal

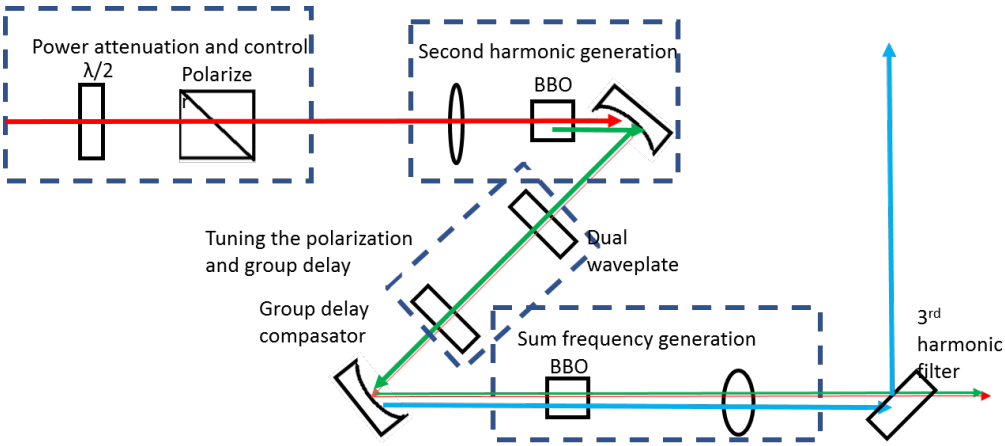

Figure 2.11: Second and Third harmonic generation layout.

damaging and the thermo effects, IR input is usually less than 14 W. The fundamental gaussian beam diameter ($1/e^2$) is 5.8 mm. The polarization is p-polorized. The beam is focused into a 0.5 mm thick BBO crystal cut for type I phase matching for second harmonic generation of 1064 nm. The second harmonic has a s-polarization. Then the fundamental and second harmonic are collimated by a concave silver mirror then sent through a Calcite time delay compensator (TDC12301-AR, Newlight Photonics Inc.) to compensate the group delay caused by the SHG crystal And a dual waveplate (WPD03-H1030-F515-SP, Newlight Photonics Inc.) to rotate the second harmonic polarization to colinear with the fundamental. Then two beams are focused by another silver concave mirror to do the sum frequency generation within a 0.3 mm thick BBO cut for type I third harmonic generation of 1056 nm (BTC5030-THG1056(I)-AR, Newlight Photonics, Inc.). The focal length of both concave silver mirrors M1 and M2 and the two lenses L1 and L2 are all 10 cm. Followed by that, the desirable wavelength is colimated by a lens and filtered out by a harmonic beam splitter.

In the perturbatively excited ARPES experiments, the incident fluence is typically less than 100 μJ/cm^2. Assuming 100 μm diamter beam spot, the average power required to achieve 100 μJ/cm^2 pump fluence at 80 MHz is about 1 W. Fig. 2.12 shows the power output of the SHG and THG. For SHG, We tried a 0.5 mm BBO crystal and 3 mm LBO crystal for Type I phase matching. The BBO crystal shows much higher conversion efficiency in our case. Interestingly, in the other project in our lab, a 2 mm LBO crystal

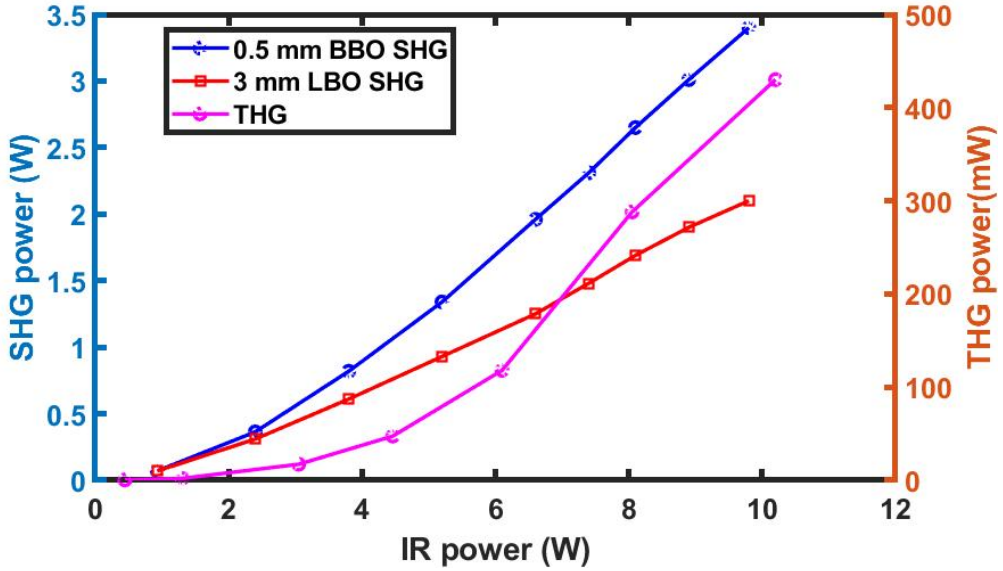

Figure 2.12: Second and Third harmonic generation power.

shows drasticly higher convsersion efficiency compared to the 3 mm one [95]. With 10 W fundamental input, we have a SHG conversion efficiency of 35% and THG convsersion efficiency of 4%. The power level of both are sufficient for the pump beam purpose.

Chapter 3

Cavity enhanced high harmonic generation XUV source

3.1 Introduction

High-power ultrafast lasers are now routinely used to drive high harmonic generation (HHG), providing extreme ultraviolet (XUV) ultrashort pulses with a table-top setup, and also attosecond pulses.[193, 194]. This is a highly nonlinear process, during which electrons are ionized by a strong laser field and then recombine with their parent ions, generating coherent light at high photon energies. Conventionally, HHG is realized by focusing high energy (> 100 μJ) laser pulses to intensities of more than 10^{13} W/cm^2 intensity in a noble gas. The repetition rate is then limited by the average laser power available, usually to less than 100 kHz, but many applications such as XUV frequency metrology,[195] surface photoemission,[196] and photoionization coincidence methods[197] demand higher repetition rates.

An elegant way to achieve this is via resonant enhancement of the fundamental pulse train in a fsEC.[93, 94] The technique is called cavity enhanced high harmonic generation (CE-HHG). Although generating high harmonics in these cavities was originally demonstrated as early as 2005,[198, 199] since then through the use of higher power driving lasers and understanding of the intracavity extreme-nonlinear optics[200, 201, 202, 203] the power from cavity-enhanced HHG systems has increased by more than 6 orders of magnitude, to more the 100 μW/harmonic (at the gas jet) for $\sim$20 eV harmonics generated in Xenon[195, 200, 202, 204, 205, 9]. Recently, Ref. [206] reports

~2 mW of 94 nm harmonic generated by high-temperature gas mixtures as the generation medium.

We have built a CE-HHG XUV source for the purpose of tr-APRES experiments. The XUV source with high flux at 80 MHz repetition rate allows nanoamperes of sample current generated from a sub-100 micron laser spot with space charge effects less than 10 meV. This enables tr-ARPES experiments in a qualitatively different regime of resolution and pump fluence than space-charge limited systems.

3.2 Cavity design and performance

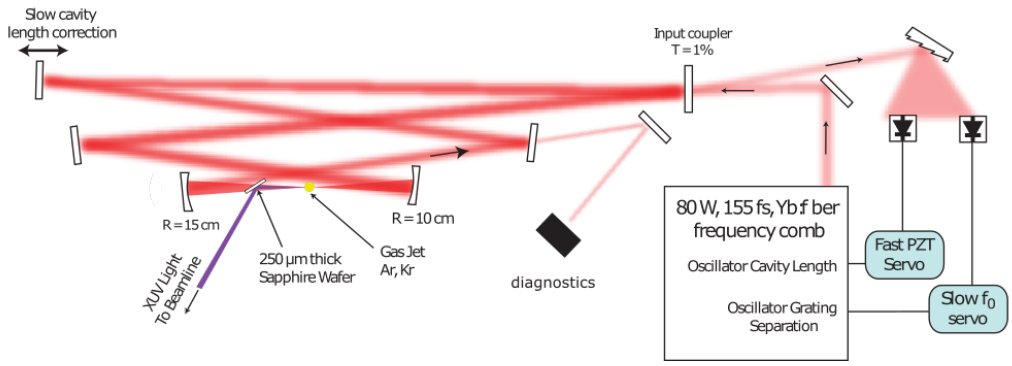

Figure 3.1: The schematic of CE-HHG XUV source.

The schematic of the CE-HHG XUV source is shown in Fig. 3.1. The enhancement cavity is located in 4 by 2 ft vacuum chamber. The optical path is folded with six mirrors. Five of the mirrors are high reflectors with R $>$ 99.95% and the sixth mirror is an input coupler with nominal transmission of 1%. These mirrors are high power low GDD mirrors purchased from Layertec gmbH. This reflectivity of the mirrors should give an over-coupled cavity [202] with a Finesse factor of $>$ 500 and the power enhancement of $>$ 250. The intracavity light is p-polarized. We operate the enhancement cavity near the middle of the stability range. This gives a 24 μm FWHM intracavity focus. Noble gasses are injected to the focus using a fused silica capillary with a 100 μm inner diameter. Harmonics are generated at the focus and reflected from a sapphire wafer placed at Brewster's angle for the resonant 1.035 μm light.

The laser is locked to the cavity using a two-point Pound-Drever-Hall lock as described in [207, 12]. As mentioned in chapter. 2, the EOM actuator in the oscillator put 2 MHz phase modulation sidebands on the frequency comb. The cavity is used as a frequency discriminator. The reflected light off the input couple mirror picks up a phase depending on the frequency detuning. This turns the phase modulation into amplitude modulation. A grating is used to disperse it in wavelength and the two different part of the spectrum is detected by 100 MHz bandwidth photodiodes for two points lock. The signal of the photodiodes are demodulated by simple RF mixed and used as the error signal of the servo loop.

For the fast PZT servo, a commercial PI^2D controller (D2-123 Vesecnt Photonics) is used as the loop filter. The fast output of the servo controller is buffered by a line driver and then goes to the PZT mirror actuator in the oscillator. The PZT mirror actuator can correct the laser length difference with > 30 kHz bandwidth. However, the travel of the PZT mirror actuator is only on the order of μm. In order to correct the longer but slower length drift, We have one cavity mirror sitting on a long PZT actuated stage. The fast output of the servo is low pass filtered (the servo controller has this function built-in) and buffered by a high voltage PZT driver and then goes to a long PZT in the cavity. Putting the long travel actuator in the cavity instead of the mode-locked laser can avoid potential interruption of the laser operation which can possibly cause amplifier damage. The lock makes the oscillator follow the cavity in short time scale while the cavity follows the laser in long time scale.

For the slow f_0 servo, a home made integrator shown in the Appendix is used as the loop filter. The output of the integrator is amplified by a high voltage PZT driver and then goes to the PZT grating actuator in the oscillator as mentioned in section 2.2.3. We only observe the f_0 drift of our laser oscillator is on minutes time scale, manually tuning the f_0 for short time experiments is sufficient. However, for the time consuming tr-ARPES experiments, the f_0 lock helps.

The intracavity power versus cavity input power is shown in Fig. 3.2. A stray light leaking through the cavity mirror is used to monitor the cavity as shown in Fig. 3.1. The red dots shows the measurements of the stretched input pulses with $\sim$ 650 fs pulse duration and the black dots shows the measurement of compressed input pulses with 155 fs pulse duration. First, we look at the red dots. The intracavity power is mostly linear with the input power, the build up factor is > 250. This agrees with the estimation based

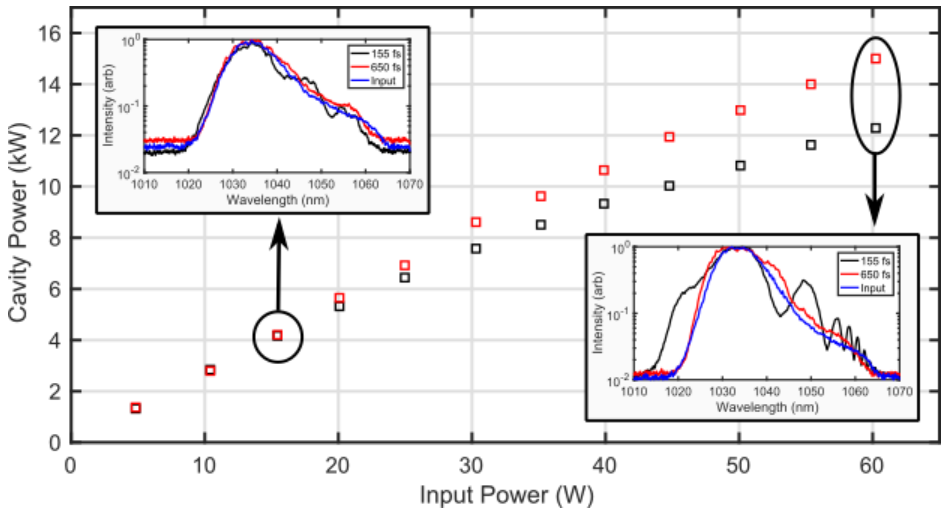

Figure 3.2: Cavity power. Intracavity power for compressed pulses (black) and chirped pulses (red) vs. incident power to the cavity. Positively chirping the input pulse to $\sim$ 650 fs reduces the peak power and intracavity nonlinearity due to the Brewster plate. Below 5 kW intracavity power, the power enhancement is very similar between compressed and chirped pulses and and the intracavity spectra closely mimic the incident laser spectrum (blue), although ripples due to self-phase modulation of the compressed pulses are observable even at 4 kW intracavity power. At higher intracavity power, significant spectral broadening and reduction of the cavity's power enhancement factor are observed. This figure is reproduced from Ref. [12]

on cavity mirror reflectivity. The fact that the build up is almost a constant means there is no significant nonlinear effects for the stretched pulses. The spectrum of the intracavity light is nearly identical to the input light. Our cavity can support the full spectrum of the input pulse and the dispersion of the mirror coatings and the sapphire Brewster plate is negligible with the current spectrum width ($\sim$ 12 nm). For the compressed pulses, the build up factor drops above 7 kW. The spectrum of the intracavity light is broadened and has fringes caused by self phase modulation due to the brewster plate. Despite the distortions of the intracavity nonlinearity, more than 12 kW of intracavity power can be obtained (without HHG gas) when exciting the cavity with 60 W of laser power.

3.3 Cavity enhanced high harmonic generation

3.3.1 Optimize the XUV flux

Much of the basic physics of HHG in optical cavity is the same as "conventional" HHG, but the cavity presents some subtleties. The propagation of intense femtosecond pulses in a noble gas medium has been previously studied theoretically and experimentally [208, 103]. The electric field of the pulses ionizes the gas medium and create a plasma as it progate through the gas medium. For the high rep rate pulses ($>$ 10 MHz), plasma expansion is not fast enough to clear the plasma from the focal volume and replenish it with neutral atoms within one cavity round trip. The accumulated plasma can have several times higher density than the plasma generated by single pass laser. The plasma acts as a highly nonlinear optical element in the cavity ultimately limits the performance of CE-HHG. First, the intracavity pulse gets an additional phase shift as it propagate through the plasma, most of which is the residual plasma from previous round trips. The phase shift varies over the pulse and this time dependent phase can cause a frequency shift to the laser pulse [209]. Second, the plasma generated by a focused laser beam is far from spatially uniform and acts as a negative lens, defocusing the beam. This effect can cause spatial distortion of the trasverse cavity mode and transfer the energy from the fundamental mode to the high order modes. These detrimental effects ultimately limits the performance of CE-HHG [205, 202].

Cavity power

The tunneling ionization rate strongly depends on the ionization potential [210]. Most implementations of CE-HHG have relied on xenon with its relatively low 12.13 eV ionization potential for generating harmonics efficiently with much lower intracavity power than is necessary for other noble gases. However, for photoemission experiments, a wide tuning range of the optimized harmonic order is desirable and also the consumption of xenon becomes prohibitively expensive. Recycling Xenon in CE-HHG is difficult due to the usage of oxygen/ozone gas for mirror cleaning as mentioned in section 3.4.1. For HHG, the optimum of the harmonic emission spectrum is controlled by many factors, but most strongly by the ionization potential of

the gas target and the corresponding optimum laser intensity [211]. We have used Xe, Kr and Ar as the generation gas.

For efficient HHG, a higher cavity power is generally wanted. However, the power of high finesse cavity clamps to a lower point due to the plasma [202, 212, 203, 208, 209]. The constructive interference in the enhancement cavity requires a round trip phase error less than $\pi/\mathcal{F}$. A significant reduction of the buildup factor provided by the cavity is expected when the phase shift caused by the plasma is $\pi/\mathcal{F}$. The intensity in the focus will thus be clamped at values generating phase shifts of this magnitude. The clamping power of the cavity depends on the pulse duration, cavity finesse and the density length product of the plasma. Shorter pulse effectively reduce the steady state plasma and increases the clamping power, however, shorter pulse inevitably broadens the harmonic linewidth which affects the energy resolution. Lower cavity finesse relieves the tolerance of the phase error, but lower cavity finesse also means lower buildup factor, more cavity input power is thus needed. The density length product of the plasma depends the ionization potential of the generation gas and its pressure. The ionization potential of Xenon, Krypton and Argon are 12.13 eV, 14.0 eV and 15.76 eV respectively. So the cavity power required for HHG is different for the 3 gases. The typical cavity power and the peak intensity for Xenon, Krypton and Argon are shown in Table. 3.1.

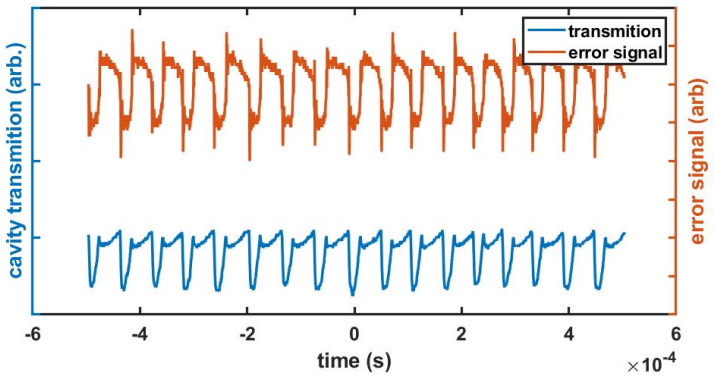

Figure 3.3: The cavity power oscillation due to the optical bistability .

The power dependent phase shift creates oscillation in the lock of the frequency comb laser to the enhancement cavity due to optical bistability [202]. As shown in Fig. 3.8 (b), When the frequency comb sweeps across the cavity

resonance from negative detuning to positive detuning, the plasma generated by xenon gas cause the resonance of the cavity shifting to the same way as the frequency comb goes. However, The response of the plasma is highly nonlinear. In the end of the sweeping, the cavity power has a sharp drop due to the saturation of the plasma phase shift and the cavity lose resonance. The sudden change of the cavity resonance frequency is beyond the bandwidth our lock electronics can handle. As a result, the cavity oscillates. A typically oscillation pattern is as shown in Fig. 3.3. It's characterized by tens of kilohertz oscillation frequency which corresponds to the characteristic timescales of the servo loop. The sudden change of the resonance frequency can be seen on the error signal as a sharp drop. The shifting of the resonant frequency also shows on the error signal as a slow drift. The oscillation induced by the plasma reduced the duty circle of the cavity and limits the XUV flux. The cavity power initializing oscillation can be postponed by offset the lock frequency as reported in Ref. [208, 213].

Gas pressure

The generation gas acts as the nonlinear gain media in the HHG process. Flowing higher pressure into the focus of the cavity increase the density length product of the media, which helps improving the conversion efficiency. However,as mentioned above, due to clamping effect caused by the plasma, the total XUV flux only weakly depends on the gas pressure after the cavity is saturated. On the other hand, Increasing the gas pressure increases the re-absoprtion of the XUV, which ultimately limits the density of the generating media. [214] Due to complicated gas dynamics, the high pressure gas can also cause a spatially nonuniform plasma which can cause cavity mode distortion. For Xe and Kr, optimal harmonic generation typically occurs for 1-2 atmospheres of nozzle pressure, while the Ar HHG flux continues to rise with up to 5 atmospheres of nozzle pressure which is the limit of our gas regulator.

Although the total flux is not very sensitive to the gas pressure, the XUV spectrum can be tuned by the gas pressure. Fig. 3.4 shows the XUV spectrum with Kr pressure of 15 psi, 20 psi and 25 psi. The harmonic order with highest flux shift from 21 at 15 psi to 23 at 20 psi and 25 at 25 psi. The possibly reason may be XUV re-absorption. As the pressure goes up, the XUV re-absorption start to cancel the power growth. However, the higher photon energy XUV has a longer mean free path and weaker re-absorption, So the

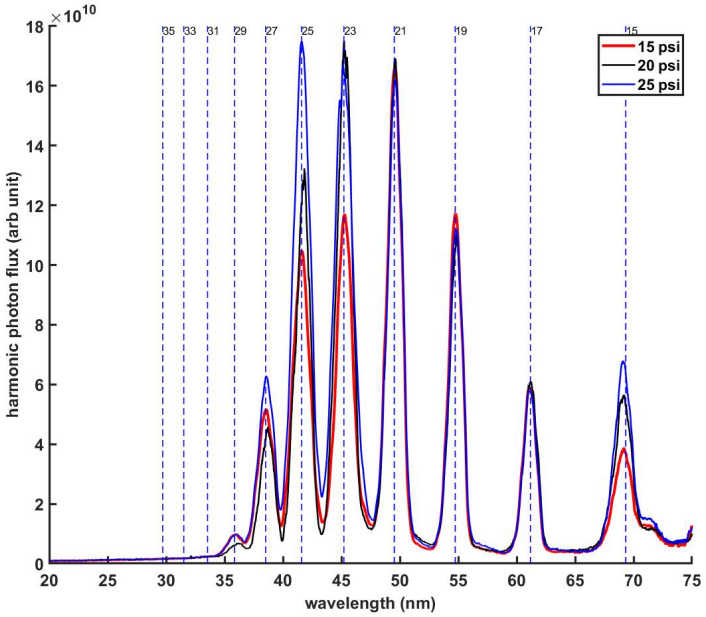

Figure 3.4: The XUV spectrum with different Kr pressure.

peak of the XUV spectrum shifts to higher photon energy side. Estimated by CXRO [215], 1 Torr·cm of Krypton has a transmission around 0.5 depending the photon energy. At 25 psi, the density length product of the gas media is roughly estimated to be on the order of several Torr·cm, on the same order of the re-absorption threshold.

Nozzle position

The XUV flux is sensitive to the alignment of the gas nozzle.During the initial setup, we locate the cavity focus by filling the HHG chamber with ∼100 mTorr Kr gas. With the cavity operating at high enough power, we observe a plasma at the cavity focus. The gas nozzle usually wants to be on the laser beam axis and get to the laser beam path as close as possible without interruption of the cavity operation. We found the bright plasma with a symmetric two lobe shape is a good indicator of nozzle position.

After the rough alignment by looking at the plasma, we optimize the HHG gas nozzle position by moving it to maximize the photocurrent observed on a stainless steel vacuum photodiode (VPD1) shown in Fig. 1.9. The gas

nozzle is held by motorized 3D stage. The picomotor actuator of the stage can break the cavity lock during optimization. To avoid the interruption of the cavity operation, The cavity is typically operated in the ramping mode. We ramp the cavity length across the resonance so the the cavity power transiently builds up and decay away. In this process, XUV is only generated in a short time window. A 30 kHz bandwidth transimpedence amplifier with better than 100 pA sensitivity is desgined for the XUV detection. The circuit diagram is shown in the Appendix. The nozzle position along the laser beam plays an important role in the XUV flux and spectrum. The effect of phase matching and XUV spot profile has been extensively studied. However, there can be substantial difference between the single pass HHG and CE-HHG. There is still a discrepancy in the literature about towards which way the nozzle moves to optimize the flux. In Ref. [216], I. Pupeza and coworkers reports moving the nozzle towards upstream increases the flux. However, in Ref. [217], T.J. Hammond et. al. reports moving the nozzle toward downstream helps phase matching the long trajectories for the near threshold harmonics. In our case, We optimize the nozzle position empirically. By ramping the cavity, the plasma phase shift can be measured as shown in Fig. 3.8 b). Assuming the intracavity focus is located where the plasma phase is strongest, the nozzle position maximizing the total XUV flux is usually right above the focus for Argon and moved to upstream for Xenon and Krypton.

XUV flux

We measure the total photon flux reflected out of the cavity by the photocurrent observed on a stainless steel vacuum photodiode (VPD1). Typically, 100 nA to 300 nA photocurrent is observed despite of generation gas. Assuming 10% quantum efficiency [218], The total XUV flux coupled out of cavity is on the order of 10^{13} γ/s. Assuming an average reflectivity of 10 % roughly estimated from Fig. 3.6, The photon flux generated in the cavity integrated over all the harmonics is on the order of 10^{14} γ/s.

An XUV spectrum generated with Xe is shown in Fig. 3.5. We detect the XUV flux exiting the monochromator and delivered to the sample using four separate detectors: an aluminum coated silicon photodiode (PD, Optodiode AXUV100Al), the photocurrent from TM3, the photocurrent from the sample, and the photocurrent from an Al2O3 vacuum photodiode (VPD2)

placed at the end of the surface science chamber. Fig. 3.5(a) shows a typical HHG spectrum from xenon gas measured using each of the four detectors. The observed harmonic linewidths are due to the intentionally small resolving power of the pulse-preserving monochromator, not the intrinsic harmonic linewidth.

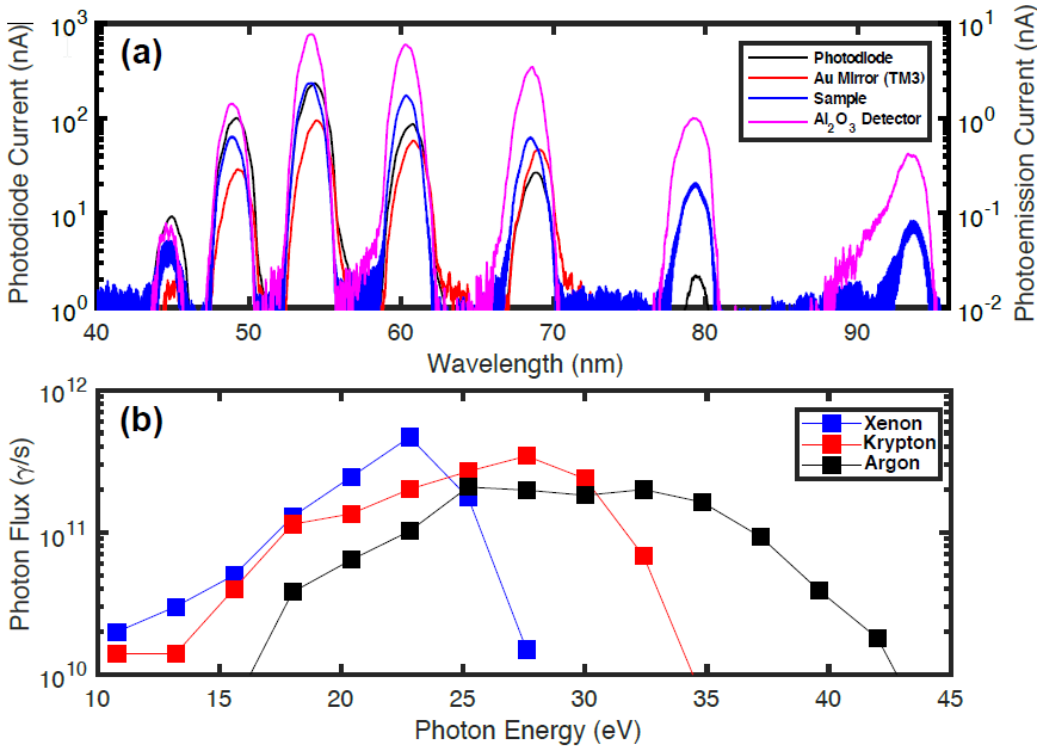

Figure 3.5: (a) An HHG spectrum from xenon gas measured by rotating the monochromator. The photodiode current (black) uses the left y-axis whereas the the photoemission current from three downstream surfaces uses the right y-axis. b) The photon flux delivered to the sample for each harmonic generated with the three gases. The flux has been calibrated using literature values for quantum efficiencies and no corrections for mirror losses have been made. This figure is reproduced from Ref. [9].

The photon flux delivered to the sample can be calculated using the measured photocurrent from all the detectors and literature values for the quantum efficiencies. All of these separate calculations agree within a factor of 2. Since contamination and surface oxidation only cause the quantum efficiency

of XUV detectors to decrease, all calculated photon fluxes represent lower limits. In Fig. 3.5 (b), the higher of the two lower limits from the PD or VPD2 are plotted as a function of photon energy and for three different generating gasses: argon, krypton, and xenon optimized separately. As can be seen in Fig. 3.5 (b), a flux of more than 10^{11} photons per second is delivered to the sample over a broad tuning range. These fluxes are within one order of magnitude of what is available from many state-of-the-art synchrotron beamlines dedicated to ARPES [219, 220, 221]. As shown in Fig. 4.5, we have observed 7×10^{11} photons/s in the 21st harmonic from krypton using a 100 g/mm grating blazed for 55 nm. Critically, since at ∼80 MHz, 7×10^{11} photons/s corresponds to only 8,000 photons/pulse, also comparable to synchrotrons. All of this flux is usable for high-resolution photoemission experiments.

3.3.2 Output coupling

A critical design decision is the method to couple the XUV light out of the cavity. Several outcoupling methods have been proposed and implemented [198, 222, 212, 204, 223]. The dielectric grating output coupler developed by Yost [222] produces the least distortions of the resonant intracavity beam, and has been demonstrated to be robust enough to enable the outcoupled harmonics to be used in several experiments [224, 195]. However, the grating output coupler produces the most distortions of the output coupled harmonics - introducing pulse front tilt on the harmonics that can degrade the temporal resolution and attainable spot size at the sample [224]. The grating output coupling technique also makes dynamic harmonic selection challenging, as the harmonics emerge from the cavity at very different angles. Alternatively, the pierced mirror technique [212] can outcouple very high-energy harmonics, but also has poor outcoupling efficiency for lower-energy harmonics, introduces significant intracavity loss, and is technically challenging to manufacture and align.

In our setup, we use the simple "Brewster plate" output coupling technique. The technique takes the advantage that the index of refraction at XUV wavelength is differently from IR. While the Brewster plate is aligned at the Brewster angle of IR wavelength, the XUV light can still be reflected out despite it's p-polarization. The drawback of this method is the dispersion and nonlinear effects introduced by the Brewster plate, the thermal issues and pointing stability of the Brewster plate and it doesn't work for the photon

energy much higher than 50 eV.

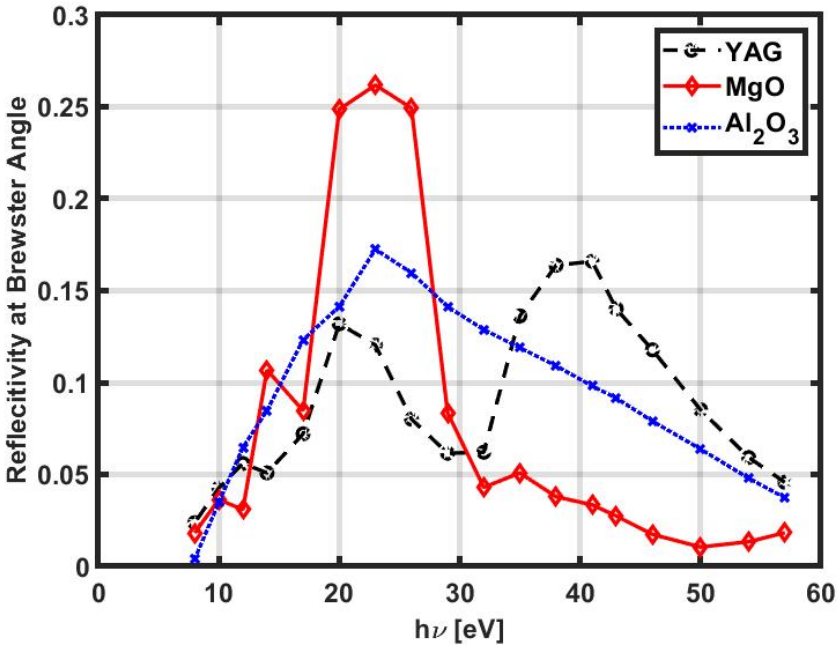

Figure 3.6: The XUV reflectivity of different Brewster plate materials.

Fig. 3.6 shows the reflectivity of the Brewster plate versus photon energy for saphire, YAG and MgO. The Brewster plate is most efficient for the photon energy from 20 to 40 eV. MgO has the highest reflectivity around 25 eV, but its bandwidth is narrow. YAG has a broader bandwidth, but We choose saphire as the Brewster plate material instead of YAG because the sapphire plate has higher thermal conductivity and lower nonlinear index of refraction n_2.The thickness of the Brewster plate is critical for the performance. Thinner Brewster plate cause less dispersion and nonlinear effects, but that weakens the mechanical stability. We found 250 μm thick saphire plate gives a good balance.

The sapphire crystal orientation is c-cut, which means the optical axis of the sapphire is perpendicular to the surface. Although sapphire is birefringent, the angle between incident light and the optical axis remains a constant when the Brewster plate rotates about the surface normal. When c-sapphire is used as Brewster plate, it in principle shouldn't cause a polarization effect.

However, due to the manufacturing error ($\pm 2^{\circ}$), the optical axis has a small angle with the surface normal. The Brewster plate needs to be rotated so the optical axis is in the incident plane.

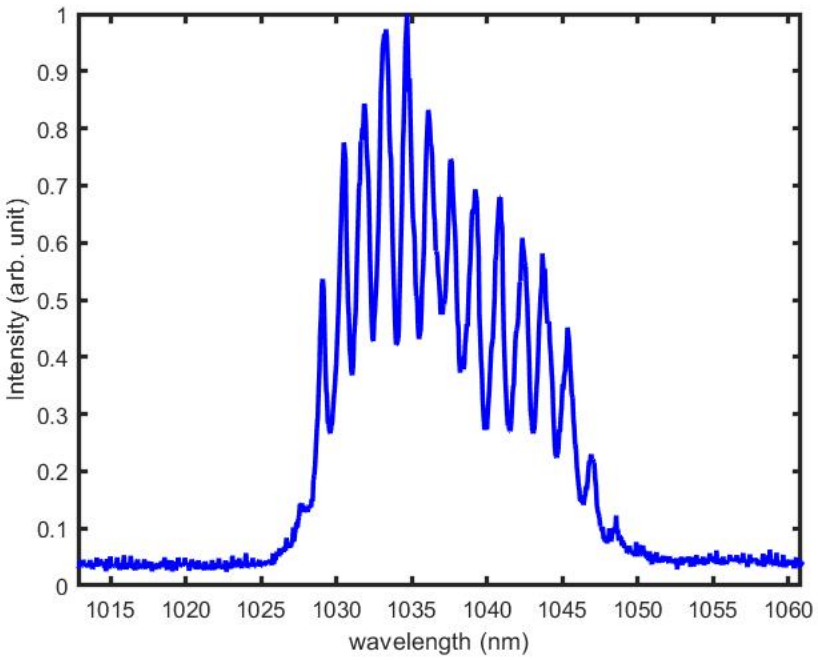

Figure 3.7: The intracavity light spectrum with the Brewster plate used at incorrect orientation. The fringes are due to the etalon effects caused by the Brewster plate.

Fig. 3.7 shows the intracavity light spectrum when the Brewster plate orientation is incorrect. The fringes is due to the etalon effect of the sapphire plate. Due to incorrect orientation, the polarization of the intracavity light is rotated. The interference of the multi-reflection of the s-polarization component cause a filtering effect. The spacing of the fringes is 0.42 THz, which agrees very well with the FSR of the 250 μm sapphire when incident at Brewster angle. The fringes can be eliminated by orienting the Brewster plate so it doesn't change the polarization of the incident light.

3.3.3 XUV linewidth and phase matching

As shown in section. 6.2, the upper limit of our XUV linewidth is 65 meV limited by the energy resolution of our electron energy analyzer. Here we show due to the fact that the plasma generated in the cavity is self limiting, ionization gating is negligible in CE-HHG when the cavity finesse greatly exceeds the harmonic order. We estimate that the XUV linewidth can be as low as 30 meV. Much of the material in this section is reproduced from Ref. [9]. The postdoc Christopher Corder played a leading role in this part of the research.

The single harmonic linewidth from HHG is determined by the duration of time over which harmonics are generated with comparable efficiency and at the same frequency, or the emission window. The emission window can be estimated using a 1D on-axis phase matching model, in which the intensity of harmonic generated over a medium with density ρ and length L is given by Equ. (1.9) [88, 10, 89] The harmonic emission can be gated by two factors: (1) the time dependence of dipole $d_q(t)$, and (2) the time dependence of $\Delta k(t)$ due to ionization and resulting time-dependent phase shifts on both the fundamental pulse and harmonics. Usually in HHG systems, the emission window is determined by loss of of phase matching ($\Delta k(t)$) due to ionization of the medium, or "ionization gating" [211, 193, 63]. Changes in the medium phase shift on the fundamental pulse on the femtosecond time scale become relevant for ionization gating when they approach $\sim \pi/q$, where q is the harmonic order, or 165 mrad for the 19th harmonic generated in Xenon and 95 mrad for the 33rd harmonic generated from Argon.

In CE-HHG, because the power enhancement relies on the constructive interference of the pulse in the cavity with pulses coming from the laser, time-dependent phase shifts are restricted to be less than $2\pi/\mathcal{F}$ [203], roughly one order of magnitude smaller than the scale relevant for ionization gating. Furthermore, the nonlinear of the response of the cavity itself can be used to estimate the magnitude of plasma phase shifts on the fundamental pulse. Figure 3.8a) shows a sweep of the cavity length through resonance at low power demonstrating a Lorentzian linewidth of 156 kHz corresponding to a cavity finesse $\mathcal{F} = 564$. At high intracavity powers the response is distorted by intensity dependent phase shifts, exhibiting a self-locking phenomenon that allows measurement of the magnitude of these phase shifts [225, 200, 203]. Figure 3.8b) shows the response of the cavity at high power without (black) and with (blue) Xenon gas, and the linear response (red) measured

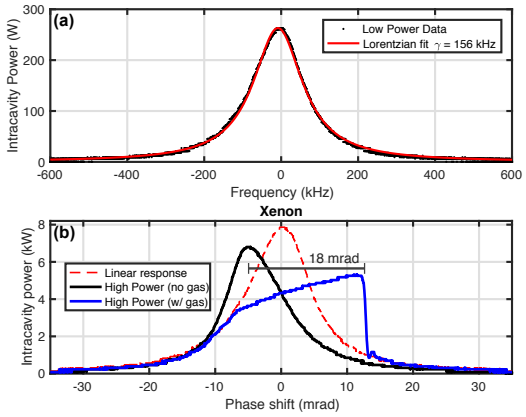

Figure 3.8: a) The Lorentzian linewidth of the cavity measured by scanning the frequency comb across the cavity resonance condition at low power. b) At high power without gas the sapphire plate near the focus induces a nonlinear phase shift (black line) distorting the resonance condition. The plasma generated when flowing xenon gas also produces a nonlinear phase shift (blue line), with opposite sign, of at most 18 mrad. The linear response (red dashed line) measured in (a) is scaled here by the ratio of laser powers incident to the cavity at high vs low power. The frequency is calibrated by the 2 MHz phase modulation sidebands for the PDH lock. The frequency is then converted to phase shift by the fact that one FSR corresponds to 2π phase shift. This figure is reproduced from Ref. [9].

at low power and scaled by the ratio of the high and low laser powers used. The high power cavity response without gas shows a phase shift induced by the nonlinear response of the sapphire Brewster plate near the cavity focus. When sweeping with Xenon gas the plasma phase shift extends for 18 mrad. The ionization rates are lower in Kr and Ar producing phase shifts of 6 and 3 mrad respectively.

As discussed by previous authors [200, 203, 201], the phase shifts observed in the sweeping data have a dynamic component due to single-pass ionization, $\phi(t) - \phi_{ss}$, and a steady state component due to the repetition rate of the laser exceeding the rate at which plasma clears from the focal volume, ϕ_{ss}. Holzberger performed detailed numerical simulations, including accounting for 3D effects, to determine a limit to the time-dependent plasma phase shift on the fundamental pulse of $2\pi/\mathcal{F}$. This bounds our transient phase

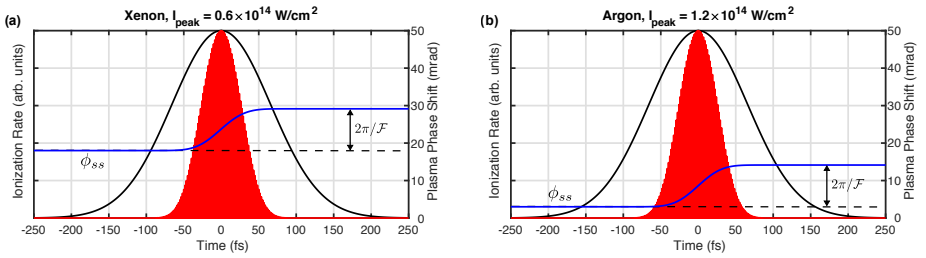

Figure 3.9: The instantaneous ionization rate (red) of (a) Xenon and (b) Argon is shown for a 155 fs pulse (intensity envelope in black) calculated for the peak intensity used to generate harmonics in the cavity. The ionization window of 62, 61 fs corresponds to a harmonic linewidth of 32, 34 meV for Xenon and Argon respectively. The time dependent plasma phase shift on the driving field (blue) increases from the steady state value by $2\pi/\mathcal{F}$ over the pulse. This figure is reproduced from Ref. [9].

shift on the fundamental during the pulse to $\phi(t=\infty) - \phi_{ss} \leq 2\pi/564 = 11$ mrad.

Figures 3.9 shows the calculated plasma phase shift on the fundamental for a worst case scenario where the phase shift determined from the sweeping data is taken to be entirely due to the steady state term and the time-dependent phase shift is an additional $2\pi/\mathcal{F}$. Figure 3.10 shows two extremes: Xenon with a large steady state ionization fraction η_{ss} but low harmonic orders, and Argon with high harmonic orders but low η_{ss}. The peak ionization rate, calculated using the modified ADK model of Tong and Lin [210] and our pulse parameters is shown in red. The phase shifts on the fundamental are related to $\Delta k(t)$ via

$$\begin{aligned}\Delta k(t)L &= qk_0(t)L - k_q(t)L \\ &= q(\phi(t) - \phi_{ss}) - (k_q(t) - k_q(t=-\infty))L + \Delta k(t=-\infty)L \quad (3.1)\end{aligned}$$

where $\Delta k(t=-\infty)$ contains all time-independent contributions to phase mismatch including the Gouy phase and the effect of the neutral gas and steady state plasma. The plasma phase shift on the harmonic is negligible compared to the fundamental so that $k_q(t)$ is determined by the change in the medium's index of refraction due to ionization of the neutral atoms. Per atom ionized, this effect is much smaller than the change in the plasma phase shift on the fundamental and thus the second term in (3.1) is typically more than

an order of magnitude smaller than the first [10]. The phase shift imparted on the fundamental by the generated the free-electron plasma dominates the time-dependent component of Δk.

For phase matching calculations, we estimate the medium length to be the nozzle diameter of 100 μm since the nozzle is placed as close possible to the cavity focus before significant degradation of the cavity finesse is observed. The density-length product of the gas can be estimated from the plasma phase shifts observed as in figure 3.8 and calculations of the ionization rate under our pulse parameters to be in the range of $4 - 10 \times 10^{15}$ cm^{-2}. Under these conditions, the dominant contribution to Δk is the Gouy phase due to the small laser spot size (24 μm). This geometric effect does reduce the overall conversion efficiency, but does not depend on time and thus does not gate the harmonic emission. Figure 3.10a,b) shows a calculation of the the time-dependent coherence length vs. harmonic order including all contributions to phase matching in the 1D model. Figure 3.10c,d) shows an estimate for the harmonic emission window assuming the single atom dipole for the plateau harmonics is proportional to the square root of the ionization rate $w(t)$ [200, 226] and the time dependent phase matching factor $F(t)$, defined as the ratio of Equ. (1.9) to its value with $\Delta k = 0$. From Fig. 3.10, one can see that while the overall phase matching is poor, the harmonic emission window is determined by $d_q(t)$ and not gating due to changes in the phase matching conditions. This leads to an emission window determined mainly by the length of the pulse and the intensity dependence of the dipole. This key result is independent of the model assumptions (e.g. medium length) as expected from the comparison of $2\pi/\mathcal{F}$ to π/q discussed in the paper. Ionization gating is negligible in CE-HHG when the cavity finesse greatly exceeds the harmonic order.

The frequency spectrum of an individual harmonic is given by the Fourier transform of the harmonic field $E_q(t)$ at the sample position. An accurate calculation of $E_q(t)$ requires solving the 3D time-dependent Schrödinger equation to determine $d_q(t)$ [227], along with the 3D Maxwell's equations to determine $E_q(t)$ in the far field. This calculation is beyond the scope of this paper. However, on axis in the far-field, the plateau harmonics are mainly due to the 'short trajectory' contribution. Then, for the purpose of estimating the emission window and harmonic linewidth, the time dependence of the induced dipole amplitude can be reasonably approximated by $d_q(t) \propto \sqrt{w(t)}e^{i\phi_d(I)}$, with $\phi_d(I) \approx 1 \times 10^{-14}$ cm^{2}W^{-1} $\times$ $I_0(t)$, where $I_0(t)$ is the intensity profile of the driving field. The intensity dependent phase

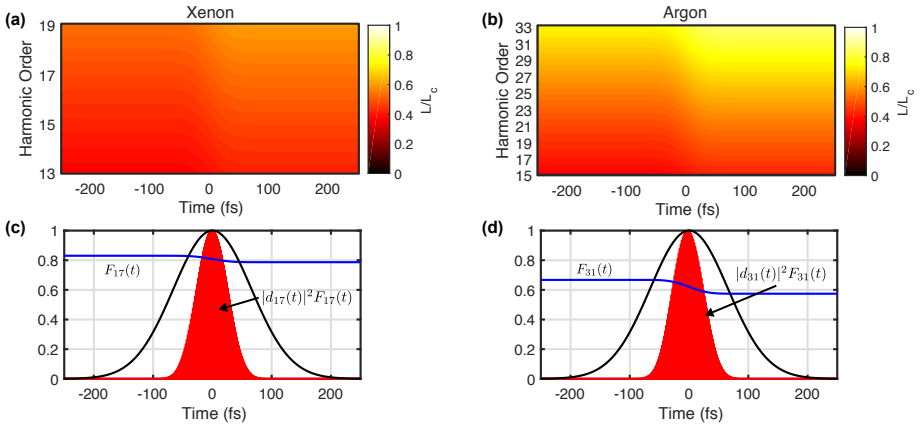

Figure 3.10: a),b) The transient change in phase matching L/L_c, where $L_c = \pi/\Delta k$ is the coherence length, for harmonics in xenon and argon respectively. While the overall phase-matching is poor at the highest harmonics, it does not significantly change during the pulse. c),d) The emission window (red) is calculated for harmonic 17/31 generated from Xenon/Argon gas given by the product of the dipole moment $d_q(t)$ with the time dependent phase matching term $F_q(t)$ (also shown separately in blue). The cavity does not allow transient phase shifts large enough to drive $F_q(t) \rightarrow 0$, preventing any ionization gating of the emission window. The intensity profile of the fundamental pulse is shown in black for reference. This figure is reproduced from Ref. [9].

can lead to instantaneous frequency shifts and broadening of the harmonic linewidth, as discussed by Chang [211]. This approximate, idealized dipole can be used to estimate a lower limit on the harmonic linewidth. For our pulse intensities the linewidth calculated from the Fourier transform of the ionization window is the same with and without the intensity dependent phase contribution. Table 3.1 shows the ionization window, and the lower limits to the harmonic linewidth estimated in this fashion.

The limits on transient phase shifts imposed by the enhancement cavity force the HHG into a regime that is ideally suited for generating harmonics with narrow linewidths. By removing the possibility of an ionization gate to the emission window, instead the linewidth is determined the HHG dipole. Further, it is possible to use the Pound-Drever-Hall lock offsets to spectrally filter the fundamental pulse [207] allowing a variable driving pulse duration

Generating Gas	Cavity Power (kW)	Peak Intensity (W/cm^2)	Single Pass Ionization Fraction	Ionization Window (fs)	Minimum Linewidth (meV)
Xenon	5.0	5.6×10^{13}	0.12	62	32
Krypton	7.5	8.4×10^{13}	0.06	61	34
Argon	10.5	1.2×10^{14}	0.03	61	34

Table 3.1: Pulse and cavity conditions for driving HHG with different gas media. The single pass ionization fraction and maximum HHG generation window were calculated using the intracavity pulse parameters for each gas. The minimum linewidth is determined from the Fourier transform of the ionization window including the intensity dependent dipole phase.

and emission window. Figure 3.11 shows the coherence length and emission window calculated for Xenon with a 310 fs pulse with the same peak intensity as Fig. 3.10, but reduced gas density to maintain $\phi(t) - \phi_{ss} = 2\pi/\mathcal{F}$. The emission window of 125 fs produces a lower harmonic linewidth of 18 meV. Appropriately calibrated, each experiment could be conducted with the optimum energy/time resolution for the system being studied. In principle single-pass HHG could also be done under these low plasma conditions, but in practice this is not done due to the reduced efficiency.

3.4 The stability

3.4.1 Optics degradation

The enhancement cavity is sensitive to losses, so the surface of the cavity mirrors and the brewster plate must be clean, even a slight degradation in their performance can be of concern. It is a well known fact that XUV and high peak power IR can induce degradation of the optics surfaces by photo-induced chemical reaction of the hydrocarbon on the optics surfaces. [228, 60] When the optics degradation occurrs, the XUV reflectivity of the brewster plate drops, the cavity build up factor decreases and the optics degradation can also cause a distortion on the spatial mode of the cavity. There is speculation that dangling bonds from the specific dielectric materials also play a role in the process. These effects can often be reversed with the introduction of oxygen gas or ozone near the mirror surface.

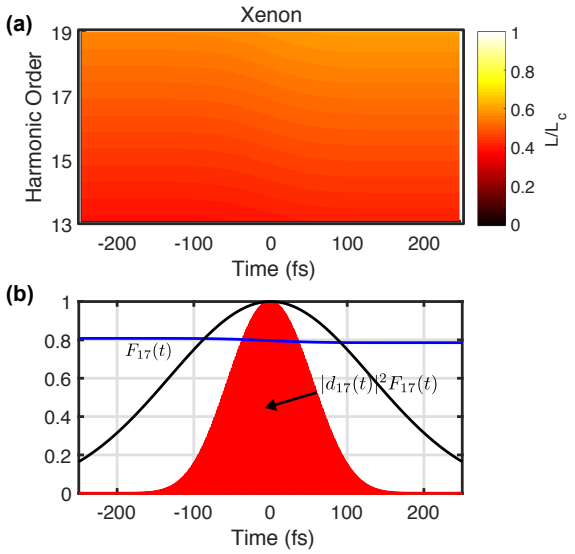

Figure 3.11: a) The coherence length calculated for harmonic generation in Xenon with a pulse duration of 310 fs. b) The ionization window for harmonic 17 is increased to 125 fs corresponding to a minimum linewidth of 18 meV. This figure is reproduced from Ref. [9].

When generating XUV light, We continuously dose the cavity mirrors with ozone to prevent the cavity performance from rapidly degrading due to hydrocarbon contamination. To do this, a mix of ozone and O_2 is produced by passing pure O_2 gas through a commercial ozone generator (Ozotech Poseidon 220) and flowed through 250 μm stainless steel capillaries aimed at each intracavity optic at a backing pressure of 150 Torr absolute. The gas through put is roughly 2 Torr·L/s. Under these conditions we observe that we can generate harmonics indefinitely without degradation.

3.4.2 Optics damage

Different from optics degradation which is usually reversible, optical damage is permanent. In the enhancement cavity, the optics damage occurs due to the high average power and the high peak power. The optical damage of dielectric mirrors at 1 μm have been extensively studied [229, 101, 133, 230]. The dielectric mirror damage typically occur above 10 kW average power in

the enhancement cavity [133]. For the femtosecond pulses, The damage of the mirror coating is initiated by a combination of multiphoton, tunneling, and avalanche ionization mechanisms [230]. However, in our experiments, most of optics damage is due to the dusts on the optics surface. The mechanism is possibly thermal damage. Some dusts in the air is absorptive and reactive. The mirrors can be contaminated by venting the chamber to the dusty air. We observe bright glowing spot when the dust is heated with multiple kilowatts power. The high temperature dust can create a local hot spot on the optics and cause damage. With the presence of the ozone, it's even worse. The ozone can ignite the reactive dusts, and cause localized explosion and flaming on the optics surface.

It's important to keep the optics clean and free of dusts. In our lab, we clean the optics by First Contact^{TM} polymer solution which can be applied to the surface as a liquid like a nail polish and peeled off like a polymer film. This cleaning method is effective and gentle to the optics while the brute force wiping method can possibly scratch the mirror surface and introduce new dusts. Once the mirrors are cleaned and the cavity is working, keeping the HHG chamber in the vacuum is the best way to keep everything safe and clean. Our XUV light source can continuously work without maintenance as long as we don't vent the HHG chamber.

3.4.3 The size of the mirrors

The enhancement cavity was initially built with $0.5''$ diameter mirrors with the same coating. We observed the cavity power decay shown in Fig. 3.12. The cavity power typically begins to decay after several minutes running. The power in the cavity falls over minutes timescale and eventually level off at very lower value as shown in the red curve. After cavity lock is broken and relocked, the cavity power can partially recover but start decay sooner as show in the blue curve. The cavity power decay was often accompanied with cavity mode blinking and distortion. However, no obvious movement of the cavity mode was observed. The reason of the cavity power decay is the combination of optics degradation and thermal effects. The cavity decay was not completely fixed until we changed to $1''$ diameter mirror. This is surprising because the beam size on the cavity mirrors are ~ 1 mm. The possible reason maybe the diffraction loss of the small mirrors are aggravated by the mirror deformation caused by the thermal effects.

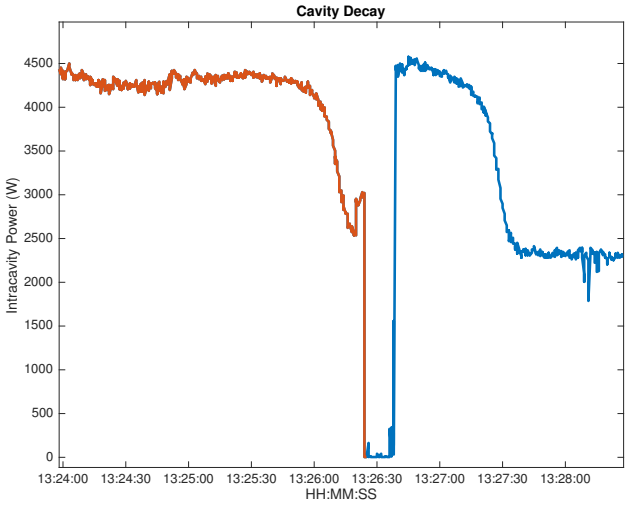

Figure 3.12: Cavity power decay related to the cavity mirror size. The power in the cavity falls over minutes timescale and eventually level off at very lower value as shown in the red curve. After cavity lock is broken and relocked, the cavity power can partially recover but start decay sooner as show in the blue curve.

3.4.4 Thermal effects of the cavity mirrors

As studied by Pupeza and co-workers [231, 133], significant thermal distortions of the intracavity mirrors can be observed upon changing the intracavity power - sometimes necessitating ultra-low-expansion glass mirror substrates. We thus studied this effect in our current fused-silica substrate cavity. Figure 3.13(a,b) shows measurements of the intracavity focus at both low power and 11 kW intracavity average power. We measure a 10% change in vertical beam waist at high power with negligible change in horizontal. The vertical dimension has a greater sensitivity due to the cavity astigmatism arising from the curved mirrors. Figure 3.13(c) shows measurements of the focal spot size over a one hour period at high average power, indicating good long-term stability of the intracavity mode in both pointing and spot size. This is aided by the fact that we operate the cavity close to the center of its range of stability, which makes the cavity's focal spot size relatively insensitive to thermal deformations of the mirrors.

We also monitor the thermo lensing effects in the cavity by looking at the

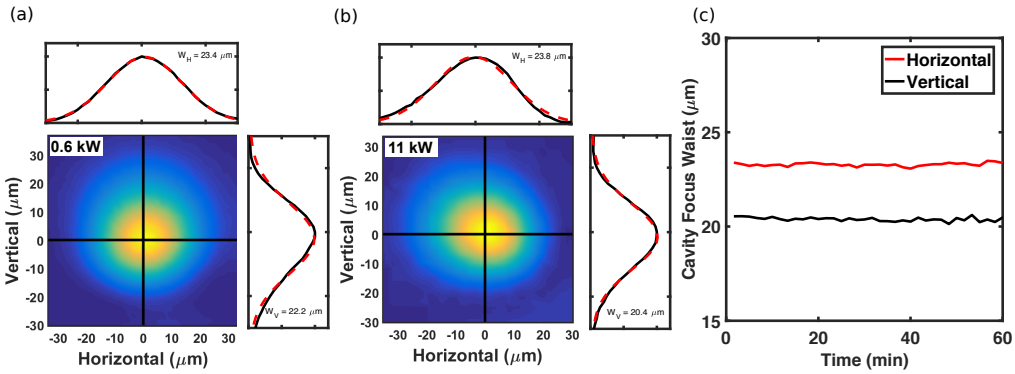

Figure 3.13: Cavity Thermal Stability. (a) and (b) The cavity focus measured at 0.6 kW and 11 kW intracavity power, respectively. Lineouts taken through the centroid (black bars) are plotted alongside the images with Gaussian fits (red dashed line) to the data. Thermal distortions of the mirrors at high power cause a $\sim 10\%$ change in vertical beamsize. (c) At 11 kW the cavity focus is measured demonstrating no significant change in size over one hour. This figure is reproduced from Ref. [12].

resonant frequency of a high order mode. We pick TM_{10} mode for simplicity. The resonant frequency of the TM(0 1) mode is measured by put variable frequency phase modulation side bands on the frequency comb light by the EOM in the oscillator. Then we monitor the cavity transmission by a RF spectrum analyzer. When the modulation frequency is equal to the resonant frequency of the high order mode, We observe a amplitude modulation side band on the RF spectrum analyzer. The resonant frequency of TM(1 0) mode is 23.4 MHz when the cavity is cold, then it shifts to 24.2 MHz when the cavity warms up at 10 kW power. The frequency change corresponds to the change of the trace of the cavity's ABCD matrix[99] M from -0.1 to -0.18 in the horizontal dimension. the thermal lensing effect only slightly shifts the cavity in its range of stability. This agrees very well with the cavity focus spot size measurements.

The PZT mirror actuator mentioned in section 2.2.3 was originally in the enhancement cavity. The transmitted power of the high reflector mirror is on the order watts which all goes to the PZT and cause substantial heating effect. By moving the PZT into the oscilator and adjusting the cavity lock accordingly, the actuator heating is avoided.

3.4.5 Brewster plate mount

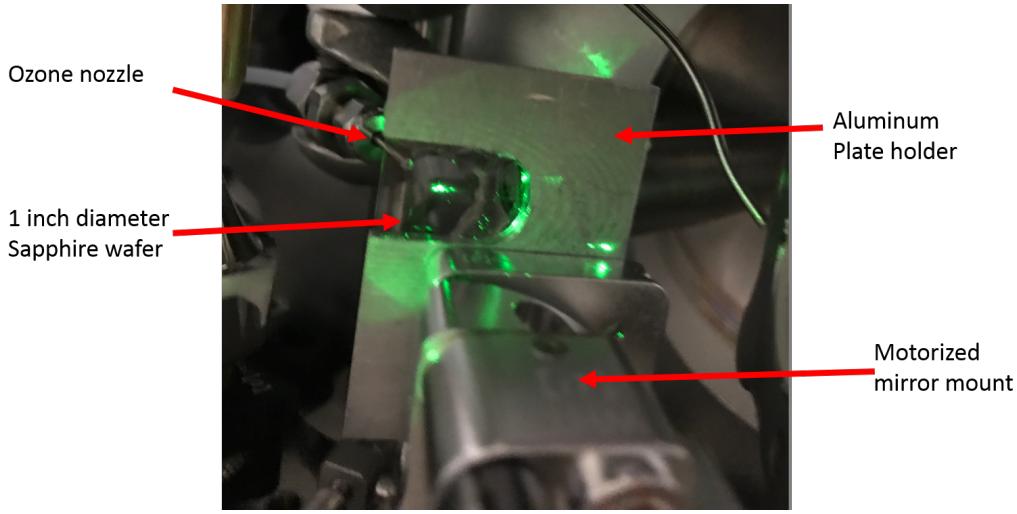

Figure 3.14: A photo of the brewster plate mount.

The pointing stability of the Brewster plate is critical for delivering the XUV photons through the beamline. Several kilowatts intracavity power transmits through the Brewster plate can cause a heat load, which deforms the brewster plate. The deformation of the brewster plate can cause XUV beam clips on the downstream monochromator optics, which reduce the XUV throughput and cause aberrations. In order to improve the pointing stability, The sapphire wafer is bonded to an anodized aluminum mount with a high thermal conductivity, low outgassing epoxy. The anodized aluminum facilitates the radiative cooling. The sapphire wafer is 1 inch in diameter but only a 1.3 cm x 1.9 cm clear aperture is left unsupported by the aluminum mount to minimize thermal deformation of the Brewster plate. The aluminum plate is mounted to a compact motorized mirror mount for easy alignment and active correction of the thermal deformation. A photo of the Brewster plate mount as shown in Fig. 3.14. We have observed this mounting scheme to provide outcoupling with stable pointing for many hours of continuous operation.

3.4.6 gas nozzle

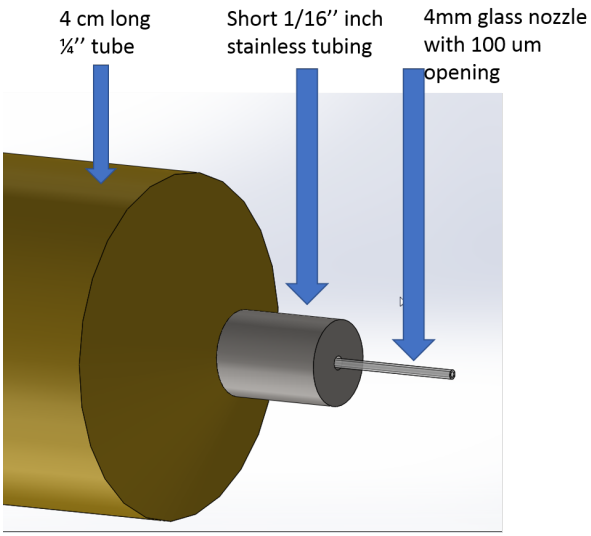

Figure 3.15: The design of HHG gas nozzle.

XUV is generated by flowing noble gas through a HHG gas nozzle. The XUV flux and the cavity power is sensitive to the nozzle position. For efficient XUV generation, the nozzle tip need to be close to the center of the cavity focus. The gas nozzle can have a substantial heat load due to the high intracavity power. Due to the thermal expansion, the nozzle can expand and get even closer to the laser beam. Eventually, the nozzle can clip on the laser beam and cause damage or interrupt the operation of the cavity. The gas nozzle design is shown in Fig. 3.15. The tip of the gas nozzle is made of 4 mm high purity fused silica capillary with 100 μm opening. The short length can effectively alleviate the thermal expansion of the glass part. The glass capillary is connected to a 0.25 inch brass tube by a 1/16 inch stainless tubing adaptor, The 0.25 inch brass tube can be conveniently connected to a Swage-lok typing fittings. The 3 parts are sealed with Hysol 1C-LV epoxy. All the gas tubing and fittings inside the HHG chamber are stainless steel for high gas pressure operation. We have tried gas pressure up to 5 atm safely. The gas nozzle assembly is helded by a 3D translation stage for easy alignment. We have observed this nozzle design works for many hours of continuous operation for XUV generation.

3.4.7 XUV flux stability and noise

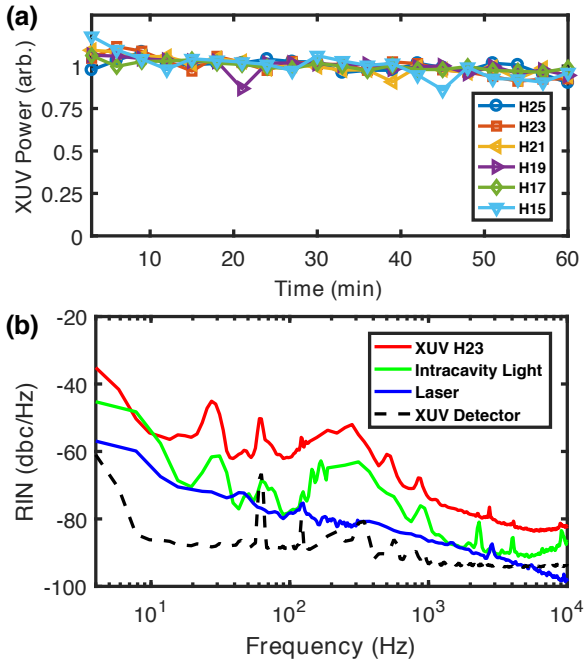

Figure 3.16: a) Normalized XUV flux measured with PD after the monochromator for harmonics 15-25 from Kr over 1 hour without human intervention. b) Relative intensity noise (RIN) of the 23rd harmonic (red), intracavity laser light (green), and Yb:fiber laser (blue), along with the detector noise floor (black dashed). This figure is reproduced from Ref. [9].

We evaluated the amplitude noise and the flux stability of the system using the PD detector. For the flux stability, we recorded a series of monochromator scans over a one hour period without any human tuning of the laser alignment or servo loop. Figure 3.16a) shows the relative power in each harmonic from Kr with a delivered flux greater than 10^{11} photons/s obtained from each mono scan. The RMS fluctuations averaged all the harmonics over this period are 5%. Similar results are obtained for HHG in Ar or Xe as well. On longer periods, slow drifts in the laser alignment into the cavity and servo-loop offsets require occasional human intervention to maintain the flux levels at those shown in figure 3.5b). It is also important

to note that since more than 100 pA of photocurrent is observed from TM3, drifts in the XUV flux can be normalized using this in-situ monitor, as is commonly done at synchrotrons.

For the amplitude noise (RIN) shown in figure 3.16b), the photodiode current from the 23rd harmonic from Kr is amplified using SRS 570 current amplifier and recorded with an FFT spectrum analyzer. For frequencies above 100 Hz, the RIN level is below -52 dBc/Hz, which can enable small differences in the photoelectron spectra to be recorded via lock-in detection. At this noise level, EDC or ARPES signals up to 10^5 counts/second/bin can be photoelectron-shot-noise limited with proper correction for drift using the TM3 photocurrent.

3.4.8 Long term XUV flux

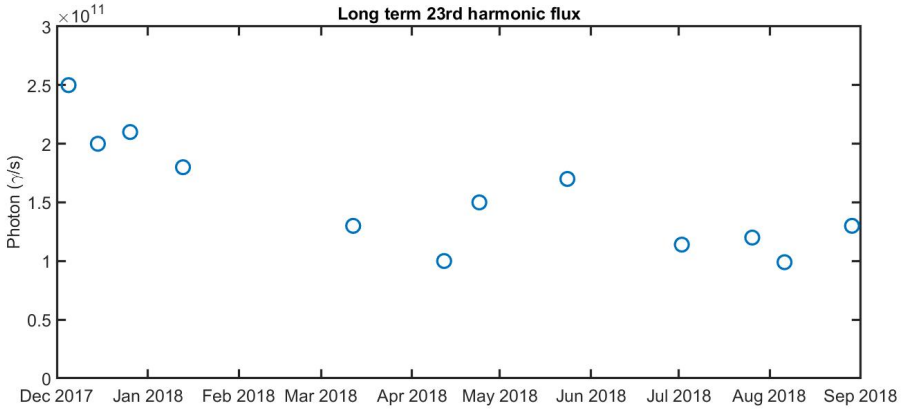

Figure 3.17: The flux of 23rd harmonic over 9 months.

Fig. 3.17 shows the flux of 23rd harmonic with Krypton over 9 months without venting the HHG chamber and maintenance. After that, we vented the HHG chamber in order to prepare the beamline for the TOF k-mic. Most of the data is taken within the first 20 min after the cavity starts running but before everything fully warms up. The photon flux only drops by about a factor of 2 over 9 month and trend seems reaching a plateau. The photon flux is still above 10^{11} γ/s. For our experiments, this kind of loss is acceptable.

Chapter 4

XUV beamline

After XUV is coupled out of the cavity, A home made time preserving monochromator is used to select the XUV wavelength. Then a refocusing mirror is used to focus the XUV on to the sample. A detailed layout of the XUV beam line is shown in instrument layout Fig. 1.9.

4.1 Toroidal mirror

In the XUV wavelength regime, it is hard to focus the XUV beam by transmission optics such as lenses due to its high absorption, e.g. a typical absorption length in the solid is on the order of 100 nm. The optics to focus XUV pulses are typically reflective. There are mainly two kinds of XUV reflectors, multilayer-coated mirrors and grazing incidence mirrors.

Multilayer-coated mirrors are composed of multiple thin layers of material with different index of refraction contrast, typically deposited on a substrate of glass or some other optical material. Multilayer-coated mirrors function based on the interference of light reflected from the different layers of the stack. The thickness of the layers can be optimized to achieve high reflectivity on a specific wavlength. Multilayer-coated mirrors don't work well for photon energy less than ~ 30 eV, because the wavelength is close to the absorption length in the material. They are typically operated at near normal-incidence to manage high-aperture beams with low aberrations. For example, the EUV lithography is based on aspherical multilayer-coated mirrors. They are also widely used in the synchrotron light sources. However, they only works at specific wavelength and their bandwidth is narrow. This type of mirrors are

not suitable for the high harmonic generation sources with a bandwidth of tens of eV.

On the other hand, the grazing incidence mirrors are good at focusing broad band and tunable XUV light. This kind of mirrors simply use the fact that the Fresnel reflectivity approaches one as the angle of incidence gets close to 90 °. This kind of mirror can be simply a glass substrate polished to atomic flatness or it can be coated with various material to enhance the reflectiviy for certain wavelength. However, due to the grazing incident angle, a spherical mirror can have significant astigmatism aberration. To avoid the astigmatism, The simplest way to focus the XUV beam is to use a toroidal mirror. A toroidal mirror is a reflector whose surface is a section of a torus, defined by two radii of curvature in two perpendicular dimensions. Such reflectors are easier to manufacture than a paraboloid or ellipsoid. So, they are much cheaper than ellipsoidal or paraboloidal mirrors for the same surface quality. When a the toroidal mirror is used to match its designed angle, it is free of astigmatism. However, it can suffer from severe coma aberration.

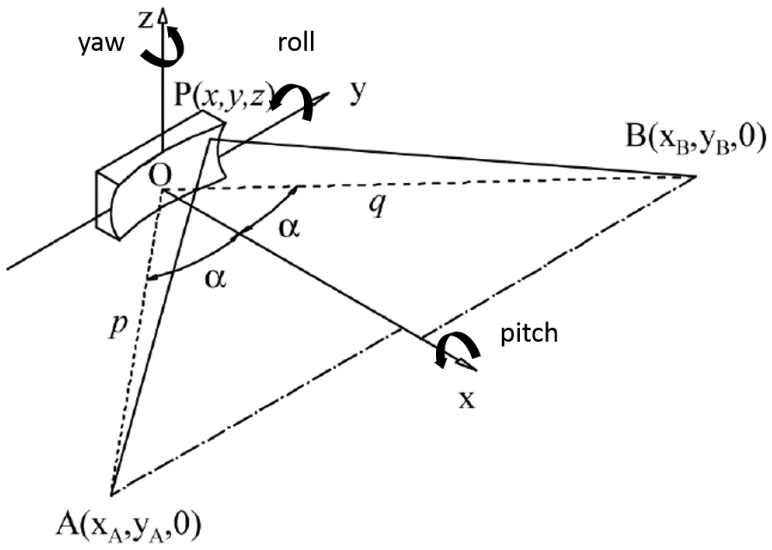

Figure 4.1: The schematic of a toroidal mirror. This image is taken from Ref. [13].

We first show the aberrations introduced by a single toroidal mirror can be canceled when it is used in the 1:1 imaging configuration. The treatment

in this section is reproduced from Ref. [13, 232]. The optical layout of a toroidal mirror is shown in Fig. 4.1. The light-path function, F, of a ray emitted from the point source A, which passes through the focal point B after reflection at the point P(x,y,z) on the mirror surface is defined as F = $\langle AP\rangle + \langle PB\rangle$. Taking into account the equation of the toroidal surface, the distances $\langle AP\rangle$ and $\langle PB\rangle$ can be expressed as functions of the variables α, p, q, y and z, where α is the angle of incidence, p and q are the lengths of the entrance and exit arms respectively (i.e. the distances between A and the mirror center, O, and between O and B respectively), y and z span on the mirror surface. The light-path function is expressed as a power series of y and z:

$$F = p + q + F_{20}y^2 + F_{02}z^2 + F_{30}y^3 + F_{12}yz^2 + O(y^4, z^4) \tag{4.1}$$

where the series has been truncated to the third-order terms. For a toroidal surface with tangential radius R and sagittal radius ρ, the F_{ij} terms are:

$$F_{20} = \frac{1}{2}\cos^2\alpha\left(\frac{1}{p} + \frac{1}{q} - \frac{2}{R\cos\alpha}\right) \tag{4.2}$$

$$F_{02} = \frac{1}{2}\left(\frac{1}{p} + \frac{1}{q} - \frac{2\cos\alpha}{\rho}\right) \tag{4.3}$$

$$F_{30} = \frac{1}{2}\sin\alpha\cos\alpha\left[\frac{1}{p}\left(\frac{\cos\alpha}{p} - \frac{1}{R}\right) - \frac{1}{q}\left(\frac{\cos\alpha}{q} - \frac{1}{R}\right)\right] \tag{4.4}$$

$$F_{12} = \frac{1}{2}\sin\alpha\left[\frac{1}{p}\left(\frac{1}{p} - \frac{\cos\alpha}{\rho}\right) - \frac{1}{q}\left(\frac{1}{q} - \frac{\cos\alpha}{\rho}\right)\right] \tag{4.5}$$

According to Fermats principle of least time, aberration-free image focusing is obtained by the conditions $dF/dy = 0$ and $dF/dz = 0$, which must be satisfied simultaneously by any pair of y and z values. This requires all F_{ij} terms are equal to zero. First, we set F_{20} and F_{02} to zero, we have

$$\frac{1}{p} + \frac{1}{q} = \frac{2}{R\cos\alpha} \tag{4.6}$$

$$\frac{1}{p} + \frac{1}{q} = \frac{2\cos\alpha}{\rho} \tag{4.7}$$

Equ. (4.6) and Equ. (4.7) takes the same form of a thin lens equation. These two equations describe how the focal length of the toroidal mirror changes with the incident angle α in the tangential plane and the sagittal plane. Usually α is chosen so that the focal length of the mirror in the tangential plane $f_{\parallel}$ and the sagittal plane $f_{\perp}$ are equal. so

$$f_{\parallel} = f_{\perp} = \frac{R\cos\alpha}{2} = \frac{\rho}{2\cos\alpha} \tag{4.8}$$

The coma aberration is controlled by the third order terms F_{30} and F_{12}. In order to achieve coma free imaging, F_{30} and F_{12} are set to zero. Then we have

$$p = q \tag{4.9}$$

Then object distance p is equal to the image distance q. So the when the toroidal mirror works in the configuration of magnification of 1, the coma abberation can be canceled.

4.2 Time-preserving XUV monochromator

The HHG spectrum generally consists of discrete of peaks corresponding to the odd harmonics of the fundamental laser frequency with an intensity distribution span tens of eV. The separation between the adjacent peaks are twice of the photon energy, which is 2.4 eV in our case. The line width of each peak is usually much narrower than the separation, in our case, it is less than 65 meV.

The XUV generated in the HHG process are colinearly with the fundamental laser pulses. The separated wavelength is highly desirable in the tr-ARPES experiment. Due to the high dynamics range of the electron counting, even a small fraction of the contaminant photons can possibly cause a confusion about the spectrum feature. At the same time, the monochromator for tr-ARPES experiments needs to preserve the temporal duration of the pulse otherwise the time resolution of the experiments is affected.

The simplest way to obtain HHG spectral selection is the use of a multilayer mirror at normal-incidence, which does not alter the pulse time duration and cause less aberrations. However, as mentioned before, multilayer mirror are normally designed to work at a fixed wavelength and it doesn't work well for <30 eV. Different sets of mirrors are required to cover a spectral region

as wide as the whole HHG spectrum. Furthermore, the reflectance contrast given by multilayer mirrors can be poor and the spectrum contamination can be a concern [233, 234, 235].

Grating monochromators give tunability in a broad band and high spectral resolution. However, a grating introduces a tilt of the pulse-front because of diffraction, since each ray that is diffracted by two adjacent grooves is delayed by a optical cycle of the light. In order to preserve the pulse duration, the pulse front tilt caused by the grating needs be less than the pulse duration. This puts a constraint on the total number of grooves which the XUV beam hit on. Since the resolving power of the grating is proportional to the total number of grooves which the XUV beam hit on, the requirement of preserving the pulse duration constraints the resolving power in a single grating monochromator design.

Luckily, most of tr-ARPES experiments we are interested in don't require the energy resolution narrower than our harmonic line width. The reason is that in tr-ARPES experiments, there is a tradeoff between the energy resolution and time resolution. The tradeoff comes from the time and energy uncertainty relationship $\Delta E \Delta t \geq 1.8$ eV·fs. Better time resolution requires a shorter pulse, and a shorter pulse requires a broader energy linewidth which can affect the energy resolution. Our 100 fs time resolution with less than 65 meV provide a good balance for the experimental needs.

Because the HHG spectrum consists of discrete peaks, the photon band width is limited by the harmonic linewidth as long as our monochromator can separate adjacent harmonics from each other. The energy resolution of the monochromator required to separate adjacent harmonics can be on the level of a few hundred meV which is much bigger than the energy resolution in the tr-ARPES experiments. So this greatly relieves the requirement of the resolving power of the grating, which makes a time-preserving monochromator with a single grating feasible. We adopt the XUV time-preserving monochromator design similar to Ref. [14].

4.2.1 Monochromator design and construction

The schematic of the monochromator is shown in Fig.1.9 and a photo is shown in Fig. 4.2. The three optical elements are indicated as toroidal mirror TM1, Grating and Toroidal mirror TM2. The first mirror (TM1) collimates the XUV beam reflecting off the brewster plate, The collimated XUV beam bounces off the grating mounted in off-plane configuration. Then

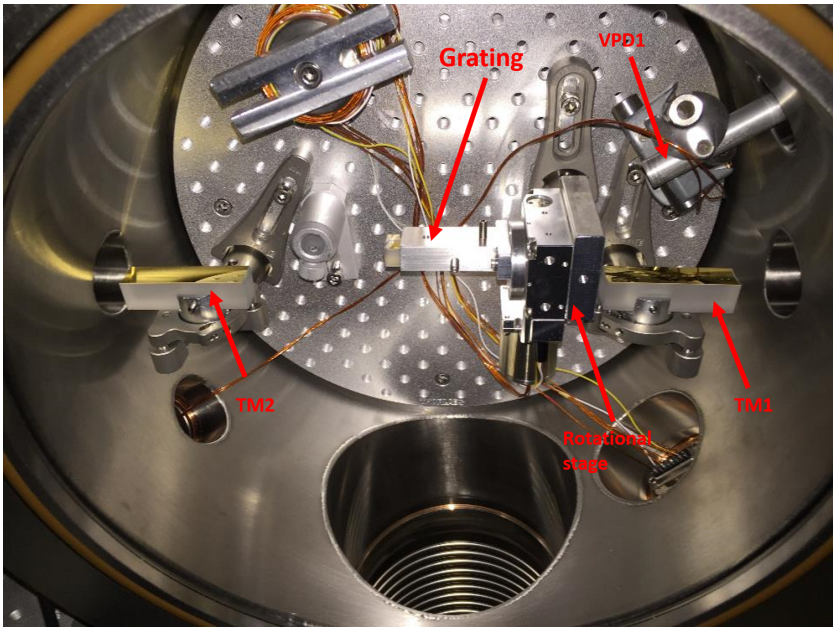

Figure 4.2: The photo of the optics in our monochromator.

the beam is focused by the mirror TM2 to the slit. The slit was salvaged from the decommissioning of the National Synchrotron Light Source (NSLS). The opening of the slit can be continuously changed from mm to completely closed. The grating is mounted to a rotational stage. The XUV wavelength can be selected by rotating the grating around axis parallel to the grooves of the gratings. The mirrors are supported by standard Thorlab polaris mirror mounts. The optics are mounted in vertical plane to take the advantage of high reflectivity of S-polarizition. The whole setup is enclosed in a custom stainless steel chamber.

The focus of the IR in the cavity is about 20 μm. That gives a divergence (half angle) of $\sim$ 16 mrad. Assuming the XUV beam has diffraction limited beam quality, the divergence of the XUV D is about the divergence of the fundamental IR divided by the harmonic order. That's less than 3 mrad for the photon energy we care. Notice that the beam quality of HHG source may not be diffraction limited, Ref. [104] reports the divergence is much higher than this simple estimation for the low order harmonics and strongly depends on the harmonic order and the position of the gas jet relative to the focus. We choose the toroidal mirrors with 350 mm focal length and 3

degree incident angle as they are easy to work with. The mirror size of 60 mm × 15 mm gives a 9 mrad full angular acceptance of the monochromator. The substrate of the mirror is pyrex and the surface is coated by bare gold coating. We estimate the reflectivity of the mirror is more than 90% based on CXRO [215]. We try to make the input length p defined by the distance from the nozzle to the center of TM1 equal to the output length q defined by the distance from the center of $TM2$ to the slit, so $p = q = 350$mm.

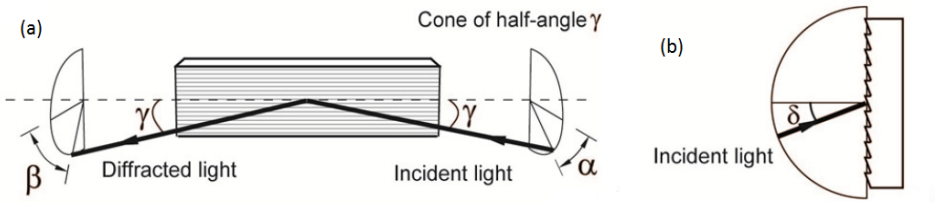

Figure 4.3: The OPM grating configuration. This image is taken from Ref. [14]

The grating is mounted in off-plane mount (OPM) configuration [236] as shown in Fig. 4.3 (a). Compared to the classic diffraction mount, the incident and diffracted wave vectors are almost parallel to the grooves of the grating in OPM. This configuration allows the beam incident at grazing angle without increasing the number of grooves hit by the beam. OPM configuration is critical for the single grating monochromator to preserve the pulse duration with high efficiency. The direction of the incoming rays is described by two parameters: the altitude γ, that is defined as the angle between the direction of the incoming rays and the direction of the grooves,and the azimuth angle α. The azimuth angle of the first diffracted order at wavelength λ is denoted as β. The grating equation of the OPM configuration is written as:

$$\sin\gamma\,(\sin\alpha + \sin\beta) = \lambda\sigma \tag{4.10}$$

where σ is grating groove density. When the grating is used as a monochromator, we take the first order diffraction, so α=β. We choose a grating with groove density σ=150 g/mm. The altitude γ is set to 4 ° for the convenience and high reflectivity. Fig. 4.4 (a) shows the diffraction angle vs XUV photon energy. The high photon energy XUV is located at small diffraction angle due to their short wavelength. For the 8 eV photons, the angle between the adjacent harmonic is about 2° and for the 40 eV photons, the angle is about

0.12°. Our rotational stage has an angle resolution of 0.001°, so it is good enough for the harmonic separation. The separation of the XUV beams on the slit plane dS can be estimated by

$$dS = q \sin\gamma \frac{d\beta}{d\lambda} \Delta\lambda \tag{4.11}$$

The calculation results are shown in Fig. 4.4 (b). The sepration of the XUV beams also decrease as the photon energy increase. For the most case which is 40 eV photon energy, the separation is about 100 μm on the slit plane. Since the magnification of the monochromator is about 1, the XUV spot in principle can be the same size as the generated at the nozzle, which is less than 20 μm. Due to some aberration and imperfect alignment, We still achieved <50 um spot size on the slit plane, which can estimated from the monochromator scan with slit closed tightly. So the 150 g/mm grating is enough to separate the XUV beams.

The number of grooves N illuminated by the XUV beam can be estimated by

$$N = 2Dp\sigma \tag{4.12}$$

where D is the divergence of the beam. Then the half width of pulse broadening $\Delta\tau_g$ due to grating can be estimated by [237]

$$\Delta\tau_g = \frac{N\lambda}{2c} = \frac{Dp\sigma\lambda}{c} \tag{4.13}$$

and Fig. 4.4 (c) shows the pulse broadening caused by the grating v.s. photon energy. We can see for all the photon energy, the pulse broadening is less than our pulse duration $\sim$ 100 fs. The monochromator design is suitable for our XUV source. The energy resolution of the monochromator is shown in Fig. 4.4 (d) with 50 μm slit opening. Slit limited energy resolution is calculated by $slitsize * dE/dS$ and the grating limited resolution is simply estimated by $h\nu/N$. The energy resolution is limited by the slit size in this case. As mentioned before, the energy resolution as big as 1.2 eV is enough to separate the adjacent harmonics, and the actual photon linewidth is much smaller than the energy resolution of the monochromator.

The blaze condition for which the diffraction efficiency is maximized is fulfilled when the diffracted light is reflected specularly from the groove surface and when the shadowing effect from adjacent grooves is minimized, $\alpha =$

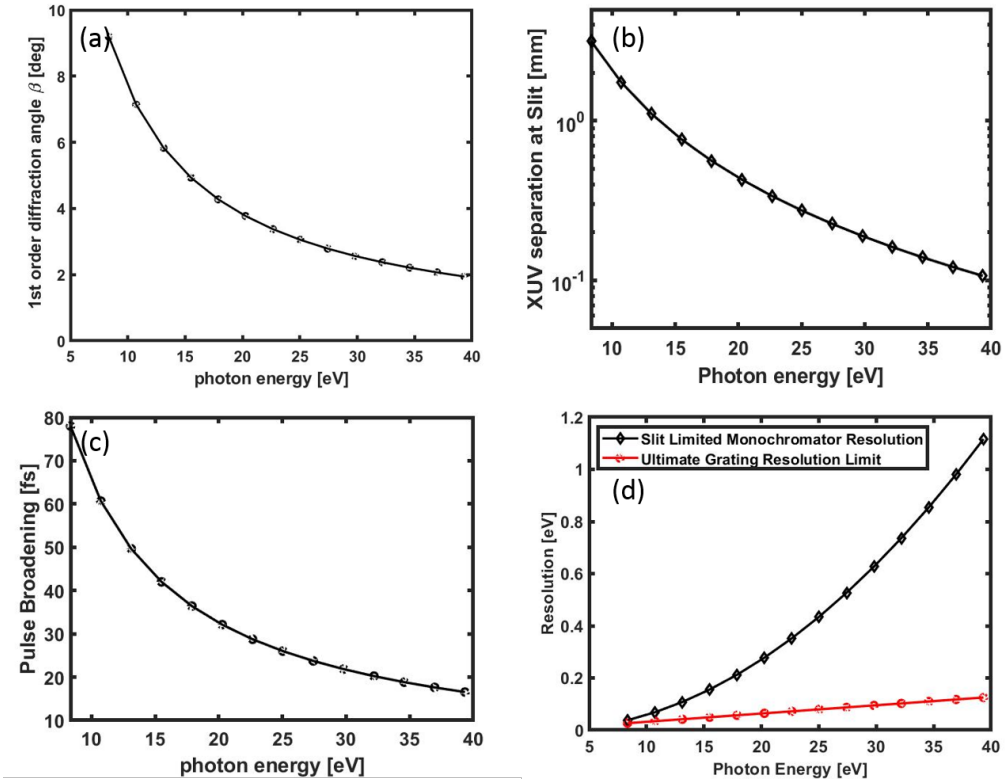

Figure 4.4: The simulation of the monochromator with 3 mrad XUV divergence, 150 g/mm grating and 50 μm slit openning.

$\beta = \delta$, where δ is the blaze angle of the grating shown in Fig. 4.3 (b). For our 150 g/mm grating, the blaze angle is designed to be 2.3 °, the maximum diffraction efficiency is at 37 nm, which corresponds to the photon energy of 34 eV. We also tried the monochromator with 100 g/mm grating blazed at 2.2 °. The maximum diffraction efficiency for this grating occurs at 22 eV which is well centered in our harmonic spectrum. However, due to less resolving power, the harmonics at 40 eV can't be fully separated by this grating.

The XUV spectrum measured by this monochromator is shown in Fig. 3.5 in section 3.3.1. Fig. 3.5(a) shows a typical HHG spectrum from Xenon gas measured using each of the four detectors as the monochromator grating is rotated. The observed harmonic linewidths are due to the intentionally small resolving power of the pulse-preserving monochromator, not the intrinsic

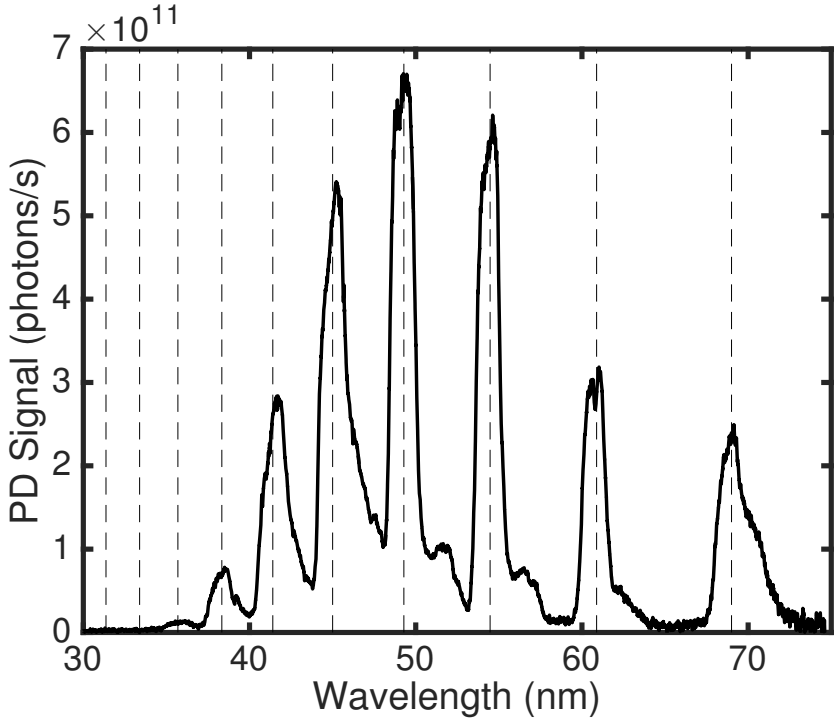

Figure 4.5: The harmonic spectrum taken with 100 g/mm grating for enhanced efficiency at 55 nm. The 21st hamronic at 49 nm has the flux of 7×10^{11} γ/s.

harmonic linewidth. The different wavelength are clearly separated from each other with a clean background in between. In Fig. 3.5 (b), the higher of the two lower limits from the PD or VPD2 are plotted as a function of photon energy and for three different generating gasses: argon, krypton, and xenon. As can be seen in Fig. 3.5 (b), even using a single monochromator grating, by changing the generating gas, a flux of more than 10^{11} photons per second is delivered to the sample over a broad tuning range. At lower photon energies, the higher efficiency of generation in Kr and Xe compensates the reduced diffraction of efficiency of the grating blazed for 35 eV. Higher fluxes can be obtained at lower photon energies using different gratings. For example, we have observed 7×10^{11} photons/s in the 21st harmonic from krypton ($h\nu = 25.2$ eV) using a 100 groove/mm grating blazed for 55 nm as shown in Fig. 4.5. These fluxes are within one order of magnitude of what is available from many state-of-the-art synchrotron beamlines dedicated to

ARPES [219, 220, 221]. Critically, since at ∼80 MHz, 7×10^{11} photons/s corresponds to only 8,000 photons/pulse, also comparable to synchrotrons. All of this flux is usable for high-resolution photoemission experiments.

4.2.2 Monochromator alignment and tracer beam

The alignment of XUV optics is challenging. First, the XUV wavelength is strongly absorbed by the air. So in order to align it in-situ, the beam line has to be pump down and all the optics need to be motorized. Spatial resolved XUV light detection is difficult. In order to get the spatial profile of the XUV directly, sophisticated detectors such as intensified CCD camera is needed. Such a detector is complicated and expensive and needs to be used in the high vacuum environment. Their are cheaper ways like knife edge scan and pin hole scan, but the process is time consuming and the measurement accuracy is not as high. Third, the grazing incidence XUV optics is sensitive to misalignment. For our toroidal mirror with 350 mm focal length and 3° incident angle, the beam profile is sensitive to mrad level missalignment. Last, due to the constraint of the enhancement cavity, it is difficult to align the XUV beam generated in the cavity into the beamline.

Since all the XUV optics are reflective, they generally has negligible chromatic aberration. So it is common practice to align the XUV optics with a visible beam. One way to align the beamline including the monochromator and the refocusing mirror is to use the IR light reflected out the cavity. IR and high order harmonics are colinear, and if we use the 0th order diffraction of the grating, they should overlap with each other very well. If we align the beamline with IR first, It should be OK for the XUV.

The problem is that the IR is focused tightly in the cavity, so the IR beam spot diverges much faster than the XUV. When the IR beam hit the TM1 mirror, it's already too big to fit on the mirror. The severe clipping makes it difficult to identify the principle ray which results inaccurate alignment.

Instead of using the IR, we use a independent green beam to guide the alignment, which is called tracer beam. The setup of the tracer beam is shown in Fig. 4.6. It starts from a green laser diode which is probably a frequency double DPSS laser. The laser beam is coupled into a 532 nm single mode fiber to transport the beam into the HHG chamber and clean up the spatial mode. The fiber goes through a vacuum feedthrough and collimated by a collimator. Then the beam size is adjusted by a telescope made of lens L1 and L2 with focal length 10 cm and 40 cm. This telescope is also used to focus

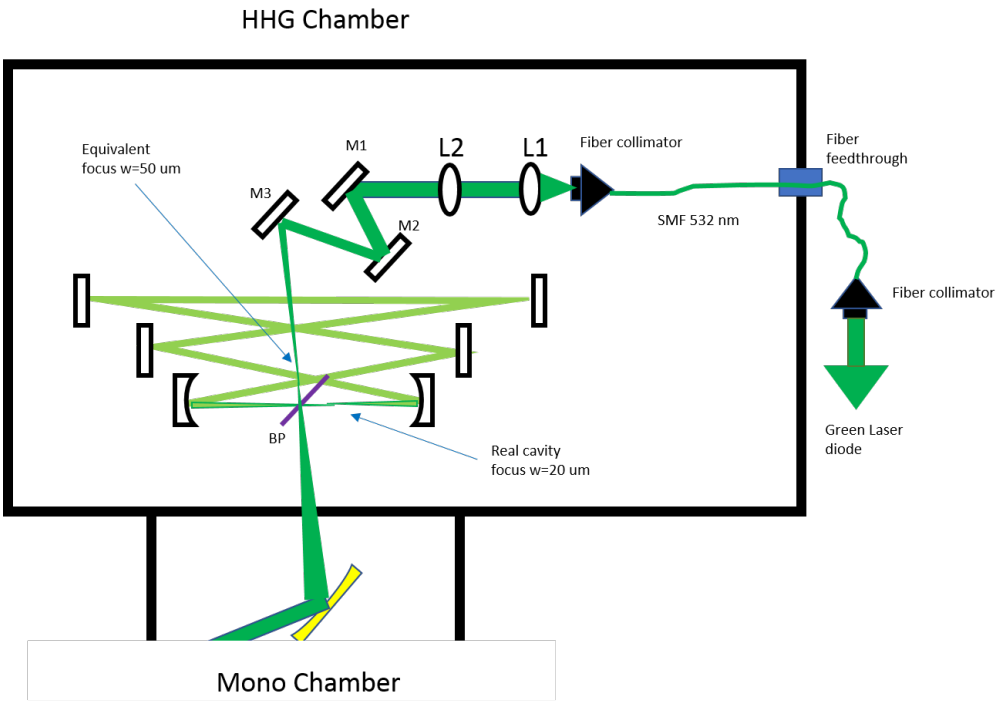

Figure 4.6: The tracer beam layout.

the tracer beam to a equivalent focal point with w=50 μm. The equivalent focal point is the mirrored image of the cavity focal point relative to the front surface of the Brewster plate. Then the tracer beam is nonpolarized, so it is partially reflected on the Brewster plate. The transmission goes into the monochromator chamber, and used for the alignment purpose. The reflection part is coupled into the enhancement cavity .

Whether the optical path of the tracer beam is overlapped with the XUV is critical for the accuracy of the alignment. Since the enhancement cavity defines the path of the IR and XUV uniquely, We couple the tracer beam into the enhancement cavity by the Brewster plate to make the tracer beam follow the IR and XUV. To achieve that during the initial setup, we reverse the direction IR in the cavity, so the IR reflected off the Brewster plate goes through the equivalent focal points. This trick allows us to easily locate the equivalent focal point. We first adjust L1 and L2 iteratively, so the tracer beam is focused to the equivalent focal point with 50 μm focus size , then we steer the mirrors M1, M2 and M3 so tracer beam makes a closed loop

in the cavity. After a few iterations, we can observe a cavity mode of the tracer beam. Notice that the mode match of the tracer beam is poor, so the cavity mode of the tracer beam is not the fundamental mode. We found that as long as we can observe any kind of the tracer beam cavity mode, the alignment of the tracer beam is good enough. The focus size of the tracer beam is set to 50 μm, this gives a divergence of 3 mrad. The Rayleigh range of the tracer beam is about 1 cm, that is also reasonably close the Rayleigh range of the XUV.

One problem we had is that the thin Brewster plate (250 μm thickness) acts as a Fabry Perot interferometer and cause a spatial profile distortion on the reflected beam. Part of the reason is that the frequency doubled DPSS laser probably has a fairly narrow line width. To solve that problem, we change the light source to a broad band semiconductor green laser diode sold by Thorlabs (LP520-SF15). The spectrum of the semiconductor laser diode is more than 2 nm, the coherence length of it is less than 100 μm, so the Brewster plate etalon is of no concern. This light source works fine for the down stream XUV optics alignment, however, due to its low spectrum energy density, we can't observe a tracer beam cavity mode with this broad band laser diode. So it can't be used in the initial tracer beam set up.

The toroidal mirror has 6 degree of freedoms. As shown in Fig. 4.1, it has 3 translations in X Y Z direction, and the 3 rotations about the X Y Z axis which is named pitch, roll and yaw. We have found that the beam profile is sensitive to the translations, but the XUV beam doesn't have to hit the exact geometry center of the toroidal mirror. The translations and rotations are coupled to each other to some extent. The toroidal mirrors TM1 and TM2 are held by simple slotted holder and mounted to standard Thorlabs Polaris^{TM} mirror mount. The mirror mount can do yaw and roll. We adjust pitch by careful torque the mirror holder while the set screw of the mirror mount is slightly loosened. The mirror mount is supported by a one inch post and clamped down to the breadboard. The translation of the mirror is done by carefully sliding the mirror in the slotted holder.

The common aberrations caused by the toroidal mirrors are shown in Fig 4.7. Fig 4.7(a) shows a fine beam profile when the the toroidal mirror is properly aligned. We found it difficult to get a perfect round spot and completely get rid of the aberrations. But the beam is mostly round and uniform. The most energy is within the main spot. Fig 4.7(b) shows the astigmatism aberration. The beam is focused in one dimension but defocused in the other. Astigmatism cause a unwanted elliptical beam shape and aberrations in the

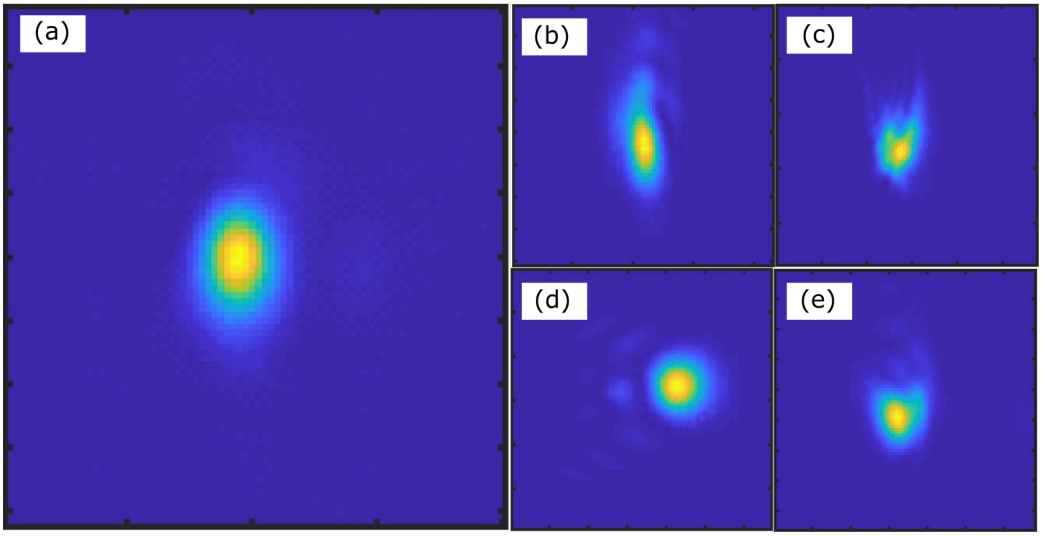

Figure 4.7: The aberrations of the tracer beam. (a) an aligned beam (b) astigmatism (c) pitch miss-aligned (d) coma (e) slightly defocused beam.

defocused dimension. This is typically caused by the incident angle of the light is not equal to the designed angle of the toroidal mirror. It may be fixed by adjusting yaw rotation. Fig 4.7(c) shows what happens to the focus of the tracer beam when the pitch is miss-aligned. The beam shows a long arc shape in one dimension and multiple images in the other dimension. We found the beam is sensitive to yaw and pitch in mrad level but it is not so sensitive the roll. Fig 4.7(d) shows coma aberration. As mentioned before, coma can be canceled when the magnification is 1. If the magnification is not equal to 1, the coma will exist no matter the mirror is well aligned or not. Fig 4.7(e) shows the beam profile of a well aligned toroidal mirror, but the detector is not at the focal point of the beam. We see a bright main spot with multiple aberration spot around it, there can be a significant amount of energy in the aberration spots. When we measure the profile of the tracer as we adjust the alignment, the detector which is usually a camera needs be on the rail so we can scan it along the beam. Similarly, when we position the monochromator slit and samples, we also need verify whether they are

at the focal point or not.

4.3 Refocusing mirror

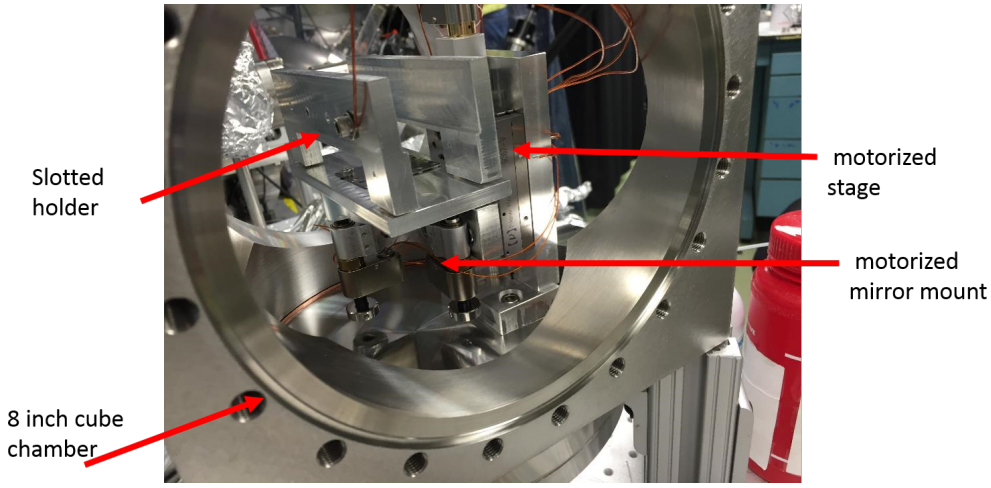

Figure 4.8: A photo of the mirror cube chamber.

The Refocusing mirror TM3 is used to image the XUV from the slit plane to the sample in the surface science chamber. TM3 is located in a compact 8 inch Cube chamber, a photo of the mechanical design is shown in Fig. 4.8. The mirror is held by a slotted holder. The mirror holder is electrically floating. So we can use the photocurrent of the mirror as an indicator of the XUV flux. The mirror holder is mounted to a motorized mirror mount. Then the mirror mount is supported by a motorized stage used in vertical direction. Thanks to the motors, TM3 can be aligned without venting the UHV chamber. It is aligned by using the tracer beam as mentioned above.

To measure the XUV spot at the sample, we image the fluorescence from a Ce:YAG scintillator placed at the sample position. Figure 4.9(a) shows the image and Fig. 4.9(b) shows Gaussian fits in the both the horizontal and vertical along lineouts corresponding to the image centroid. The data indicate a clean elliptical beam with a FWHM of 58 μm in the horizontal 100 μm in the vertical. Also, we measure that approximately 70% of the XUV light can be transmitted through a 100 μm diameter pinhole oriented at 45 degrees to the beam axis. This spot size is again similar to what

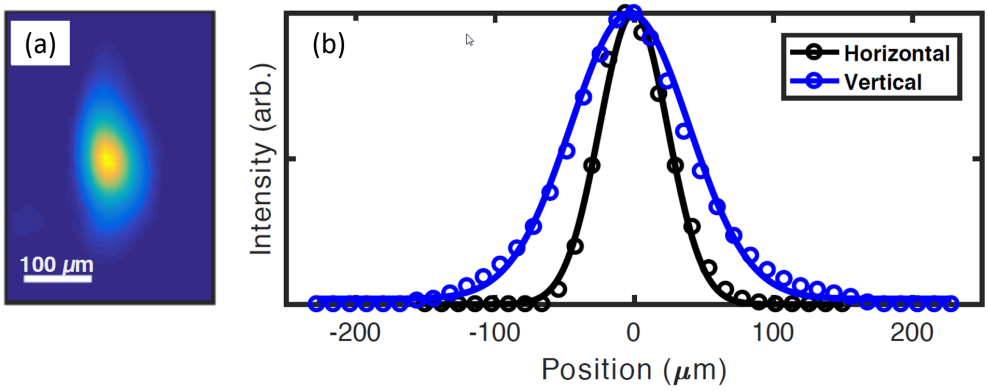

Figure 4.9: a) The 27th harmonic from Ar imaged with a Ce:YAG crystal at the sample position. (b) Lineouts through the centroid of (a) fit with Gaussian functions demonstrating 58 μm x 100 μm spot size (FWHM). This figure is reproduced from Ref. [9].

is used at synchrotron beamlines [219, 220]. When comparing to previous HHG results it is important to note that in our case this small spot size and high flux are actually usable for experiments due to the absence of space-charge effects at 80 MHz repetition rate. A small spot size enables studying spatially inhomogeneous samples (for example produced by exfoliation [238]), requires less pump-pulse energy in pump/probe experiments, and is necessary for achieving high angular resolution in ARPES.

4.4 Differential pumping

There are several orders of magnitude pressure drop across the beam line as shown in Fig. 1.9, The pressure in the HHG chamber is on the order of mTorr, and the pressure in the surface science chamber is $\leq 10^{-9}$ Torr. The main gas load go through the beam is the HHG gas media such as Krypton and the oxygen and ozone mixture. We achieve the pressure drop by several differential pump stages.

- First, there is a aperture and thin pipe between the HHG chamber and monochromator chamber. With a 900 L/s turbo pump in the monochromator chamber, we achieve $< 10^{-5}$ Torr pressure.

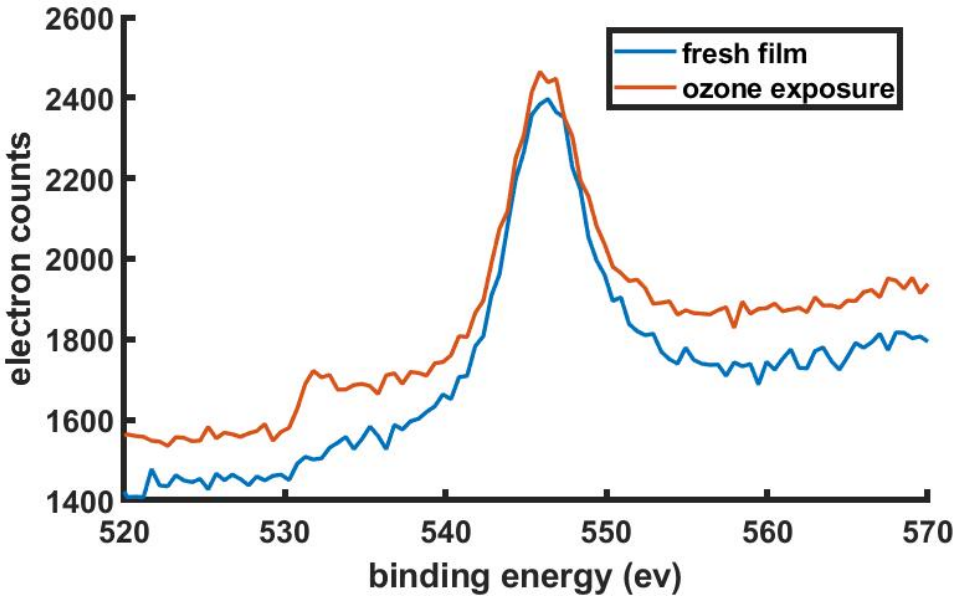

Figure 4.10: The XPS measurement of a thin pentacene film on the Au(111) surface. O_{1s} shows up at 531 eV after the ozone and oxygen exposure. The peak at 547 is $Au_{4p3/2}$.

- Second, The slit of the monochromator has a conductance about 2 L/s and it also helps differential pumping. After the slit, there is choker chamber with a choke installed between the choker chamber and the mirror chamber. The conductance of the choke is 2.5 L/s. The pumping speed of the choker chamber turbo is 90 L/s and the pumping speed of the mirror chamber turbo is 500 L/s. The pressure of the mirror chamber drops to $< 10^{-8}$ Torr.

- Last, the surface science chamber is equipped with 600 L/s turbo pump and a getter pump. We achieve the pressure of $\leq 10^{-9}$ Torr. Because the TOF k-mic has a large volume but a small aperture, it got its own turbo pump for differential pumping.

The turbo pumps on the HHG chamber and monochromator chamber need to be able handle corrosive gas due to the oxygen and ozone. The normal turbo pump on the monochromator chamber was damaged by the ozone although the pressure of the monochromator chamber is lower than

10^{-5} Torr. The downstream turbo pump seems OK with the ozone residue gas. Since the turbo pumps can be potentially damaged by running without proper foreline pressure, All the turbo pumps are equipped with pneumatic valves in the foreline controlled by a interlock shown in Appendix.

The oxygen and ozone also can cause potential sample damaging issue although the partial pressure of O_2 in the surface science chamber is on the order of 10^{-11} Torr. Fig. 4.10 shows XPS measurements of a pentacene film on Au(111) surface before and after exposure to the gas coming from the beam line. We didn't intentionally expose the film to oxygen and ozone. However, the residual gas coming from the HHG chamber reacts with the pentacene film. The O_{1s} peak at 531 eV shows up on the XPS spectrum after exposure. The peak at 547 eV is Au$4p_{3/2}$ which is not affected. The choke between choker chamber and the mirror chamber can effectively reduce the oxygen and ozone gas going go downstream and that's sufficient for the most experiments in our lab. Considering there may be some samples extremely sensitive to the residual oxygen and ozone, we achieve complete isolation by inserting an Aluminum foil between the choker chamber and the mirror chamber. The thickness of the Aluminum foil is on the order of 100 nm. It is mounted to on a gate valve. In principle, it transmits XUV photons higher than 15 eV with $> 60\%$ efficiency. However, due to the oxidation and contamination of the surface, the XUV transmission is much lower than that.

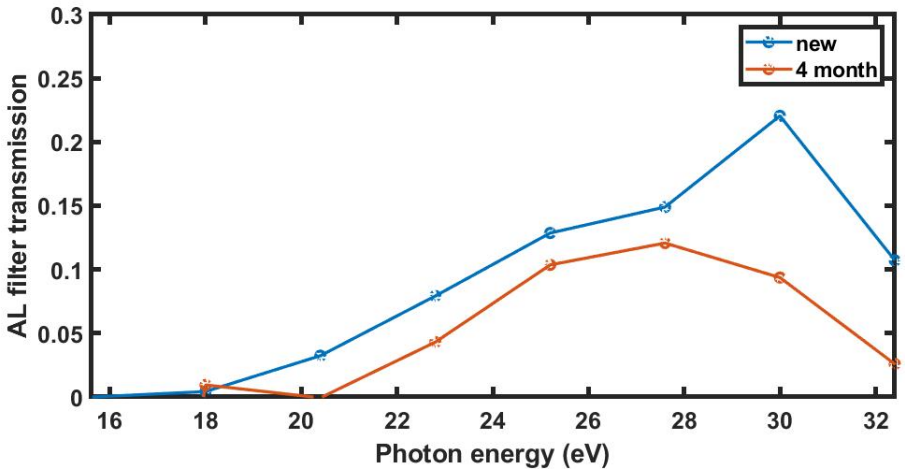

Figure 4.11: Comparison of The transmission of the newly installed Aluminum filter and the same one after 4 months.

Fig. 4.11 shows the transmission of the newly installed Aluminum filter and the same one after 4 months use. For the newly installed one, the transmission is lower than 30%. After 4 months use, as the surface oxidation and contamination occurs, the transmission over all wavelength drops by about 5%. Despite this Aluminum filter cuts the photon flux by an order of magnitude, we found it isolate the residue gas very well. Thanks to our high photon flux, ARPES experiments can still be conducted on the oxygen sensitive sample with one order of magnitude loss in photon flux.

Chapter 5

Surface science chamber

5.1 Surface science chamber construction

The surface science chamber, shown in Fig. 5.1, is a cylinder shaped chamber with 3 levels of flanges for instruments. The diameter of the chamber is 16″. The chamber is equipped with double μ-metal shield for the earth magnetic field shielding. It is pumped by a 600 L/s turbo pump and a getter pump which is particularly effective for pumping hydrogen. The pressure of the chamber can get to $< 10^{-9}$ Torr.

The surface science chamber is equipped with a standard set of surface science instruments:

- Sputter gun. This is our major tool to clean the sample. Our sputter gun uses the background dosed Ar as the atom source. The ion voltage can range from 500 V to 2 kV. Its ion beam size is about an inch, this big spot size can provide uniform sputter without rastering on the sample. The ion current on the sample is typically 5 μA or so, that's usually enough for most sample cleaning needs. Fig. 5.7 shows the XPS of C 1s before and after sample cleaning.

- X-ray gun. It provides steady Al Kα (1486 eV) X-ray. The X-ray photoelectron spectroscopy can be implemented with the hemispherical energy analyzer. This is a powerful tool for chemical contents identification and surface characterization.

- Low energy electron diffraction (LEED). It is used to determined the surface strucuture and lattice constant of a single crystal substrate and

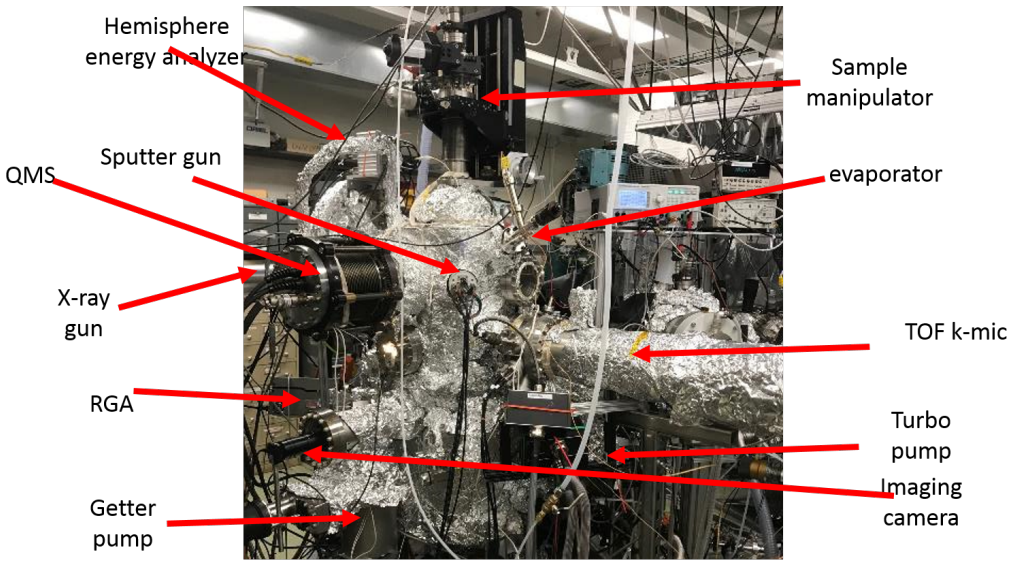

Figure 5.1: A photo of the surface science chamber with the instruments.

molecular film. Our LEED model controls the electron beam voltage with a extra retarding stage. This allows electron gun running at the optimized voltage independently. This is a useful feature for LEED measurements with low electron beam voltage on the order of 10 eV. Fig. 7.3 shows LEED partterns of a C_{60} monolayer film and a C_{60} 12 ML film with 15 eV and 24 eV electron energy.

- Hemispherical energy analyzer. Our hemispherical energy analyzer (VSW HA100) was initially used as the electron detector of XUV experiments. It was originally designed for XPS. Later, it was rebuilt and includes the electron optics for XUV experiments. It is specified to have an angular acceptance of $\pm$ 4 degrees at the input and has a channeltron detector at the exit. Its channeltron detector has high dynamic range, but it falls short in the electron collection efficiency and parallel detection.

- TOF k-mic. The TOF k-mic will be introduced in chapter 8. It is currently used as the electron detector for the XUV photoemission experiments.

- Quadruple Mass spectrometer (QMS). The mass detection range of this

state of art QMS is up to 1000 amu which is important for detection of large organics molecular such as C_{60}. The channeltron detector is integrated with a conversion dynode plate which is helpful for the detection efficiency of large mass ions. The whole instrument is mounted on an 8 inch linear drive, So it can get close to the sample surface and retract out easily. This QMS is useful for mass spectrum measurements of photo ions ejected from the surface and temperature programmed desorption measurement.

- Residue gas analyzer (RGA). The RGA is used for diagnostic purpose of UHV chamber. It is basically a compact quadruple mass spectrometer with mass range goes up to 200 amu. It is mainly used to identify the background gas of the UHV chamber, measure their partial pressure and leak test.

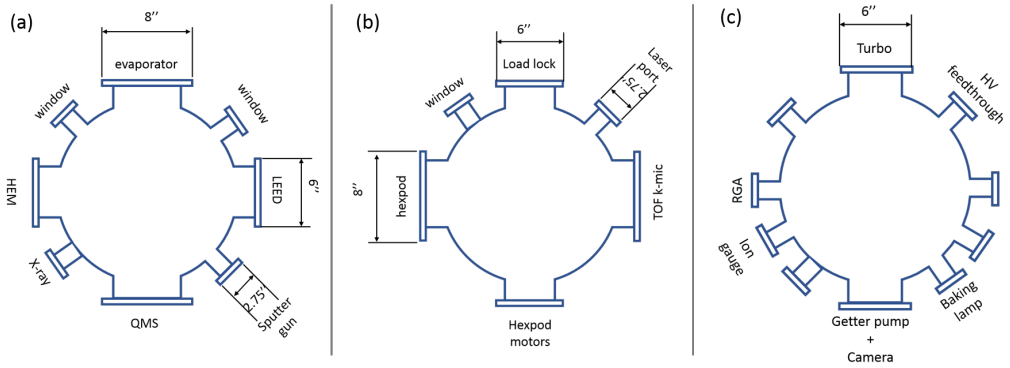

Figure 5.2: The layout of the instruments on the surface science chamber (a) top level (b) middle level (c) bottom level.

The layout of the instruments are shown in Fig. 5.2 for (a) TOP level (b) middle level and (c) bottom level. The top level includes most of the surface science tools for sample preparation and characterization. The middle level service as the space for the XUV tr-ARPES experiments. The laser port and the TOF k-mic is located in this level as well as the load lock chamber. The 8″ flange and the 6″ flange is reserved for the hexapod sample manipulator. The bottom level is the space for diagnostics and pumps. The turbo pump and a getter pump is installed in this level. The RGA, ion gauge, baking lamp and a viewing mirror is also located in this level.

5.2 Sample manipulator and sample transfer

Currently, our sample manipulator is a rod style sample manipulator. The sample plate is held by a home made Omicron style sample holder. The sample holder is integrated with a electricly insolated heater. The assembly is held by a aluminum bracket mounted to the bottom of a long rod. There is a dewar built in the rod so the sample can be cooled by the liquid nitrogen. A copper braid is used to connect the sample mount to the bottom of the rod in order to provide extra heat conduction. The drawing of the sample mount is shown in the appendix. The long rod sits on stage with X, Y, Z and rotation 4 degree of freedoms.

The sample manipulator has several advantages. First, the sample can be conveniently cooled to 100K and heated up to 1000 K. Second, due to long rod and long travel in vertical direction, the sample can be easily moved between the top level and the middle level of the surface science chamber. Third, the sample is electrical floating by this design. This allows us to control the sample voltage and measure the sample current in photoemission experiments. Fourth, the sample holder is fully compatible with standard Omicron sample plate. This allows easy sample transfer. However, the major drawback of this sample manipulator is the mechanical stability. The sample vibrates constantly due to the long rod holding it. And the sample is not steady when cooled with liquid nitrogen. It is fine when fully filled with liquid nitrogen. Once the top part of dewar start to warm up due to liquid nitrogen evaporation, the sample may slightly move a little bit. For some experiments, this can make a difference. In the near future, we are going to install a hexapod sample manipulator for the TOF k-mic measurements as introduced in chapter 8. This rod manipulator will still used for other surface science experiments and sample transfer. In the daily experiments, we need swap the sample under study for various reasons. In order to conveniently change the sample without venting the surface science chamber and baking it again, we have built a load lock chamber for the purpose. The load lock chamber is a 2.75 inch cube connected with the surface science chamber by a gate valve. Due to its small volume, it can be pumped down rapidly without baking. The samples are mounted to the standard Omicron sample plates and then stored in the sample magazine. The sample magazine is mounted to a linear drive, so the sample can be picked up by the sample transfer stick. The sample transfer stick is a dual shaft continuous rotation wobblestick purchased from FerroVac. It has 610 mm travel range and a pincer style

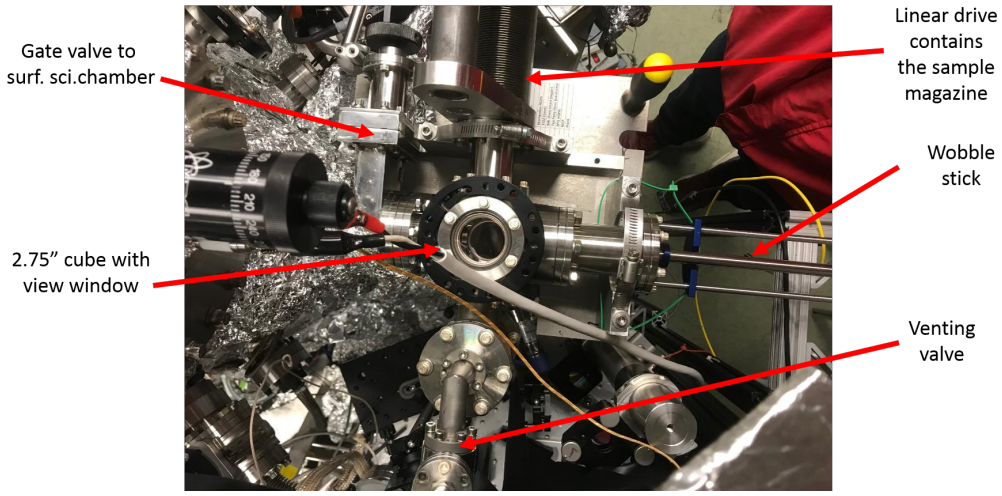

Figure 5.3: A photo of the load lock chamber

sample grabber.

5.3 Inlet system

The sample preparation may require dosing the molecules onto the surface or into the background gas. The external molecules source and tubing connecting to the surface science chamber all need be pumped and baked for UHV operation. A inlet system is used to handle the external molecule sources. The design of the inlet system provides a convenient way for the multiple isolated gas module to share the same turbo pump. The structure is shown in Fig. 5.4. It is made of a network of pipes and valves. The main body is a pipe network pumped by a 60 L/s turbo pump. Since the inlet system are often used to pump high pressure gas (> 1 atm), a bypass channel is designed so the high pressure gas goes directly to the roughing pump while the turbo is isolated. Then the different gas modules are connected to the main body of the inlet system via UHV valves, and each gas modules has its own dosing valve or doser going into the surface science chamber. One gas module can be opened to the main body for pumping while other gas modules are not affected. A penning gauge is used to measure the pressure in a broad range ($10^{-3} - 10^{-8}$ Torr) without the filament damaging like the ion gauge.

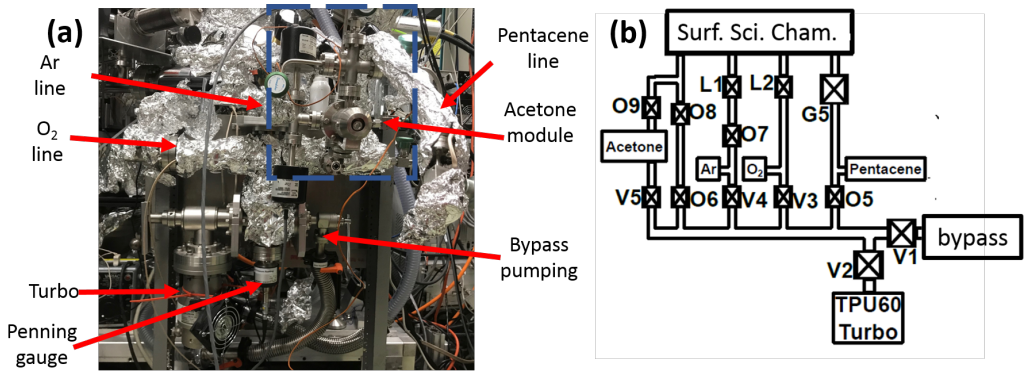

Figure 5.4: (a) A photo of inlet system. (b) the schematic of the network of pipes and valves. G means gate valve. V means Mannual UHV valve L means leak valve. O means bellows sealed manual valve.

5.4 Surface Science chamber positioning

The surface science chamber positioning is a demanding task. The reason is that the XUV optics are constrained by the image aberrations, and can't be freely used to steer the XUV for light delivery purpose. The XUV beam generated in the enhancement cavity also can't be freely steered due to the constraint of the cavity. The surface science chamber has to move as a unit to catch the XUV beam. The field of view (FOV) of the TOF k-mic is less than half a millimeter. So the surface science chamber has to be position precisely in order to get the XUV beam into FOV of the k-mic. The initial positioning of the surface science chamber is done with the aid of pump light and tracer beam. Since both beams are visible, they can be easily monitored by the camera. The tracer beam is used to visualize the XUV spot. The pump light can generate electrons by 2PPE, so it is used to visualize the field of view of the TOF k-mic. Overlapping the pump light and the tracer beam while keeping the 2PPE of the pump inside the FOV of the TOF k-mic makes the XUV into the FOV of the TOF k-mic.

To move the surface science chamber smoothly and precisely, we design our chamber positioning tools as shown in Fig. 5.5. The surface chamber is supported by feet with jack screws. The height and the tilt of the chamber can be adjusted by the jack screws. The bottom of the feet is lubricated by Teflon. This reduces the friction between the feet and the floor and allows the chamber to be moved smoothly in the horizontal plane. The position and

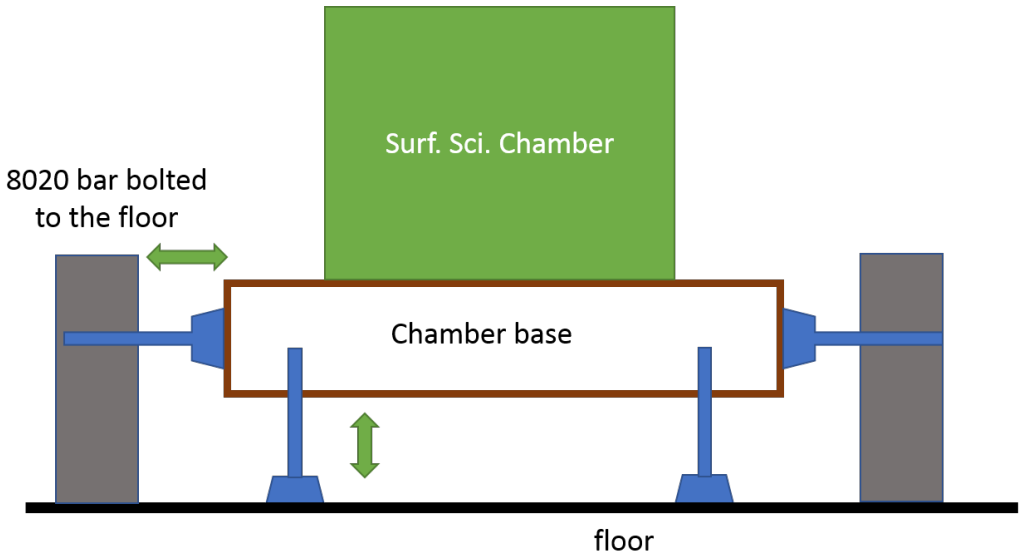

Figure 5.5: The schematic of the chamber positioning tools.

orientation of the chamber in horizontal is controlled by chamber nudgers. The chamber nudgers are also feet with jack screws, which push the chamber in the horizontal plane against a aluminum bar bolted to the floor. There are 2 chamber nudgers located at each of the four corners of the chamber base plate. Each of them has a travel range of 2 inches. Normally, all the feet are tighten and chamber is clamped to its position. By loosening one foot and tightening the opposite side slightly, the chamber can be moved smoothly. We found this setup works very well, The position accuracy is better than the XUV beam spot size when using the electron microscopy as feedback.

5.5 Thin film deposition

We use a home made evaporator for thin film deposition. The evaporator is shown in Fig. 5.6 (a). The alumina crucible contains the source molecules. A type K thermo couple wire is clipped inside the crucible. The crucible is wrapped by a tantalum heater filament. The resistance of the heater is less than 0.5 Ω. The 0.25″ copper rod of the power feedthrough holds the assembly through an adapter. A shutter which is driven by a rotation feedthrough is used to control the dosing process. This evaporator can be made on a 2.75

inch flange and compactly fit into the chamber. A 20 Amp DC power supply is used to drive the heater, and the temperature is controlled by a commercial temperature controller. This evaporator can work at the temperature above 1000 $°C$. But limited by our current source, the temperature is up to 400 $°C$ practically.

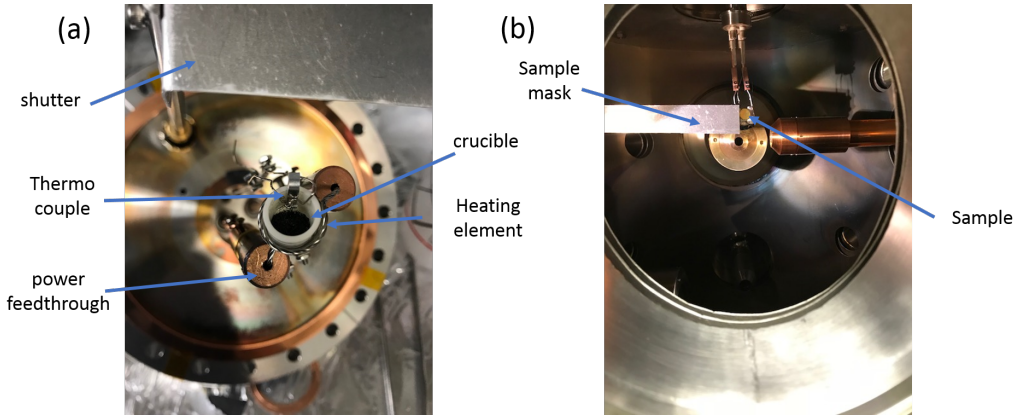

Figure 5.6: (a) A photo of the evaporator. (b) A photo of the sample mask.

With the aid of a simple mask shown in Fig .5.6 (b), we can control the dose time on different part of the sample. The sample mask is simply a metal plate on a linear drive. We have successfully grow C_{60} films with different thickness on a 10 mm Au(111) crystal. This simple feature is useful for film thickness dependent study.

5.6 X-ray photoelectron spectroscopy

The X-ray photoelectron spectroscopy (XPS) is powerful tool for chemical content identification and surface characterization. In our setup, the X-ray gun shoots Al Kα xray to the sample and the kinetic energy of the electrons is measured with our hemispherical energy analyzer. It provides qualitative and quantitative the information about element composition of the surface and their chemical status. XPS is a surface sensitive tool. The probe depth is typically a few nm. It is useful tool for daily diagnostic purposes. For example, it is routinely used to exam the cleanness of the sample. A XPS spectrum of Au(111) surface around C_{1s} peak before and after the sputtering cleaning is shown in Fig. 5.7 The integration time each data point in the

curves is only 0.5 s. It not only works for the substrate but also work for the molecular film. For example, the Fig. 4.10 shows pentacene film before and after very low pressure oxygen/zone gas exposure. The oxygen 1s peak clearly reveal the film damaging caused by oxygen/ozone gas. Fig. 7.2 shows the XPS is used to calibrate the growth rate of the C_{60} film.

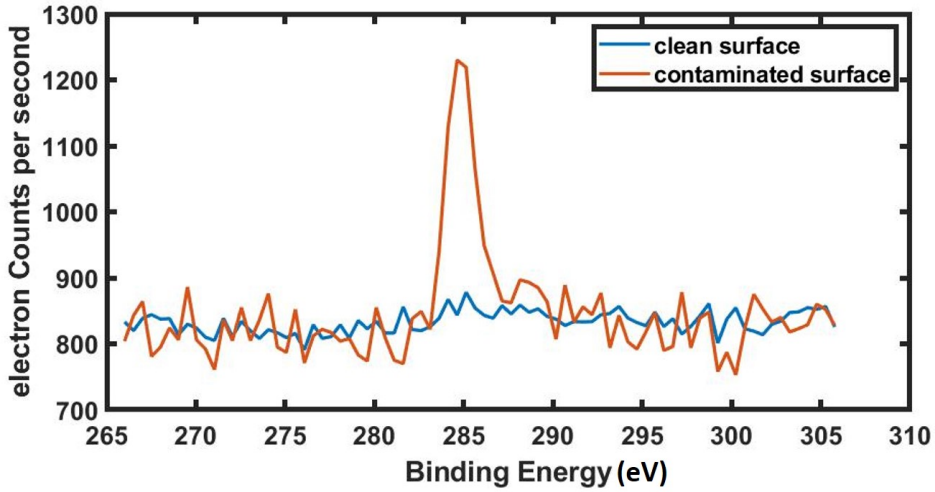

Figure 5.7: The XPS of carbon 1s for a hydrocarbon contaminated sample and a surface cleaned by the sputter gun.

The instrument requires the cooling water of anode on the same voltage as the anode, which is typically above 10 kV. So the cooling water need to be high purity deionized water. Otherwise, water tubing erosion can happen.

5.7 Temperature programmed desorption

The temperature programmed desorption (TPD)) technique has been widely applied to the surface science studies. In a typical TPD run, a sample surface starts with molecule species adsorbed on the surface [239]. Then the surface is heated at a linear temperature ramp. The change of the surface temperature causes molecule species to desorb from the surface, the molecule leaving the surface is typically monitored by a mass spectrometer as a function of temperature. The TPD data can be quantitatively analyzed by using Redhead method [240], leading edge method [241] or other methods reviewed

in Ref. [239]. The quantitative analysis gives rich information such as the activation energy of desorption, the surface coverage, the desorption rate and desorption order. TPD is particularly successful in the catalyst study. Because the technique allows one to study the interaction of reactive gases with solid surfaces, thereby being a powerful tool for both the evaluation of active sites e.g. terraces vs. steps. and reaction products on catalyst surfaces and the understanding of the mechanisms of catalytic reactions including adsorption, surface reaction and desorption [242].

In our TPD setup, we abandoned the software temperature control. Instead, The temperature of the sample is controlled by a Eurothermo temperature controller which has a better performance. Besides that, the sample heater power supply can use a continuous error signal from the temperature controller instead of simple on/off switch. In this way, the temperature ramp is precise and smooth. The heating rate is typically from 0.5 K/s to several K/s. The QMS with large mass range is used as the detector. It is mounted on an 8 inch linear drive, So it can get close to the sample surface. The data of the QMS and the sample temperature is conveniently logged by a labview program.

Chapter 6

Laser assisted photoemission on Au(111) surface

6.1 Introduction

Gold is one of the most widely studied metal sample by the photoemission spectroscopy experiments. Due to chemical inert surface and pronounced Shockley surface state near the Fermi edge, it is widely used as the benchmark sample of the photoemission instruments. [243, 244, 245] In this chapter, We benchmark our instrument by the static photoemission and Laser assisted photoemission study of the Au(111) sample. Much of the material in the chapter is reproduced from Ref. [9].

When atoms are simultaneously irradiated by XUV and intense infrared IR pulse, the presence of the IR laser modulates the xuv photoelectron spectrum. This effect is called Laser assisted photoemission or laser assisted photoelectric effect (LAPE) . It was first observed by Glover et al [246] using a high harmonic generation source in the gas phase. Later it was also observed in solid phase [56, 247] and liquid phase [248]. This effect can be described as the simultaneous absorption or stimulated emission of an IR photon with the EUV photon, which leads to sidebands in the EUV photoelectron spectrum. Alternatively, LAPE can be considered as due to dressing of the free-electron continuum; i.e., the photo-ionized electron is born into a state where the free electron is driven by the IR laser field. The oscillation of this field results in energy sidebands in the photoelectron spectrum [249, 56, 247].

The LAPE happens in a time scale even shorter than the optical cycle of the XUV pulse. The time scales is shorter than the pulse duration in most femtosecond sources. The observation of laser-assisted dynamics of the emitted photoelectrons indicates the time of their emission. As a result, LAPE is widely used for characterization of femtosecond and attosecond ultrafast pulses [250, 246, 251]. By varying the time delay between the XUV and IR pulses, the LAPE signal can provide the cross correlation between the laser and XUV fields.

In the limit of electron kinetic energies much larger than the dressing laser photon energy and pondermotive energy much less than the photon energy, LAPE is well described by the simplemans theory [252]. In this model, LAPE is considered as a two-step process. The first step is the XUV photoemission of an electron unaffected by the IR laser field. This can be justified by the fact that at moderate laser intensities, because the initial ground states are more tightly bound to the nuclei than the continuum electrons, and are thus only slightly affected by the laser field. In the second step, the released electron evolves in the laser field and is unaffected by the target potential. The interaction of the electron with the laser field in the continuum can thus be described using the Volkov wave function as a final state of the XUV photoemission process. The amplitude of the nth sideband (A_n) can be derived from the dipole matrix element and is shown in Equ. (6.1) (in atomic units)

$$A_n = J_n^2\left(\frac{\mathbf{p}\cdot\mathbf{E_0}}{\omega^2}\right) \tag{6.1}$$

where $\mathbf{p}$ is the vector momentum of the electron, $\mathbf{E_0}$ the laser electric field vector amplitude at the surface, and ω is the laser frequency, J_n is the nth order Bessel function of the 1st kind. The geometry of the experiment influences observed sideband amplitudes in two ways. First, energy can only be transferred between the laser field and the electron at the surface, such that for metallic surfaces only the component of the electric field normal to the surface vector contributes to LAPE [56]. Second, due to the dot product in Eq. 6.1, only the component of the electric field along the detection direction contributes. For our geometry, with the sample oriented 45 degrees to incident p-polarized beam and electrons detected along the surface normal, these factors are one and the same, and in the limit that the argument of the Bessel function in (6.1) is much less than one we have (in SI units):

$$A_1 \approx \frac{4\pi\alpha I E_{\text{kin}}}{m_e \hbar \omega^4} \cos^2 45^\circ \tag{6.2}$$

where α is the fine structure constant, I is the laser intensity ignoring the effects of the surface on the laser electric field, E_{kin} is the kinetic energy of the electron, m_e is the mass of the electron, and $\hbar$ is Planck's constant. In the experiment, the laser intensity at which free electrons are generated varies in both space and time due to the finite extent of the XUV and laser beams. The observed sideband amplitude will thus be the space-time average

$$\begin{aligned} \langle A_1 \rangle &= \frac{2\pi\alpha E_{\text{kin}}}{m_e \hbar \omega^4} I_{\text{peak}} \times \\ &\int_{-\infty}^{\infty} dx \int_{-\infty}^{\infty} dy \int_{-\infty}^{\infty} dt G_{\text{laser}}(x,y,t) G_{\text{XUV}}(x,y,t) \end{aligned} \tag{6.3}$$

where I_{peak} is the peak intensity of the laser, $G_{\text{laser}}(x,y,t)$ is a 3D Gaussian envelope function for the incident laser beam with unit amplitude and $G_{\text{XUV}}(x,y,t)$ is a normalized 3D Gaussian envelope function for the XUV beam.

6.2 Static photoemission spectroscopy on Au(111) surface

Photoemission spectroscopy measurements are preformed with our hemispherical electron energy analyzer. For all data presented here, the sample is oriented normal to the analyzer axis and 45 degrees to the XUV beam. The electric field vector of the XUV light is in the plane of incidence (p-polarized) and the analyzer axis.

Figure 6.1 shows photoelectron spectra from an Au (111) surface at 100 K temperature obtained using each harmonic between the 7th ($h\nu = 8.4$ eV) and 33rd ($h\nu = 39.5$ eV). Each spectrum was acquired with 34 meV steps individually measured with 1 second of integration for a total scan time of ∼6 minutes or less. At the d-band peaks, the electron count rates can exceed 1 MHz. These static spectra are in good agreement with those recorded by Kevan et al. [253, 254] using tunable synchrotron radiation. The clearly visible dispersion of the d-bands at binding energies between 3 and 7 eV and the large photon energy dependence of the relative amplitudes of

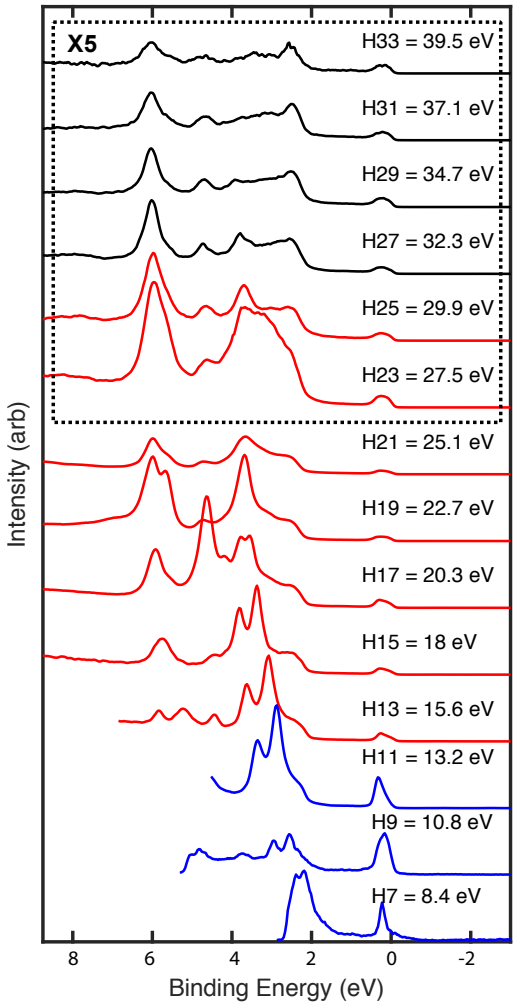

Figure 6.1: Static photoelectron spectra of a Au (111) surface taken with harmonics 7 through 33, vertically offset for clarity. The color indicates the gas used to generate the harmonic; Ar (black), Kr (red), Xe (blue). Each EDC is normalized to the photocurrent measured at TM3, and spectra taken with photon energies above 25.1 eV have been enlarged by $\times 5$. This figure is reproduced from Ref. [9].

the peaks highlight the importance of conducting photoemission experiments with a tunable source as discussed in chapter 1. The same final state effects also strongly influence time-resolved photoelectron spectra and tunability

should be considered no less important, as has been emphasized by previous authors [255].

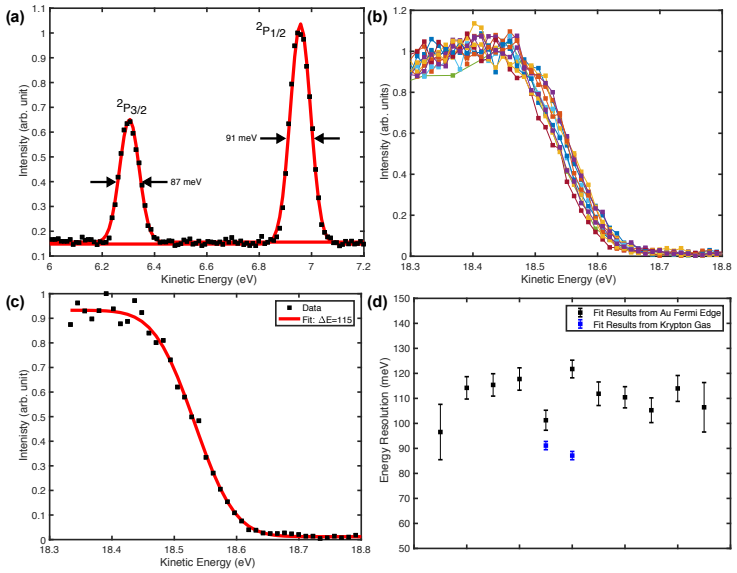

Figure 6.2: a) Ionization of Kr gas target taken with a He I lamp fit to Gaussian distributions. b) Individual scans of Au Fermi edge used to determine the energy resolution. c) An example fit of one of the scans using a convolution of Fermi Dirac distribution with a Gaussian energy distribution. d) Results of fits to each of the measurements in a) and c). This figure is reproduced from Ref. [9].

The resolution of the setup can be determined by analyzing the sharpness of the Fermi edge and is dominated by the energy analyzer.The electron energy analyzer analyzer was used with a He I lamp ($h\nu = 21.2$ eV) where the analyzer resolution was determined from photoelectron measurements using a Krypton gas target. Figure 6.2a) plots the EDC showing the two final states individually fit to Gaussian distributions to determine the analyzer resolution, combined giving $\Delta E_{analyzer} = 89 \pm 3$ meV. Using the CE-HHG source, measurements of the Fermi edge of Au were taken with the sample held at a temperature of 100 K ($k_B T = 8.6$ meV) using a photon energy of 20.3 eV (harmonic energy closest to He lamp). The data was then fit to a convolution of the Fermi Dirac distribution with a Gaussian energy resolution. Figure 6.2b) shows a set of 11 individual scans, and Fig. 6.2c) an

example fit to one of the scans. The fit parameters include the Fermi energy (E_F), resolution FWHM (ΔE), and amplitude. The results of each fit are plotted in Fig. 6.2d). The combined energy resolution given by the average and standard deviation of the fits is $\Delta E = 110 \pm 8$ meV. This resolution is given by the combined contributions from the electron energy analyzer and photon bandwidth $\Delta E = \sqrt{\Delta E^2_{analyzer} + \Delta E^2_{h\nu}}$. Using the analyzer resolution measured with the He I lamp, deconvolution gives a harmonic bandwidth of 65 ± 13 meV.

As discussed in section 3.3.3, this measurement of the linewidth is limited by the energy resolution of our electron energy analyzer. We estimate that the transform limited XUV linewidth can be as low as 30 meV. The simulation shows that our CE-HHG is free of ionization gating due to the restriction of the cavity. There are also several experimental evidence supporting this argument. First, the observed Fermi edge sharpness is found to be completely independent of the HHG generating conditions or harmonic used under variation of a large range of parameters. For example, reducing the driving laser intensity or using the cavity to narrow the bandwidth of the driving pulse [207] should both reduce the harmonic bandwidth, but no change in the the photoelectron spectrum is observed. Furthermore, Mills et al. [224] have reported single harmonic linewidths from a cavity-enhanced HHG source similar to ours, but using even shorter driving pulses, with FWHM as low as 32 meV. Starting with longer driving pulses in our setup, we expect harmonic linewidths narrower than this are obtainable.

6.3 Laser assisted photoemission on Au(111) surface

Even with the current analyzer-limited resolution, we demonstrate here that the absence of space-charge allows for time-resolved photoemission experiments that are both qualitatively and quantitatively different than what is done with space-charge limited systems. Figure 6.3 shows two photoelectron spectra near the Fermi edge of the Au (111) on a logarithmic scale, one with and another without a parallel polarized 1.035 μm wavelength laser excitation overlapped with 30 eV XUV beam in space and time. The spectra were taken with 3 nA of sample current, or approximately 215 electrons/pulse. The energy broadening due to space charge effects is less than 10 meV es-

timated by Equ. (1.5). Consider first the black curve taken with the pump laser off. For a 100 kHz system with our spot size (or even somewhat larger), this sample current would result in broadening and shifting of the Fermi edge on the eV scale instead of the < 10 meV effects here. Furthermore, on a logarithmic scale, space charge effects can cause long high energy tails in the photoemissio spectrum [44, 59, 56] that make it difficult to observe small signals from weakly excited samples. Here, with excellent harmonic isolation from our time-preserving monochromator and the absence of space charge effects, a precipitous drop of four orders of magnitude is observed in the EDC at the Fermi edge.

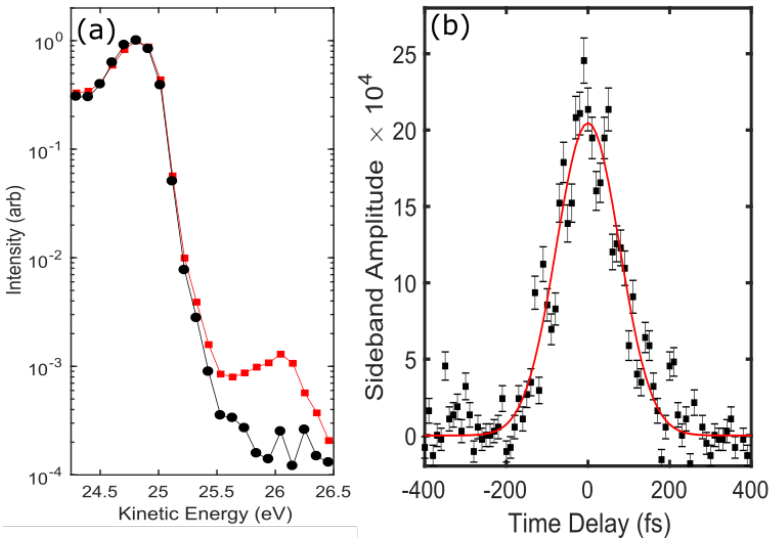

Figure 6.3: a) The photoelectron spectrum of the Au (111) Fermi edge taken without (black) and with a 1.035 μm pump pulse (red) at a peak intensity of 1.3×10^9 W/cm^2. A LAPE sideband of the surface state peak at 24.8 eV is observed at 26 eV. b) The magnitude of the sideband at a kinetic energy of 26 eV as a function of pump probe time delay. The cross-correlation has a FWHM of 181 fs.

Next consider the red curve taken with the pump laser on. Before discussing the laser-induced features of the spectrum, consider first what is *not* observed. The photoelectron spectrum is not shifted, broadened, or distorted due to space charge produced by the laser excitation is as commonly

observed in pump probe experiments [57, 58, 59, 56]. This is because the high data rate enables the experiment to be performed under the low pump intensity of 1.3×10^9 W/cm^2. We measured the sample current from the pump excitation alone and found it to depend strongly on the region of sample probed, as in [56], but always at least one order of magnitude less than the XUV probe, or less than 22 electrons/pulse produced by the pump.

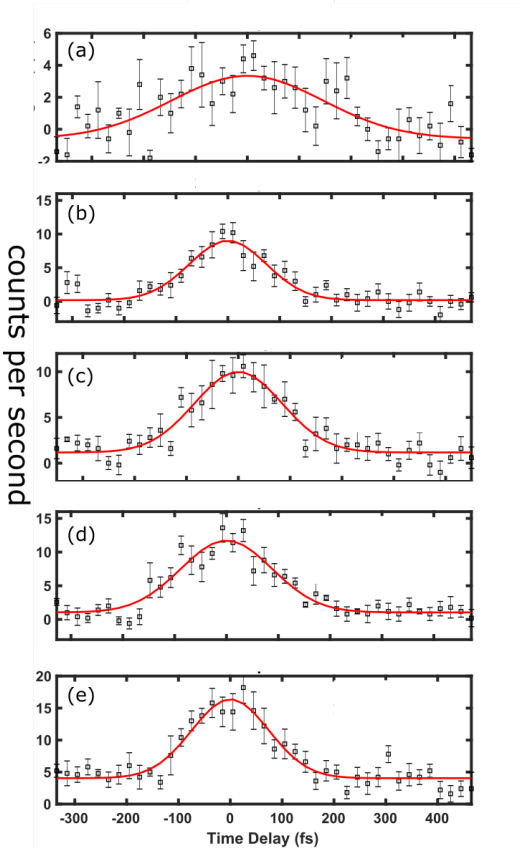

Figure 6.4: The cross-correlation trace taken with different IR intensity. (a) 0.4×10^9 W/cm^2 (b) 0.8×10^9 W/cm^2 (c) 1.0×10^9 W/cm^2 (d) 1.2×10^9 W/cm^2 (e) 1.6×10^9 W/cm^2

The reflectivity of the gold sample is $> 97\%$ and the the laser-induced features in the EDC are dominated by LAPE [56]. In Fig. 6.3a) a sideband

of the surface state peak at 24.8 eV is observed 1.2 eV higher at 26 eV. Figure 6.3b) shows a measurement of the sideband amplitude at 26.0 eV kinetic energy as a function of the time delay between the IR pump and XUV probe. The data were accumulated in 10 minutes. Within statistical error, identical widths and time-zero positions are observed for cross correlations taken at both higher and lower kinetic energies, further confirming the LAPE mechanism, as hot electrons closer to the Fermi energy would show observable lifetimes [256, 257].

A gaussian fit to the cross-correlation in Fig. 6.3b) gives a FWHM of 181 fs. The pump laser pulse duration at the sample position was not independently measured for this experiment, but at the output of the laser the pulse duration was measured to be 165 ± 10 fs and optimal compression gives 155 fs [11]. Taking the lowest possible value of the laser pulse duration then gives a conservative upper limit for the XUV pulse duration at the sample of $\sqrt{(181 \text{ fs})^2 - (155 \text{ fs})^2} = 93$ fs.

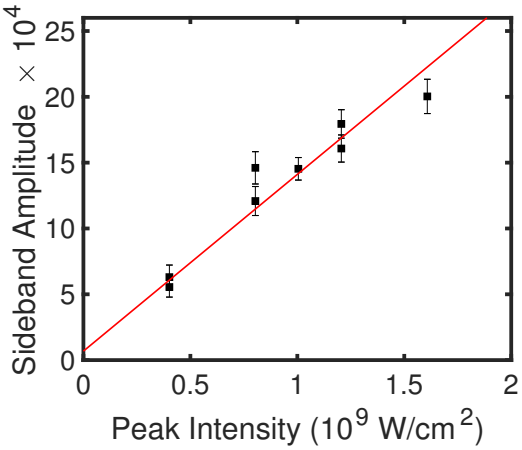

Figure 6.5: The amplitude of the sideband at 26 eV as a function of pump peak intensity. A fit to the data gives a slope of 1.34×10^{-12} cm^2/W.

Fig. 6.4 shows the cross-correlation trace at 26 eV kinetic energy for different IR intensity. (a) $4{\times}10^8$ W/cm^2 (b) $8{\times}10^8$ W/cm^2 (c) $1.0{\times}10^9$ W/cm^2 (d) $1.2{\times}10^9$ W/cm^2 (e) $1.6{\times}10^9$ W/cm^2. With the intensity on the order of 10^8 W/cm^2, We can still clearly observe the time resolved LAPE signal. To our best knowledge, this is the smallest LAPE signal observed on the surface. The IR intensity is at least two orders of magnitude lower

compared to Ref. [56, 247]. In Ref. [56, 247], the LAPE on the solid surface is observed with IR intensity on the order of 10^{11} W/cm^2. The modulation caused by such high intensity IR is strong enough to change the overall shape of the photoemission spectrum. And the 2nd order sidebands also start to play a role. Besides that, the intense pump pulses produces a large amount of electrons which cause space charge effects. The pump induced electron has a long tail extending into > 30 eV range. In our case, each of the cross-correlation trace only takes 10 min to acquire the data, each data points has an integration time of 6s. The count rate on the fermi edge is on the order of 10^4. The sideband amplitude is thus on the order of 10^{-4}. Such data rate is impossible with the conventional low rep rate HHG source.

Fig. 6.5 shows the sideband amplitude versus its intensity in Fig. 6.4. The sideband amplitude is observed to be linear in the laser intensity with a slope of $1.34 \pm 0.13 \times 10^{-12}$ cm^2/W. The theoretical sideband amplitude can be evaluated by Equ. (6.2) and Equ. (6.3) with $1/e^2$ radii $w_{x,\mathrm{laser}} = 150$ μm, $w_{y,\mathrm{laser}} = 150$ μm, $w_{x,\mathrm{XUV}} = 49$ μm, $w_{y,\mathrm{XUV}} = 85$ μm, and FWHM pulse durations $T_{\mathrm{laser}} = 165$ fs and $T_{\mathrm{XUV}} = 93$ fs. and the theoretical estimate for the observed sideband amplitude is $\langle A_1 \rangle = 1.3 \times 10^{-12} \times I_{\mathrm{peak}}$ [W/cm^2], which is in good agreement with our experiment. This result confirms that LAPE theory discussed in section 6.1 works well in the low intensity regime.

After we took the data with 30 eV photon, we changed the photon energy by rotating the grating of the monochromator and then continued to take data without re-aligning any beam. Fig. 6.6 shows the cross correlation of LAPE sideband taken with (a) 27.6 eV and (b) 25.2 eV. The IR intensity is 2.4×10^9 W/cm^2. We observe the same cross-correlation width as 30 eV. The signal rate is slightly different because different photon flux and pump intensity but on the same order of magnitude. The fact that we can continue the experiment without re-alignment indicates the alignment of the monochromator is good, the XUV beam still has spatial overlap with the IR beam after grating rotation. The tunable source is capable of switching photon energy seamlessly.

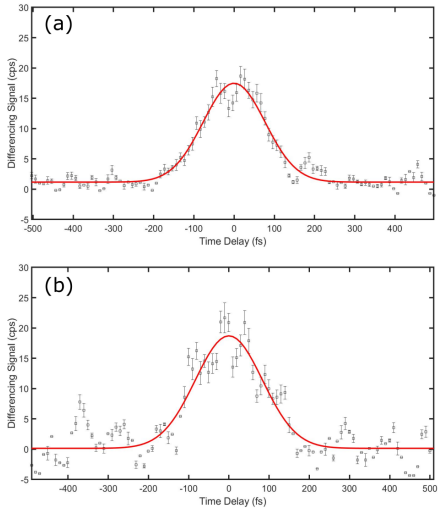

Figure 6.6: The cross correlation of LAPE sideband taken with (a) 27.6 eV and (b) 25.2 eV without re-alignment. The IR intensity is 2.4×10^9 W/cm^2.

Chapter 7

Ultrafast electron dynamics of a thin C60 film

7.1 Introduction

C_{60} derivatives have been used as electron acceptors since the invention of organics solar cells. So far, there is not a kind of acceptor material can match the performance of the C_{60} derivatives. Part of the reason is its unique electron dynamic properties that promotes the charge separation rate by an order of magnitude while they do not affect the charge recombination rate [258]. Understanding the electron dynamics of C_{60} film is crucial for improving its performance [259, 260].

Time resolve photoelectron spectroscopy is a powerful tool to study electron dynamics. The energy structure diagram of C_{60} molecule is shown in Fig. 7.1 [15]. The energy levels are determined by calculations [261, 262] and experiments [263, 264, 265, 266, 267, 268, 269, 270]. On the left side is the molecular orbitals with their parities. Importantly, the dipole transition can't happen between the two states with the same parity. So the HOMO-LUMO transition is forbidden in gas phase C_{60}. However, in the solid, this transition can happen due to the perturbation of the adjacent molecules. Due to the forbidden nature of this transition, the life time of LUMO and LUMO related excitons are long. The HOMO orbital is located 6.8 eV below the vacuum level, which is beyond the photon energy of vis-UV sources. On the right side is the exciton states. The shaded area on the right side means high order excitons. The singlet exciton and triplet exciton associated with

LUMO is labeled as ${}^1E$ and ${}^3E$.

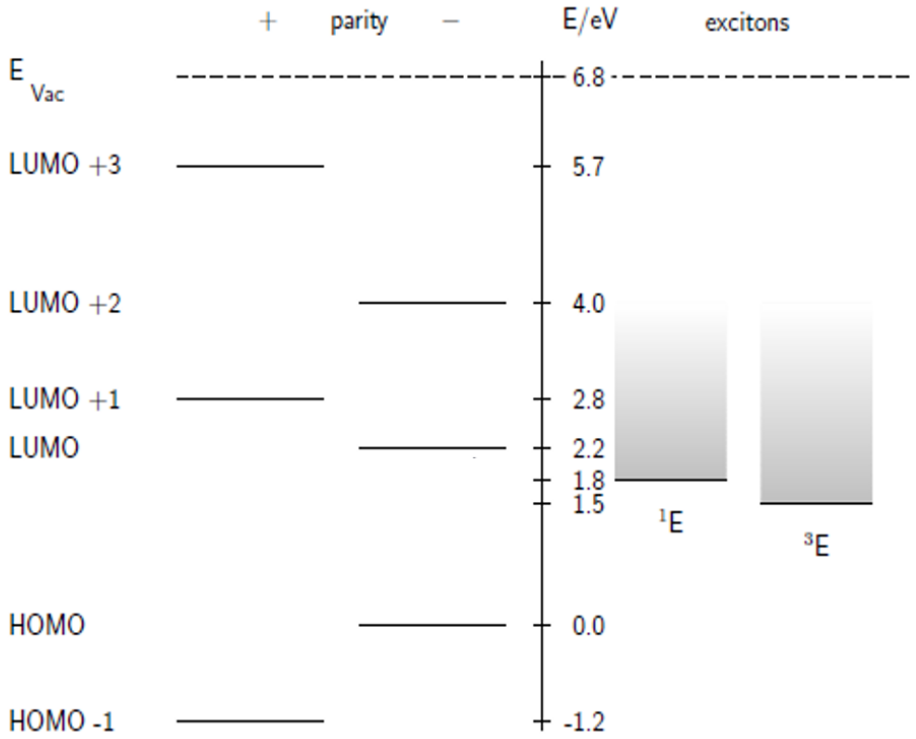

Figure 7.1: The energy level diagram of a C_{60} molecule. On the left side is the molecular orbitals with their parities and on the right side is the exciton states. The shaded area on the right side means high order excitons. This image is taken from Ref. [15]

The 2PPE method has been used to investigate the electronic state of C_{60}. However, due to the limited photon energy of 2PPE experiments, only the electronic states close to the vacuum level can be probed such as LUMO+3 [271], LUMO+2 [272, 273, 274], LUMO+1 [272, 273, 275, 266, 274], and image potential states [276, 275, 266, 271, 274] The LUMO and HOMO related states which play an important role during charge transportation and charge separation can't be probed in the 2PPE. The experiments with XUV photon energy have been done with synchrotron light source [265, 277], but the synchrotron pulse are inherently long. The time resolution in the synchrotron experiment is limited to ∼100 ps.

In order to faithfully study the electron dynamics, perturbative excitation is mandatory. In Ref. [265], it is observed under high fluence pump of 530 nm, the life time of triplet exciton and singlet exciton associated with LUMO orbital is drastically shortened due to the exciton-exciton interaction. In order to suppress this kind of multi-body interaction, the pump fluence needs to be less than 50 μJ/cm^2. In Ref. [15], it is reported that at 50 μJ/cm^2 of 400 nm pump fluence, half of the singlet exciton delay is due to exiton-exciton interaction.

We demonstrate the time resolved photoemission spectroscopy on perturbatively excited sample by applying our high rep rate XUV photoemission instrument to a C_{60} thin film on Au(111) substrate. The research is still in progress. Here we show some preliminary data of this project.

7.2 Sample preparation

The Au(111) crystal substrate is mounted to the rod sample manipulator. The crystal is sputtered with 2 kV Ar^+ ion beam and then anealed at 770 K for a few cycles until the XPS don't see any carbon residue on the surface and a clear Au(111) LEED pattern is observed. The C_{60} molecule (99.9% purity) is purchased from Sigma Aldrich. it was degassed at 250 ∘C for 50 hours prior to use.

The film is deposited in the surface science chamber in-situ with the home made evaporator shown in section 5.5. The film growth rate is calibrated by monitoring the XPS signal of carbon 1s peak (285 eV) and the Au $4f_{7/2}$ peak (84 eV). The heating current of the evaporator is 16 A. The temperature of the crucible is 308 °C. The temperature of the substrate is 573 K during calibration. It is well known that at this substrate temperature, only monolayer C_{60} can stay on the surface. The XPS signal v.s. dosing time is show in Fig. 7.2. The film grows as the dosing time increases, carbon signal increases linearly and the Au signal decreases linearly. When the monolayer closes, Both XPS signal reach a plateau. At the growth condition mentioned above, the growth rate is 8 min per ML. This growth rate is also used for the subsequent multilayers growth.

To grow the C_{60} film, first the Au(111) substrate is held at the 573 K, dose C_{60} for $>$ 10 min. according to Ref. [278], at elevated substrate temperature and a growth rate slower than 5 min/ML, the high quality $2\sqrt{3}\times2\sqrt{3}$R30°

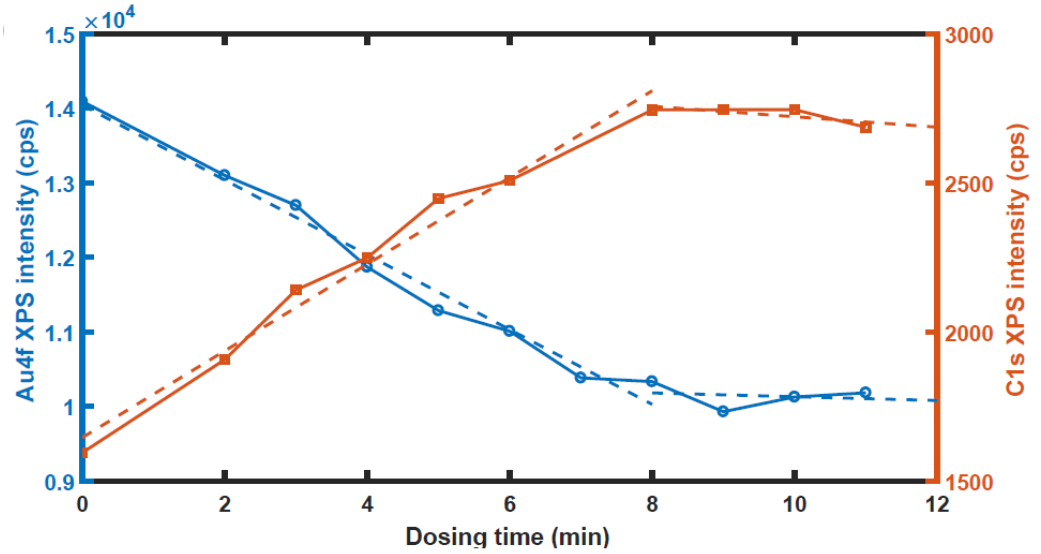

Figure 7.2: C_{60} growth rate calibration. carbon 1s and Au $4f_{7/2}$ XPS signal versus dosing time.

film can form. Ag (111) substrate has a similar behavior [273], but Cu(111) forms 4 × 4 structure instead of $2\sqrt{3}\times2\sqrt{3}$R30° [279]. Fig. 7.3 (a) shows the LEED pattern of our monolayer C_60 film. We observe 6 fold symmetry diffraction with 30° orientation relative to Au(111).

Then the substrate temperature is lowered to 373 K for multilayer film growth if needed. No subsequent film anealing is needed. The chamber pressure is on the order of 10^{-9} Torr during deposition. The LEED pattern of a 12 ML C_{60} film is shown in Fig. 7.3 (b).

7.3 Static photoemission of a thin C_{60} film on Au(111) surface

Fig. 7.4 shows the photoemission spectrum of 10 ML C_{60} film by 22.8 eV, 27.6 eV and 32.4 eV photon energy. The energy resolution of the hemisphere energy analyzer is set to 120 meV. The sample is placed normal to the hemisphere. The measurements are done at the room temperature. The integration time of each data point is 1 s. Thanks to our high photon energy,

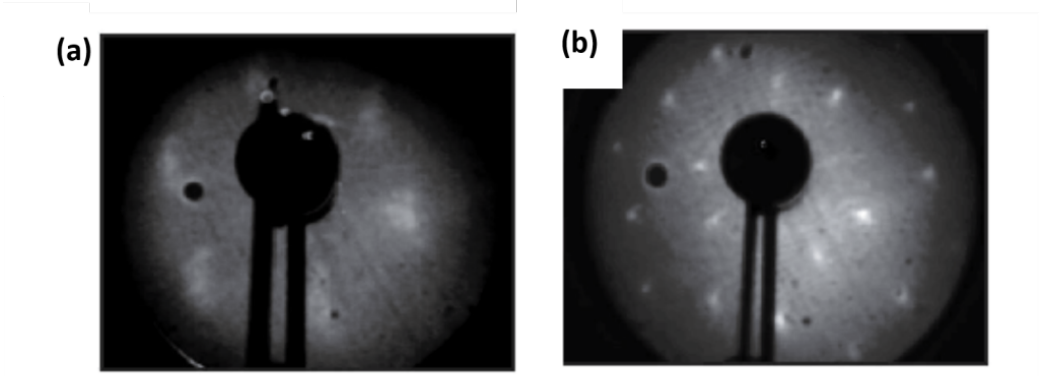

Figure 7.3: (a) LEED pattern of a C_{60} monolayer film with 15 eV electron energy. (b) LEED pattern of a 12 ML C_{60} film with 24 eV electron energy.

we can probe deep molecular orbitals such as HOMO, HOMO-1, HOMO-2 and deeper ones. A typical DUV light source can't reach this deep binding energy. The counts rate is on the order of 10^4. The data has 4 orders of magnitude dynamic range even with only 1 s integration time. By comparing the different photon energy, we can see the ratio of the HOMO and HOMO-1 vary with photo energy. This implies the photoemission dipole matrix element is photon energy dependent.

The photoemission spectrum of bare Au(111) surface and 1-5 ML C_{60} film is shown in Fig. 7.5. The photon energy is 22.8 eV. The sample orientation is normal to the hemisphere energy analyzer. There is a sharp Fermi edge on the bare Au(111) substrate. The intensity of Fermi edge drastically decreases with one ML C_{60} on the surface. For the monolayer C_{60} film, electrons transfers from the metal substrate into the molecular orbital of C_{60} since C_{60} is a good electron acceptor material. This causes a strong screening effect. The photoemission spectrum of monolayer C_{60} film is a hydrid of the subtrate and its molecular orbitals. For the film $\geq$ 3 ML, there are no electrons from Au(111) discernible. The molecular orbitals of C_{60} are observed. For the 5 ML C_{60} film, the photoemission spectrum doesn't change as the film gets thicker, the molecular orbitals are basically same as the bulk material [272, 266].

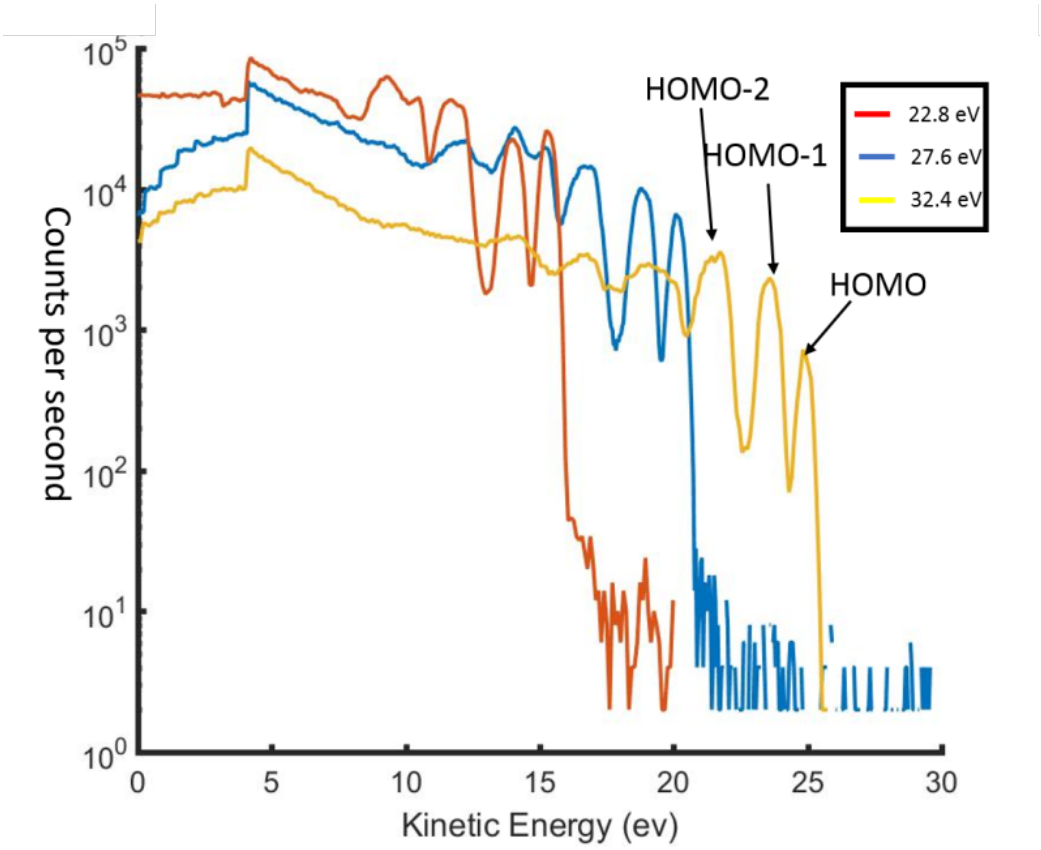

Figure 7.4: Photoemission spectrum of 10 ML C_{60} film by 22.8 eV, 27.6 eV and 32.4 eV photon energy.

7.4 Time resolved photoemission of a thin C_{60} film on Au(111) surface

In the pump probe experiment, 2.4 eV pulses generated by 2nd harmonic generation are used as pump light. The 2.4 eV pump light directly excites the HOMO-LUMO transition. The subsequent electron dynamics of LUMO, singlet exciton ^1E and HOMO are probed with 22.8 eV photon.The sample is cooled by liquid nitrogen. A mechanical chopper is used to modulate the pump light so the pump induced changes can be extracted by lock in detection. The pump fluence is 40 μJ/cm^2. Assuming the absorption crosssection is roughly 1×10^{-17} cm^2 [280], the resulting excitation fraction is estimated to

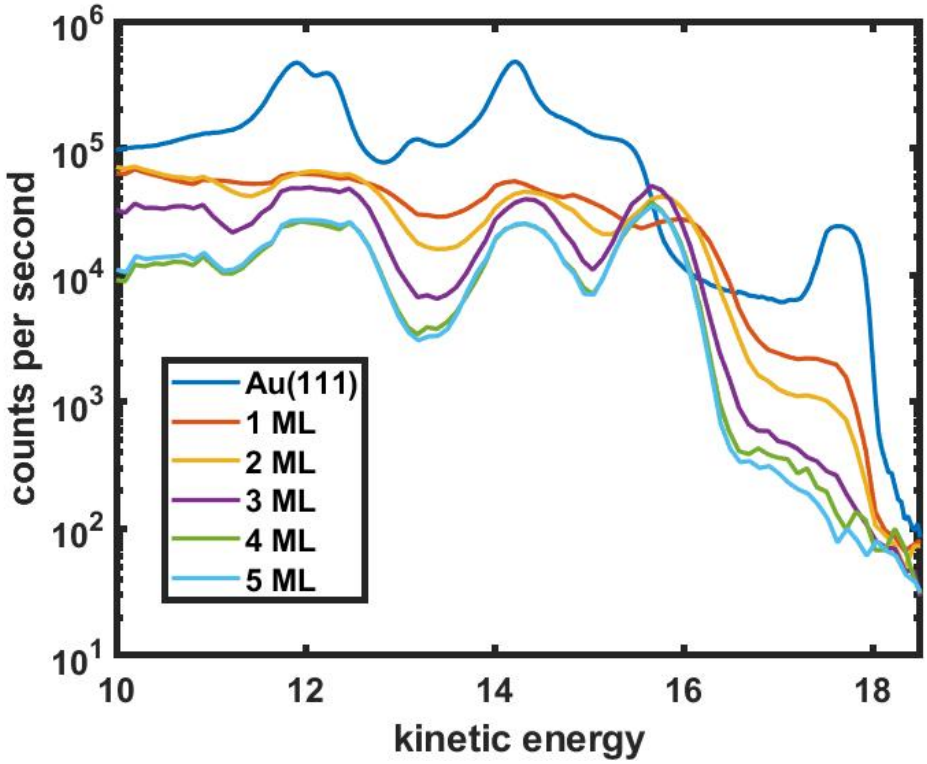

Figure 7.5: Photoemission spectrum of 1-5 ML C_{60} film and bare Au(111) substrate by 22.8 eV photon.

be 2×10^{-3}. The sample is cooled liquid nitrogen and initially its temperature is 100 K without the pump light. With the pump light, sample temperature during the experiment goes up to 250 K as discussed in section 7.5.

For the excited states including direct excitation (pump), LUMO and singlet, we see a rise edge about 200 fs at zero time delay. Followed by that, there is a plateau that the electron population doesn't change in 5 ps. The reason is the LUMO associated states has a long life time due to its forbidden transition nature. From previous studies, the lifetime of LUMO is reported as $\sim$ 100 ps and the singlet exciton is longer than 1 ns [265, 15]
For the HOMO orbital, we see a negative signal. Interestingly, even the excitation fraction is on the order of 10^{-3}, this bleach signal is on the order of 10^{-2}, which is almost one order of magnitude stronger. More than that, the recover time of the signal looks faster than the excited states, possibly on the

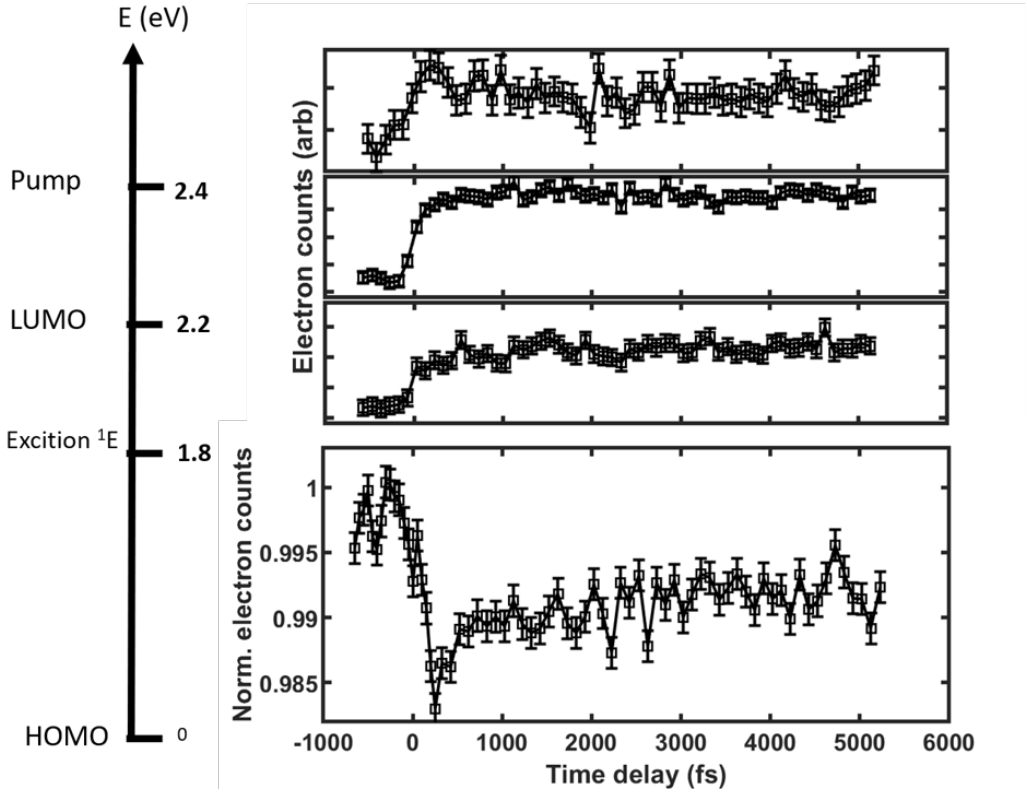

Figure 7.6: Time resolved photoemission spectrum of C_{60} pumped by 2.4 eV.

order of 10 ps. So this bleach signal is not caused by the electron population change on the HOMO level. A similar spectrum feature is reported by Benjamin Stadtmller and coworkers from University of Kaiserslautern in their recent publication [281]. They attribute this bleach signal to the collective dielectric screening of the organic film to the excited molecules.

7.5 The current problems and future plan

As the TOF k-mic introduced in chapter. 8 is installed as the electron detector, the TOF k-mic will be used in the future experiments. The preliminary results of static photoemission of C_{60} 10 ML film on Ag(111) are shown in Fig. 7.7. The TOF k-mic can record high quality data as the hemisphere

energy analyzer. The TOF k-mic is well suited for the C_{60} experiments.

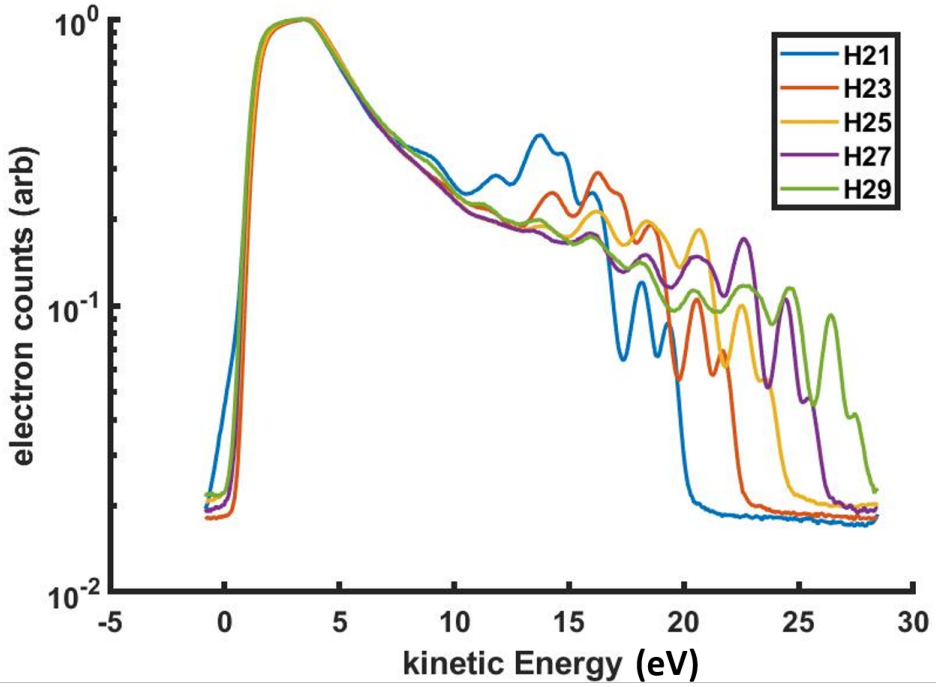

Figure 7.7: Photoemission spectrum of a C_{60} thin film on Ag (111) measured by TOF k-mic detector

- First, high energy resolution is not required for the C_{60} experiments. To observe the molecular orbital of C_{60}, 200 meV energy resolution is enough. At 80 MHz, The TOF k-mic can easily satisfy the needs but can't do an order of magnitude better easily.
- Second, the high momentum resolution is required for the momentum mapping. Because the lattice spacing of the C_{60} crystal film is about 4 times bigger than a typical metal substrate, its fist brillouin zone is only about 0.3 $\mathring{A}^{-1}$. The high momentum space resolution and massive momentum pixels fits this experiments very well.
- Third, with the Delay line detector, the experiment can be done pulse-wise. This can be conveniently combined with pump light pulse picker as mentioned below.

- Fourth, the TOF k-mic measures all the energy at once, so the measurement is not so sensitive to the photon flux drift This feature is useful for the study of such broad energy features.

- Last, its capability of highly parallel detection can boost the data rate by orders of magnitude.

We had several problems during the C_{60} experiments. These problems need to be solved in the future experiments. The first one is the sample heating problem. At 80 MHz, the average power of the pump is up to 2.5 watts. Because the gold substrate has substantial absorption at 2.4 eV, The pump light causes a heat load on the substrate. This cause the sample temperature goes up to 250K while cooled by liquid nitrogen simultaneously. The high heat load of the substrate can also potentially cause sample damaging. The sample heating problem has been solved by using Ag(111) as a substrate. Different from gold, silver is highly reflective at 2.4 eV. With 2.5 watts pump light incident on Ag (111) surface, the temperature change is less than 10 K. That's acceptable.

The sample heating problem is also related to photo induced polymerization problem. It is known that under visible light exposure at the room temperature, the photo induced polymerization reaction can happen [265]. In order to prevent that, the sample need to be cooled below 180 K. The hexapod sample manipulator with continuous flow cryostat will be installed in the near future. The sample will be cooled to the temperature of liquid nitrogen or liquid helium with the hexapod which is enough for the this experiment.

Chapter 8

Time of flight electron momentum microscope

8.1 Introduction

We have updated our hemispherical energy analyzer to the electron momentum microscope (k-mic) as electron detector.The underlying idea is of k-mic is that similar to the photoemission electron microscope (PEEM), The reciprocal image forms in the backfocal plane of a cathode lens, which directly shows the surface-projected band structure of the sample [282]. Detection of the reciprocal image with optimized resolution is the essence of electron momentum microscope as pioneered in J. Kirschners group at the MPI Halle [283, 284] The original k-mic uses retarding field energy filter then switched to two hemispherical energy analyzer in the orthogonal configuration to get the dispersion of electrons in energy.

Time of flight electron momentum microscope (TOF k-mic) shown in Fig. 8.1 was developed at Johannes Gutenberg University Mainz by G. Schönhense, in cooperation with J. Kirschner's group at MPI Halle [285, 20, 16] The TOF k-mic replace the hemispherical energy analyzers with an imaging ToF section similar to that of the ToF-PEEM developed at the University of Mainz [286, 287]; however, the lens system is optimized for best k-resolution. Compared to the our previous hemispherical energy analyzer, The TOF k-mic has significant advantages:

- Highly parallel 3D data collection. By using the TOF, 3D data in k_x, k_y and Energy can be acquired simultaneously. In our previous

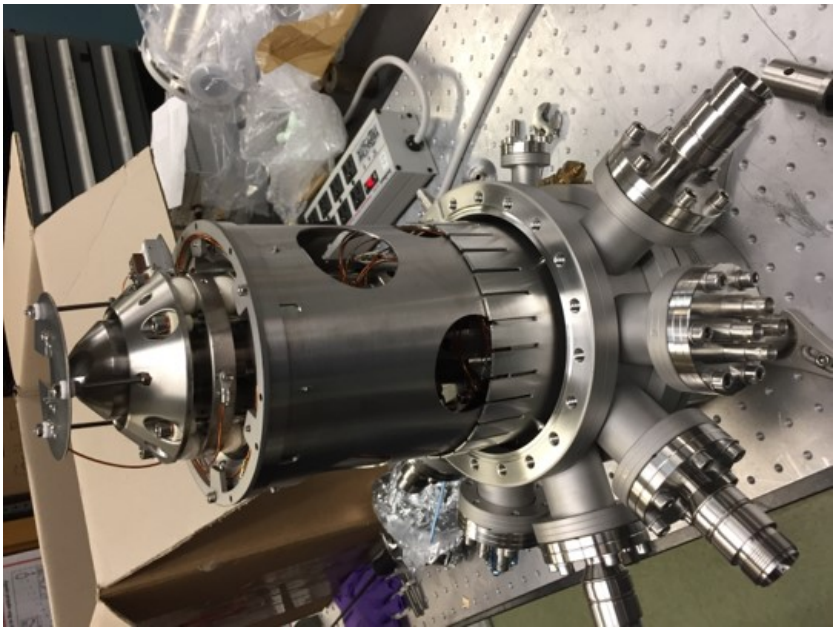

Figure 8.1: A photo of electron optics of the k-mic column. The TOF spectrometer is not included in this photo.

hemispherical analyzer, I can only detect one point in in k_x, k_y and energy space. This boosts the data rate in our experiment by orders of magnitude.

- Full solid angle electron detection. Due to the cathode lens, all the electrons over 2π solid angle are extracted into the detector. In the hemispherical analyzer, only $\pm$ 4° can be collected. This greatly increases the momentum range can probed in the experiments as shown Equ. (1.3).

- Spatial resolution. The k-mic can also operate in real space imaging mode with resolution comparable to PEEM. Moreover, by using the field aperture, $< \mu m$ level spatial resolution can be achieved in momentum space imaging mode.

- Electron energy filter and spin filters can be easily combined in this configuration.

8.2 Working principle

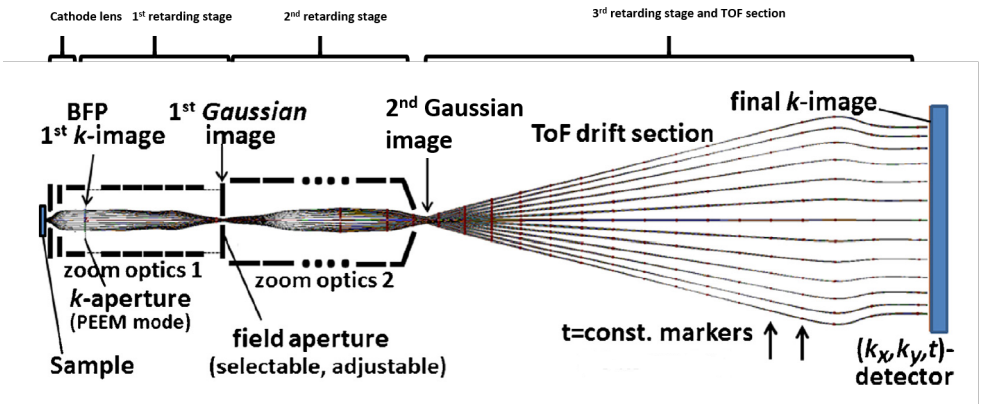

Figure 8.2: Cross section of the ToF k-mic with electron trajectories in momentum imaging mode. This image is taken from Ref. [16]

Fig. 8.2 shows the schematic cross section of the ToF k-mic with trajectories for electrons in the momentum imaging mode [16]. The trajectories of electrons from sample to the delay line detector (DLD) go through 4 stages: the cathode lens, the first retarding stage, the second retarding stage, and the third retarding stage with the TOF section.

The cathode lens is made of 3 parts, the sample, the extractor and the Focus lens.The sample to extractor distance is typicaly 4-8 mm, the field of view (FOV) of the cathode lens is typically 400 μm. The extractor is typically running at the voltage of 4 - 20 kV. The extractor is followed by a decelerating lens "Focus", and then the first momentum image forms in the backfocal plane (BFP) of the cathode lens at a voltage about 1200 V. A contrast aperture is located at the backfocal plane.

The first retarding stage focuses the electrons to form the 1st Gaussian image. The position of the spatial image is usually kept fixed, such that a field aperture can be used to select sample area. It defines the source spot on the sample surface in a wide range from a few 100 μm down to the region of < 1 μm, independent of the focusing quality of the photon source and the operation mode of the subsequent electron lenses. Both contrast aperture and field aperture are motorized and selectable among of a grid of pinholes with different sizes.

Followed by that, The zoom optics in the second retarding stage and third retarding stage serves the following functions:

- Forming the 2nd gaussian image in the end of 2nd retarding stage.
- Deceleration the electrons to the desired drift energy into the TOF spectrometer.
- transformation between momentum image mode or real space image mode.
- Variation of the magnification factor.

The length of the TOF tube is 0.9 m. Thanks to the high extraction voltage and small filling factor in most lenses, there is essentially no correlation between the transversal momentum and the kinetic energy. This is a outstanding feature compared to the common TOF spectroscopy instrument [288, 289, 290]. At the exit of the TOF tube, the delay line detector is used to detect the electrons. The electron momentum map and the time of flight can be recorded simultaneously. All the electron optics are driven by high voltage supplies with mV resolution.

8.3 Application

TOF k-mic has been applied in high resolution ARPES experiments [291, 292, 293]. The energy resolution on the order of 10 meV and momentum resolution on the order of 0.01 $\mathring{A}$ has been demonstrated. Due to its high data rate, it's particularly successful in spin-resolved ARPES experiments [16, 294, 295]. The other breakthrough is that it's used to explore the connection of bulk and surface states. With the high momentum resolution, the bulk band structure can be probed with soft X-ray light source as well as the surface [296].

However, like other PEEM instruments, space charge issue is a big limitation factor of the performance of the k-mic [54] As mentioned in section 8.5, due to the fact that large amount of electrons including all the secondary electron are sucked into the k-mic and travel together, the space charge effects are even worse. High rep rate sources without space charge effects are desirable. On the other hand, the synchrotron light sources typically have a

rep rate of hundreds of megahertz, the time of flight interval is only a few nanoseconds. That's too short for time of flight spectrometer in most cases. As shown in Ref. [293] and Ref. [9], The light source with tens of Megahertz rep rate reach a good balance between the data rate and the energy resolution, So our XUV source is well suited for the TOF k-mic detector.

The time resolved ARPES experiment is demanding on data rate. Our high rep rate source without space charge effects boosts the data rate by about two orders of magnitude, while the TOF k-mic can boost the data rate by another two orders of magnitude. With the combination of our high rep rate XUV source and TOF k-mic detector, the data rate can be boosted by approximately 4 orders of magnitude. This unprecedentedly high data rate enables enables time resolved ARPES experiments in the perturbatively excited regime.

Besides its high data rate, high electron collection efficiency and large momentum range, another important feature is that the experiment can be done pulse-wise. In the TOF k-mic experiments, electron hit events are sorted out pulse by pulse relative to the trigger signal, this pulse-wise manner enables advanced experimental techniques, two examples are:

- One pump/multiple probe experiments scheme. Because the delay line detector can access μs recording length, which is much bigger than our rep rate $\sim$ 12 ns. In the pump probe experiment, it's possible that we can do one pump then multiple probe scheme. The sample is excited once by the pump, then probed by multiple probe XUV pulses separated by the rep rate. we get the fine time steps ($<$ ns) by delay stage, and the Delay line detector can record the longer time scales ($>$ 12 ns) directly in time domain. This technique can be particularly useful when study the long living electronic states such as triplets.

- Advanced noise cancelling technique. For example, we can implement pump pulses at the half rep rate of the probe pulses. Then the pump probe signal has a modulation frequency of half rep rate of the probe pulse which can be tens of Megahertz. Thanks to the storage nature of the optical cavity, the CE-HHG source filters the noise whose frequency is higher than the cavity linewidth. At the modulation frequency $f_{rep}/2$, the noise is dominated by the shot noise of electron counting. High quality signal with high signal to noise can be retrieved by lock-in detection.

8.4 Delay Line Detector

The electron detector of the TOF k-mic needs be able to detector (t, x, y) 3D data [287]. The DLD we use has an active area of 40 mm diameter and a spatial resolution of 80 μm, resolving 200,000 image points. The maximum count rate is about 4 Mcps.

8.4.1 Trigger signal

The time resolution of the DLD is critical for the energy resolution in the measurements. In order to achieve the time resolution of specs of the DLD, the time jittering of trigger signal should be small enough so it doesn't contribute. At the same time, the DLD only takes trigger signal up to 8 MHz, much lower than our rep rate $\sim$ 80 MHz. The electric signal derived from the optical signal needs to be divided down. The Fig. 8.3 shows how the trigger signal is generated.

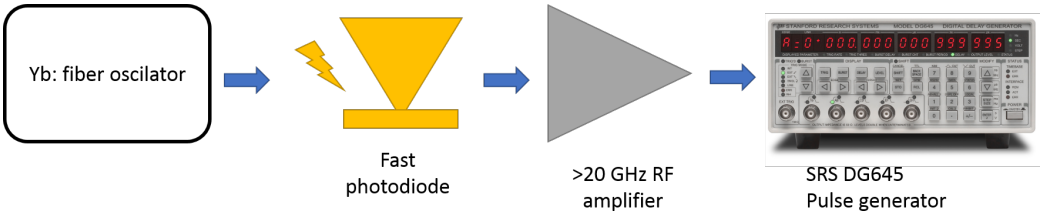

Figure 8.3: Schematic for DLD trigger signal generation.

We capture a stray beam in the Yb fiber oscillator, and couple the light into a single mode fiber. The oscillator has extraordinary noise performance, and the signal derived from the oscillator should be quiet. The fiber delivers the light to the photodiode located next to the DLD time to digital converter (TDC). Transportation of the optical signal instead of electric signal preserves the pulse duration because optical dispersion of the fiber is less than the RF dispersion of the cable. A fast photodiode (EOT 3000) with rise time $<$ 175 ps is is used to convert light into electric signal. Then the signal is amplified by a 20 GHz RF amplifier so it's amplitude is big enought to trigger the SRS DG 645 pulse generator. The SRS DG 645 is basically a quiet phase locked loop, divide the rep rate down and can be used to adjust the delay of the trigger. Then the output of SRS DG645 is fed into the DLD.

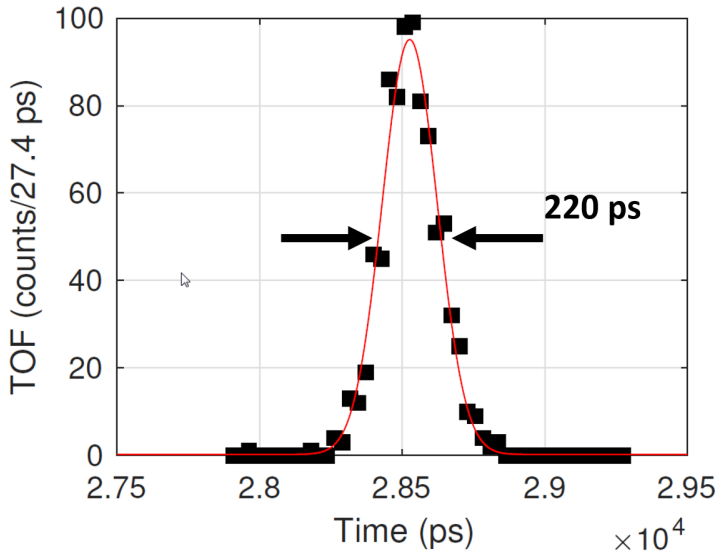

Figure 8.4: Measurement of time resolution of DLD by XUV scattering.

We measure the time resolution of the DLD by using the scattering of the XUV pulses. Because XUV pulse is only 100 fs, the reponse time of the DLD should be its time resolution. To distinguish the signal due to photons, We shut down all the electron optics except the DLD. By doing that, the dominant counts comes from the XUV scattering off the sample, the counts rate was a few thousand. As shown in Fig. 8.4, the measured time resolution is 220 ps, which is close to the specs 207 ps.

8.5 Space charge effects in electron momentum microscope

Even with 80 MHz rep rate, it is possible to observe space charge effects in our setup under extreme conditions. The extractor field of the cathode lens effectively collects all slow electrons and forms a charge cloud with high density travelling along the optical axis behind the fast primary electrons. The large number of slow secondary electrons gives rise to a net acceleration to the primary photoelectrons. Just using the field aperture can't get rid of them, because they focus differently due to chromatic aberration. It has been observed that at $h\nu = 1000$ eV with photon-flux densities between 10^2 and

10^4 photons per pulse per μm^2, space-charge induced energy shifts can be up to 10 eV. In order to correct the essential part of the energy shift and restore the electron distributions close to the Fermi energy, a semi-analytical theory for the space-charge effects in k-mic has been developed by G. schöhense [54].

The space-charge problem can be even more severe in time resolved ARPES experiments. The pump laser can release a large amount of slow electrons due to multiphoton photoemission or optical field emission. The amount of electrons can be much more than electrons ejected by the XUV pulse. In the case of a C60 thin film on Ag(111) surface, we have measured more than a micro Ampere sample current at the pump fluence on the order of 100 $\mu J/cm^2$ compared to the nA level sample current induced by XUV. More than that, the charge density caused by intense pump lasers can be strongly inhomogeneous. For example, the small spots of the contaminants and defects on the surfaces may emit one order of magnitude more electrons than the uniform sample area. Such hot spots can cause spatially inhomogeneous space-charge shifts and deformation of the electron momentum map.

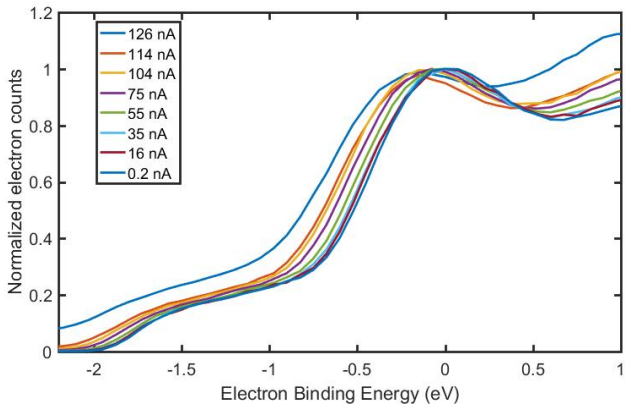

Figure 8.5: Space charge induced energy shifts in photoemission study of a C60 thin film.

We have experimentally observed the energy shifts induced by space charge effects in the pump probe experiment as shown in Fig. 8.5. The experiment is 515 nm pumped C60 thin film on Ag(111) sample. The high pass filter discussed in section. 8.7 is used and the energy resolution of this measurement is about 0.2 eV. With probe only, the sample current is 0.2

nA as the last curve in the figure. As the pump fluence increases, the pump induced sample current is much bigger than the probe, and a energy shift is observed at the sample current > 35 nA which is about 2700 electrons per pulse. At 126 nA sample current (10^4 electrons per pulse), the energy shift of the curve is about 0.25 eV. This gives us a rough estimation that in order to keep the the energy shift less than 20 meV, the sample current needs to be less than 10 nA.

8.6 Field Aperture

The field aperture is located in the 1st gaussian image plane. We have the 9 field apertures with different sizes from a few micrometers to a few millimeters. Since the typical magnification of the cathode lens and 1st retarding stage is about 8. The field aperture allows us to select regions on the sample from less than a micrometer to a few hundred micrometers. The field aperture is very useful feature for our experiments, due to following reasons:

- It defines the spatial region of interest no matter what mode is the down stream optics are running in. This feature allows for less than micrometer spatial resolution in the momentum imaging mode and is useful for ARPES studies on small crystal domains.

- It can enhance the momentum space resolution. By using a smaller field aperture, we effectively get a smaller XUV beam size, that helps improve the momentum resolution.

- It blocks the stray electrons. Due to the high extraction voltage, there can be a significant amount of stray electrons sucked into the k-mic such as field emission electron. The field emission electron may come outside of the field of view and may not form a image at the field aperture plane. so having a moderate sized field aperture can block most of the stray electron without affecting the signal too much.

- In pump probe experiment, it relieve the requirement of the beam spot quality. Since the region of interest is defined by the field aperture, it relieve the requirements such as pump beam shape and pump probe overlapping.

8.7 High pass filter

An electron high pass filter allows electrons with kinetic energy higher than the threshold go through but blocks the lower kinetic energy electrons. Such a potential energy bump can be realized by having the sample at a positive voltage, Then put a element with the voltage lower than the sample later in the path of electrons, so only the electrons with kinetic energy bigger than the voltage difference can pass. In this process, at the high pass filter, electrons are decelerated to near zero kinetic energy and after filtering, electrons may be accelerated back.

Electron high pass filter is a critical for time resolved ARPES experiments. First, the DLD has a maximum count rate of about 4 Mcps. Potential damage can occur above this count rate. Due to the high collection efficiency, all the electrons enter the k-mic, but most of them are the low energy electrons. Usually, only electrons near the Fermi edge matters in the experiments, which is only a small fraction of the total electrons. With large amount of useless electrons hitting the DLD, the data rate is severely limited by the maximum count rate of the DLD and the big background can degrade the signal to noise ratio of the data. For the same reason, only tiny bit of the XUV photon flux can be used in the experiments, the efficiency is low. For example, assuming 10% quantum efficiency, 4 Mcps means only 4×10^7 photons/s hit the sample. Compared to our photon flux on the order of 10^{11} photons/s, most of the photons are wasted. In the pump probe experiments, the pump pulse can generate large amount of low energy electrons, the DLD may be saturated by the electrons induced pump.

Second, at our high rep rate as 80 MHz, there is only about 12 ns time window for time of flight. As discussed in section 8.8, XUV photons produce electrons over an energy range of tens of eV, in order to achieve moderate energy resution like 100 meV, we need narrow the energy span down to about 5 eV. High pass filter is critical for the energy resolution of the detector.

The original high pass filter design is to use the zoom lens element at the end of the 2nd electron retarding stage, where the 2nd gaussian image is formed.However, as shown in Fig 8.6, this has a problem. (a) in Fig 8.6 shows that TOF spectrum without high pass filter. The part in the red box is supposed to go through the go pass fiter used in (b). But, because the length of this high pass filter element is long and electron travel through it with near zero kinetic energy, The electron pulse is significantly stretched in

time during propagation with low velocity. Due to our high rep rate, our TOF window is narrow. The desirable TOF spectrum shown in the red box is stretched much longer than the interval between the adjacent pulses. The adjacent electron pulses start to overlap with each other as shown in (b). This measurement is done with TOF drift energy as high as 400 V, so electron doesn't get much dispersion due to the TOF tube. Most of the dispersion in time of flight comes from the high pass filter element. The overlapping part of the TOF spectrum makes a big background. In pump probe experiments, the excitation signal can be buried in the massive background and hard to retrieve. And the shape of the TOF spectrum is significantly distorted.

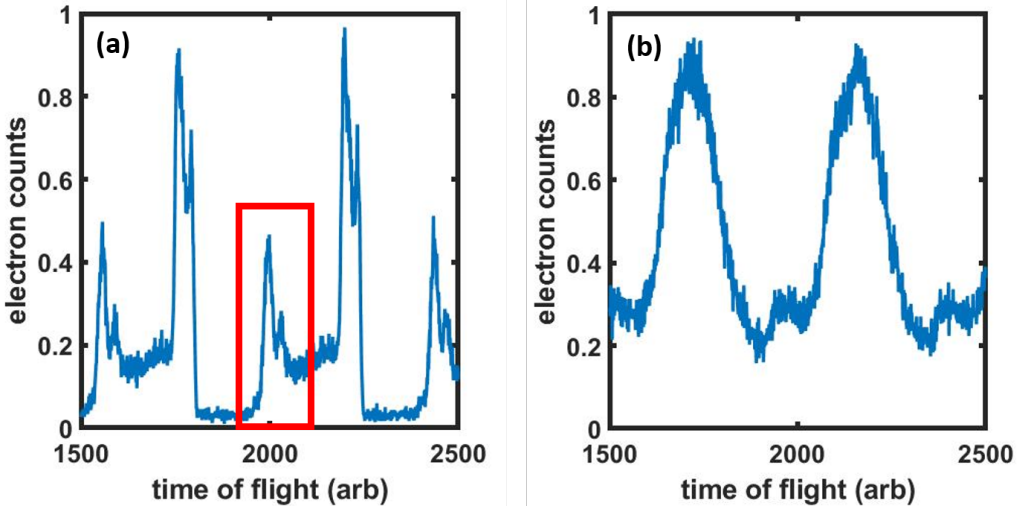

Figure 8.6: The problem of the original high pass filter design.(a) The TOF spectrum of a C60 thin film without the high pass filter. The part within the red box is supposed to preserved by the high pass filter used in (b). (b) the high pass filter results.

To solve this problem, we developed a new high pass filter. The underlying idea is that just like a femtosecond laser beam propagates through a media, the pulse duration can be stretched by the material dispersion. But if the propagation distance is very short, then the pulse duration can be preserved. So if the length of the electron high pass filter is short and it is close to the electron detector, then the pulse stretching effect and the defocusing effect cause by the high pass filter is minimal. Based on this idea, we try to use MCP Front voltage as the high pass filter. The MCP is the front end of

the DLD detector. It is located close to the exit the TOF tube. Electrons coming through the TOF tube are decelerated and filtered. Because it is the end of the electron trajectory, no propagation happens after MCP, so it doesn't stretch the electron pulse too much. Due to the strong deceleration, it provides extra magnification and affects the imaging, but these problems can be easily compensated by the upstream optics in the 2nd retarding stage and 3rd retarding stage.

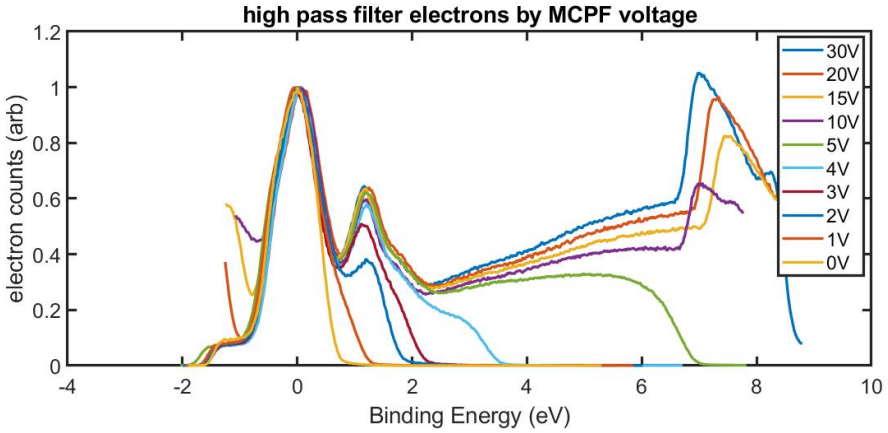

Figure 8.7: The photoemission spectrum of a C60 thin film with different MCP Front voltages.

Fig. 8.7 shows the TOF spectrum of a thin C60 film on Ag(111) surface. The photon energy is 25.2 eV. The sample voltage is set to 20 V. We can see the TOF spectrum is cut off at lower binding energy as the MCP front voltage decrease. The high pass filter causes a hard cutting edge of about 1 eV wide. The secondary tails are removed, and the high energy part is unaffected. The TOF spectrum is still stretched a little bit, that's why for the voltage between 10 V and 20 V, the TOF spectrum curves still wrap a little bit. In the case that MCP front $<$ 10 V, the high pass filter narrows the energy span effectively, then the wrapping is not observed anymore.

In the pump probe experiment, the pump pulses can produce large amount of low energy electrons. That put a demanding requirement on the extinction ratio of the high pass filter, meaning the fraction of electrons can break through the high pass filter. For example, if the pump produces 10 nA sample current, that's about 10^{10} per second, assuming in order to retrieve the pump induced excitation faithfully, no more than $1{\times}10^3$ electrons breaking

through the high pass filter can be tolerated. The required extinction ratio is better than 10^{-7}. Fig. 8.8 shows the extinction ratio as the MCP Front voltage is tuned down. The low energy electrons are generated by intense 515 nm femtosecond pulses from a C60 thin film on Ag(111) surface. The sample voltage is set to 20 V. The electron break through the high pass filter roughly drops one order of magnitude per volt. We typically run the MCP at less than 5 V which creates a potential bump > 15 V and sample current is less than 10 nA, So extinction ratio of this high pass filter design is good enough for the pump probe experiment.

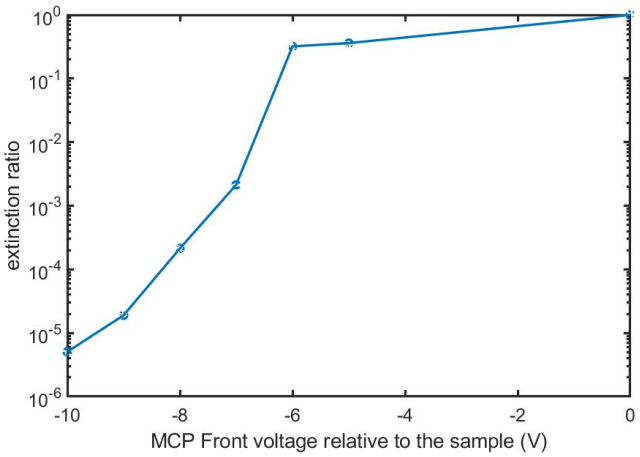

Figure 8.8: Measurement of the extinction ratio of the MCP front high pass filter versus the MCP front voltage.

The other concerns about this high pass filter design is that since we run the MCP front at such a low voltage, electrons are decelerated to only a few eV when hit the MCP. While it is a common believe that to fully use its gain, MCP usually needs 100 eV or higher impinging energy [297]. Running the MCP front at such a low voltage could drop the detection efficiency. We measured the MCP relative efficiency v.s. the MCP front voltage. The result is shown in Fig. 8.9. The measurement is done by imaging the 2PPE electrons induced by pump light. Those electron typically have near zero kinetic energy. The sample is grounded, so the MCP front doesn't act as high pass filter. The MCP front voltage is then roughly the kinetic energy impinging on the MCP. The efficiency of the MCP peaks at 200 V. And the efficiency of the MCP drops by a factor of 3 or so at low kinetic energies. It certainly

reduces the data of the experiments, but the loss is still acceptable. And fortunately, the efficiency near zero is fairly flat. The TOF spectrum taken this way is not severely shaped by the detection efficiency. This problem can be potentially fixed by using grids as a high pass filter in front of MCP [283]. The concern about using a grid is the microlens action of the grid meshes that sets a principal limit to the achievable energy and angle resolution [298] and the projection of the mesh pattern to the DLD.

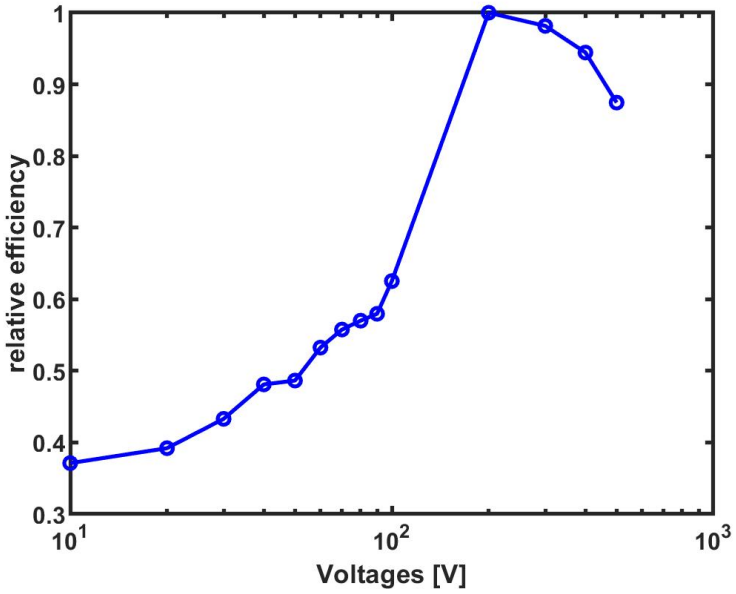

Figure 8.9: MCP efficiency vs MCP front voltage

The other idea of high pass filter is to use the momentum filter. The idea of this kind high pass filter is that the low energy electrons must have small momentum range. The momentum of the electrons can be estimated by $k_{\parallel}^{max} \approx 0.5\mathring{A}^{-1}\sqrt{KE(ev)}$. On the back focal plane, where the 1st momentum space images forms, we can block the electrons with near zero momentum and let the electrons with high momentum pass. This kind of high pass filter has the advantages that it doesn't need to change any voltage of the lenses, so it doesn't affect the electron imaging performance or stretch the electron pulse in time. Ideally, this can be realized by having a contrast aperture with a little blocker in the center. In our case, we start with by the contrast aperture holder plate. We move in the contrast aperture holder far enough

so the edge of the holder pass the center part of momentum image. This needs to the momentum image by more than half in order to cut the near zero momentum electrons. it cuts the data rate by more than a factor of two, but the loss is usually acceptable.

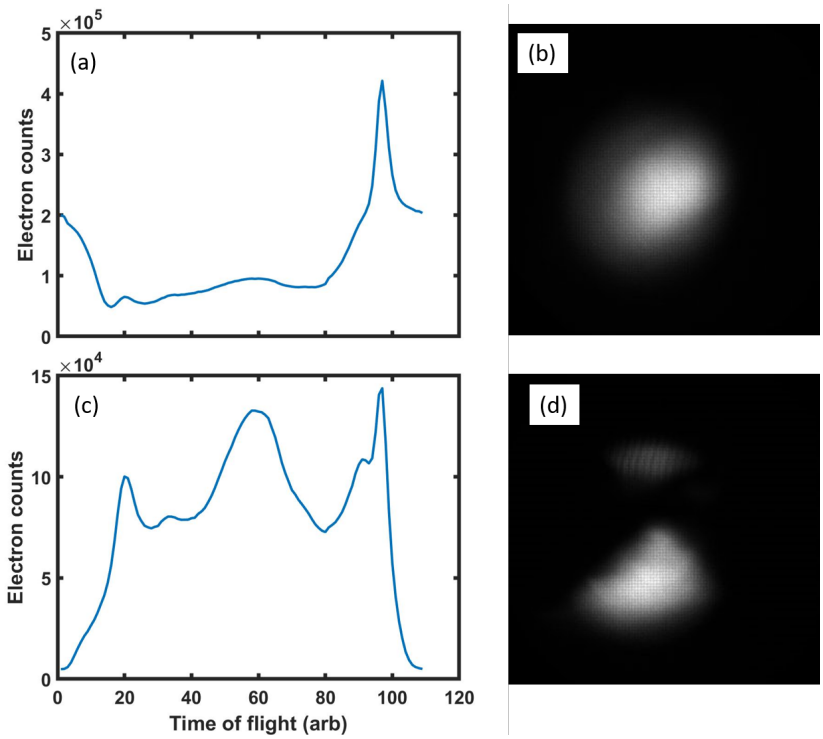

Figure 8.10

Fig. 8.10 shows the example of using the momentum filter as a high pass filter. The photon energy is 20.8 eV. The sample is HOPG. The TOF spectrum and the momentum space image is shown in (a) and (b). The TOF spectrum in (a) doesn't fit in the time of flight window. it wraps around and makes a background doesn't go to zero. Fig (b) looks like a blob in the k space because most electron hitting the detector is secondary electron, due to the chromatic aberration, these low energy electron are not focused well at all when the zoom lenses are set up to image the electrons near the Fermi edge. With the contrast aperture holder, the TOF spectrum and the momentum space image is shown in (c) and (d). The momentum filter effective cut the low energy electrons and the secondary electron tail in the TOF spectrum is

chopped off, so TOF spectrum is not wrapped any more. A clean TOF spectrum is observed. The majority of electrons hitting on the detector are still low energy electrons, so the integrated momentum space image doesn't show a sharp cutting edge. But now the high energy electron are not overlapping with low energy electrons in time. The momentum image at certain time of flight can be retrieved. The momentum filter can be easily combined with the potential bump filter mentioned before, the combination can effectively improve the extinction ratio of the pump produced electrons thus helps reduced the background counts induced by pump pulses. This is critical for improving the signal to noise ratio in the pump/probe experiments.

8.8 Energy resolution

The energy resolution is a critical aspect in many ARPES experiments. In the time of flight experiments, the electrons with different kinetic energy are dispersed in time. The energy resolution of TOF spectrometer is mainly up to two factors, the total time span and the time resolution. Mathematically, the electron flight time τ going over a TOF tube of length L with drift energy E_d is given by Equ. (8.1)

$$\tau = L\sqrt{\frac{m_e}{2E_d}} \tag{8.1}$$

where m_e is the mass of electron. and the energy resolution ΔE is given by Equ (8.2)

$$\Delta E = 2\frac{1}{L}\sqrt{\frac{2E_d^3}{m_e}}\Delta\tau \tag{8.2}$$

where $\Delta\tau$ is the time resolution of the delay line detector. From this equation, we can see the drift energy strongly affects the energy resolution. The lowest drift energy we can possibly use is determined by filling the time interval between two pulses with the desired TOF spectrum. The energy relution can be understood in a easier way. At 83 MHz, the time interval is about 12 ns. Our time resolution is about 220 ps. The TOF spectrum can be understood as a histogram, and the bin width is the time resolution of DLD. Total number of bins is about 12 ns/220 ps=55. And the energy resolution is the overall energy span divided by the bin number. For example, with 25

eV photon energy, the electron energy span is about 20 eV, then the best energy resolution is 20 eV/55=360 meV. This energy resolution is achieved by adjust the drift energy so the TOF spectrum fills the entire time interval of 12 ns.

In order to achieve a moderate energy resolution such as 100 meV at 88 MHz rep rate, we need be able to narrow the total energy span in the experiments. This can be done with high pass filter mentioned before.

Besides cut the energy span with high pass filter, the other way to improve the energy resolution is to make the time interval longer. The can be possibly done in two ways. One is to drop the rep rate of the XUV source. It has been demonstrated that a 18.4 MHz cavity enhanced high harmonic generation can be used in photoemission measurements [299]. The other way is to pick the electron pulses instead of the light source by using high speed electron deflector built in the TOF k-mic [300]. The method is more flexible and the rep rate can be adjusted easily as needed.

8.9 Real space imaging

The TOF k-mic can operate in the real space imaging mode just like PEEM. The spatial resolved photoemission spectroscopy can be implemented in this mode. This is potentially useful for study of small area samples. For example, a single domain crystal with μm size. In our experiments, real space imaging is also useful for k-mic setup and diagnostic purpose. Imaging spatial feature of the sample and field aperture grid allows us to easily check whether the cathode lens and the downstream optics are correctly set up. To do ARPES experiment, we also usually start with real space imaging, then derive the k-space setting from real space. It is also useful for locating the XUV spot and measuring XUV spot size. In the pump probe experiments, it is a very convinient way to check pump/probe overlap. The field of view is typically less than half a milimeter and the magnification can be as big as 200, giving a nominal resolution of 80 μm/400=400 nm.

Due to work function contrast, photon energy for near threshold excitation, for example 6 eV lamp, is good for high imaging contrast. we have found that the 2PPE of 2.4 eV femtosecond pulses which is used as the pump laser for our current pump probe experiments, also provides similar imaging contrast. Compared to the lamp, such a laser beam can be easily delivered to the sample and its power can be easily controlled by the optics, it is con-

venient to use. In our experiments, We routinely use the pump beam for diagonal purpose.

A chess board sample is used to test the real space imaging as shown in Fig. 8.11 (a). The measurement is done with 2PPE of the green femtosecond pulse as the light source. The images has a field of view of 160 μm. The

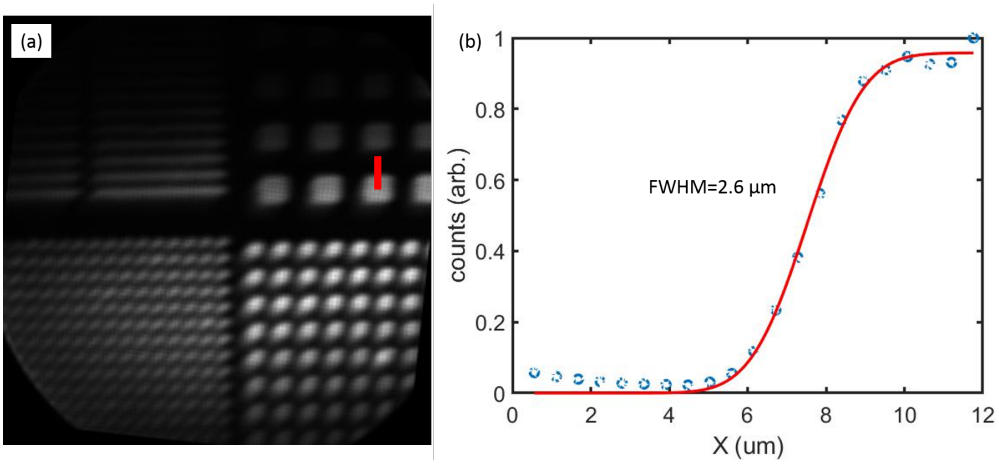

Figure 8.11: (a) Chess board pattern imaged by the TOF k-mic in real space imaging mode. (b) Line out of the red line in (a).

magnification is about 200. Fig. 8.11. The smallest square array on the image is 3μm $\times$ 3μm. we can clearly resolved the square array but with significant blurring. (b) shows the line out of the red line in (a). The fitting gives a FWHM of 2.6 μm. A real space imaging resolution of 300 nm has been reported [243]. The reason for the blurring is probably that the sample is tilted and our current sample manipulator can't fully correct the sample tilt and sample vibration especially in the vertical direction. As will be mentioned in section 8.11, the hexapod sample manipulator can easily solve the sample tilt problem.

8.10 Momentum space imaging

Momentum space imaging mode is mainly used for ARPES experiments. As mentioned before, it works by imaging the reciprocal image formed at back focal plane to the delay line detector. The momentum resolution of 0.01 $\mathring{A}^{-1}$ has been reported [16]. Thank to the time of flight configuration, k_x and k_y

2D momentum map can be recorded with high data rate. However, due to the chromatic aberration, usually less than 5 eV energy span can be imaged with acceptable resolution.

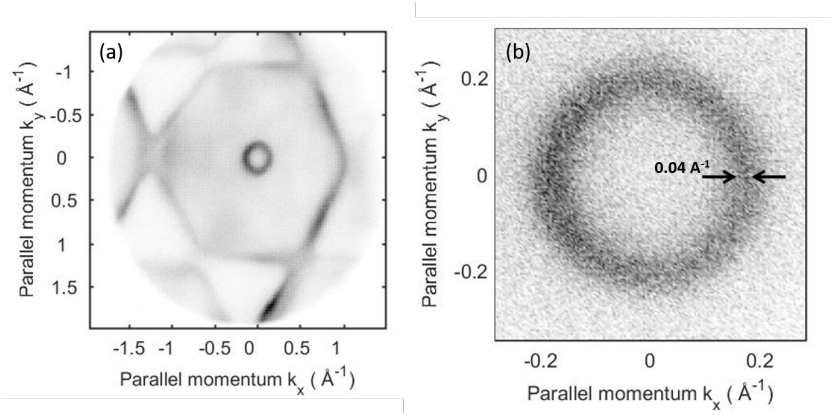

Figure 8.12: (a) Fermi surface of Au (111) over a full brillouin zone. (b) Fermi surface of the shockley surface state zoomed in.

We demonstrate the momentum space imaging of TOF k-mic by ARPES of Au(111) Fermi surface. The experiment is done with 18 eV photon energy. High pass filter is set up so the energy span is 0.73 eV. This narrow energy span can in principle give us the energy resolution of < 15 meV. The measurements are done in room temperature so the actual energy resolution is larger. The integration time of the data is 300 s. Fig. 8.12 (a) shows the Au (111) Fermi surface. The data is integrated over a energy range of 67 meV. We can see the high quality ARPES data with momentum range covering the brillouin zone. The circle in the center is the well know Shockley surface state. Then we zoom in the Shockley surface state by changing the magnification of second retarding stage. The result is shown in Fig. 8.12 (b). Fig. 8.12 (b) is binned over 38 meV energy range. More than 10^4 momentum pixels are included in this image. The FWHM of the ring is 0.04 $\mathring{A}^{-1}$. Because the measurement is done in the room temperature, the momentum resolution is limited by our energy resolution.

Fig. 8.13 shows the ARPES measurement of the gold band structure. The measurement is done with 10.8 eV photon energy in the room temperature. No high pass filter is used. The dispersion relation of the schockley surface state and the d-band can be clearly seen.

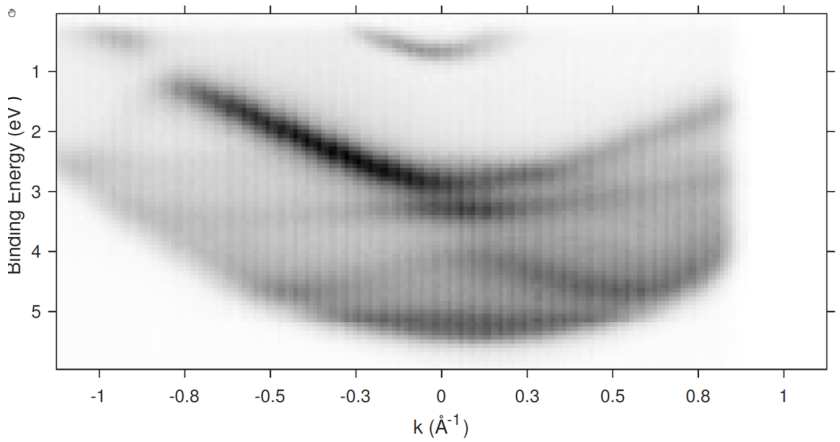

Figure 8.13: The band structure of Au (111) surface measured by 10.8 eV photon energy.

8.11 In progress

In the near future, we will install a hexapod sample manipulator. As the sample is part of the cathode lens, the mechanical alignment with respect to the electron optical axis is critical for the performance of the electron optical system. Our current rod style sample manipulator doesn't have the degree of freedom to correct the sample tilt in the vertical direction. Moreover, because a long dewar is built in the rod, the temperature change of the dewar due to liquid nitrogen evaporation can cause enough sample position change and affect the ARPES measurements. The sample vibration due to the long rod is a concern as well. Soon, we will adopt a hexapod manipulator shown in Fig. 8.14. It provides alignment in six degrees of freedom, which is enough to correct any sample misalignment. A commercial helium continuous flow cryostat was connected directly with the sample mount and is moved together with the sample. Sample can be cool without worrying about the misalignment caused by the thermal effects.

Figure 8.14: A photo of the hexapod sample manipulator.

Chapter 9

Towards spatial-, time- and angle- resolved photoemission

9.1 Introduction

ARPES and tr-ARPES are powerful tools to investigate the band structure of the materials. Important characteristics of materials can be measured such as electron effective mass, Fermi velocity, the energy band structure, doping, and many-body effects. In ARPES experiments, a typical beam spot size in the synchrotron light source is about a few hundred micrometers. The measurement result is an average of the material over the beam spot. The typical sample used for ARPES is a single crystal. However, for many interesting materials, growth of a few hundred micrometer single crystal is hard [41]. The measurements averaging over large areas of inhomogeneous samples can blur and even completely miss the desired feature. In such cases, the capability of spatially resolving the sample is required in the ARPES experiment on the inhomogeneous sample.

As mentioned in section 1.2.1, for the spatial resolved ARPES implemented with PEEM and field aperture, the data rate scales inversely with the beam spot area. In other words, the data rate C in spatial resolved ARPES scales with the sample current density instead of sample current.

$$C \sim \frac{I_{sample}}{D^2} \tag{9.1}$$

where D is the beam spot diameter. Then as mentioned in section 1.3, the sample current I_{sample} scales with the rep rate f_{rep} and the beam spot

diameter D due to space charge effects

$$I_{sample} \sim f_{rep} D \tag{9.2}$$

Then the net result is the data rate C scales with rep rate and inversely with beam spot diameter.

$$C \sim \frac{f_{rep}}{D} \tag{9.3}$$

For the space charge limited low rep rate ARPES experiments, the beam spot has to be big in order to allievate the space charge effects. However, the big spot size as well as the low rep rate reduced the data rate in spatial resolved ARPES. Thanks to the high rep rate of our XUV source, we are not space charge limited. The beam spot size is only limited by the aberration of the XUV optics. We not only produce sample current orders of magnitude higher but also use a smaller beam spot size, leading to additional improvement in the current density. Plus the highly parallel detection capability of TOF k-mic boosts our data rate further. The unprecedentedly high data rate us to afford the data rate loss due caused by field aperture.

Two-dimensional (2D) materials [301] including graphene, transition metal dichalcogenides (TMDCs) and 2D heterostructures are important class of materials due to their potential application for future electronic, photonic and spintronic devices [302]. The common features of this group of materials are their extremely small thickness, typically a few atomic layers, with strong in-plane bonds and weak interlayer bonds. Their properties are versatile, covering the complete range of electrical proprieties from superconducting to insulating.

The preparation methods of 2D material include Chemical Vapor Deposition (CVD), Physical Vapor Deposition (PVD) , and mechanical exfoliation [303]. The latter is widely used in the lab environment, because it is simple, easy, and prepared 2D materials are of high quality. It can be applied to most 2D materials because it is possible as long as small bulk pieces of a material are produced. Importantly, it is the main technique to form 2D heterostructures. But it is difficult to thin down the material to a single layer homogenously. The single domain of the exfoliated flakes typically have the dimensions of a few micrometers.

Highly ordered pyrolytic graphite (HOPG) is used in our first demonstration experiments. The diameters of the individual crystallites in HOPG are typically in the range from 1 to 10 μm. We are working towards the spatial-, time- and angle- resolved photoemission spectroscopy on HOPG sample.

9.2 ARPES on the single domain of HOPG

The sample is ZYA grade HOPG purchased from Momentive Performance. The size of the sample is 12 mm × 12 mm. The sample is mounted to a standard Omicron sample plate. Then it is cleaved in the air by the scotch tape method. The sample is held by a rod style manipulator as mentioned in chapter 8. It is outgassed at the temperature of 900 K for an hour. The experiments are done at room temperature. The chamber pressure is below 3×10^{-9} Torr during the experiments. 25.2 eV XUV pulses are used for the measurements. The momentum range of the 25.2 eV photon can probe is $> 2.2\ \mathring{A}^{-1}$. That's enough to cover the whole brillouin zone of the graphite. The extractor voltage of the k-mic is set to 5 kV, lower than 8 kV we typically use. The reason is the field emission problem when using this sample with k-mic. The high extractor voltage causes less aberration to the image. However, compared to the gold or silver, HOPG has a much stronger field emission. The extractor power supply already has a current load about 50 μA when running at 5 kV compared to tens of nA in the normal condition. The electrons hitting the DLD due to field emission is on the order of 10^4 counts per second. The power dissipation in the vacuum and the background counts start to be the problem. So we used 5kV for the extractor voltage. The zoom optics is adjusted so the maximum magnification of the momentum space is achieved without of electron clipping on the DLD. The MCP front is used as the high pass filter. The sample voltage is held at 20 V. MCP front voltage is set to 3 V. This setting gives a energy span of 11 eV. The energy resolution estimated by the time pixel binning is about 0.2 eV.

In order to conduct the ARPES on a single domain of HOPG, a field aperture is used to crop a 5 μm diameter area on the sample. The Fermi surface of the HOPG sample with and without the field aperture is shown in Fig. 9.1. In Fig. 9.1 (a), no field aperture is used, with the XUV spot size of about 100 μm, about 3 domains are observed. The count rate of the measurement is about 3 Mcps, which is basically close the upper limit of the DLD. We still have to attenuate our light source to prevent detector saturation. The integration time is one minute. In Fig. 9.1 (b), the field aperture is used to select 5 μm area on the sample, this drops the count rate by three orders of magnitude. The data rate in this case is limited by the photon flux. The count rate of the measurement is on the order of 10^4 cps. However, the field aperture also get rid of most field emission electrons, so this measurement has a cleaner background. The data has a integration time

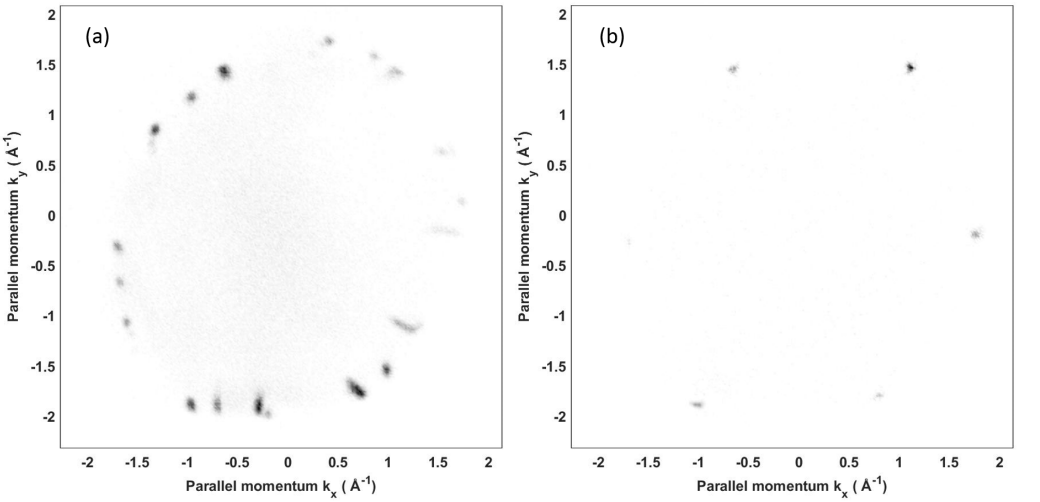

Figure 9.1: Fermi surface of HOPG sample (a) without any field aperture and (b) 5 μm sample area is selected by a field aperture.

of 20 min. Instead of multiple domains, 6 Dirac points with six fold symmetry are clearly seen. With the field aperture, we can select small enough sample area so the single domain ARPES is performed.

Fig. 9.2 shows the momentum map v.s. the binding energy of a single domain HOPG. Since the energy resolution is 0.2 eV in this measurement, we step up the binding energy in 0.2 eV step. We can see that the cross section of the Dirac cone grows bigger as the energy cuts deeper on the Dirac cone.

9.3 Time- and angle- resolve photoemission on HOPG

First we start with tr-ARPES without sample area selection. So the results is on multiple sample domains. This gives us faster data acquisition speed. In the pump/probe experiments, P-polarized 515 nm pulses generated by SHG as mentioned in section 2.4 are used as pump light. The pump beam has a spot size of 130 μm by 55 μm on the sample. Part of the reason for such a long beam is that the incident angle of the pulse light at sample is 45°. The 2.4 eV pump photon energy excites the electrons 1.2 eV below the Fermi level

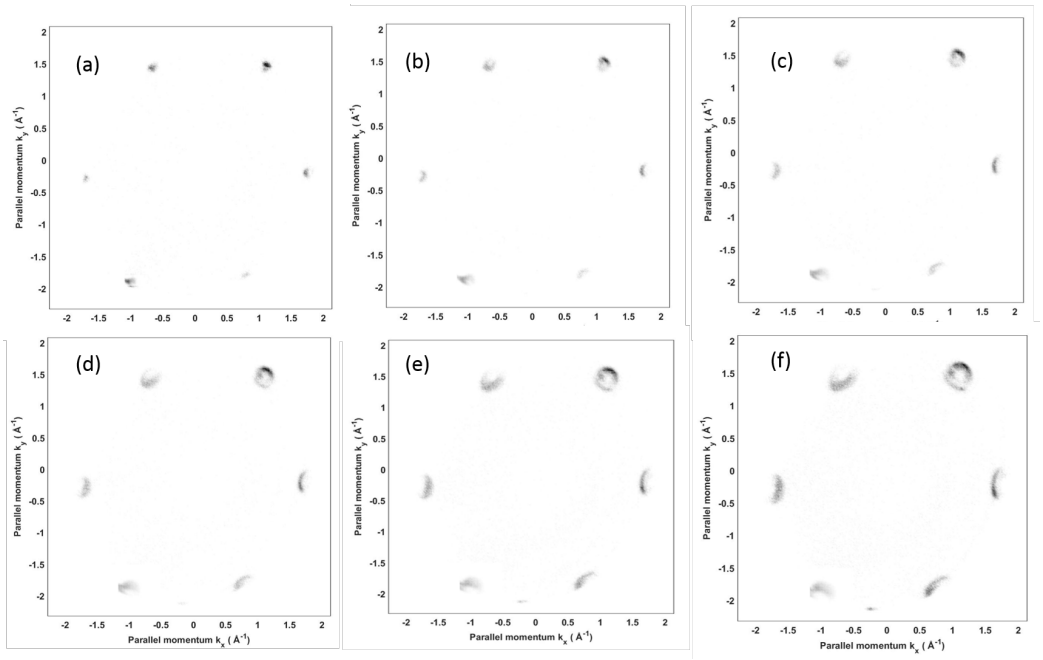

Figure 9.2: The momentum map of a single domain HOPG v.s. the binding energy (a) 0.2 eV (b) 0.4 eV (c) 0.6 eV (d) 0.8 eV (e) 1.0 eV (f) 1.2 eV.

to 1.2 eV above the Fermi level by the direct transition. The same setting as the previous section is used. The pump fluence in the measurements is about 200 μJ/cm^2.

The EDC with and without the pump light at zero time delay is shown in Fig. 9.3 (a). The signal is integrated over the whole momentum range. The electron counts are normalized to the maximum of the curves. The count rate is about 3 Mcps. The integration time of each curve is 1 minute. Fig. 9.3 (b) shows the difference of pump on and pump off in (a). The blue curve means positive difference and the black curve means negative difference. The excitation spans from the Fermi edge up to 1.2 eV above the Fermi edge, which is maximum that the pump light can reach. The higher energy part goes to zero within the error bar. The amplitude of the signal falls off as the energy increases, because the lifetime of the excitation gets shorter as the energy increases. We can see the change on the order of 10^{-4} with one minute integration time.

Fig 9.4 shows the momentum map of the Fermi surface at zero time

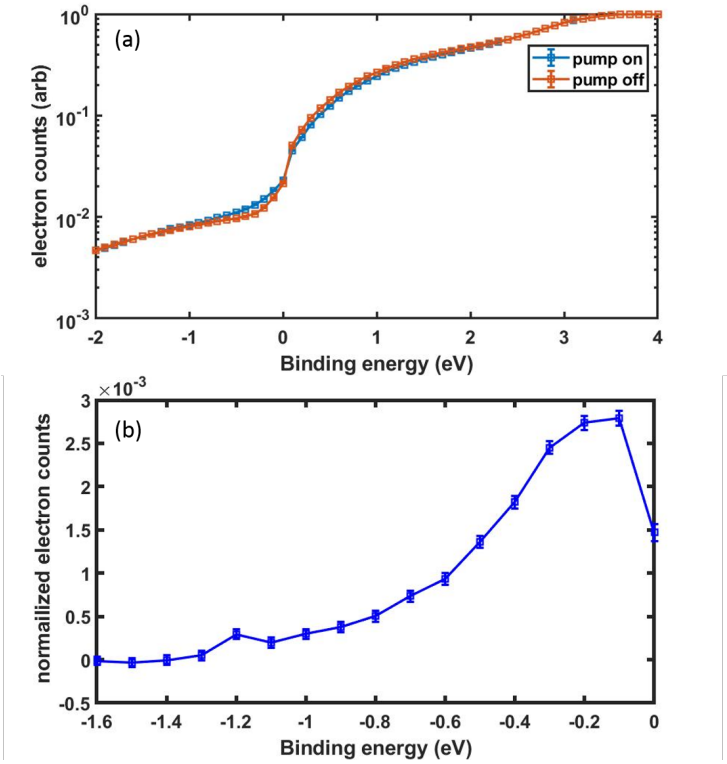

Figure 9.3: (a) EDC of HOPG sample with and without the pump light at zero time delay. (b) difference of the 2 curves in (a). The errorbar indicates the shot noise of electrons.

delay. The momentum map is the difference of pump on and pump off without any normalization. Due to the multiple domains are included in the region of interest, the multiple Dirac points show up. However, there are some background due to field emission smearing over the image and the subtraction of pump on/off doesn't completely get rid of it. Then we scan the the binding energy, the results are shown in Fig 9.5 (a) 0 eV relative to Fermi energy (b) -0.2 eV (c) -0.4 eV (d) -0.6 eV (e) -0.8 eV (f) -1.0 eV (g) -1.2 eV (h) -1.4 eV. In order to see the feature clearly, we crop the momentum range within the red circle on Fig 9.4 and The actual magnification of the k-mic setting is the same. As the energy goes up, the displacement of the excited population from the Dirac point gets bigger, as expected for a Dirac cone. At the binding energy of -1.4 eV, the pump induced features are gone

because the pump photon doesn't reach. Even it is a small part of the whole momentum range measured in the experiments, each image still has > 200 momentum pixels in this small momentum range. Thanks to our high data rate, the features are clearly resolved with just one minite integration time.

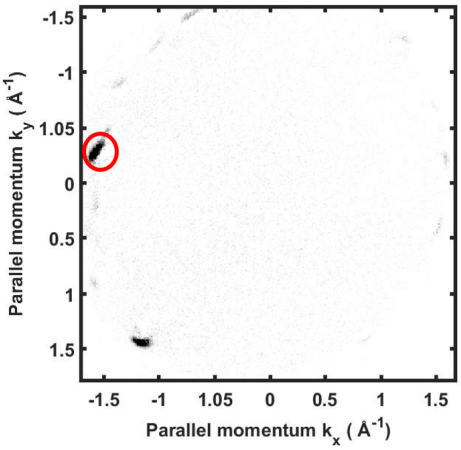

Figure 9.4: The Fermi surface of the HOPG sample with 200 μJ/cm^2 2.4 eV pump pulses. The integration time is 1 min. The momentum map is the difference of pump on and pump off without any normalization.

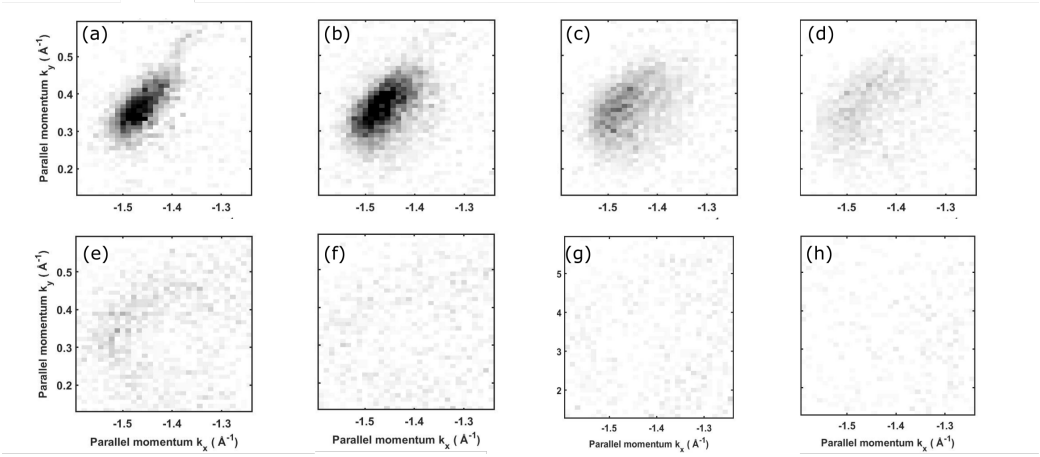

Figure 9.5: The momentum map zoomed in at the red circle in Fig. 9.4 with binding energy (a) 0 eV (b) -0.2 eV (c) -0.4 eV (d) -0.6 eV (e) -0.8 eV (f) -1.0 eV (g) -1.2 eV (h) -1.4 eV. The momentum map is the difference of pump on and pump off without any normalization.

Chapter 10

Conclusion and outlook

By using the combination of 80 MHz rep rate CE-HHG XUV source and TOF k-mic, we demonstrate an increase of the data rate in tr-ARPES experiments by approximately four orders of magnitude. The high rep rate enables experiments to be done with approximately 2 orders of magnitude higher sample current than conventional setups, as detailed in the introduction chapter and Ref. [9]. and the TOF k-mic with high electron collection efficiency and highly parallel detection capability gives another two orders of magnitude boost according to the analysis of Ref. [20].

With a hemispherical energy analyzer, we benchmarked the performance of the instrument with LAPE study on Au(111) surface and we discovered the new electron dynamics of the HOMO orbital of the C_{60} film on Au(111). With the TOF k-mic, we have applied the instrument to the study the unoccupied states of HOPG sample, we are working towards the spatial-, time- and angle-resolved photoemission experiments on a single domain of HOPG.

In this chapter, I will talk about some experiments planned for the setup, the upgrades of the instrument for further improvement of its performance in the near future and the outlook for the future development of the ARPES techonology.

10.1 The plan for future experiments

10.1.1 Singlet fission of a pentacene film

Singlet fission [304] is a process where a high energy singlet exciton of the organic photovoltac, resultant from the absorption of a photon, is efficiently converted into two triplet excitons through a spin allowed process. Since it doubles the number of charge carriers, it has been proposed that singlet fission in organic photovoltaic devices could improve the photoconversion efficiencies [304, 305]

The singlet fission happens through a coupled triplet pair intermediate states which maintains electronic coherence between the two constituent triplets [306]. Extensive research has been done to study the nature of coupled triplet pair states in singlet fission process, as reviewed in Ref. [307], but it's still not clear yet. 2PPE studies [260, 308, 309, 310, 311] and quatum simulation [308, 310] shows that the binding energy of the coupled triplet states are very close to the separated triplet states. So it is hard to distinguish them simply by binding energy. It has been reported by Michael Ramsey and coworkers that for the planar organic molecules like pentacene, the electron momentum map can be directly interpreted as the Fourier transform of the molecular orbitals [26]. In tr-ARPES experiments, we propose to directly image the evolution of molecular orbitals of the excited electrons, particularly, the coherence decay of the coupled triplet states. The wavefunction of the coupled triplet pair, Ψ, is the combination of the uncoupled states Ψ_1 and Ψ_2 as shown in Equ. (10.1).

$$|\Psi>=\frac{1}{\sqrt{2}}\left(|\Psi_1>+e^{i\phi(t)}|\Psi_2>\right) \tag{10.1}$$

where $\phi(t)$ is the relative phase between the two molecular orbitals. For a coherent triplet pair, there is a defined phase relationship $\phi(t)$, which corresponds to a pure state while for the uncoupled triplets, the phase is random which is a mixed state. Due to the coherence, the two molecular orbitals can interfere with each other like two optical waves. In momentum space, this interference shows up as the modulation or fringes on the wavefunction envelope. The evolution of the coupled triplet states can be easily monitored by watching the interference fringes decay.

Our TOF k-mic can simutaneouly take the 2D momentum map thus is very suitable for this study. Tens of Megahertz sources works with this

experiment very well [260]. The sample will be a pentacene crystal grown on Cu(110) substrate, the C_{60} will be used as electron acceptor material. So this is also a extension of the C_{60} experiment.

10.1.2 Photocatalytic reaction on TiO_2 surface

Heterogeneous catalytic reactions play a indispensable role in chemical and energy conversion, material and environmental protection. The photocatalytic reaction is a complicated process consisting of many elementary processes and spans over several order of magnitude timescales as discussed in section. 1.2. TiO_2 is one of the most extensively investigated metal oxides in semiconductor photocatalysis due to its relatively high efficiency, nontoxicity, low cost and high stability. However, the lifetime of conduction band (CB) electron is still under debate, the reported values in the literature differ orders of magnitude from picosecond to microsecond [312, 313, 314, 315, 316]. tr-ARPES studies on Ti(110) crystal surface, pertubatively excited, can monitor the CB electron dynamics of the catalyst. Moreover, with the superior data rate and signal to noise ratio, it is possible that we can directly observe the hole dynamics under perturbative excitation, by looking at the depletion of the valence band. Direct observation of electron and hole evolution in the momentum space can provide key insight to the underlying mechanism of photocatalysis.

Recently, M.G. White and coworkers from Stony Brook University observe the coverage dependent fractal-like kinetics of methyl radicals formation in substrate-induced photooxidation of acetone on a TiO_2(110) surface [317]. In their experiment, the high fluence (> 1 mJ/cm^2) UV pump light at 260nm is used to initiate carrier-induced fragmentation of adsorbed acetone on a TiO_2(110) surface that was pretreated with oxygen. The photoreaction results in the ejection of methyl radicals into the gas-phase that are detected by the probe pulse via resonant multiphoton ionization. The time dependent methyl radial yield at 0.1ML, 0.2 ML and 0.7 ML acetone coverage fits the fractal kinetics model very well at the known limiting values of 1/3 and 1/4. This key result suggest a mechanism for methyl formation that involves a low dimensional fractal network, which is attributed to the anisotropy of the TiO_2(110) surface structure and its effect on spatial ordering of adsorbed acetone species. The rate limiting process of methyl formation is the transport of energetic holes to reaction sites, e.g., a percolation network, and not the dynamics associated with fragmentation of the acetone species. This

fratal-like behavior is critical for the photooxidation reaction on surface.

For tr-ARPES experiments, we will start with the carrier dynamics of the TiO_2 substrate. tr-ARPES experiments on the adsorbed molecules in photocatalytic reaction is still technically challenging because the pump light induced reaction consumes the adsorbed molecules. For example, if each pump pulse excites a fraction of 10^{-4} acetone molecules, which turns into methyl by the chemical reaction. At our rep rate, all the acetone molecules will be depleted in less than 1 ms. Fast sample rastering combined with continuous dosing is required to perform these experiments.

10.1.3 Electron dynamics of 2D materials

2D materials have attracted great interest recently due to their potential application for future electronic, photonic and spintronic devices [302]. Their properties are versatile, covering the complete range of electrical proprieties from superconducting to insulating. Time resolved ARPES has been used in the study of electron relaxation pathways in 2D materials, for example, intervalley scattering of transition metal dichalcogenides(TMDCs) [318, 42]. But with the <100 kHz rep rate sources, the experiment is restricted to strongly excited regime [319], or long acquistion time [320]. We have been working on spatially resolved tr-ARPES on graphite as discussed in chapter 9. Recently, D. Jones and coworkers from the University of British Columbia reported directly extracting the electron-phonon coupling strength on single crystal graphite by time- and angle-resolved photoemission spectroscopy with CE-HHG XUV source at 25 eV [321]. The pump fluence <10 $\mu J/cm^2$ is demonstrated [322]. With our tunable XUV source and TOF k-mic detector, we believe that we can investigate the electron dynamics of 2D material in greater detail and faster data rate, enabling even lower pump fluence. In many of 2D materials, most of the interesting electronic structure features and dynamics after photoexcitation occur at the edge of the Brillouin zone, the 2PPE experiment can't be used in these studies due to limited momentum range of low photon energy.

The spin orbital coupling plays an important role in the property of 2D material. For example, One important feature of the semiconductor TMDCs such as WSe_2 is their band structure around the K points which is composed by two spin-polarized branches due to the strong spin-orbit interaction originating from the transition metal ions d-orbitals [323]. The time-reversal symmetry leads a spin-valley locking relationship [324] which means the spin

and momentum of the electrons are strongly coupled. The Spin resolved ARPES and spin resolve tr-ARPES is powerful tool to study the electron scattering between the spin-polarized bands. However, the data rate of the spin resolved ARPES is challenging. The electron spin filter works by the spin-dependent reflectivity of electrons due to spin-orbit coupling in the solid state scattering target. This scattering process is very lossy and reduces the data rate by orders of magnitude.

A novel multichannel spin detector can be conveniently implemented with TOF k-mic [325]. The multichannel spin detection is base on preserving a two-dimensional electron distribution in the spin-polarized low-energy electron diffraction process. The spin filter is implemented in the TOF k-mic as a W(100) crystal located in the end of 2nd restarding stage where 2nd gaussian image forms and the spin filter crystal is used in specular geometry deflecting the electrons by 90 degree. The conservation of the electron momentum component parallel to the crystal surface, guarantees a transfer of the two-dimensional lateral image information that is encoded in the scattering coordinates and angle. Then TOF spectrometer is used to record momentum map and time of flight data. This scheme improves the efficiency of spin detection by 4 orders of magnitude [243].

With our unprecedented data rate, we can attempt spin resolved time resolved ARPES on TMDCs materials in pertubatively excited regime. The research will elucidate the electron dynamics of spin-polarized bands of TMDCs.

10.2 Future upgrades of the tr-ARPES instrument

In order to further improve the performance of our tr-ARPES instrument, several upgrades will be done in the near future.

- The hexapod sample manipulator. As discussed in section 8.11. the hexpod sample manipulator will provide reliable sample cooling and sample alignment.
- Grid-based high pass filter. MCP detection efficiency is reduced when it is used as the high pass filter as mentioned in section 8.7. Using the grid-based high pass filter can solve this problem.

- Lock in detection at half the rep rate. As discussed in section 8.3, lock in detection at half the rep rate can effectively cancel the noise and drift such as electron caused by field emission. This requires the pump pulse picker as discussed in section 10.2.1.

- High frequency (HF) electron deflector. Our measurements of the photon linewidth as discussed in section 6.2 is limited by the energy resolution of our previous hemispherical energy analyzer. The energy resolution of the TOF k-mic is demonstrated to be 19 meV [16]. To achieve high energy resolution, >50 ns electron flight time is favorable which is longer than our 12 ns interval between pulses due to our high rep rate. As discussed in section 8.8, this can be done with HF electron deflector as demonstrated in Ref. [300]. The HF deflector is complemented with two pinholes in two additional beam crossovers and 2 pairs of deflector electrodes placed in between. The deflector electrodes are driven by 20 GHz RF supply with up to 20 V amplitude. The complete extinction of the adjacent pulses is demonstrated in 100 MHz synchrotron light source.

- Fully integrated software. Currently our high voltage power supply, DLD, photon flux monitor and motors are on their own separate software. We need to manually click on each software which is time consuming and inconvenient. Besides instrument control, handling the large amount of data generated in tr-ARPES experiment is a challenge [326]. tr-ARPES experiment generates (k_x, k_y, E, t) 4 dimensional data where E is the electron kinetic energy related to the time of flight and t is the time delay between pump and probe pulses. The data is typically stored as a set of 2D momentum images, each of the image has $> 10^5$ pixels. In some of our experiments, total data file size on the order of 10 GB is generated within half an hour. How to process this kind of big data is a challenge. More than that, visualization of the band structure features are of great importance for understanding the momentum space electronic structure and dynamics. In addition to the large amount of data, the contrast of the data is also a concern [326]. For example, the intensity difference between the ground states and the excited states can be 3 orders of magnitude or more in pertubatively excited tr-ARPES. We are currently working on developing a fully integrated software which directly talk to different parts of

the instrument and also can do quick data analysis and visualization. This software will simplify the operation and accelerate the tr-ARPES experiments.

10.2.1 Design of pump pulse picker

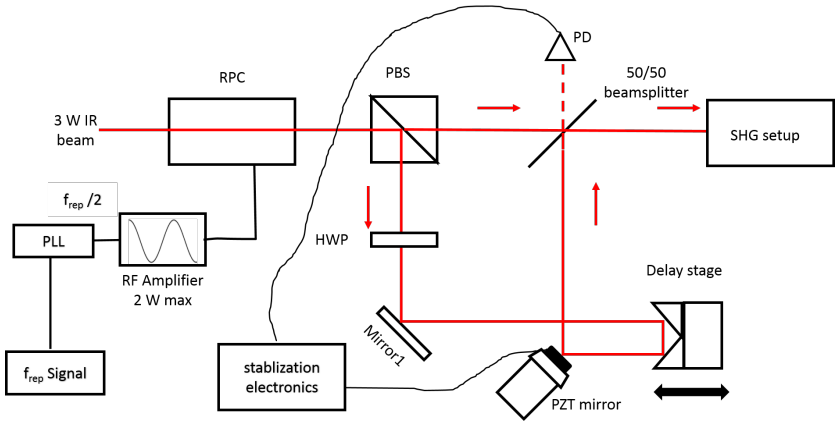

Figure 10.1: The design of the pump pulse picker. RPC= resonantly driven pockels cell PBS=polarization beam splitter PD=photodiode HWP= half waveplate PLL= phase locked loop.

To the pump pulse picker enables the lock in detection at half the rep rate and allows longer sample relaxation time. However, selection of femtosecond pulses at tens of Megahertz and a few watts average power is technically challenging. The traditional AOM pulse picker requires the beam to be focused to a small spot in order to achieve fast enough speed [96]. The small spot cause potential damaging issues. Our pulse picker is based on resonantly driven pockels cell as shown in Fig. 10.1. The power of the incoming IR beam is restricted to be < 3 W to prevent pockels cell damage. The resonantly driven pockels cell (RPC) is purchased from Quantum Technology, which has a built-in tank-circuit resonant at $f_{rep}/2$. The $f_{rep}/2$ signal can be derived from a phase locked loop and share the photodiode generating the TOF k-mic trigger as mentioned in section 8.4.1. A RF amplifier will be used to drive the pockels cell. IR beam will change its polarization every other pulse. Then the IR goes through a polarization beam splitter and we obtain two sets of $f_{rep}/2$ pulse train. Then we make them colinear polarization by a half wave

plate and combine the two pulse trains with a MachZehnder interferometer. A PZT mirror is used to generate the error signal and stabilize the path length. A delay stage is used to compensated the time delay between the two arms. By doing this, we obtain the $f_{rep}/2$ pulses with doubled pulse energy and without losing the average power, which improves the conversion efficiency of the down stream nonlinear optical conversion stage.

10.3 An outlook for future ARPES technology

10.3.1 Single pass HHG with high power femtosecond laser

Because the high average power on the order of kW is required for efficient high harmonic generation at tens of Megahertz rep rate, it is first realized by CE-HHG. However, CE-HHG has drawbacks such as high photon energy XUV output coupling and difficulty of generating isolated attosecond pulses. Thanks to the rapid development of the high power laser technology, the average power of femtosecond lasers based on based on ytterbium-doped gain media has been approaching kilowatt range for example, Innoslab lasers [327], thin disk lasers [328] and fiber lasers [329].

For fiber lasers, tremendous improvements have been made in the average power, pulse energy and peak power over the last few decades. The average powers over 3 kW [329, 330] and pulse energies of up to 2.2 mJ [331] has been demonstrated. However, modal instabilities which is a threshold-like degradation of the beam quality above a certain average power value constrains further power scaling of a single fiber amplifier [332]. As a result, the coherent combination of multiple parallel fiber amplifiers has been the major path of power scaling. In order to realize the coherent combination of multiple amplifier, the path lengths in the channels need to be matched with sub-wavelength precision, differences between dispersion and nonlinear effects in the the parallel amplifier channels limits combination efficiency [333]. So far, systems comprising four parallel main amplifiers delivering gigawatt peak powers and average powers of more than 3.5 kW have been demonstrated [330, 334], as well as peak powers of up to 22 GW [335]. In some sense, cavity enhanced high harmonic generation can be understood

as the coherent combination one laser with itself for a few hundred times which reduces the system complexity and costs.

Some progress has been made applying these lasers to HHG. In order to generate HHG efficiently, spectrum broadening and the pulse compression by propagating in large mode area (LMA) fibers [336] or gas filled capillaries [337, 338, 339] is usually needed. Although short IR pulses can generate short XUV pulses, the photon linewidth is inevitably broadened. HHG with > 100 μW between 25 eV and 33 eV at 600 kHz is demonstrated [340] as well as the 600 kHz isolated attosecond pulses by OPCPA system pumped by short pulse fiber lasers [338]. HHG with frequency doubled Yb fiber laser is capable of delivering > 800 μW at 21.7 eV at 120 kHz due to better single atom response [341], while stable operation of CE-HHG with the same wavelength is not achieved yet [342].

Besides fiber lasers, Innoslab lasers and thin disk lasers are also competitive technology for high rep rate HHG due to its excellent capability of power scaling, heat management and high beam quality. Compared to the fiber laser, the bandwidth of the gain media is much narrower. The pulse duration of this Innoslab lasers and thin disk lasers is typical a few hundred fs [343]. Further spectrum broadening and pulse compression is needed. HHG at at 20.8 MHz rep rate is demonstrated with a Innoslab laser, although the highest power of the harmonics is only 1 nW [336]. Ref. [344] reports 500 kHz time resolved ARPES facility based on a Innoslab laser pumped optical parametric chirp pulse amplifier (OPCPA). Photon flux on the order of 10^{12} γ/s at 21.7 eV is generated at the nozzle and 10^{11} γ/s is delivered to the sample. However, due to the low rep rate, the sample current has to be attenuated to 130 pA in order to mitigate the space charge effects. Another interesting attempt is direct HHG inside the thin disk laser cavity [67, 345], however the photon flux and the photon energy is far from enough for practical tr-ARPES experiments.

In addition to the gas phase HHG, solid state high harmonic generation [346] is also emerging as a promising route to compact ultrafast XUV light sources. By HHG in solids, photon energies up to 30 eV can be generated with an intensity $10-100$ times lower than comparable HHG in gases [347]. At these reduced intensities, HHG at MHz rates becomes feasible. In an initial demonstration, a conventional Ti:sapphire oscillator with a repetition rate of 75 MHz has been converted to up to 20 eV harmonics in a single pass through sapphire nanocones coated with Au film [348], the photon flux of the highest harmonic is on the order of 10^6 γ/s. Recently, Ref. [349] reports

76 MHz HHG in solids with photon energies up to 11 eV generated by a femtosecond Cr:ZnS laser operating at 2−3 μm, The highest flux is on the order of 10^8 γ/s. Although HHG in solids allows high rep rate XUV with lower average power, the conversion efficiency and the photon flux of HHG in solids is still orders of magnitude lower than gas phase, limited by sample damage. Its microscopic mechanism is not clear yet.

Although the technology mentioned above looks promising, we believe the CE-HHG will have its place in the future for several reasons. First, the attainable average power and rep rate of CE-HHG is still orders of magnitude higher. As discussed in section 1.6.4, the average power of 10 kW and the rep rate of hundreds of MHz have been demonstrated. Second, CE-HHG source has the advantage of the cost and complexity. The structure of high power lasers including coherently combined fiber lasers, Innoslab lasers and thin disk laser is highly complicated compared to the enhancement cavity whose major components is several cavity mirrors and few simple optics. Third, the narrow photon linewidth of CE-HHG. In order to improve the conversion efficiency, short pulses have to be used in single pass HHG, while in CE-HHG, the low conversion efficiency of the fairly long pulses on the order of 100 fs is compensated by the passive amplification of the cavity, plus the fact that CE-HHG is free of ionization gating due to the constrain of the cavity, this leads XUV sources with much narrow photon linewidth.

10.3.2 Direct electron detection

In this thesis, I have described substantial progress on both light sources and energy analyzers for tr-ARPES. Currently, one bottleneck of the performance of our tr-ARPES instrument is the attainable count rate of the micro-channel plate (MCP) based delay line detector (DLD). This detector provides adequate time (220 ps) and spatial (80 μm) resolution for recording high-resolution ARPES data, but it has two major limitations. First, the quantum efficiency (fraction of incident particles detected) of the detector is limited to ∼50 % by the MCP. Second, and more critical, is that the electron count rate the detector can handle is limited to a few MHz by both the MCP and the delay-line method. For comparison, we can generate $> 10^{10}$ photoelectrons/second at the sample. Both these limitations impose technical challenges to the experiments and require compromises to be made on the momentum microscope performance and the samples that can be studied. An electron detector with close to 100% quantum efficiency, GHz count

rates, time resolution in tens of picosend and spatial resolutions in the tens of microns is highly desirable.

A novel type of silicon electron detection technology named low gain avalanche diode (LGAD) is a promising solution. The development of the LGAD technology was prompted by the need to time resolve the tremendous number of particle tracks emerging from the interaction regions, in future high energy physics experiments, to help reconstruct the position of the primary particle interaction [350]. The LGAD is based on simple diode fabricated on a thin p-type silicon substrate with the n^+ implant. Application of a reverse bias voltage creates an intense electric field in this superficial region, able to trigger avalanche multiplication for the electrons. The gain is kept low for low noise. The time resolution achievable on these devices has been measured to be in the order of 30 ps. The device concept is relatively new and is under intense development to maximize the sensor performance in the various conditions in which it can operate. The LGAD was originally conceived for the detection of high-energy charged particles, however it can also be used for the detection of low-energy electrons. For example, electrons at keV energies can be detected by LGAD developed by BNL [351]. The low energy electron has a shorter mean free path inside silicon. In order to improve the detection efficiency of the low energy electron, new LGAD with modified doping profiles needs to be developed so as to minimize the dead silicon thickness, similar to other direct electron detector architectures [352]

The Timepix camera [353, 354] is another competitive technology. The timepix camera uses a light sensitive silicon sensor bump bonded onto a Timepix chip [355]. The light sensitive silicon sensor can have up to 1024×1024 pixels, with each pixel in the sensor being connected to its own set of signal processing circuitry in the Timepix chip. When photons are absorbed by a pixel of the silicon sensor, the circuitry in Timepix chip accumulates the excited electrons in a capacitor, and if the accumulated charge exceeds a certain threshold then the pixel registers a hit. Using the fast internal clock within the chip, the pixel records the time at which the hit occurred, i.e. the Time of Arrival (ToA). Then, the capacitor is discharged at a constant rate, and the pixel records the length of time for which the charge in the capacitor remains above the threshold, i.e. the Time over Threshold (ToT). This value is proportional to the number of photons absorbed by the pixel. The 4D information including ToA, ToT, and the location of the pixel x,y is stored in the pixel until it's read out which happens at a much slower rate eg. 100 Hz. The timepix camera was originally design for 400 nm $-$ 1000

nm wavelength range. Now, the sensors with thin entrance window is also commercially available as CheeTah model which allows direct detection of several keV electrons. The newest version Timepix3 has a time resolution of 1.6 ns, which is still not fast enough for high resolution electron TOF spectrometer. The next version Timepix4 is expected to have a 200 ps time resolution, and it will be available in the market in a few years.

There are other novel silicon based detectors for direct electron detection. For example, back illuminated CCD sensors. By illuminating and collecting charge through the back surface, the photons can enter the back surface of the detector unobstructed, without having to pass through the silicon gate electrodes. Commercial back illumiated CCD sensors are capable of direct detection of <20 keV photons, for example iKon SO and Newton SO from Andor Technology. Another CMOS based technology is named monolithic active pixel sensor (MAPS), the working principle of MAPS is reviewed in Ref. [356]. Different from CCD, MAPS detector works for the electrons with tens of keV energy. The development of these electron detectors are driven by the development of high energy physics and electron cryo-microscopy (cryo-EM). They feature high quantum efficiency and low readout noise. However, they don't have the capability of recording the timing of the events. Further development is still needed for TOF electron spectrometer.

Appendix 11

Appendix

11.A High speed transimpedence amplifier

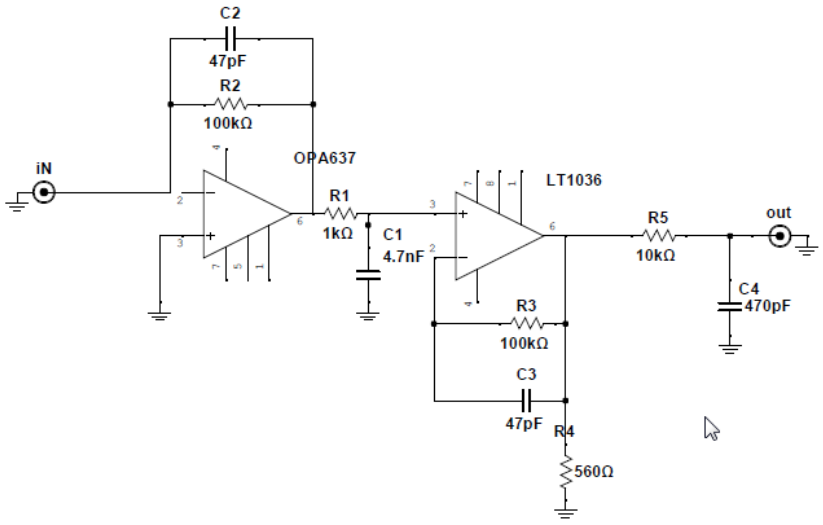

11.B Integrator

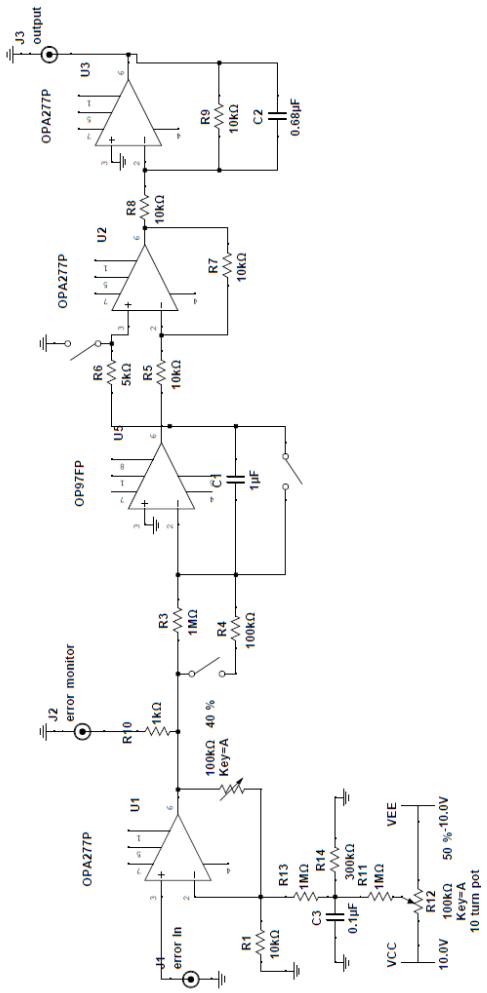

11.C Vacuum interlock

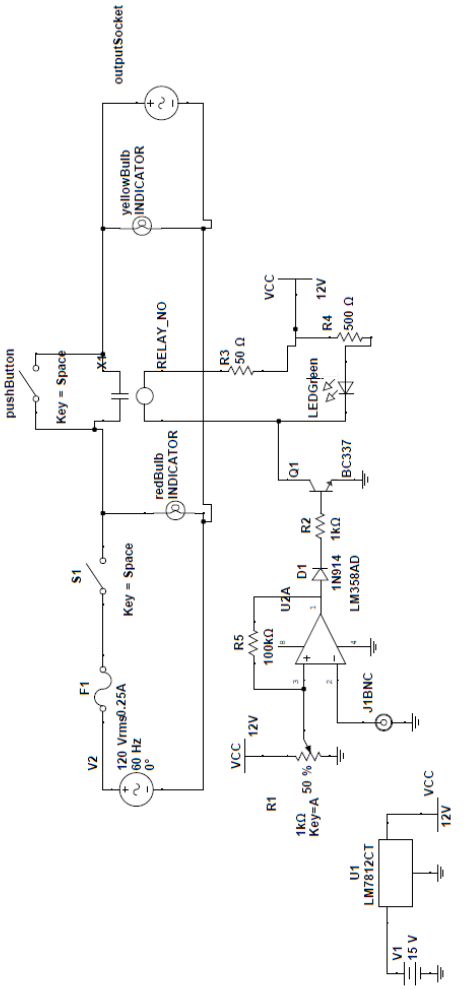

11.D Sample mount mechanical design

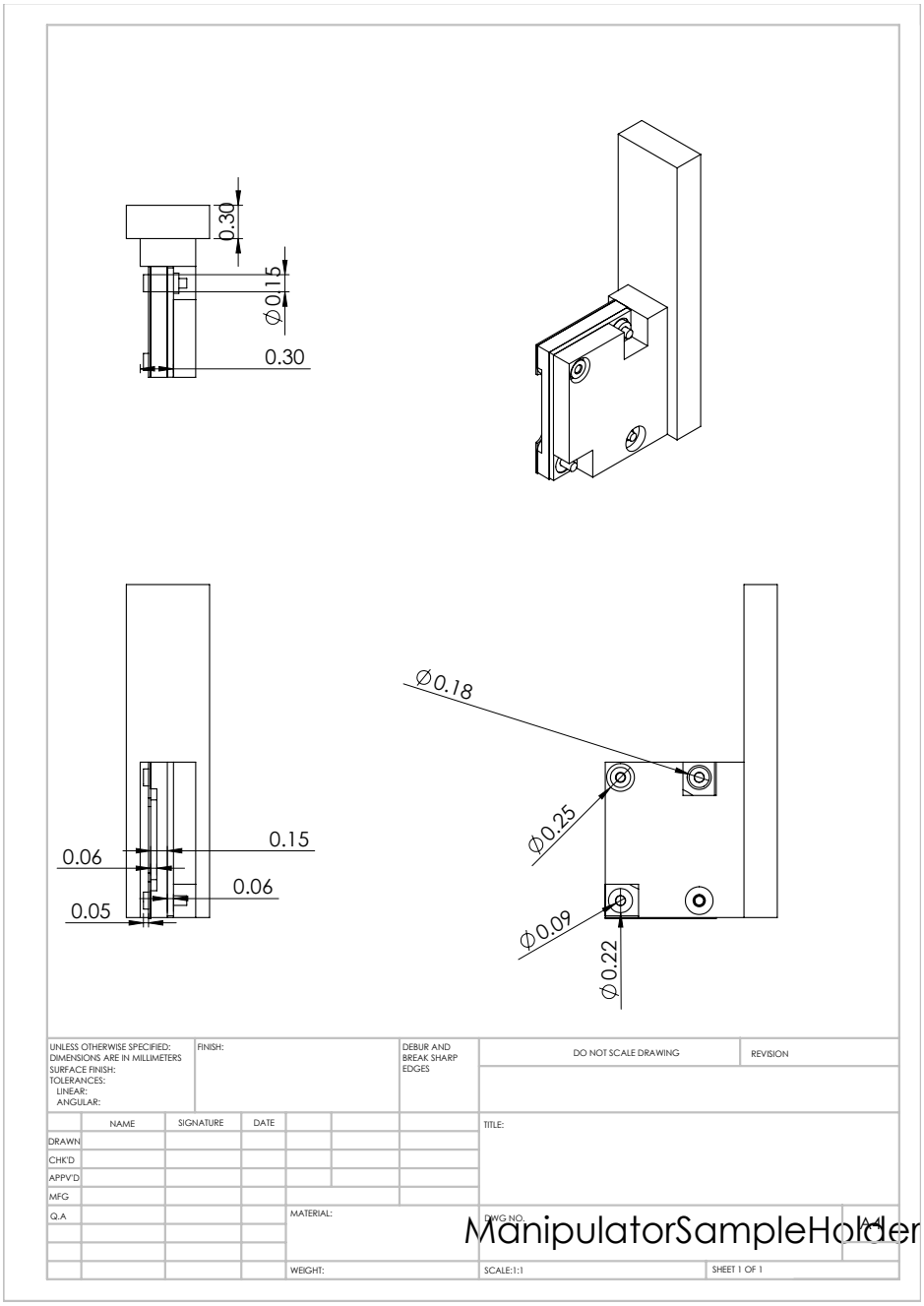

Bibliography

[1] Arthur K Mills, T J Hammond, Matthew H C Lam, and David J Jones. Xuv frequency combs via femtosecond enhancement cavities. *Journal of Physics B: Atomic, Molecular and Optical Physics*, 45(14):142001, 2012.

[2] Jan Heye Buss, Julian Maklar, Frederic Joucken, He Wang, Yiming Xu, Sung-Kwan Mo, Alessandra Lanzara, and Robert A. Kaindl. Ultrafast extreme-ultraviolet arpes studies of electronic dynamics in two-dimensional materials. *Proc. SPIE*, 10102:10102I–1, 2017.

[3] S. Eich, A. Stange, A. V. Carr, J. Urbancic, T. Popmintchev, M. Wiesenmayer, K. Jansen, A. Ruffing, S. Jakobs, T. Rohwer, S. Hellmann, C. Chen, P. Matyba, L. Kipp, K. Rossnagel, M. Bauer, M. M. Murnane, H. C. Kapteyn, S. Mathias, and M. Aeschlimann. Time- and angle-resolved photoemission spectroscopy with optimized high-harmonic pulses using frequency-doubled ti:sapphire lasers. *Journal of Electron Spectroscopy and Related Phenomena*, 195:231 – 236, 2014.

[4] J. Ojeda, C. A. Arrell, J. Grilj, F. Frassetto, L. Mewes, H. Zhang, F. van Mourik, L. Poletto, and M. Chergui. Harmonium: A pulse preserving source of monochromatic extreme ultraviolet (30?110?ev) radiation for ultrafast photoelectron spectroscopy of liquids. *Structural Dynamics*, 3(2):023602, 2016.

[5] M Plötzing, R Adam, C Weier, L Plucinski, S Eich, S Emmerich, M Rollinger, M Aeschlimann, S Mathias, and C M Schneider. Spin-resolved photoelectron spectroscopy using femtosecond extreme ultraviolet light pulses from high-order harmonic generation. *Review of Scientific Instruments*, 87(4):043903, April 2016.

[6] B. Frietsch, R. Carley, K. Döbrich, C. Gahl, M. Teichmann, O. Schwarzkopf, Ph. Wernet, and M. Weinelt. A high-order harmonic generation apparatus for time- and angle-resolved photoelectron spectroscopy. *Review of Scientific Instruments*, 84(7):075106, 2013.

[7] Cheng-Tien Chiang, Michael Huth, Andreas Trtzschler, Frank O. Schumann, Jrgen Kirschner, and Wolf Widdra. Efficient and tunable high-order harmonic light sources for photoelectron spectroscopy at surfaces. *Journal of Electron Spectroscopy and Related Phenomena*, pages –, 2015.

[8] Artemis Beamline: https://www.clf.stfc.ac.uk/Pages/Artemis.aspx.

[9] Christopher Corder, Peng Zhao, Jin Bakalis, Xinlong Li, Matthew D Kershis, Amanda R Muraca, Michael G White, and Thomas K Allison. Ultrafast extreme ultraviolet photoemission without space charge. *Structural Dynamics*, 5(5):054301, 2018.

[10] T. K. Allison. *Femtosecond Molecular Dynamics Studied with Vacuum Ultraviolet Pulse Pairs*. PhD thesis, University of California at Berkeley, 2010.

[11] Xinlong Li, Melanie A. R. Reber, Christopher Corder, Yuning Chen, Peng Zhao, and Thomas K. Allison. High-power ultrafast yb:fiber laser frequency combs using commercially available components and basic fiber tools. *Review of Scientific Instruments*, 87(9):093114, 2016.

[12] Christopher Corder, Peng Zhao, Xinlong Li, Matthew D. Kershis, Michael G. White, and Thomas K. Allison. Development of a tunable high repetition rate xuv source for time-resolved photoemission studies of ultrafast dynamics at surfaces. In *Proceedings of SPIE*, In Press.

[13] L Poletto, F Frassetto, Francesca Calegari, S Anumula, Andrea Trabattoni, and Mauro Nisoli. Micro-focusing of attosecond pulses by grazing-incidence toroidal mirrors. *Optics express*, 21(11):13040–13051, 2013.

[14] Fabio Frassetto, Cephise Cacho, Chris A Froud, IC Edmund Turcu, Paolo Villoresi, Will A Bryan, Emma Springate, and Luca Po-

letto. Single-grating monochromator for extreme-ultraviolet ultrashort pulses. *Optics express*, 19(20):19169–19181, 2011.

[15] Arne C Rosenfeldt, Benjamin Göhler, and Helmut Zacharias. Time-resolved photoelectron spectroscopy of low-energy excitations of 4× 4 c60/cu (111). *The Journal of chemical physics*, 133(23):234704, 2010.

[16] Gerd Schönhense, Katerina Medjanik, and Hans-Joachim Elmers. Space-, time-and spin-resolved photoemission. *Journal of Electron Spectroscopy and Related Phenomena*, 200:94–118, 2015.

[17] Stephan Hüfner. *Photoelectron Spectroscopy: Principles and Applications*. Springer, 2003.

[18] David Warren Turner. Molecular photoelectron spectroscopy. *Philosophical Transactions for the Royal Society of London. Series A, Mathematical and Physical Sciences*, pages 7–31, 1970.

[19] Stephan Hüfner. *Photoelectron spectroscopy: principles and applications*. Springer Science & Business Media, 2013.

[20] Katerina Medjanik, Olena Fedchenko, Sergii Chernov, Dmytro Kutnyakhov, Martin Ellguth, Andreas Oelsner, B Schönhense, Thiago RF Peixoto, Peter Lutz, C-H Min, et al. Direct 3d mapping of the fermi surface and fermi velocity. *Nature materials*, 16(6):615, 2017.

[21] Dimitri N Basov, Richard D Averitt, Dirk Van Der Marel, Martin Dressel, and Kristjan Haule. Electrodynamics of correlated electron materials. *Reviews of Modern Physics*, 83(2):471, 2011.

[22] EW Plummer and W Eberhardt. Angle-resolved photoemission as a tool for the study of surfaces. *Advances in Chemical Physics*, pages 533–656, 1982.

[23] Andrea Damascelli. Probing the electronic structure of complex systems by arpes. *Physica Scripta*, 2004(T109):61, 2004.

[24] Weibin Chu, Wissam A Saidi, Qijing Zheng, Yu Xie, Zhenggang Lan, Oleg V Prezhdo, Hrvoje Petek, and Jin Zhao. Ultrafast dynamics of photongenerated holes at a ch3oh/tio2 rutile interface. *Journal of the American Chemical Society*, 138(41):13740–13749, 2016.

[25] Masanori Miyashita, Kenji Sunahara, Tomohiro Nishikawa, Yu Uemura, Nagatoshi Koumura, Kohjiro Hara, Atsunori Mori, Takao Abe, Eiji Suzuki, and Shogo Mori. Interfacial electron-transfer kinetics in metal-free organic dye-sensitized solar cells: combined effects of molecular structure of dyes and electrolytes. *Journal of the American Chemical Society*, 130(52):17874–17881, 2008.

[26] Peter Puschnig, Stephen Berkebile, Alexander J Fleming, Georg Koller, Konstantin Emtsev, Thomas Seyller, John D Riley, Claudia Ambrosch-Draxl, Falko P Netzer, and Michael G Ramsey. Reconstruction of molecular orbital densities from photoemission data. *Science*, 326(5953):702–706, 2009.

[27] Matthew D. Kershis, Daniel P. Wilson, and Michael G. White. Dynamics of acetone photooxidation on tio2(110): State-resolved measurements of methyl photoproducts. *The Journal of Chemical Physics*, 138(20):204703, 2013.

[28] Matthew D Kershis and Michael G White. Photooxidation of ethanol and 2-propanol on tio 2 (110): evidence for methyl radical ejection. *Physical Chemistry Chemical Physics*, 15(41):17976–17982, 2013.

[29] Chenbiao Xu, Wenshao Yang, Qing Guo, Dongxu Dai, Maodu Chen, and Xueming Yang. Molecular hydrogen formation from photocatalysis of methanol on anatase-tio2 (101). *Journal of the American Chemical Society*, 136(2):602–605, 2014.

[30] Qing Guo, Chuanyao Zhou, Zhibo Ma, Zefeng Ren, Hongjun Fan, and Xueming Yang. Elementary photocatalytic chemistry on tio 2 surfaces. *Chemical Society Reviews*, 45(13):3701–3730, 2016.

[31] Akira Fujishima, Xintong Zhang, and Donald A Tryk. Tio2 photocatalysis and related surface phenomena. *Surface science reports*, 63(12):515–582, 2008.

[32] Mario Borgwardt, Martin Wilke, Thorsten Kampen, Sven Mähl, Wanchun Xiang, Leone Spiccia, Kathrin M. Lange, Igor Yu. Kiyan, and Emad F. Aziz. Injection kinetics and electronic structure at the n719/tio2 interface studied by means of ultrafast xuv photoemission

spectroscopy. *The Journal of Physical Chemistry C*, 119(17):9099–9107, 2015.

[33] Uwe Bovensiepen, Hrvoje Petek, and Martin Wolf, editors. *Dynamics at Solid State Surfaces and Interfaces*. WILEY-VCH Verlag, 2010.

[34] MP Seah. An accurate and simple universal curve for the energy-dependent electron inelastic mean free path. *Surface and interface analysis*, 44(4):497–503, 2012.

[35] S. Mathias, S. Eich, J. Urbancic, S. Michael, A. V. Carr, S. Emmerich, A. Stange, T. Popmintchev, T. Rohwer, M. Wiesenmayer, A. Ruffing, S. Jakobs, S. Hellmann, P. Matyba, C. Chen, L. Kipp, M. Bauer, H. C. Kapteyn, H. C. Schneider, K. Rossnagel, M. M. Murnane, and M. Aeschlimann. Self-amplified photo-induced gap quenching in a correlated electron material. *Nature Communications*, 7:12902 EP –, 10 2016.

[36] D. N. Basov, Richard D. Averitt, Dirk van der Marel, Martin Dressel, and Kristjan Haule. Electrodynamics of correlated electron materials. *Rev. Mod. Phys.*, 83:471–541, Jun 2011.

[37] Uwe Bovensiepen and Patrick S Kirchmann. Elementary relaxation processes investigated by femtosecond photoelectron spectroscopy of two-dimensional materials. *Laser & Photonics Reviews*, 6(5):589–606, 2012.

[38] Timm Rohwer, Stefan Hellmann, Martin Wiesenmayer, Christian Sohrt, Ankatrin Stange, Bartosz Slomski, Adra Carr, Yanwei Liu, Luis Miaja Avila, Matthias Kallane, Stefan Mathias, Lutz Kipp, Kai Rossnagel, and Michael Bauer. Collapse of long-range charge order tracked by time-resolved photoemission at high momenta. *Nature*, advance online publication:–, 03 2011.

[39] J. Faure, J. Mauchain, E. Papalazarou, M. Marsi, D. Boschetto, I. Timrov, N. Vast, Y. Ohtsubo, B. Arnaud, and L. Perfetti. Direct observation of electron thermalization and electron-phonon coupling in photoexcited bismuth. *Phys. Rev. B*, 88:075120, Aug 2013.

[40] Y Ishibashi, Y Inoue, and T Asahi. The excitation intensity dependence of singlet fission dynamics of a rubrene microcrystal studied by

femtosecond transient microspectroscopy. *Photochemical & Photobiological Sciences*, 15(10):1304–1309, 2016.

[41] Joel Berry, Songsong Zhou, Jian Han, David J Srolovitz, and Mikko P Haataja. Domain morphology and mechanics of the h/t transition metal dichalcogenide monolayers. *Physical Review Materials*, 2(11):114002, 2018.

[42] Mattia Cattelan and Neil Fox. A perspective on the application of spatially resolved arpes for 2d materials. *Nanomaterials*, 8(5):284, 2018.

[43] José Avila, Antoine Boury, Borja Caja-Muñoz, Chaoyu Chen, Stephane Lorcy, and Maria C Asensio. Optimal focusing system of the fresnel zone plates at the synchrotron soleil nanoarpes beamline. In *Journal of Physics: Conference Series*, volume 849, page 012039. IOP Publishing, 2017.

[44] S. Hellmann, K. Rossnagel, M. Marczynski-Bühlow, and L. Kipp. Vacuum space-charge effects in solid-state photoemission. *Phys. Rev. B*, 79:035402, Jan 2009.

[45] Eli Rotenberg and Aaron Bostwick. microarpes and nanoarpes at diffraction-limited light sources: opportunities and performance gains. *Journal of synchrotron radiation*, 21(5):1048–1056, 2014.

[46] Roberto Salemme. Space charge compensation and electron cloud effects in modern high intensity proton accelerators. 2016.

[47] NM Buckanie, J Göhre, P Zhou, D Von der Linde, M Horn-von Hoegen, and FJ Meyer Zu Heringdorf. Space charge effects in photoemission electron microscopy using amplified femtosecond laser pulses. *Journal of Physics: Condensed Matter*, 21(31):314003, 2009.

[48] Adriano Verna, Giorgia Greco, Valerio Lollobrigida, Francesco Offi, and Giovanni Stefani. Space-charge effects in high-energy photoemission. *Journal of Electron Spectroscopy and Related Phenomena*, 209:14–25, 2016.

[49] XJ Zhou, B Wannberg, WL Yang, V Brouet, Z Sun, JF Douglas, D Dessau, Z Hussain, and Z-X Shen. Space charge effect and mirror charge effect in photoemission spectroscopy. *Journal of electron spectroscopy and related phenomena*, 142(1):27–38, 2005.

[50] M Plötzing, R Adam, C Weier, L Plucinski, S Eich, S Emmerich, M Rollinger, M Aeschlimann, S Mathias, and CM Schneider. Spin-resolved photoelectron spectroscopy using femtosecond extreme ultraviolet light pulses from high-order harmonic generation. *Review of Scientific Instruments*, 87(4):043903, 2016.

[51] S Passlack, S Mathias, O Andreyev, D Mittnacht, M Aeschlimann, and M Bauer. Space charge effects in photoemission with a low repetition, high intensity femtosecond laser source. *Journal of applied physics*, 100(2):024912, 2006.

[52] R Al-Obaidi, M Wilke, M Borgwardt, J Metje, A Moguilevski, N Engel, D Tolksdorf, A Raheem, T Kampen, S Mähl, et al. Ultrafast photoelectron spectroscopy of solutions: space-charge effect. *New Journal of Physics*, 17(9):093016, 2015.

[53] S Hellmann, K Rossnagel, M Marczynski-Bühlow, and L Kipp. Vacuum space-charge effects in solid-state photoemission. *Physical Review B*, 79(3):035402, 2009.

[54] B Schönhense, K Medjanik, O Fedchenko, S Chernov, M Ellguth, D Vasilyev, A Oelsner, J Viefhaus, D Kutnyakhov, W Wurth, et al. Multidimensional photoemission spectroscopythe space-charge limit. *New Journal of Physics*, 20(3):033004, 2018.

[55] Th Schmidt, Alessandro Sala, Helder Marchetto, E Umbach, and H-J Freund. First experimental proof for aberration correction in xpeem: Resolution, transmission enhancement, and limitation by space charge effects. *Ultramicroscopy*, 126:23–32, 2013.

[56] G. Saathoff, L. Miaja-Avila, M. Aeschlimann, M. M. Murnane, and H. C. Kapteyn. Laser-assisted photoemission from surfaces. *Phys. Rev. A*, 77:022903, Feb 2008.

[57] Søren Ulstrup, Jens Christian Johannsen, Federico Cilento, Alberto Crepaldi, Jill A. Miwa, Michele Zacchigna, Cephise Cacho, Richard T. Chapman, Emma Springate, Felix Fromm, Christian Raidel, Thomas Seyller, Phil D.C. King, Fulvio Parmigiani, Marco Grioni, and Philip Hofmann. Ramifications of optical pumping on the interpretation of

time-resolved photoemission experiments on graphene. *Journal of Electron Spectroscopy and Related Phenomena*, 200(Supplement C):340 – 346, 2015. Special Anniversary Issue: Volume 200.

[58] L.-P. Oloff, K. Hanff, A. Stange, G. Rohde, F. Diekmann, M. Bauer, and K. Rossnagel. Pump laser-induced space-charge effects in hhg-driven time- and angle-resolved photoelectron spectroscopy. *Journal of Applied Physics*, 119(22):225106, 2016.

[59] Mario Borgwardt. *Electronic Structure and Electron Transfer Dynamics at Dye-Semiconductor Interfaces Studied by Means of Time-Resolved XUV Photoelectron Spectroscopy*. PhD thesis, Freie Universitat Berlin, 2016.

[60] Arthur K Mills, T J Hammond, Matthew H C Lam, and David J Jones. Xuv frequency combs via femtosecond enhancement cavities. *Journal of Physics B: Atomic, Molecular and Optical Physics*, 45(14):142001, 2012.

[61] H. Carstens, M. Högner, T. Saule, S. Holzberger, N. Lilienfein, A. Guggenmos, C. Jocher, T. Eidam, D. Esser, V. Tosa, V. Pervak, J. Limpert, A. Tünnermann, U. Kleineberg, F. Krausz, and I. Pupeza. High-harmonic generation at 250 mhz with photon energies exceeding 100 ev. *Optica*, 3(4):366–369, Apr 2016.

[62] T. Haarlammert and H. Zacharias. Application of high harmonic radiation in surface science. *Current Opinion in Solid State and Materials Science*, 13(1Äì2):13 – 27, 2009.

[63] He Wang, Yiming Xu, Stefan Ulonska, Joseph S. Robinson, Predrag Ranitovic, and Robert A. Kaindl. Bright high-repetition-rate source of narrowband extreme-ultraviolet harmonics beyond 22 ev. *Nature Communciations*, 6:7459 EP –, 06 2015.

[64] Cheng-Tien Chiang, Michael Huth, Andreas Trützschler, Mario Kiel, Frank O Schumann, Juergen Kirschner, and Wolf Widdra. Boosting laboratory photoelectron spectroscopy by megahertz high-order harmonics. *New Journal of Physics*, 17(1):013035, January 2015.

[65] Michele Puppin, Yunpei Deng, Oliver Prochnow, Jan Ahrens, Thomas Binhammer, Uwe Morgner, Marcel Krenz, Martin Wolf, and Ralph Ernstorfer. 500 khz opcpa delivering tunable sub-20 fs pulses with 15 w average power based on an all-ytterbium laser. *Opt. Express*, 23(2):1491–1497, Jan 2015.

[66] Steffen Hädrich, Arno Klenke, Jan Rothhardt, Manuel Krebs, Armin Hoffmann, Oleg Pronin, Vladimir Pervak, Jens Limpert, and Andreas Tünnermann. High photon flux table-top coherent extreme-ultraviolet source. *Nat Photon*, 8(10):779–783, 10 2014.

[67] François Labaye, Maxim Gaponenko, Valentin J Wittwer, Andreas Diebold, Clément Paradis, Norbert Modsching, Loïc Merceron, Florian Emaury, Ivan J Graumann, Christopher R Phillips, et al. Extreme ultraviolet light source at a megahertz repetition rate based on high-harmonic generation inside a mode-locked thin-disk laser oscillator. *Optics letters*, 42(24):5170–5173, 2017.

[68] Florian Emaury, Andreas Diebold, Clara J. Saraceno, and Ursula Keller. Compact extreme ultraviolet source at megahertz pulse repetition rate with a low-noise ultrafast thin-disk laser oscillator. *Optica*, 2(11):980–984, Nov 2015.

[69] Kevin F Lee, Xiaoyan Ding, TJ Hammond, ME Fermann, G Vampa, and PB Corkum. Harmonic generation in solids with direct fiber laser pumping. *Optics letters*, 42(6):1113–1116, 2017.

[70] Shima Gholam-Mirzaei, John Beetar, and Michael Chini. High harmonic generation in zno with a high-power mid-ir opa. *Applied Physics Letters*, 110(6):061101, 2017.

[71] G Vampa, BG Ghamsari, S Siadat Mousavi, TJ Hammond, A Olivieri, E Lisicka-Skrek, A Yu Naumov, DM Villeneuve, A Staudte, P Berini, et al. Plasmon-enhanced high-harmonic generation from silicon. *Nature Physics*, 13(7):659, 2017.

[72] A Grüneis, R Saito, Ge G Samsonidze, T Kimura, MA Pimenta, A Jorio, AG Souza Filho, G Dresselhaus, and MS Dresselhaus. Inhomogeneous optical absorption around the k point in graphite and carbon nanotubes. *Physical Review B*, 67(16):165402, 2003.

[73] Pourya Ayria, Ahmad RT Nugraha, Eddwi H Hasdeo, Thomas R Czank, Shin-ichiro Tanaka, and Riichiro Saito. Photon energy dependence of angle-resolved photoemission spectroscopy in graphene. *Physical Review B*, 92(19):195148, 2015.

[74] R. W. Schoenlein, S. Chattopadhyay, H. H. Chong, T. E. Glover, P. A. Heimann, C. V. Shank, A. A. Zholents, and M. S. Zolotorev. Generation of femtosecond pulses of synchrotron radiation. *Science*, 287:2237–2240, 2000.

[75] Y-x Liu, M Seminario, FG Tomasel, C Chang, JJ Rocca, and DT Attwood. Achievement of essentially full spatial coherence in a high-average-power soft-x-ray laser. *Physical Review A*, 63(3):033802, 2001.

[76] Y Wang, E Granados, MA Larotonda, M Berrill, BM Luther, D Patel, CS Menoni, and JJ Rocca. High-brightness injection-seeded soft-x-ray-laser amplifier using a solid target. *Physical review letters*, 97(12):123901, 2006.

[77] Anthony E. Siegman. *Lasers*. University Science Books, 1986.

[78] A McPherson, G Gibson, H Jara, U Johann, Ting S Luk, IA McIntyre, Keith Boyer, and Charles K Rhodes. Studies of multiphoton production of vacuum-ultraviolet radiation in the rare gases. *JOSA B*, 4(4):595–601, 1987.

[79] M Ferray, A L'Huillier, X F Li, L A Lompre, G Mainfray, and C Manus. Multiple-harmonic conversion of 1064 nm radiation in rare gases. *Journal of Physics B: Atomic, Molecular and Optical Physics*, 21(3):L31, 1988.

[80] R. Haight and M. Baeumler. Ultrafast-electron dynamics and recombination on the ge(111)(2x1) π-bonded surface. *Phys. Rev. B*, 46:1543–1552, Jul 1992.

[81] R. Haight and D. R. Peale. Tunable photoemission with harmonics of subpicosecond lasers. *Review of Scientific Instruments*, 65(6):1853–1857, 1994.

[82] M. Bauer, C. Lei, K. Read, R. Tobey, J. Gland, M. M. Murnane, and H. C. Kapteyn. Direct observation of surface chemistry using ultrafast soft-x-ray pulses. *Phys. Rev. Lett.*, 87:025501, Jun 2001.

[83] Jeffrey L. Krause, Kenneth J. Schafer, and Kenneth C. Kulander. High-order harmonic generation from atoms and ions in the high intensity regime. *Phys. Rev. Lett.*, 68:3535–3538, Jun 1992.

[84] KJ Schafer, Baorui Yang, LF DiMauro, and KC Kulander. Above threshold ionization beyond the high harmonic cutoff. *Physical review letters*, 70(11):1599, 1993.

[85] P. B. Corkum. Plasma perspective on strong-field multiphoton ionization. *Phys. Rev. Lett*, 71:1994–1997, 1993.

[86] M. Lewenstein, Ph. Balcou, M. Yu Ivanov, Anne L'Huillier, and P. B. Corkum. Theory of high order harmonic generation by low-frequency laser fields. *Phys. Rev. A*, 49:2117–2132, 1994.

[87] Tenio Popmintchev, Ming-Chang Chen, Dimitar Popmintchev, Paul Arpin, Susannah Brown, Skirmantas Ališauskas, Giedrius Andriukaitis, Tadas Balčiunas, Oliver D Mücke, Audrius Pugzlys, et al. Bright coherent ultrahigh harmonics in the kev x-ray regime from mid-infrared femtosecond lasers. *science*, 336(6086):1287–1291, 2012.

[88] E. Constant, D. Garzella, P. Breger, E. Mevel, Ch. Dorrer, C. Le Blanc, F. Salin, and P. Agostini. Optimization of high harmonic generation in absorbing gasss model and experiment. *Phys. Rev. Lett.*, 82:1668, 1999.

[89] C M Heyl, J Güdde, A L'Huillier, and U Höfer. High-order harmonic generation with j laser pulses at high repetition rates. *Journal of Physics B: Atomic, Molecular and Optical Physics*, 45(7):074020, 2012.

[90] David Attwood and Anne Sakdinawat. *X-rays and extreme ultraviolet radiation: principles and applications*. Cambridge university press, 2017.

[91] Mette B Gaarde and Kenneth J Schafer. Quantum path distributions for high-order harmonics in rare gas atoms. *Physical Review A*, 65(3):031406, 2002.

[92] Y Mairesse, A De Bohan, LJ Frasinski, H Merdji, LC Dinu, P Monchicourt, P Breger, M Kovačev, R Taïeb, B Carré, et al. Attosecond synchronization of high-harmonic soft x-rays. *Science*, 302(5650):1540–1543, 2003.

[93] R. Jason Jones and Jun Ye. Femtosecond pulse amplification by coherent addition in a passive optical cavity. *Opt. Lett.*, 27(20):1848–1850, 2002.

[94] R. Jason Jones and Jun Ye. High-repetition-rate coherent femtosecond pulse amplification withan external passive optical cavity. *Opt. Lett.*, 29(23):2812–2814, Dec 2004.

[95] Yuning Chen. *Cavity-Enhanced Ultrafast Spectroscopy*. PhD thesis, 2018.

[96] Warren Nagourney. *Quantum Electronics for Atomic Physics*. Oxford University Press, 2010.

[97] Nicolai Lilienfein, Christina Hofer, Simon Holzberger, C Matzer, P Zimmermann, M Trubetskov, V Pervak, and Ioachim Pupeza. Enhancement cavities for few-cycle pulses. *Opt. Lett*, 42(2):271, 2017.

[98] Simon Holzberger, N Lilienfein, M Trubetskov, Henning Carstens, F Lücking, V Pervak, Ferenc Krausz, and Ioachim Pupeza. Enhancement cavities for zero-offset-frequency pulse trains. *Optics letters*, 40(10):2165–2168, 2015.

[99] A.E. Siegman. *Lasers*. University Science Books, 1986.

[100] Henning Carstens, N Lilienfein, Simon Holzberger, C Jocher, T Eidam, J Limpert, A Tünnermann, J Weitenberg, Dylan C Yost, A Alghamdi, et al. Megawatt-scale average-power ultrashort pulses in an enhancement cavity. *Optics letters*, 39(9):2595–2598, 2014.

[101] Ioachim Pupeza, Tino Eidam, Jens Rauschenberger, Birgitta Bernhardt, Akira Ozawa, Ernst Fill, Alexander Apolonski, Thomas Udem, Jens Limpert, Zeyad A Alahmed, et al. Power scaling of a high-repetition-rate enhancement cavity. *Optics letters*, 35(12):2052–2054, 2010.

[102] N Lilienfein, H Carstens, Simon Holzberger, C Jocher, T Eidam, J Limpert, A Tünnermann, A Apolonski, Ferenc Krausz, and Ioachim Pupeza. Balancing of thermal lenses in enhancement cavities with transmissive elements. *Optics letters*, 40(5):843–846, 2015.

[103] Simon Holzberger, Nicolai Lilienfein, Henning Carstens, Tobias Saule, Maximilian Högner, F Lücking, M Trubetskov, V Pervak, T Eidam, J Limpert, et al. Femtosecond enhancement cavities in the nonlinear regime. *Physical review letters*, 115(2):023902, 2015.

[104] Henning Carstens, Maximilian Högner, Tobias Saule, Simon Holzberger, Nicolai Lilienfein, Alexander Guggenmos, C Jocher, T Eidam, D Esser, V Tosa, et al. High-harmonic generation at 250 mhz with photon energies exceeding 100 ev. *Optica*, 3(4):366–369, 2016.

[105] Henning Carstens, Simon Holzberger, Jan Kaster, Johannes Weitenberg, Volodymyr Pervak, Alexander Apolonski, Ernst Fill, Ferenc Krausz, and Ioachim Pupeza. Large-mode enhancement cavities. *Optics express*, 21(9):11606–11617, 2013.

[106] Ioachim Pupeza, Tino Eidam, Jan Kaster, Birgitta Bernhardt, Jens Rauschenberger, Akira Ozawa, Ernst Fill, Thomas Udem, Matthias F Kling, Jens Limpert, et al. Power scaling of femtosecond enhancement cavities and high-power applications. In *Fiber Lasers VIII: Technology, Systems, and Applications*, volume 7914, page 79141I. International Society for Optics and Photonics, 2011.

[107] Gregory M Harry, LIGO Scientific Collaboration, et al. Advanced ligo: the next generation of gravitational wave detectors. *Classical and Quantum Gravity*, 27(8):084006, 2010.

[108] Rüdiger Paschotta. Beam quality deterioration of lasers caused by intracavity beam distortions. *Optics express*, 14(13):6069–6074, 2006.

[109] I. Pupeza. *Power scaling of enhancement cavities for nonlinear optics*. PhD thesis, 2011.

[110] Nikolai Lilienfein, Christina Hofer, Maximilian Högner, Tobias Saule, Michael Trubetskov, Volodymyr Pervak, Ernst Fill, Claudius Riek, Alfred Leitenstorfer, J Limpert, et al. Temporal solitons in free-space femtosecond enhancement cavities. *Nature Photonics*, 13(3):214, 2019.

[111] Nathan R. Newbury. Searching for applications with a fine-tooth comb. *Nat Photon*, 5(4):186–188, 04 2011.

[112] Scott A. Diddams. The evolving optical frequency comb. *J. Opt. Soc. Am. B*, 27(11):B51–B62, Nov 2010.

[113] Tilo Steinmetz, Tobias Wilken, Constanza Araujo-Hauck, Ronald Holzwarth, Theodor W. Hänsch, Luca Pasquini, Antonio Manescau, Sandro D'Odorico, Michael T. Murphy, Thomas Kentischer, Wolfgang Schmidt, and Thomas Udem. Laser frequency combs for astronomical observations. *Science*, 321(5894):1335–1337, 2008.

[114] CoddingtonI., SwannW. C., NenadovicL., and NewburyN. R. Rapid and precise absolute distance measurements at long range. *Nat Photon*, 3(6):351–356, 06 2009.

[115] Ferenc Krausz and Misha Ivanov. Attosecond physics. *Rev. Mod. Phys.*, 81(1):163–234, Feb 2009.

[116] Craig Benko, Thomas K. Allison, Arman Cingoz, Linqiang Hua, Francois Labaye, Dylan C. Yost, and Jun Ye. Extreme ultraviolet radiation with coherence time greater than 1 s. *Nat Photon*, 8(7):530–536, 07 2014.

[117] Florian Adler, Michael J. Thorpe, Kevin C. Cossel, and Jun Ye. Cavity-enhanced direct frequency comb spectroscopy: Technology and applications. *Annual Review of Analytical Chemistry*, 3(1):175–205, 2010.

[118] Ian Coddington, Nathan Newbury, and William Swann. Dual-comb spectroscopy. *Optica*, 3(4):414–426, Apr 2016.

[119] R. Paschotta, J. Nilsson, A.C. Tropper, and D.C. Hanna. Ytterbium-doped fiber amplifiers. *Quantum Electronics, IEEE Journal of*, 33(7):1049–1056, 1997.

[120] M.E. Fermann and I. Hartl. Ultrafast fiber laser technology. *Selected Topics in Quantum Electronics, IEEE Journal of*, 15(1):191 –206, jan. 2009.

[121] Hanieh Fattahi, Helena G. Barros, Martin Gorjan, Thomas Nubbemeyer, Bidoor Alsaif, Catherine Y. Teisset, Marcel Schultze, Stephan

Prinz, Matthias Haefner, Moritz Ueffing, Ayman Alismail, Lénárd Vámos, Alexander Schwarz, Oleg Pronin, Jonathan Brons, Xiao Tao Geng, Gunnar Arisholm, Marcelo Ciappina, Vladislav S. Yakovlev, Dong-Eon Kim, Abdallah M. Azzeer, Nicholas Karpowicz, Dirk Sutter, Zsuzsanna Major, Thomas Metzger, and Ferenc Krausz. Third-generation femtosecond technology. *Optica*, 1(1):45–63, Jul 2014.

[122] V. Cautaerts, D. J. Richardson, R. Paschotta, and D. C. Hanna. Stretched pulse yb3+:silica fiber laser. *Opt. Lett.*, 22(5):316–318, Mar 1997.

[123] C. Hönninger, A. Giesen, G. Zhang, and U. Keller. Femtosecond yb:yag laser using semiconductor saturable absorbers. *Opt. Lett.*, 20(23):2402–2404, Dec 1995.

[124] Tino Eidam, Stefan Hanf, Enrico Seise, Thomas V. Andersen, Thomas Gabler, Christian Wirth, Thomas Schreiber, Jens Limpert, and Andreas Tünnermann. Femtosecond fiber cpa system emitting 830 w average output power. *Opt. Lett.*, 35(2):94–96, Jan 2010.

[125] Cesar Jauregui, Jens Limpert, and Andreas Tunnermann. High-power fibre lasers. *Nat Photon*, 7(11):861–867, 11 2013.

[126] Schibli T. R., Hartl I., Yost D. C., Martin M. J., Marcinkevicius A., Fermann M. E., and Ye J. Optical frequency comb with submillihertz linewidth and more than 10 w average power. *Nat Photon*, 2(6):355–359, 06 2008.

[127] L. Kuznetsova, F.W. Wise, S. Kane, and J. Squier. Chirped-pulse amplification near the gain-narrowing limit of yb-doped fiber using a reflection grism compressor. *Applied Physics B*, 88(4):515–518, 2007.

[128] Jian Zhao, Wenxue Li, Chao Wang, Yang Liu, and Heping Zeng. Pre-chirping management of a self-similar yb-fiber amplifier towards 80 w average power with sub-40 fs pulse generation. *Opt. Express*, 22(26):32214–32219, Dec 2014.

[129] Wei Liu, Damian N. Schimpf, Tino Eidam, Jens Limpert, Andreas Tünnermann, Franz X. Kärtner, and Guoqing Chang. Pre-chirp managed nonlinear amplification in fibers delivering 100 w, 60 fs pulses. *Opt. Lett.*, 40(2):151–154, Jan 2015.

[130] I. Hartl, T. R. Schibli, A. Marcinkevicius, D. C. Yost, D. D. Hudson, M. E. Fermann, and Jun Ye. Cavity-enhanced similariton yb-fiber laser frequency comb: 3×10^{14} w/cm^2 peak intensity at 136 mhz. *Opt. Lett.*, 32(19):2870–2872, 2007.

[131] Axel Ruehl, Andrius Marcinkevicius, Martin E. Fermann, and Ingmar Hartl. 80 w, 120 fs yb-fiber frequency comb. *Opt. Lett.*, 35(18):3015–3017, Sep 2010.

[132] Lora Nugent-Glandorf, Todd A. Johnson, Yohei Kobayashi, and Scott A. Diddams. Impact of dispersion on amplitude and frequency noise in a yb-fiber laser comb. *Opt. Lett.*, 36(9):1578–1580, May 2011.

[133] H. Carstens, N. Lilienfein, S. Holzberger, C. Jocher, T. Eidam, J. Limpert, A. Tünnermann, J. Weitenberg, D. C. Yost, A. Alghamdi, Z. Alahmed, A. Azzeer, A. Apolonski, E. Fill, F. Krausz, and I. Pupeza. Megawatt-scale average-power ultrashort pulses in an enhancement cavity. *Opt. Lett.*, 39(9):2595–2598, May 2014.

[134] A. Fernández, K. Jespersen, L. Zhu, L. Grüner-Nielsen, A. Baltuška, A. Galvanauskas, and A. J. Verhoef. High-fidelity, 160fs, 5μj pulses from an integrated yb-fiber laser system with a fiber stretcher matching a simple grating compressor. *Opt. Lett.*, 37(5):927–929, Mar 2012.

[135] John M. Dudley, Christophe Finot, David J. Richardson, and Guy Millot. Self-similarity in ultrafast nonlinear optics. *Nat Phys*, 3(9):597–603, 09 2007.

[136] M. E. Fermann, V. I. Kruglov, B. C. Thomsen, J. M. Dudley, and J. D. Harvey. Self-similar propagation and amplification of parabolic pulses in optical fibers. *Phys. Rev. Lett.*, 84:6010–6013, Jun 2000.

[137] G. P. Agrawal. *Applications of Nonlinear Fiber Optics*. Academic Press, 2008.

[138] G. P. Agrawal. *Nonlinear Fiber Optics*. Academic Press, 2012.

[139] Melanie T. Asaki, Chung-Po Huang, Dennis Garvey, Jianping Zhou, Henry C. Kapteyn, and Margaret M. Murnane. Generation of 11-fs pulses from a self-mode-locked ti:sapphire laser. *Opt. Lett.*, 18(12):977–979, 1993.

[140] A. Stingl, R. Szipöcs, M. Lenzner, Ch. Spielmann, and F. Krausz. Sub-10-fs mirror-dispersion-controlled ti:sapphire laser. *Opt. Lett.*, 20(6):602–604, Mar 1995.

[141] Sergey Kobtsev, Sergey Kukarin, and Yurii Fedotov. Ultra-low repetition rate mode-locked fiber laser with high-energy pulses. *Opt. Express*, 16(26):21936–21941, Dec 2008.

[142] Nick G. Usechak, Govind P. Agrawal, and Jonathan D. Zuegel. Tunable, high-repetition-rate, harmonically mode-locked ytterbium fiber laser. *Opt. Lett.*, 29(12):1360–1362, Jun 2004.

[143] Andy Chong, Joel Buckley, Will Renninger, and Frank Wise. All-normal-dispersion femtosecond fiber laser. *Opt. Express*, 14(21):10095–10100, Oct 2006.

[144] S. M. J. Kelly. Characteristic sideband instability of periodically amplified average soliton. *Electronics Letters*, 28(8):806–807, April 1992.

[145] Martin Baumgartl, Caroline Lecaplain, Ammar Hideur, Jens Limpert, and Andreas Tünnermann. 66w average power from a microjoule-class sub-100fs fiber oscillator. *Opt. Lett.*, 37(10):1640–1642, May 2012.

[146] R. Paschotta. Noise of mode-locked lasers (part i): numerical model. *Applied Physics B*, 79(2):153–162, 2004.

[147] R. Paschotta. Noise of mode-locked lasers (part ii): timing jitter and other fluctuations. *Applied Physics B*, 79(2):163–173, 2004.

[148] Ingmar Hartl, Genady Imeshev, Liang Dong, Gyu C. Cho, and Martin E. Fermann. Ultra-compact dispersion compensated femtosecond fiber oscillators and amplifiers. In *Conference on Lasers and Electro-Optics/Quantum Electronics and Laser Science and Photonic Applications Systems Technologies*, page CThG1. Optical Society of America, 2005.

[149] Xiangyu Zhou, Dai Yoshitomi, Yohei Kobayashi, and Kenji Torizuka. Generation of 28-fs pulses from a mode-locked ytterbium fiber oscillator. *Opt. Express*, 16(10):7055–7059, May 2008.

[150] J. R. Buckley, S. W. Clark, and F. W. Wise. Generation of ten-cycle pulses from an ytterbium fiber laser with cubic phase compensation. *Opt. Lett.*, 31(9):1340–1342, May 2006.

[151] M. Hofer, M.H. Ober, F. Haberl, and M.E. Fermann. Characterization of ultrashort pulse formation in passively mode-locked fiber lasers. *Quantum Electronics, IEEE Journal of*, 28(3):720–728, 1992.

[152] Andrew Weiner. *Ultrafast Optics*. Wiley, 2009.

[153] N. Newbury. Understanding noise sources and stabilization strategies in frequency combs - part 2. Winter College on Optics: Optical Frequency Combs, 2016.

[154] L. C. Sinclair, J.-D. Desch$^{\text{TM}}$nes, L. Sonderhouse, W. C. Swann, I. H. Khader, E. Baumann, N. R. Newbury, and I. Coddington. Invited article: A compact optically coherent fiber frequency comb. *Review of Scientific Instruments*, 86(8), 2015.

[155] F. Ö Ilday, J. Chen, and F. X. Kärtner. Generation of sub-100-fs pulses at up to 200 mhz repetition rate from a passively mode-locked yb-doped fiber laser. *Opt. Express*, 13(7):2716–2721, 2005.

[156] Nathan R. Newbury and William C. Swann. Low-noise fiber-laser frequency combs (invited). *J. Opt. Soc. Am. B*, 24(8):1756–1770, 2007.

[157] Katherine J. Bock. *Femtosecond Fiber Lasers*. PhD thesis, School of Electrical Engineering and Computer Science, University of Ottawa, Ottawa, Canada, 2012.

[158] Jinendra K. Ranka, Alexander L. Gaeta, Andrius Baltuska, Maxim S. Pshenichnikov, and Douwe A. Wiersma. Autocorrelation measurement of 6-fs pulses based on the two-photon-induced photocurrent in a gaasp photodiode. *Opt. Lett.*, 22(17):1344–1346, Sep 1997.

[159] W. H. Knox. In situ measurement of complete intracavitydispersion in an operating ti:sapphire femtosecond laser. *Opt. Lett.*, 17(7):514–516, 1992.

[160] A. Cingöz, D. C. Yost, T. K. Allison, A. Ruehl, M. E. Fermann, I. Hartl, and J. Ye. Broadband phase noise suppression in a yb-fiber frequency comb. *Opt. Lett.*, 36(5):743–745, Mar 2011.

[161] Youjian Song, Chur Kim, Kwangyun Jung, Hyoji Kim, and Jungwon Kim. Timing jitter optimization of mode-locked yb-fiber lasers toward the attosecond regime. *Opt. Express*, 19(15):14518–14525, 2011.

[162] Udem Th. The frequency comb (r)evolution. In *Winter College on Optics: Optical Frequency Combs - from multispecies gas sensing to high precision interrogation of atomic and molecular targets*, International Centre for Theoretical Physics, Feb. 2016.

[163] Th. Udem, J. Reichert, R. Holzwarth, and T. W. Hänsch. Accurate measurement of large optical frequency differences with a mode-locked laser. *Opt. Lett.*, 24(13):881–883, Jul 1999.

[164] Kasturi Saha, Yoshitomo Okawachi, Bonggu Shim, Jacob S. Levy, Reza Salem, Adrea R. Johnson, Mark A. Foster, Michael R. E. Lamont, Michal Lipson, and Alexander L. Gaeta. Modelocking and femtosecond pulse generation in chip-based frequency combs. *Opt. Express*, 21(1):1335–1343, Jan 2013.

[165] M. Kourogi, K. Nakagawa, and M. Ohtsu. Wide-span optical frequency comb generator for accurate optical frequency difference measurement. *IEEE Journal of Quantum Electronics*, 29(10):2693–2701, Oct 1993.

[166] N. Kuse, C.-C. Lee, J. Jiang, C. Mohr, T. R. Schibli, and M.E. Fermann. Ultra-low noise all polarization-maintaining er fiber-based optical frequency combs facilitated with a graphene modulator. *Opt. Express*, 23(19):24342–24350, Sep 2015.

[167] Darren D. Hudson, Kevin W. Holman, R. Jason Jones, Steven T. Cundiff, Jun Ye, and David J. Jones. Mode-locked fiber laser frequency-controlled with an intracavity electro-optic modulator. *Opt. Lett.*, 30(21):2948–2950, 2005.

[168] W. Zhang, M. Lours, M. Fischer, R. Holzwarth, G. Santarelli, and Y. L. Coq. Characterizing a fiber-based frequency comb with electro-optic modulator. *IEEE Transactions on Ultrasonics, Ferroelectrics, and Frequency Control*, 59(3):432–438, 2012.

[169] Kana Iwakuni, Hajime Inaba, Yoshiaki Nakajima, Takumi Kobayashi, Kazumoto Hosaka, Atsushi Onae, and Feng-Lei Hong. Narrow

linewidth comb realized with a mode-locked fiber laser using an intracavity waveguide electro-optic modulator for high-speed control. *Opt. Express*, 20(13):13769–13776, 2012.

[170] William C. Swann, Esther Baumann, Fabrizio R. Giorgetta, and Nathan R. Newbury. Microwave generation with low residual phase noise from a femtosecond fiber laser with an intracavity electro-optic modulator. *Opt. Express*, 19(24):24387–24395, Nov 2011.

[171] Yoshiaki Nakajima, Hajime Inaba, Kazumoto Hosaka, Kaoru Minoshima, Atsushi Onae, Masami Yasuda, Takuya Kohno, Sakae Kawato, Takao Kobayashi, Toshio Katsuyama, and Feng-Lei Hong. A multi-branch, fiber-based frequency comb with millihertz-level relative linewidths using an intra-cavity electro-optic modulator. *Opt. Express*, 18(2):1667–1676, Jan 2010.

[172] C. Benko, A. Ruehl, M. J. Martin, K. S. E. Eikema, M. E. Fermann, I. Hartl, and J. Ye. Full phase stabilization of a yb:fiber femtosecond frequency comb via high-bandwidth transducers. *Opt. Lett.*, 37(12):2196–2198, Jun 2012.

[173] C.-C. Lee, C. Mohr, J. Bethge, S. Suzuki, M. E. Fermann, I. Hartl, and T. R. Schibli. Frequency comb stabilization with bandwidth beyond the limit of gain lifetime by an intracavity graphene electro-optic modulator. *Opt. Lett.*, 37(15):3084–3086, 2012.

[174] Tim Hellwig, Steffen Rieger, and Carsten Fallnich. Toward an all-optically stabilized frequency comb based on a mode-locked fiber laser. *Opt. Lett.*, 39(3):525–527, 2014.

[175] Chengying Bao, Andrew C. Funk, Changxi Yang, and Steven T. Cundiff. Pulse dynamics in a mode-locked fiber laser and its quantum limited comb frequency uncertainty. *Opt. Lett.*, 39(11):3266–3269, 2014.

[176] Travis C Briles, Dylan C Yost, Arman Cingöz, Jun Ye, and Thomas R Schibli. Simple piezoelectric-actuated mirror with 180 khz servo bandwidth. *Optics express*, 18(10):9739–9746, 2010.

[177] E. D. Black. An introduction to pound-drever-hall laser stabilization. *Am. J. Phys.*, page 79, 2001.

[178] R. W. P. Drever, J. L. Hall, F. V. Kowalski, J. Hough, G. M. Ford, A. J. Munley, and H. Ward. Laser phase and frequency stabilization using an optical resonator. 31(2):97–105, 1983.

[179] Chengquan Li, Eric Moon, and Zenghu Chang. Carrier-envelope phase shift caused by variation of grating separation. *Opt. Lett.*, 31(21):3113–3115, Nov 2006.

[180] E. Treacy. Optical pulse compression with diffraction gratings. *IEEE Journal of Quantum Electronics*, 5(9):454–458, 1969.

[181] Stacy Wise, V. Quetschke, A. J. Deshpande, G. Mueller, D. H. Reitze, D. B. Tanner, B. F. Whiting, Y. Chen, A. Tünnermann, E. Kley, and T. Clausnitzer. Phase effects in the diffraction of light: Beyond the grating equation. *Phys. Rev. Lett.*, 95:013901, 2005.

[182] Shian Zhou, Lyuba Kuznetsova, Andy Chong, and Frank W. Wise. Compensation of nonlinear phase shifts with third-order dispersion in short-pulse fiber amplifiers. *Opt. Express*, 13(13):4869–4877, Jun 2005.

[183] F. Röser, J. Rothhard, B. Ortac, A. Liem, O. Schmidt, T. Schreiber, J. Limpert, and A. Tünnermann. 131 w 220 fs fiber laser system. *Opt. Lett.*, 30(20):2754–2756, Oct 2005.

[184] Zhigang Zhao and Yohei Kobayashi. Ytterbium fiber-based, 270 fs, 100 w chirped pulse amplification laser system with 1 mhz repetition rate. *Applied Physics Express*, 9(1):012701, 2016.

[185] Marcel Wunram, Patrick Storz, Daniele Brida, and Alfred Leitenstorfer. Ultrastable fiber amplifier delivering 145-fs pulses with 6-μj energy at 10-mhz repetition rate. *Opt. Lett.*, 40(5):823–826, Mar 2015.

[186] Axel Ruehl. Advances in yb:fiber frequency comb technology. *Optics and Photonics News*, May 2012:31, 2012.

[187] Sheyerman A. Levy G. Damascelli A. Mills A. K., Zhadnovich S. and Jones D. J. An xuv source using a femtosecond enhancement cavity for photoemission spectroscopy. *SPIE*, 2015.

[188] Tsung-Han Wu, David Carlson, and R.Jason Jones. A high-power fiber laser system for dual-comb spectroscopy in the vacuum-ultraviolet. In

Frontiers in Optics 2013, page FTu2A.4. Optical Society of America, 2013.

[189] Lyuba Kuznetsova, Frank W. Wise, Steve Kane, and Jeff Squier. Chirped-pulse amplification near the gain-narrowing limit of an yb-doped fiber amplifier using a reflection grism compressor. In *Conference on Lasers and Electro-Optics/Quantum Electronics and Laser Science Conference and Photonic Applications Systems Technologies*, page CMEE7. Optical Society of America, 2007.

[190] A. Offner and D. Conn. U. S. Patent Number 3748015, 1973.

[191] G. Cheriaux, Barry Walker, L. F. Dimauro, P. Rousseau, F. Salin, and J. P. Chambaret. Aberration-free stretcher design for ultrashort-pulse amplification. *Opt. Lett.*, 21(6):414–416, Mar 1996.

[192] S. Kane and J. Squier. Fourth-order-dispersion limitations of aberration-free chirped-pulse amplification systems. *J. Opt. Soc. Am. B*, 14(5):1237–1244, 1997.

[193] T. Brabec and F. Krausz. Intense few cycle laser fields: Frontiers of nonlinear optics. *Rev. Mod. Phys.*, 72:545–591, 2000.

[194] Michael Chini, Kun Zhao, and Zenghu Chang. The generation, characterization and applications of broadband isolated attosecond pulses. *Nat Photon*, 8(3):178–186, 03 2014.

[195] Arman Cingöz, Dylan C. Yost, Thomas K. Allison, Axel Ruehl, Martin E. Fermann, Ingmar Hartl, and Jun Ye. Direct frequency comb spectroscopy in the extreme ultraviolet. *Nature*, 482(7383):68–71, 02 2012.

[196] S. Passlack, S. Mathias, O. Andreyev, D. Mittnacht, M. Aeschlimann, and M. Bauer. Space charge effects in photoemission with a low repetition, high intensity femtosecond laser source. *Journal of Applied Physics*, 100(2), 2006.

[197] Arvinder S. Sandhu, Etienne Gagnon, Robin Santra, Vandana Sharma, Wen Li, Phay Ho, Predrag Ranitovic, C. Lewis Cocke, Margaret M. Murnane, and Henry C. Kapteyn. Observing the Creation of Electronic

Feshbach Resonances in Soft X-ray-Induced O-2 Dissociation. *Science*, 322(5904):1081–1085, 2008.

[198] C. Gohle, T. Udem, M. Herrmann, J. Rauschenberger, R. Holzwarth, H. A. Schuessler, F. Krausz, and T. W. Hänsch. A frequency comb in the extreme ultraviolet. *Nature*, 436(7048):234–237, 2005.

[199] R. Jason Jones, Kevin D. Moll, Michael J. Thorpe, and Jun Ye. Phase-coherent frequency combs in the vacuum ultraviolet via high-harmonic generation inside a femtosecond enhancement cavity. *Physical Review Letters*, 94(19):193201, 2005.

[200] T. K. Allison, A. Cingöz, D. C. Yost, and J. Ye. Extreme nonlinear optics in a femtosecond enhancement cavity. *Phys. Rev. Lett.*, 107:183903, Oct 2011.

[201] D. R. Carlson, Jane Lee, John Mongelli, E. M. Wright, and R. J. Jones. Intracavity ionization and pulse formation in femtosecond enhancement cavities. *Opt. Lett.*, 36(15):2991–2993, Aug 2011.

[202] D. C. Yost, A. Cingöz, T. K. Allison, A. Ruehl, M. E. Fermann, I. Hartl, and J. Ye. Power optimization of xuv frequency combs for spectroscopy applications [invited]. *Opt. Express*, 19(23):23483–23493, Nov 2011.

[203] S. Holzberger, N. Lilienfein, H. Carstens, T. Saule, M. Högner, F. Lücking, M. Trubetskov, V. Pervak, T. Eidam, J. Limpert, A. Tünnermann, E. Fill, F. Krausz, and I. Pupeza. Femtosecond enhancement cavities in the nonlinear regime. *Phys. Rev. Lett.*, 115:023902, Jul 2015.

[204] I. Pupeza, M. Högner, J. Weitenberg, S. Holzberger, D. Esser, T. Eidam, J. Limpert, A. Tünnermann, E. Fill, and S. Yakovlev, V.˙ Cavity-enhanced high-harmonic generation with spatially tailored driving fields. *Phys. Rev. Lett.*, 112:103902, Mar 2014.

[205] Jane Lee, David R. Carlson, and R. Jason Jones. Optimizing intracavity high harmonic generation for xuv fs frequency combs. *Opt. Express*, 19(23):23315–23326, Nov 2011.

[206] Gil Porat, Christoph M Heyl, Stephen B Schoun, Craig Benko, Nadine Dörre, Kristan L Corwin, and Jun Ye. Phase-matched extreme-ultraviolet frequency-comb generation. *Nature Photonics*, 12(7):387, 2018.

[207] A. Foltynowicz, P. Masłowski, A. J. Fleisher, B. J. Bjork, and J. Ye. Cavity-enhanced optical frequency comb spectroscopy in the mid-infrared application to trace detection of hydrogen peroxide. *Applied Physics B*, 110(2):163–175, Feb 2013.

[208] T. K. Allison, A. Cingöz, D. C. Yost, and J. Ye. Extreme nonlinear optics in a femtosecond enhancement cavity. *Phys. Rev. Lett.*, 107:183903, Oct 2011.

[209] DR Carlson, Jane Lee, John Mongelli, Ewan M Wright, and Ronald J Jones. Intracavity ionization and pulse formation in femtosecond enhancement cavities. *Optics letters*, 36(15):2991–2993, 2011.

[210] X M Tong and C D Lin. Empirical formula for static field ionization rates of atoms and molecules by lasers in the barrier-suppression regime. *Journal of Physics B: Atomic, Molecular and Optical Physics*, 38(15):2593, 2005.

[211] Zenghu Chang. *Fundamentals of Attosecond Optics*. CRC Press, 2011.

[212] I. Pupeza, S. Holzberger, T. Eidam, H. Carstens, D. Esser, J. Weitenberg, P. Rußbüldt, J. Rauschenberger, J. Limpert, Th Udem, A. Tünnermann, T. W. Hänsch, A. Apolonski, F. Krausz, and E. Fill. Compact high-repetition-rate source of coherent 100 ev radiation. *Nat Photon*, 7(8):608–612, 08 2013.

[213] D C Yost, A Cingoez, T K Allison, A Ruehl, M E Fermann, I Hartl, and J Ye. Power optimization of XUV frequency combs for spectroscopy applications [Invited]. *Optics express*, 19(23):23483–23493, 2011.

[214] E Constant, D Garzella, P Breger, E Mével, Ch Dorrer, C Le Blanc, F Salin, and P Agostini. Optimizing high harmonic generation in absorbing gases: Model and experiment. *Physical Review Letters*, 82(8):1668, 1999.

[215] X CXRO. ray interactions with matter, 2018.

[216] Tobias Saule, Maximilian Högner, Nikolai Lilienfein, Oliver de Vries, Marco Plötner, Vladislav S Yakovlev, Nicholas Karpowicz, Jens

Limpert, and Ioachim Pupeza. Cumulative plasma effects in cavity-enhanced high-order harmonic generation in gases. *APL Photonics*, 3(10):101301, 2018.

[217] T. J. Hammond, Arthur K. Mills, and David J. Jones. Near-threshold harmonics from a femtosecond enhancement cavity-based euv source: effects of multiple quantum pathways on spatial profile and yield. *Opt. Express*, 19(25):24871–24883, Dec 2011.

[218] B. Feuerbacher and B. Fitton. Experimental investigation of photoemission from satellite surface materials. *Journal of Applied Physics*, 43(4):1563–1572, 1972.

[219] M. Hoesch, T. K. Kim, P. Dudin, H. Wang, S. Scott, P. Harris, S. Patel, M. Matthews, D. Hawkins, S. G. Alcock, T. Richter, J. J. Mudd, M. Basham, L. Pratt, P. Leicester, E. C. Longhi, A. Tamai, and F. Baumberger. A facility for the analysis of the electronic structures of solids and their surfaces by synchrotron radiation photoelectron spectroscopy. *Review of Scientific Instruments*, 88(1):013106, 2017.

[220] Ruben Reininger, John Bozek, YiDe Chuang, Malcolm Howells, Nicholas Kelez, Soren Prestemon, Steve Marks, Tony Warwick, Chris Jozwiak, Alessandra Lanzara, M. Zahid Hasan, and Zahid Hussain. Merlin — a mev resolution beamline at the als. *AIP Conference Proceedings*, 879(1):509–512, 2007.

[221] H. Iwasawa, K. Shimada, E. F. Schwier, M. Zheng, Y. Kojima, H. Hayashi, J. Jiang, M. Higashiguchi, Y. Aiura, H. Namatame, and M. Taniguchi. Rotatable high-resolution ARPES system for tunable linear-polarization geometry. *Journal of Synchrotron Radiation*, 24(4):836–841, Jul 2017.

[222] D. C. Yost, T. R. Schibli, and J. Ye. Efficient outpult coupling of intracavity high harmonic generation. *Opt. Lett.*, 33:1099–1101, 2008.

[223] Ioachim Pupeza, Ernst E. Fill, and Ferenc Krausz. Low-loss vis/ir-xuv beam splitter for high-power applications. *Opt. Express*, 19(13):12108–12118, Jun 2011.

[224] Arthur K. Mills, Sergey Zhdanovich, Fabio Boschini, MengXing Na, Michael Schneider, Pinder Dosanjh, Doug Wong, Giorgio Levy, Andrea

Damascelli, and David J. Jones. Time-resolved femtosecond photoemission spectroscopy using a 60-mhz enhancement cavity xuv source. In *Conference on Lasers and Electro-Optics*, page STu1I.2. Optical Society of America, 2017.

[225] P. Dubé, L.-S. Ma, J. Ye, P. Jungner, and J. L. Hall. Thermally induced self-locking of an optical cavity by overtone absorption in acetylene gas. *J. Opt. Soc. Am. B*, 13(9):2041–2054, Sep 1996.

[226] Gabriel Tempea, Michael Geissler, and Thomas Brabec. Phase sensitivity of high-order harmonic generation with few-cycle laser pulses. *J. Opt. Soc. Am. B*, 16(4):669–673, 1999.

[227] Mette B. Gaarde and Kenneth J. Schafer. Quantum path distributions for high-order harmonics in rare gas atoms. *Phys. Rev. A*, 65(3):031406, Mar 2002.

[228] Alexandre Pereira, Etienne Quesnel, and Maryse Reymermier. Dynamic measurements of ultraviolet-enhanced silica contamination by photoluminescence-based diagnostic. *Journal of Applied Physics*, 105(1):013109, 2009.

[229] Ivan B Angelov, Maximilian von Pechmann, Michael K Trubetskov, Ferenc Krausz, and Vladimir Pervak. Optical breakdown of multilayer thin-films induced by ultrashort pulses at mhz repetition rates. *Optics express*, 21(25):31453–31461, 2013.

[230] B C Stuart, M D Feit, S Herman, AM Rubenchik, BW Shore, and MD Perry. Nanosecond-to-femtosecond laser-induced breakdown in dielectrics. *Physical review B*, 53(4):1749, 1996.

[231] N. Lilienfein, H. Carstens, S. Holzberger, C. Jocher, T. Eidam, J. Limpert, A. Tünnermann, A. Apolonski, F. Krausz, and I. Pupeza. Balancing of thermal lenses in enhancement cavities with transmissive elements. *Opt. Lett.*, 40(5):843–846, Mar 2015.

[232] DE Aspnes. Imaging performance of mirror pairs for grazing-incidence applications: a comparison. *Applied optics*, 21(14):2642–2646, 1982.

[233] Alexander Rack, Heinrich Riesemeier, Patrik Vagovič, Timm Weitkamp, Frank Siewert, Reiner Dietsch, Wolfgang Diete, Sondes Bauer Trabelsi, Timm Waterstradt, and Tilo Baumbach. Fully automated, fixed exit, in vacuum double-multilayer monochromator for synchrotron-based hard x-ray micro-imaging applications. In *AIP Conference Proceedings*, volume 1234, pages 740–743. AIP, 2010.

[234] Richard L Sandberg, Ariel Paul, Daisy A Raymondson, Steffen Hädrich, David M Gaudiosi, Jim Holtsnider, I Tobey Raanan, Oren Cohen, Margaret M Murnane, Henry C Kapteyn, et al. Lensless diffractive imaging using tabletop coherent high-harmonic soft-x-ray beams. *Physical review letters*, 99(9):098103, 2007.

[235] Hironori Igarashi, Ayumu Makida, Motohiko Ito, and Taro Sekikawa. Pulse compression of phase-matched high harmonic pulses from a time-delay compensated monochromator. *Optics express*, 20(4):3725–3732, 2012.

[236] W Werner and H Visser. X-ray monochromator designs based on extreme off-plane grating mountings. *Applied optics*, 20(3):487–492, 1981.

[237] Fabio Frassetto, Cephise Cacho, Chris A. Froud, I.C. Edmund Turcu, Paolo Villoresi, Will A. Bryan, Emma Springate, and Luca Poletto. Single-grating monochromator for extreme-ultraviolet ultrashort pulses. *Opt. Express*, 19(20):19169–19181, Sep 2011.

[238] Yuan Huang, Eli Sutter, Norman N. Shi, Jiabao Zheng, Tianzhong Yang, Dirk Englund, Hong-Jun Gao, and Peter Sutter. Reliable exfoliation of large-area high-quality flakes of graphene and other two-dimensional materials. *ACS Nano*, 9(11):10612–10620, 2015.

[239] AM De Jong and JW Niemantsverdriet. Thermal desorption analysis: Comparative test of ten commonly applied procedures. *Surface Science*, 233(3):355–365, 1990.

[240] PA Redhead. Thermal desorption of gases. *vacuum*, 12(4):203–211, 1962.

[241] E Habenschaden and J Küppers. Evaluation of flash desorption spectra. *Surface science letters*, 138(1):L147–L150, 1984.

[242] John L Falconer and James A Schwarz. Temperature-programmed desorption and reaction: applications to supported catalysts. *Catalysis Reviews Science and Engineering*, 25(2):141–227, 1983.

[243] Ch Tusche, M Ellguth, AA Ünal, C-T Chiang, A Winkelmann, A Krasyuk, M Hahn, G Schönhense, and J Kirschner. Spin resolved photoelectron microscopy using a two-dimensional spin-polarizing electron mirror. *Applied Physics Letters*, 99(3):032505, 2011.

[244] Anna Regoutz, Manfred Mascheck, Tomas Wiell, Susanna K Eriksson, Cristopher Liljenberg, Kornelius Tetzner, Benjamin AD Williamson, David O Scanlon, and Paul Palmgren. A novel laboratory-based hard x-ray photoelectron spectroscopy system. *Review of Scientific Instruments*, 89(7):073105, 2018.

[245] Yu He, Inna M. Vishik, Ming Yi, Shuolong Yang, Zhongkai Liu, James J. Lee, Sudi Chen, Slavko N. Rebec, Dominik Leuenberger, Alfred Zong, C. Michael Jefferson, Robert G. Moore, Patrick S. Kirchmann, Andrew J. Merriam, and Zhi-Xun Shen. Invited article: High resolution angle resolved photoemission with tabletop 11 ev laser. *Review of Scientific Instruments*, 87(1):011301, 2016.

[246] T. E. Glover, R. W. Schoenlein, A. H. Chin, and C. V. Shank. Observation of laser assisted photoelectric effect and femtosecond high order harmonic radiation. *Phys. Rev. Lett.*, 76:2468–2471, Apr 1996.

[247] L. Miaja-Avila, C. Lei, M. Aeschlimann, J. L. Gland, M. M. Murnane, H. C. Kapteyn, and G. Saathoff. Laser-assisted photoelectric effect from surfaces. *Phys. Rev. Lett.*, 97:113604, Sep 2006.

[248] CA Arrell, J Ojeda, L Mewes, J Grilj, F Frassetto, L Poletto, F Van Mourik, and M Chergui. Laser-assisted photoelectric effect from liquids. *Physical review letters*, 117(14):143001, 2016.

[249] Lars Bojer Madsen. Strong-field approximation in laser-assisted dynamics. *American Journal of Physics*, 73(1):57–62, 2005.

[250] Lukas Gallmann, Inga Jordan, Hans J Wörner, Luca Castiglioni, Matthias Hengsberger, Jürg Osterwalder, Christopher A Arrell, Majed Chergui, Elisa Liberatore, U Rothlisberger, et al. Photoemis-

sion and photoionization time delays and rates. *Structural Dynamics*, 4(6):061502, 2017.

[251] T. E. Glover, D. M. Fritz, M. Cammarata, T. K. Allison, Sinisa Coh, J. M. Feldkamp, H. Lemke, D. Zhu, Y. Feng, R. N. Coffee, M. Fuchs, S. Ghimire, J. Chen, S. Shwartz, D. A. Reis, S. E. Harris, and J. B. Hastings. X-ray and optical wave mixing. *Nature*, 488(7413):603–608, 08 2012.

[252] HG Muller, HB van Linden van den Heuvell, and MJ van der Wiel. Dressing of continuum states and mpi of xe in a two-colour experiment. *Journal of Physics B: Atomic and Molecular Physics*, 19(21):L733, 1986.

[253] K. A. Mills, R. F. Davis, S. D. Kevan, G. Thornton, and D. A. Shirley. Angle-resolved photoemission determination of Λ-line valence bands in pt and au using synchrotron radiation. *Phys. Rev. B*, 22:581–592, Jul 1980.

[254] S. D. Kevan and R. H. Gaylord. High-resolution photoemission study of the electronic structure of the noble-metal (111) surfaces. *Phys. Rev. B*, 36:5809–5818, Oct 1987.

[255] X.-Y. Zhu. Photoemission from excitons in organic semiconductors. *Journal of Electron Spectroscopy and Related Phenomena*, 204:75 – 79, 2015.

[256] W. S. Fann, R. Storz, H. W. K. Tom, and J. Bokor. Electron Thermalization in Gold. *Physical Review B*, 46(20):13592–13595, 1992.

[257] J Cao, Y Gao, H E Elsayed-Ali, RJD Miller, and D A Mantell. Femtosecond photoemission study of ultrafast electron dynamics in single-crystal Au(111) films. *Physical Review B*, 58(16):10948–10952, 1998.

[258] Tao Liu and Alessandro Troisi. What makes fullerene acceptors special as electron acceptors in organic solar cells and how to replace them. *Advanced Materials*, 25(7):1038–1041, 2013.

[259] Akshay Rao, Mark WB Wilson, Justin M Hodgkiss, Sebastian Albert-Seifried, Heinz Bassler, and Richard H Friend. Exciton fission and

charge generation via triplet excitons in pentacene/c60 bilayers. *Journal of the American Chemical Society*, 132(36):12698–12703, 2010.

[260] Wai-Lun Chan, Manuel Ligges, Askat Jailaubekov, Loren Kaake, Luis Miaja-Avila, and X-Y Zhu. Observing the multiexciton state in singlet fission and ensuing ultrafast multielectron transfer. *Science*, 334(6062):1541–1545, 2011.

[261] Eric L Shirley and Steven G Louie. Electron excitations in solid c 60: Energy gap, band dispersions, and effects of orientational disorder. *Physical review letters*, 71(1):133, 1993.

[262] Eric L Shirley, Lorin X Benedict, and Steven G Louie. Excitons in solid c 60. *Physical Review B*, 54(15):10970, 1996.

[263] S Link, A Scholl, R Jacquemin, and W Eberhardt. Electron dynamics at a ag/c60 metal–semiconductor interface. *Solid state communications*, 113(12):689–693, 2000.

[264] R Jacquemin, S Kraus, and W Eberhardt. Direct observation of the dynamics of excited electronic states in solids: F-sec time resolved photoemission of c60. *Solid state communications*, 105(7):449–453, 1998.

[265] JP Long, SJ Chase, and MN Kabler. Photoelectron spectroscopy and dynamics of excitons in c60 and photopolymerized c60 films. *Chemical physics letters*, 347(1-3):29–35, 2001.

[266] Gregory Dutton, Daniel P Quinn, CD Lindstrom, and X-Y Zhu. Exciton dynamics at molecule-metal interfaces: C 60/ au (111). *Physical Review B*, 72(4):045441, 2005.

[267] Ying Wang, JM Holden, AM Rao, PC Eklund, UD Venkateswaran, DeLyle Eastwood, Russell L Lidberg, G Dresselhaus, and MS Dresselhaus. Optical absorption and photoluminescence in pristine and photopolymerized c 60 solid films. *Physical Review B*, 51(7):4547, 1995.

[268] A-M Janner, R Eder, B Koopmans, HT Jonkman, and GA Sawatzky. Excitons in c 60 studied by temperature-dependent optical second-harmonic generation. *Physical Review B*, 52(24):17158, 1995.

[269] R Könenkamp, R Engelhardt, and R Henninger. Photogeneration and carrier transport in c60 films. *Solid state communications*, 97(4):285–288, 1996.

[270] B Mishori, Yoram Shapira, A Belu-Marian, M Manciu, and A Devenyi. Studies of c60 thin films using surface photovoltage spectroscopy. *Chemical physics letters*, 264(1-2):163–167, 1997.

[271] X-Y Zhu, G Dutton, DP Quinn, CD Lindstrom, NE Schultz, and DG Truhlar. Molecular quantum well at the c 60/ au (111) interface. *Physical Review B*, 74(24):241401, 2006.

[272] Gregory Dutton and X-Y Zhu. Distance-dependent electronic coupling at molecule- metal interfaces: C60/cu (111). *The Journal of Physical Chemistry B*, 108(23):7788–7793, 2004.

[273] Steven T Shipman, Sean Garrett-Roe, Paul Szymanski, Aram Yang, Matthew L Strader, and Charles B Harris. Determination of band curvatures by angle-resolved two-photon photoemission in thin films of c60 on ag (111). *The Journal of Physical Chemistry B*, 110(20):10002–10010, 2006.

[274] Gregory Dutton and X-Y Zhu. Unoccupied states in c60 thin films probed by two-photon photoemission. *The Journal of Physical Chemistry B*, 106(23):5975–5981, 2002.

[275] Masahiro Shibuta, Kazuo Yamamoto, Tsutomu Ohta, Masato Nakaya, Toyoaki Eguchi, and Atsushi Nakajima. Direct observation of photocarrier electron dynamics in c 60 films on graphite by time-resolved two-photon photoemission. *Scientific reports*, 6:35853, 2016.

[276] Chad Lindstrom, Gregory Dutton, Daniel P Quinn, and Xiaoyang Zhu. Electron transfer/transport at metal-molecule interfaces probed by femtosecond time-resolved two-photon photoemission: Heptane and fullerene on au (111). *Israel journal of chemistry*, 45(1-2):195–203, 2005.

[277] JP Long, BS Itchkawitz, and MN Kabler. Photoelectron spectroscopy of laser-excited surfaces by synchrotron radiation. *JOSA B*, 13(1):201–208, 1996.

[278] C-T Tzeng, W-S Lo, J-Y Yuh, R-Y Chu, and K-D Tsuei. Photoemission, near-edge x-ray-absorption spectroscopy, and low-energy electron-diffraction study of c 60 on au (111) surfaces. *Physical Review B*, 61(3):2263, 2000.

[279] Ku-Ding Tsuei, Jih-Young Yuh, Chyuan-Tsyr Tzeng, Ren-Yu Chu, Shih-Chun Chung, and King-Lung Tsang. Photoemission and photoabsorption study of c 60 adsorption on cu (111) surfaces. *Physical Review B*, 56(23):15412, 1997.

[280] H Yagi, K Nakajima, KR Koswattage, K Nakagawa, C Huang, Md SI Prodhan, BP Kafle, H Katayanagi, and K Mitsuke. Photoabsorption cross section of c60 thin films from the visible to vacuum ultraviolet. *Carbon*, 47(4):1152–1157, 2009.

[281] Benjamin Stadtmüller, Sebastian Emmerich, Dominik Jungkenn, Norman Haag, Markus Rollinger, Steffen Eich, Mahalingam Maniraj, Martin Aeschlimann, Mirko Cinchetti, and Stefan Mathias. Strong modification of the transport level alignment in organic materials after optical excitation. *Nature communications*, 10(1):1470, 2019.

[282] E Bauer. Low energy electron microscopy. *Reports on Progress in Physics*, 57(9):895, 1994.

[283] M Kotsugi, W Kuch, F Offi, LI Chelaru, and J Kirschner. Microspectroscopic two-dimensional fermi surface mapping using a photoelectron emission microscope. *Review of scientific instruments*, 74(5):2754–2758, 2003.

[284] B Krömker, M Escher, D Funnemann, D Hartung, H Engelhard, and J Kirschner. Development of a momentum microscope for time resolved band structure imaging. *Review of Scientific Instruments*, 79(5):053702, 2008.

[285] Gerd Schönhense. Fast k-space mapping of electronic bands using time-of-flight based cathode-lens microspectroscopy. *Microscopy and Microanalysis*, 21(S4):118–123, 2015.

[286] G Schönhense, A Oelsner, O Schmidt, GH Fecher, V Mergel, O Jagutzki, and H Schmidt-Böcking. Time-of-flight photoemission

electron microscopy–a new way to chemical surface analysis. *Surface science*, 480(3):180–187, 2001.

[287] A Oelsner, O Schmidt, M Schicketanz, M Klais, G Schönhense, V Mergel, O Jagutzki, and H Schmidt-Böcking. Microspectroscopy and imaging using a delay line detector in time-of-flight photoemission microscopy. *Review of Scientific Instruments*, 72(10):3968–3974, 2001.

[288] Yoichi Uehara, Tadamasa Ushiroku, Sukekatsu Ushioda, and Yoshitada Murata. High resolution time-of-flight electron spectrometer. *Japanese Journal of Applied Physics*, 29(12R):2858, 1990.

[289] CA Arrell, Jose Ojeda, Mazyar Sabbar, WA Okell, Tobias Witting, T Siegel, Z Diveki, S Hutchinson, L Gallmann, Ursula Keller, et al. A simple electron time-of-flight spectrometer for ultrafast vacuum ultraviolet photoelectron spectroscopy of liquid solutions. *Review of scientific instruments*, 85(10):103117, 2014.

[290] Alexander Kothe, Jan Metje, Martin Wilke, Alexandre Moguilevski, Nicholas Engel, Ruba Al-Obaidi, Clemens Richter, Ronny Golnak, Igor Yu Kiyan, and Emad F Aziz. Time-of-flight electron spectrometer for a broad range of kinetic energies. *Review of Scientific Instruments*, 84(2):023106, 2013.

[291] A Zaporozhchenko-Zymaková, D Kutnyakhov, K Medjanik, C Tusche, O Fedchenko, S Chernov, M Ellguth, SA Nepijko, HJ Elmers, and G Schönhense. Momentum-resolved photoelectron absorption in surface barrier scattering on ir (111) and graphene/ir (111). *Physical Review B*, 96(15):155108, 2017.

[292] A Kronenberg, J Braun, J Minár, H-J Elmers, D Kutnyakhov, AV Zaporozhchenko, R Wallauer, S Chernov, K Medjanik, G Schönhense, et al. Dirac cone and pseudogapped density of states in the topological half-heusler compound yptbi. *Physical Review B*, 94(16):161108, 2016.

[293] C Tusche, P Goslawski, D Kutnyakhov, M Ellguth, K Medjanik, HJ Elmers, S Chernov, R Wallauer, D Engel, A Jankowiak, et al. Multi-mhz time-of-flight electronic bandstructure imaging of graphene on ir (111). *Applied Physics Letters*, 108(26):261602, 2016.

[294] G Schönhense, K Medjanik, S Chernov, D Kutnyakhov, O Fedchenko, M Ellguth, D Vasilyev, A Zaporozhchenko-Zymakova, D Panzer, A Oelsner, et al. Spin-filtered time-of-flight k-space microscopy of ir–towards the complete photoemission experiment. *Ultramicroscopy*, 183:19–29, 2017.

[295] D Kutnyakhov, S Chernov, K Medjanik, R Wallauer, C Tusche, M Ellguth, SA Nepijko, M Krivenkov, J Braun, S Borek, et al. Spin texture of time-reversal symmetry invariant surface states on w (110). *Scientific reports*, 6:29394, 2016.

[296] HJ Elmers, D Kutnyakhov, SV Chernov, K Medjanik, O Fedchenko, A Zaporozhchenko-Zymakova, M Ellguth, C Tusche, J Viefhaus, and G Schönhense. Hosting of surface states in spin–orbit induced projected bulk band gaps of w (1 1 0) and ir (1 1 1). *Journal of Physics: Condensed Matter*, 29(25):255001, 2017.

[297] RR Goruganthu and WG Wilson. Relative electron detection efficiency of microchannel plates from 0–3 kev. *Review of scientific instruments*, 55(12):2030–2033, 1984.

[298] H Matsuda, K Goto, L Toth, M Morita, S Kitagawa, F Matsui, M Hashimoto, C Sakai, T Matsushita, and H Daimon. Development of display-type ellipsoidal mesh analyzer: Computational evaluation and experimental validation. *Journal of Electron Spectroscopy and Related Phenomena*, 195:382–398, 2014.

[299] Tobias Saule, Stephan Heinrich, Johannes Schötz, Nicolai Lilienfein, Maximilian Högner, O deVries, M Plötner, Johannes Weitenberg, D Esser, J Schulte, et al. High-flux ultrafast extreme-ultraviolet photoemission spectroscopy at 18.4 mhz pulse repetition rate. *Nature communications*, 10(1):458, 2019.

[300] G. Schonhense, K. Medjanik, O. Fedchenko, M. Ellguth1, S. Chernov, A. Zaporozhchenko-Zymakova, D. Vasilyev, S. Babenkov, A. Oelsner, G. hrwall, P. Baumgrtel, B. Schnhense, and H. J. Elmers. Variable bunching of electron beams for time-of-flight k-space microscopy using a fast electron-optical chopper. *In preparation.*

[301] Andre K Geim and Irina V Grigorieva. Van der waals heterostructures. *Nature*, 499(7459):419, 2013.

[302] Jingang Wang, Fengcai Ma, Wenjie Liang, and Mengtao Sun. Electrical properties and applications of graphene, hexagonal boron nitride (h-bn), and graphene/h-bn heterostructures. *Materials Today Physics*, 2:6–34, 2017.

[303] Min Yi and Zhigang Shen. A review on mechanical exfoliation for the scalable production of graphene. *Journal of Materials Chemistry A*, 3(22):11700–11715, 2015.

[304] Millicent B Smith and Josef Michl. Singlet fission. *Chemical reviews*, 110(11):6891–6936, 2010.

[305] MC Hanna and AJ Nozik. Solar conversion efficiency of photovoltaic and photoelectrolysis cells with carrier multiplication absorbers. *Journal of Applied Physics*, 100(7):074510, 2006.

[306] M Tuan Trinh, Andrew Pinkard, Andrew B Pun, Samuel N Sanders, Elango Kumarasamy, Matthew Y Sfeir, Luis M Campos, Xavier Roy, and X-Y Zhu. Distinct properties of the triplet pair state from singlet fission. *Science Advances*, 3(7):e1700241, 2017.

[307] Kiyoshi Miyata, Felisa S Conrad-Burton, Florian L Geyer, and X-Y Zhu. Triplet pair states in singlet fission. *Chemical reviews*, 119(6):4261–4292, 2019.

[308] Wai-Lun Chan, Timothy C Berkelbach, Makenzie R Provorse, Nicholas R Monahan, John R Tritsch, Mark S Hybertsen, David R Reichman, Jiali Gao, and X-Y Zhu. The quantum coherent mechanism for singlet fission: Experiment and theory. *Accounts of chemical research*, 46(6):1321–1329, 2013.

[309] Eric G Fuemmeler, Samuel N Sanders, Andrew B Pun, Elango Kumarasamy, Tao Zeng, Kiyoshi Miyata, Michael L Steigerwald, X-Y Zhu, Matthew Y Sfeir, Luis M Campos, et al. A direct mechanism of ultrafast intramolecular singlet fission in pentacene dimers. *ACS central science*, 2(5):316–324, 2016.

[310] Samuel N Sanders, Elango Kumarasamy, Andrew B Pun, M Tuan Trinh, Bonnie Choi, Jianlong Xia, Elliot J Taffet, Jonathan Z Low, John R Miller, Xavier Roy, et al. Quantitative intramolecular singlet

fission in bipentacenes. *Journal of the American Chemical Society*, 137(28):8965–8972, 2015.

[311] N Monahan and X-Y Zhu. Charge transfer–mediated singlet fission. *Annual review of physical chemistry*, 66:601–618, 2015.

[312] Daiki Shingai, Yusuke Ide, Woon Yong Sohn, and Kenji Katayama. Photoexcited charge carrier dynamics of interconnected tio 2 nanoparticles: evidence of enhancement of charge separation at anatase–rutile particle interfaces. *Physical Chemistry Chemical Physics*, 20(5):3484–3489, 2018.

[313] Detlef W Bahnemann, Marcus Hilgendorff, and Ruediger Memming. Charge carrier dynamics at tio2 particles: reactivity of free and trapped holes. *The Journal of Physical Chemistry B*, 101(21):4265–4275, 1997.

[314] Yasuhiro Yamada and Yoshihiko Kanemitsu. Determination of electron and hole lifetimes of rutile and anatase tio2 single crystals. *Applied Physics Letters*, 101(13):133907, 2012.

[315] Mingchun Xu, Youkun Gao, Elias Martinez Moreno, Marinus Kunst, Martin Muhler, Yuemin Wang, Hicham Idriss, and Christof Wöll. Photocatalytic activity of bulk tio 2 anatase and rutile single crystals using infrared absorption spectroscopy. *Physical Review Letters*, 106(13):138302, 2011.

[316] Ryuzi Katoh, Miki Murai, and Akihiro Furube. Electron–hole recombination in the bulk of a rutile tio2 single crystal studied by subnanosecond transient absorption spectroscopy. *Chemical Physics Letters*, 461(4-6):238–241, 2008.

[317] Amanda R Muraca, Matthew D. Kershis, Nicholas Camillone, and Michael G. White. Ultrafast dynamics of acetone photooxidation on tio2(110). *In preparation.*

[318] Robert Wallauer, Johannes Reimann, Nico Armbrust, Jens Güdde, and Ulrich Höfer. Intervalley scattering in mos2 imaged by two-photon photoemission with a high-harmonic probe. *Applied Physics Letters*, 109(16):162102, 2016.

[319] Fang Liu, Mark E Ziffer, Kameron R Hansen, Jue Wang, and Xiaoyang Zhu. Direct determination of band-gap renormalization in the photoexcited monolayer mos 2. *Physical Review Letters*, 122(24):246803, 2019.

[320] Jan Heye Buss, He Wang, Yiming Xu, Julian Maklar, Frederic Joucken, Lingkun Zeng, Sebastian Stoll, Chris Jozwiak, John Pepper, Yi-De Chuang, et al. A setup for extreme-ultraviolet ultrafast angle-resolved photoelectron spectroscopy at 50-khz repetition rate. *Review of Scientific Instruments*, 90(2):023105, 2019.

[321] MengXing Na, Arthur K Mills, Fabio Boschini, Matteo Michiardi, Benjamin Nosarzewski, Ryan P Day, Elia Razzoli, Alexander Sheyerman, Michael Schneider, Giorgio Levy, et al. Direct determination of mode-projected electron-phonon coupling in the time-domain. *arXiv preprint arXiv:1902.05572*, 2019.

[322] AK Mills, S Zhdanovich, MX Na, F Boschini, E Razzoli, M Michiardi, A Sheyerman, M Schneider, TJ Hammond, V Süss, et al. Cavity-enhanced high harmonic generation for xuv time-resolved arpes. *arXiv preprint arXiv:1902.05997*, 2019.

[323] Xiaodong Xu, Wang Yao, Di Xiao, and Tony F Heinz. Spin and pseudospins in layered transition metal dichalcogenides. *Nature Physics*, 10(5):343, 2014.

[324] Di Xiao, Gui-Bin Liu, Wanxiang Feng, Xiaodong Xu, and Wang Yao. Coupled spin and valley physics in monolayers of mos 2 and other group-vi dichalcogenides. *Physical review letters*, 108(19):196802, 2012.

[325] M Kolbe, P Lushchyk, B Petereit, HJ Elmers, G Schönhense, A Oelsner, C Tusche, and J Kirschner. Highly efficient multichannel spin-polarization detection. *Physical review letters*, 107(20):207601, 2011.

[326] Vincent Stimper, Stefan Bauer, Ralph Ernstorfer, Bernhard Schölkopf, and R Patrick Xian. Multidimensional contrast limited adaptive histogram equalization. *arXiv preprint arXiv:1906.11355*, 2019.

[327] P Russbueldt, T Mans, J Weitenberg, HD Hoffmann, and R Poprawe. Compact diode-pumped 1.1 kw yb: Yag innoslab femtosecond amplifier. *Optics letters*, 35(24):4169–4171, 2010.

[328] Jan-Philipp Negel, Andreas Voss, Marwan Abdou Ahmed, Dominik Bauer, Dirk Sutter, Alexander Killi, and Thomas Graf. 1.1 kw average output power from a thin-disk multipass amplifier for ultrashort laser pulses. *Optics letters*, 38(24):5442–5445, 2013.

[329] Davis J Richardson, J Nilsson, and WA Clarkson. High power fiber lasers: current status and future perspectives. *JOSA B*, 27(11):B63–B92, 2010.

[330] Michael Müller, Arno Klenke, Albrecht Steinkopff, Henning Stark, Andreas Tünnermann, and Jens Limpert. 3.5 kw coherently combined ultrafast fiber laser. *Optics letters*, 43(24):6037–6040, 2018.

[331] Tino Eidam, Jan Rothhardt, Fabian Stutzki, Florian Jansen, Steffen Hädrich, Henning Carstens, Cesar Jauregui, Jens Limpert, and Andreas Tünnermann. Fiber chirped-pulse amplification system emitting 3.8 gw peak power. *Optics express*, 19(1):255–260, 2011.

[332] K Hejaz, M Shayganmanesh, R Rezaei-Nasirabad, A Roohforouz, S Azizi, A Abedinajafi, and V Vatani. Modal instability induced by stimulated raman scattering in high-power yb-doped fiber amplifiers. *Optics letters*, 42(24):5274–5277, 2017.

[333] Jens Limpert, Arno Klenke, Marco Kienel, Sven Breitkopf, Tino Eidam, Steffen Hädrich, Cesar Jauregui, and Andreas Tünnermann. Performance scaling of ultrafast laser systems by coherent addition of femtosecond pulses. *IEEE Journal of Selected Topics in Quantum Electronics*, 20(5):268–277, 2014.

[334] Arno Klenke, Sven Breitkopf, Marco Kienel, Thomas Gottschall, Tino Eidam, Steffen Hädrich, Jan Rothhardt, Jens Limpert, and Andreas Tünnermann. 530 w, 1.3 mj, four-channel coherently combined femtosecond fiber chirped-pulse amplification system. *Optics letters*, 38(13):2283–2285, 2013.

[335] Arno Klenke, Steffen Hädrich, Tino Eidam, Jan Rothhardt, Marco Kienel, Stefan Demmler, Thomas Gottschall, Jens Limpert, and Andreas Tünnermann. 22 gw peak-power fiber chirped-pulse-amplification system. *Optics letters*, 39(24):6875–6878, 2014.

[336] Andreas Vernaleken, Johannes Weitenberg, Thomas Sartorius, Peter Russbueldt, Waldemar Schneider, Sarah L. Stebbings, Matthias F. Kling, Peter Hommelhoff, Hans-Dieter Hoffmann, Reinhart Poprawe, Ferenc Krausz, Theodor W. Hänsch, and Thomas Udem. Single-pass high-harmonic generation at 20.8 mhz repetition rate. *Opt. Lett.*, 36(17):3428–3430, Sep 2011.

[337] S. Hädrich, M. Krebs, J. Rothhardt, H. Carstens, S. Demmler, J. Limpert, and A. Tünnermann. Generation of w level plateau harmonics at high repetition rate. *Opt. Express*, 19(20):19374–19383, Sep 2011.

[338] Manuel Krebs, Steffen Hädrich, Stefan Demmler, Jan Rothhardt, Amelle Zaïr, Luke Chipperfield, Jens Limpert, and Andreas Tünnermann. Towards isolated attosecond pulses at megahertz repetition rates. *Nature photonics*, 7(7):555, 2013.

[339] Jan Rothhardt, Steffen Hädrich, Arno Klenke, Stefan Demmler, Armin Hoffmann, Thomas Gotschall, Tino Eidam, Manuel Krebs, Jens Limpert, and Andreas Tünnermann. 53 w average power few-cycle fiber laser system generating soft x rays up to the water window. *Optics letters*, 39(17):5224–5227, 2014.

[340] Steffen Hädrich, Arno Klenke, Jan Rothhardt, Manuel Krebs, Armin Hoffmann, Oleg Pronin, Vladimir Pervak, Jens Limpert, and Andreas Tünnermann. High photon flux table-top coherent extreme-ultraviolet source. *Nature Photonics*, 8(10):779, 2014.

[341] Robert Klas, Stefan Demmler, Maxim Tschernajew, Steffen Hädrich, Yariv Shamir, Andreas Tünnermann, Jan Rothhardt, and Jens Limpert. Table-top milliwatt-class extreme ultraviolet high harmonic light source. *Optica*, 3(11):1167–1170, 2016.

[342] Birgitta Bernhardt, Akira Ozawa, Andreas Vernaleken, Ioachim Pupeza, Jan Kaster, Yohei Kobayashi, Ronald Holzwarth, Ernst Fill, Ferenc Krausz, Theodor W. Hänsch, and Thomas Udem. Vacuum ultraviolet frequency combs generated by a femtosecond enhancement cavity in the visible. *Opt. Lett.*, 37(4):503–505, Feb 2012.

[343] Florian Emaury, Andreas Diebold, Clara J Saraceno, and Ursula Keller. Compact extreme ultraviolet source at megahertz pulse repetition rate with a low-noise ultrafast thin-disk laser oscillator. *Optica*, 2(11):980–984, 2015.

[344] Michele Puppin, Yunpei Deng, CW Nicholson, Johannes Feldl, NBM Schröter, Hendrik Vita, PS Kirchmann, Claude Monney, Laurenz Rettig, Martin Wolf, et al. Time-and angle-resolved photoemission spectroscopy of solids in the extreme ultraviolet at 500 khz repetition rate. *Review of Scientific Instruments*, 90(2):023104, 2019.

[345] Francois Labaye, Maxim Gaponenko, Valentin J Wittwer, Clément Paradis, Norbert Modsching, Loc Merceron, Andreas Diebold, Florian Emaury, IJ Graumann, CR Phillips, et al. Sesam-modelocked thin-disk laser (tdl) with intracavity high-harmonic generation (hhg). In *Advanced Solid State Lasers*, pages ATh5A–3. Optical Society of America, 2017.

[346] Shambhu Ghimire, Anthony D DiChiara, Emily Sistrunk, Pierre Agostini, Louis F DiMauro, and David A Reis. Observation of high-order harmonic generation in a bulk crystal. *Nature physics*, 7(2):138, 2011.

[347] Tran Trung Luu, M Garg, S Yu Kruchinin, Antoine Moulet, M Th Hassan, and Eleftherios Goulielmakis. Extreme ultraviolet high-harmonic spectroscopy of solids. *Nature*, 521(7553):498, 2015.

[348] Seunghwoi Han, Hyunwoong Kim, Yong Woo Kim, Young-Jin Kim, Seungchul Kim, In-Yong Park, and Seung-Woo Kim. High-harmonic generation by field enhanced femtosecond pulses in metal-sapphire nanostructure. *Nature communications*, 7:13105, 2016.

[349] Giulio Vampa, Sergey Vasilyev, Hanzhe Liu, Mike Mirov, Philip H Bucksbaum, and David A Reis. Characterization of high-harmonic emission from zno up to 11 ev pumped with a cr: Zns high-repetition-rate source. *Optics letters*, 44(2):259–262, 2019.

[350] HF-W Sadrozinski, M Baselga, S Ely, V Fadeyev, Z Galloway, J Ngo, C Parker, D Schumacher, A Seiden, A Zatserklyaniy, et al. Sensors for ultra-fast silicon detectors. *Nuclear Instruments and Methods in*

Physics Research Section A: Accelerators, Spectrometers, Detectors and Associated Equipment, 765:7–11, 2014.

[351] Gabriele Giacomini, Francesco Lanni, and Alessandro Tricoli. Development of a technology for the fabrication of low-gain avalanche detectors at bnl. *arXiv preprint arXiv:1811.04152*, 2018.

[352] AR Faruqi and G McMullan. Electronic detectors for electron microscopy. *Quarterly reviews of biophysics*, 44(3):357–390, 2011.

[353] M Fisher-Levine and Andrei Nomerotski. Timepixcam: A fast optical imager with time-stamping. *Journal of Instrumentation*, 11(03):C03016, 2016.

[354] Adam Roberts, P Svihra, A Al-Refaie, H Graafsma, J Küpper, K Majumdar, K Mavrokoridis, Andrei Nomerotski, D Pennicard, B Philippou, et al. First demonstration of 3d optical readout of a tpc using a single photon sensitive timepix3 based camera. *Journal of Instrumentation*, 14(06):P06001, 2019.

[355] T Poikela, J Plosila, T Westerlund, M Campbell, M De Gaspari, X Llopart, V Gromov, R Kluit, M van Beuzekom, F Zappon, et al. Timepix3: a 65k channel hybrid pixel readout chip with simultaneous toa/tot and sparse readout. *Journal of instrumentation*, 9(05):C05013, 2014.

[356] AR Faruqi, R Henderson, M Pryddetch, P Allport, and A Evans. Direct single electron detection with a cmos detector for electron microscopy. *Nuclear Instruments and Methods in Physics Research Section A: Accelerators, Spectrometers, Detectors and Associated Equipment*, 546(1-2):170–175, 2005.